Quantitative Multiscale Modelling of Magnetic Materials: From First Principles to Atomic and Continuum Models

Sean Stansill

University of Leeds

School of Physics and Astronomy

Submitted in accordance with the requirements for the degree of

Doctor of Philosophy

February, 2024

Intellectual Property Statement

The candidate confirms that the work submitted is his own and that appropriate credit has been given where reference has been made to the work of others.

Acknowledgements

This work is dedicated to my family who've stood by me and shaped me into the person I am today. Without their support and belief in me, this work would've never been possible.

I give special thanks to Joe, my supervisor, who has been a great mentor, teacher and friend, since even before I began my PhD. He has given me invaluable opportunities for personal and profession growth. For this, I'll always be grateful.

I thank my friends Pete, Emily, and Riccardo for helping me survive the COVID-19 lockdowns and being the most supportive housemates anyone could hope for. Emily and Riccardo in particular have been great mentors in the magnetism community and have generated great discussions about my work, my future, life advice. My colleagues Giannis, Robert, and Thomas have always happy endured my ramblings when banging my head against a wall with a problem. And when we couldn't find a solution, they proved great drinking buddies too! Without their support, stimulating conversation, and camaraderie, I would've never survived completing a PhD. I also want to thank my good friend Alex for her saint-like patience and sound advice through all my personal difficulties.

Finally, I extend my thanks internationally to my colleagues at Kyoto university, in particular Taka, Ono-san, Ryusuke, and Taga who were incredibly welcoming and made my stay in Japan unforgettable.

Abstract

In recent years, antiferromagnets have become one of the the primary classes of magnetic materials studied for spintronic device applications. The development of new experimental techniques has made these materials easier to study, though challenges remain as the compensated order makes it difficult to resolve the dynamics of individual sublattices, and their multi-sublattice structure means the magnetic symmetry is typically lower than their ferromagnetic counterparts, permitting more complicated Hamiltonians and making the development of physical models difficult. As a result, computational techniques are playing an increasing role in advancing research on antiferromagnets. Proper parameterisation of these computational models is vital for realistic and reproducible research.

This work aimed to better understand the thermodynamics of the prototypical easy-plane antiferromagnet NiO. NiO is considered to be a simple antiferromagnet, yet there are several conflicting models which have been used to explain different phenomena in this material. No model thus far has been able to describe all aspects of this material. In order to understand complex antiferromagnetic materials, it is vital that we have a complete understanding of the simplest examples.

In this work, a combination of analytic and numerical calculations are used which are compared to the best available experimental measurements throughout. Analytic calculations of the finite temperature behaviour of antiferromagnets are primarily based on Linear Spin Wave Theory (LSWT). Numerical simulations are a combination of spin dynamics calculations using the Landau-Lifshitz-Gilbert (LLG) equation and Monte Carlo methods applied to atomistic models of magnetic materials. A stochastic Langevin term is used to augment the LLG equation which allows modelling at finite temperatures.

In Chapter 4 of this work, we develop a framework of tools to create an atomistic model of NiO which hasn't been used previously in the literature and is consistent with both neutron scattering experiments and advanced ab-initio calculations, has the correct ground state, and is consistent with the magnetic symmetry of the crystal. In Chapter 5, we use constrained Monte Carlo and analytic calculations to show that the temperature dependence of the easy-plane anisotropy in NiO–from magnetic

dipole-dipole interactions–deviates from the Callen-Zenner scaling for a uniaxial magnetocrystalline anisotropy. Further, we derive new expressions for the temperature dependence of the sublattice magnetisation and spin wave stiffness using linear spin wave theory, then compare this to atomistic simulations implemented with a thermal Langevin field which is consistent with Bose-Einstein statistics, as well as experimental measurements. From this, we are able to quantify at which temperature the first order expansion of Holstein-Primakoff operators breaks down, and we show that the temperature dependence of the Kittel mode is approximately the same as the sublattice magnetisation. Using atomistic simulations, we calculate the temperature dependence of the magnetic damping (magnon scattering) and, by comparing with experimental measurements, we show that damping due to magnon-electron and magnon-phonon scattering is negligible at low temperatures. In Chapter 6, we show that all experimentally observed resonant modes in NiO appear using our model but that many of these modes are non-linear in origin so cannot be understood using the linear spin wave approximations which have been used previously. This gives new insight into the physics of NiO which helps the interpretation of dynamical experiments, and resolves the discrepancies between previous models and the observed phenomena in NiO. In the final chapter, we develops a new method for calculating the finite temperature value of macroscopic parameters in any magnetic material. This leverages the fundamentals of thermodynamics and statistical mechanics, and has broad applications for the multiscale modelling of magnetic materials.

Contents

Abbreviations

AC	Alternating Current
AFMR	Antiferromagnetic Resonance
ASD	Atomistic Spin Dynamics
ASIC	Application Specific Integrated Circuit
bcc	Body Centred Cubic
BE	Bose-Einstein
BLS	Brillouin Light Scattering
CAS	Computer Algebra System
CMC	Constrained Monte Carlo
CMOS	Complimentary Metal Oxide Semiconductor
CPU	Central Processing Unit
CPW	Co-Planar Waveguide
DFT	Density Functional Theory
DMI	Dzyaloshinskii-Moriya Interaction
DMFT	Dynamic Mean Field Theory
DRAM	Dynamics Random Access Memory
EM	Electromagnet(ic)
ESR	Electron Spin Resonance
fcc	Face Centred Cubic
FD	Fermi-Dirac
FMR	Ferromagnetic Resonance
FWHM	Full Width Half Maximum
GGA	Generalised Gradient Approximation
GMR	Giant Magnetoresistance
GPU	Graphics Processing Unit
HAMR	Heat Assisted Magnetic Recording
HDD	Hard Drive Disk
INS	Inelastic Neutron Scattering
IP	In-Plane
ISHE	Inverse Spin Hall Effect
ISRS	Impulsive Stimulated Raman Spectroscopy
LCAO	Linear Combination of Atomic Orbitals
LDA	Local Density Approximation

LL	Landau-Lifshitz
LLB	Landau-Liftshiz-Bloch
LLG	Landau-Liftshiz-Gilbert
LSD	Local Spin Density
MB	Maxwell-Boltzmann
MFT	Mean Field Theory
NMR	Nuclear Magnetic Resonance
NPU	Neural Processing Unit
OOP	Out-of-Plane
OPTP	Optical Pump THz Probe
OPOP	Optical Pump Optical Probe
PIMM	Pulsed Inductive Microwave Magnetometry
PSD	Power Spectral Density
QSGW	Quasiparticle Self-Consistent GW Method
RAM	Random Access Memory
RF	Radio Frequency
RIXS	Resonant Inelastic X-ray Scattering
SBMF	Schwinger Boson Mean-Field
sc	Simple Cubic
SOC	Spin-Orbit Coupling
SOI	Spin-Orbit Interaction
SOT	Spin-Orbit Torque
SRAM	Static Random Access Memory
SSD	Solid State Disk
STT	Spin-Transfer Torque
TD-DFT	Time-Dependent Density Functional Theory
THz-TDS	THz Time Domain Spectroscopy
TPOP	THz Pump Optical Probe
TPU	Tensor Processing Unit
VNA	Vector Network Analyser
XRD	X-Ray Diffraction

Mathematical Notation

$\mathbf{v}$	Vector
$\mathbb{A}$	Matrix
$\hat{\mathbf{u}}$	Unit Vector
$\langle M \rangle$	Thermal/Time Average
$\langle \hat{\mathcal{H}} \rangle$	Thermal Expectation Value of a Quantum Operator
†	Hermitian Conjugate
$^\intercal$	Matrix transpose
$\hat{p}$	Quantum operator
$\mathbb{1}$	Identity Matrix
$\times$	Cross product
$\cdot$	Dot Product
$\hat{\mathcal{H}}$	Quantum Hamiltonian Operator
$\mathcal{H}$	Classical Hamiltonian Function
$[\hat{\mathcal{H}}]$	Matrix Form of a Hamiltonian
$\mathbb{P}$	Group
$[001]$	Crystallographic Direction
(001)	Crystallographic Plane
$\langle 001 \rangle$	Family of Crystal Directions
$\{001\}$	Family of Crystal Planes
$\mathcal{FT}[f]$	Fourier Transform
$a := b$	a defined as b
$f \equiv g$	f is equivalent to g
$a : \mathbf{x} \to \mathbf{y}$	a is a linear map
Y_{lm}	Real Spherical Harmonics
Y_l^m	Complex Spherical Harmonics

Common Symbols

f	Non-Angular Frequency
ω	Angular Frequency ($2\pi f$)
m_e	Electron Rest Mass
c	Speed of Light
e	Elementary Charge
ϵ_0	Permittivity of Free Space
μ_0	Permeability of Free Space
μ_B	Bohr Magneton
h	Planck's Constant
$\hbar$	$h/2\pi$
$\mathbf{B}$	Magnetic Flux Density
$\mathbf{H}$	Magnetic Field
μ_S	Spin Magnetic Moment
a	Conventional Lattice Parameter
T	Temperature
T_c	Critical/Curie Temperature
T_N	Néel Temperature
k_B	Boltzmann's Constant
$\mathcal{H}$	Classical Hamiltonian
$\hat{\mathcal{H}}$	Quantum Hamiltonian Operator
E	(Internal) Energy
γ	Gyromagnetic Ratio of a Free Electron
ν_{WS}	Wigner-Seitz Volume
S	Spin Quantum Number
$\mathbf{S}$	Classical Spin Vector
K	Anisotropy Constant
J	Exchange Interaction Strength

Chapter 1

Introduction

Modern computers use semicondutor transistors to do computation. At the time of writing, the Taiwan Semiconductor Manufacturing Company (TSMC) uses a 3nm lithography processes to produce computing chips, and Intel has a roadmap which includes plans for a 2nm lithography node which corresponds to less than 10 silicon atomic spacings. Single atom control of semiconductor manufacturing will mark the end of semiconductor innovation in both speed and power usage. To combat the slow-down of performance improvements for computing devices, companies are increasingly using specialist accelerator cards such as:

- Graphics processing units (GPUs)
- Neural processing units (NPUs)
- Tensor processing units (TPUs)
- Application specific integrated circuits (ASICs),

as well as traditional central processing units (CPUs). Each of these have architectures (configurations of transistors and memory technologies) which are optimised to perform specific tasks. These accelerator cards are used in everything from internet of things (IoT) devices to supercomputers. But, they suffer from the physical limits of semiconductor technologies.

Moving data between dynamic random access memory (DRAM), static RAM (SRAM), and the CPU itself uses a huge amount of energy (over 50% for a microprocessor in 2012 [1]). So, another technique to improve efficiency is to use new, innovative computing architectures called non Von Neumann architectures such as in-memory computing [2] which combines the role of random access memory (RAM) and CPU to improve energy efficiency; others are exploring completely new models of non-deterministic computing (probabilistic computing) [3].

Memory storage manufacturers are struggling with similar problems. Semiconductor-based solid state disks (SSDs) are now sold in greater quantities than magnetic hard drive disks (HDDs), though hard drives still dominate in the total storage produced [4]. Technologies like heat assisted magnetic recording (HAMR) are being developed to improve the performance and storage capacities of hard drives but SSDs have the same difficulties innovating as CPUs because of the physical limits of near single atom control

of semiconductor manufacturing. Other technologies like phase change memory were promising, but have now been abandoned by all large companies.

For all of these applications, magnetic materials offer a new path to innovation. These are spintronic devices which combine the control of spin degrees of freedom with conventional electronics. Magnetic random access memory (MRAM)–a spintronics technology–is already used in low power devices [5]. MRAM uses ferromagnetic tunnel junctions to encode information in the relative orientation of two ferromagnetic layers which can be controlled electrically using bit lines and word lines, as with SSDs. But, MRAM devices are much more energy efficient and are resistant to data corruption from rare events like cosmic rays, so create fewer errors in data sensitive applications like space and banking [2, 6]. MRAM is a large part of TSMC's technology roadmap for embedded devices [5] with new spin-orbit torque (SOT) switching mechanisms driving innovation. Ferromagnets have the problem of stray fields, slow dynamics, and poor integration with complementary metal oxide (CMOS) manufacturing processes which are ubiquitous in the semiconductor industry. Stray fields limit the density of bits in MRAM devices, slow dynamics limits the operational frequency of these devices, and poor compatibility with CMOS makes adoption by private companies slow. Yet magnetic materials can be used to make accelerator cards discussed above; probabilistic computing devices, and compute-in-memory devices, so are a viable route to post-silicon computing. The emerging field of quantum computing promises exponential improvements in computing performance for specific applications like catalysis, medicine, and AI [7]. Magnetic materials can also be used as storage devices for quantum processors [8, 9] which is one of the most significant problems for the long-term scalability of quantum computers.

Antiferromagnets don't suffer from the same drawbacks as ferromagnets because of their compensated order, so are being explored as a class of materials which could be used in next generation computing and memory storage devices. They're fast (THz resonant dynamics), and have no stray field. But, they still suffer with poor CMOS compatibility. Compensated order means these materials can be difficult to measure experimentally. So, to better understand these materials, and to aid the design of devices, computational simulations–like those used in this work–are an important tool

to advance the field. Even some of the most well studied antiferromagnets like NiO are still poorly understood. It's very difficult to create useful devices from these materials until we understand them at a fundamental level. The work carried out here aims to do just this; using fundamental physical laws including symmetry and thermodynamics, and applying multiscale parameterisation using cutting edge methods, we study NiO and resolve the discrepancies in the literature of this material. In this work, we show that its dynamics are more complex than have been considered in previous works, that the thermodynamics requires careful consideration, that magnetocrystalline anisotropy isn't needed to fully explain observations of NiO, and we are able to separate different sources of energy losses from the magnetic system. The final chapter develops a new framework for studying thermodynamics in magnetic materials to ensure correct parameterisation of finite temperature theoretical and continuum models which is applicable to both ferromagnets and antiferromagnets.

Chapter 2

Theory of Magnetism

2.1 The Spin Angular Momentum of an Electron

Electrons carry angular momentum. For electrons bound to atoms, there are two sources of angular momentum: orbital angular momentum and spin angular momentum. Orbital angular momentum, given by the quantum operator $\hat{\mathbf{L}}$ or the classical vector $\mathbf{L}$, is simple to understand. It arises from the motion of electrons around the nucleus of an atom which creates current loops and induces magnetic fields by Faraday's law. Spin angular momentum has no classical analogue; it is predicted by quantum mechanics and is an intrinsic property of the electron, rather than emergent from its motion in space. Spin can be derived from the Pauli exclusion principle of fermions, and the first experimental confirmation that subatomic particles carry spin was the Stern-Gerlach experiment in 1921 which led to Stern winning the 1943 Nobel prize in physics [10, 11].

The spin of an electron is represented by the total spin angular momentum $|S| = \sqrt{S(S+1)}$*, where S is the spin quantum number (equal to $\frac{1}{2}$ for an electron), or as a classical magnetic moment $\boldsymbol{\mu} = \mu_S \mathbf{S}$, where μ_S is the spin magnetic moment and $\mathbf{S}$ is the classical spin vector of unit length. Since electrons are spin-$\frac{1}{2}$ particles, the measurement of an electron's spin along a quantisation axis is either $+\frac{1}{2}$ or $-\frac{1}{2}$. Magnetic order arises because of the interaction of electron spins with their environment. Each spin is a dipole moment which has an associated magnetic field. When the spins of electrons in matter are correlated, there is magnetic order. In crystalline materials, electrons orbiting an atom can have an effective (spin) magnetic moment which isn't an integer multiple of $\frac{1}{2}$, either because of the delocalisation of electrons (so atoms don't have an integer average number of electrons) or because of the orbital contribution to the total magnetic moment (due to spin-orbit coupling). The approximation of representing quantised spins as classical vectors is valid in the limit of large spin $S \gg \frac{1}{2}$. In this limit, there are many spin states that a particle can occupy and the quantum spin state can be thought of as occupying an approximately continuous set of states (ie a vector). Under this approximation, all information about quantum states is lost and quantum effects such as superposition and the exclusion principle are lost.

In the rest of this chapter, we introduce and/or derive the interactions between electron spins and their environment in crystalline materials which will be used in this

*We choose to drop factors of $\hbar$ for simplicity.

work. Other interactions exist in different materials, but we limit ourselves to those found in NiO.

2.2 Origin of Exchange

The classical Heisenberg Hamiltonian is the most common model for exchange in three-dimensional materials with localised charges. Heisenberg exchange is written as*

$$\mathcal{H} = -\frac{1}{2}\sum_{i,j} \mathbf{S}_i \mathbb{J}_{ij} \mathbf{S}_j, \tag{2.1}$$

where the sum is over all spins, $\mathbb{J}_{ij}$ is the exchange tensor which permits anisotropic terms such as Dzyaloshinskii-Moriya interaction (DMI) and two-ion anisotropy, $\mathbf{S}$ are classical spin vectors of unit length, and the factor of $\frac{1}{2}$ accounts for the double counting of interactions in the summation. This choice of classical Hamiltonian is an approximation. Spontaneous magnetic order is a purely quantum effect which is most clearly shown by the Bohr-van Leeuwen theorem [12]. It proves the net magnetisation of a classical electron gas, which is held in a constant magnetic field and in thermal equilibrium, must be zero. So, any Hamiltonian model of a magnetic material should be composed of quantum operators (not classical vectors), and may not necessarily take the same form as Heisenberg exchange†. The approximation of Heisenberg exchange is most valid for insulating magnetic materials‡ and at low temperatures; though scientists have long been surprised by the close agreement of analytic theories and computational models with experiments when using this very simple Hamiltonian.

To understand the origin of exchange, first consider the magnitude of different energies for electrons in solids (see Fig. 2.1). The energy of magnetic dipole-dipole interactions–in units of the Boltzmann constant k_B–is of the order of 1K for unpaired electron spins on neighbouring atoms. This is much too low to account for ferromagnets with Curie temperatures of $\sim$ 1000K. Electrostatic interactions within an atom are of

*Technically this is an augmented Heisenberg model. The typical definition Heisenberg exchange is $\mathcal{H} = -\frac{1}{2}\sum_{i,j} J_{ij}\mathbf{S}_i \cdot \mathbf{S}_j$.

†Higher order model Hamiltonians like biquadratic exchange can be important in certain material systems [13].

‡Under the Born-Oppenheimer / adiabatic approximation–electron dynamics are much faster than spin dynamics, and lattice dynamics are much slower, so can be separated–Heisenberg exchange can still be used.

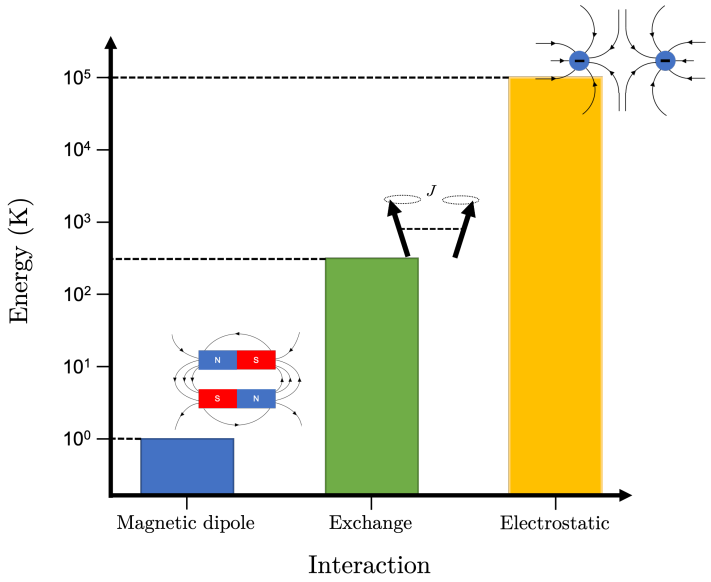

Figure 2.1: Comparison of energy scales for electrons in solids.

the order 10^5K which is too large to account for magnetic behaviour. Instead exchange lies in between these energy scales and electrostatic interactions between unpaired electrons on *neighbouring* atoms must be responsible for magnetic ordering. In the first theories of bonding between atoms, the repulsion of unpaired electrons was ignored as a perturbation. Including this perturbation leads to magnetic order in many-body electron theories.

By the Pauli exclusion principle, overall antisymmetry of electron wavefunctions must be preserved. This, combined with Coulomb interactions between electrons, means ferromagnetic and antiferromagnetic exchange interactions can be derived in a variety of model systems. In Appendix A, we derive a very simple model of both ferromagnetic and antiferromagnetic direct exchange in a hydrogen molecule. The combination of Coulomb interactions between electrons and the Pauli exclusion principle, which couples the kinetic and spin degrees of freedom, leads to Heisenberg exchange in all solids and molecules. Table 2.1 gives some microscopic theories of exchange and the materials they apply to. An analytic expression for the exchange interactions cannot be obtained because the many-body problem is usually incalculable. In this case ab-initio methods such as density functional theory (DFT) can be used to numerically

approximate the solution of the many-body Schrödinger equation, from which exchange interactions can be extracted.

Table 2.1: Common models of the exchange interaction in solids.

Type of Exchange	Materials	Key Concepts
Direct Exchange [14, 15]	N/A	Electrons which give rise to magnetism are localised and have non-zero covalency. Examples include Fe, Co, Ni, EuS, EuO.
Superexchange [16]	Mott and Charge-Transfer Insulators	Ionic bonding, non-magnetic atoms mediate the coupling.
Double exchange [17]	Mixed Valence Metals	High oxidation atoms have unoccupied states which are coupled by non-magnetic atoms.
RKKY [18–20]	Heavy Metals	Coupling between itinerant electrons and nuclear magnetic moments or localised electron spins. Dominant in rare-earth metals and alloys.
Antisymmetric exchange [21, 22]	N/A	DMI–bonds between neighbours lack an inversion centre. Mediated by relativistic spin-orbit coupling at non-magnetic sites.

2.2.1 Superexchange Interaction

We give additional qualitative consideration to the superexchange interaction as it is the dominant mechanism for exchange in NiO. In many materials of scientific interest within antiferromagnetic spintronics, there is very little overlap of orbitals between nearest atoms–species are ionically bonded. Early models of the electron structure in $3d$ transition metal salts struggled to reconcile the conflicting properties of a antiferro-

magnetic exchange and their insulating nature*. This is remedied by considering both next nearest neighbour electron tunnelling and direct exchange [16, 23].

Consider a MnO crystal, the Mn^{2+} cations have a single valence electron and the O^{2-} anions have a filled $2p$ orbital. Non-zero overlap of orbitals only occurs over 180° bond angles (see Fig. 2.2). Electron transfer events from one manganese ion to another permits an indirect exchange interaction via the oxygen ligand over a 180° bond. An antiferromagnetic exchange interaction of the form (A.5) is recovered. For exchange over a 90° bond angle, there is zero overlap of electron orbitals so a purely ferromagnetic, direct exchange Hamiltonian governs the interactions between these spins.

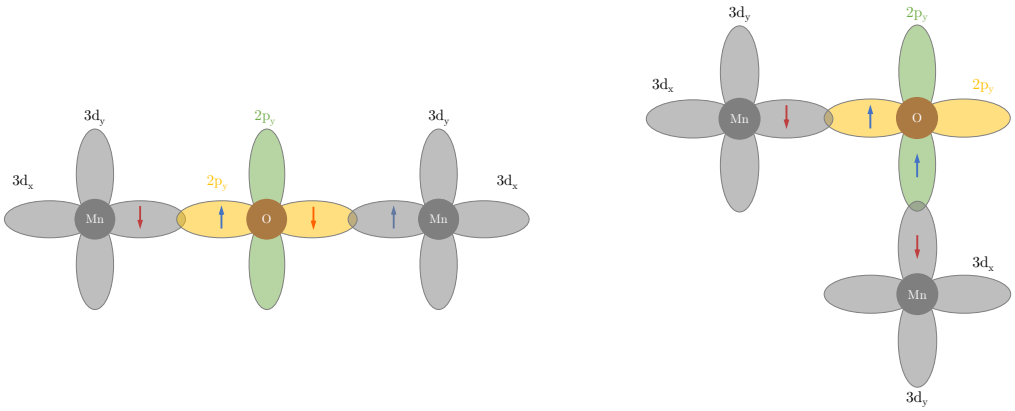

Figure 2.2: Representation of superexchange in MnO. The exchange interaction over a 180° bond is antiferromagnetic due to non-zero overlap of orbitals (*left*). Over a 90° bond, exchange is ferromagnetic due to direct exchange (*right*).

These effects are most concisely expressed by the Goodenough-Kanamori rules [24–27] which state the following:

- When there is a non-zero overlap of orbitals both direct exchange and electron transfer events occur (antiferromagnetic exchange).
- When there is no overlap of orbitals only (ferromagnetic) direct exchange can occur.

*Only theories of direct exchange existed during this period. Antiferromagnetic direct exchange requires large hopping integrals (delocalisation) as can be seen in Appendix A.

- The interaction has a higher energy when there is a greater overlap of orbitals.

This gives a qualitative argument why transition metal salts are almost exclusively antiferromagnets with small ferromagnetic interactions.

2.3 Magnetocrystalline Anisotropy

Exchange couples spins in crystals and molecules such that there is a quantisation axis along which all electron spins are aligned. Considering only exchange, the choice of quantisation axis, $\hat{\mathbf{z}}$, is free; there is continuous symmetry of the magnetisation vector around the unit sphere. Magnetocrystalline anisotropy breaks this continuous symmetry so that there are well defined preferred directions for the magnetisation vector with respect to the crystal axes. Magnetocrystalline anisotropy requires both crystal field splitting, which gives preferred directions for orbital moments, and the relativistic spin-orbit interaction which couples the preferred directions of orbital moments to the spin moments. In Appendix B, we derive the relativistic Hamiltonian which gives rise to spin-orbit coupling and derive expressions for the magnetocrystalline anisotropy in rare earth elements (limit of strong spin-orbit coupling), and in a lighter transition metal with hexagonal crystal symmetry (limit of strong crystal field splitting). Here, we state these results and give a qualitative discussion for a cubic $4f$ material. The first order relativistic Hamiltonian for a single electron orbiting an atom in a magnetic field with hydrogen-like electron orbitals can be written as

$$\begin{aligned}\hat{\mathcal{H}} =& \frac{\hat{\mathbf{p}}^2}{2m_e} - \frac{\hat{\mathbf{p}}^4}{8m_e^2c^2} + V + \frac{\hbar^2}{8m_e^2c^2}\nabla^2 V - \frac{e}{2m_e c}(\hat{\mathbf{L}} + 2\hat{\mathbf{S}}) \cdot \mathbf{B} \\ &+ \frac{\hbar^2}{2m_e^2c^2}\nabla V(\hat{\mathbf{L}} \cdot \hat{\mathbf{S}}) + \frac{e^2}{2m_e c^2}\mathbf{A}^2,\end{aligned} \tag{2.2}$$

where $\hat{\mathbf{p}}$ is the momentum operator, m_e is the electron rest mass, c is the speed of light in a vacuum, V is the electric potential due to the atomic nucleus, $\hat{\mathbf{L}} = \hat{\mathrm{L}}_x\hat{\mathbf{x}} + \hat{\mathrm{L}}_y\hat{\mathbf{y}} + \hat{\mathrm{L}}_z\hat{\mathbf{z}}$ is the vector orbital angular momentum operator, $\hat{\mathbf{S}} = \hat{S}_x\hat{\mathbf{x}} + \hat{S}_y\hat{\mathbf{y}} + \hat{S}_z\hat{\mathbf{z}}$ is the vector spin angular momentum operator, $\mathbf{B}$ is the applied magnetic field, $\hbar$ is the reduced Planck constant and $\mathbf{A}$ is the vector potential of the magnetic field. The most relevant single electron terms for studying magnetic systems are

$$\hat{\mathcal{H}} = -\frac{e}{2m_e c}(\hat{\mathbf{L}} + 2\hat{\mathbf{S}}) \cdot \mathbf{B} + \frac{\hbar^2}{2m_e^2c^2}\nabla V(\mathbf{r})(\hat{\mathbf{L}} \cdot \hat{\mathbf{S}}) + V(\mathbf{r}). \tag{2.3}$$

The first term is the Zeeman energy for an electron in a magnetic field, the second is the spin-orbit coupling and the final term is the electric potential. Next, a simple phenomenological description of the origin of magnetocrystalline anisotropy is given for $4f$ elements where spin-orbit coupling is the dominant energy term. For the $3d$ elements, see Appendix B.

To minimise the energy of an atom in free space, spherically symmetric orbitals with unquenched angular momentum ($\langle \hat{\mathbf{L}} \rangle \neq 0$) are occupied. The electron density (probability amplitude of the wavefunction) of this orbital is shown in Fig. 2.3.

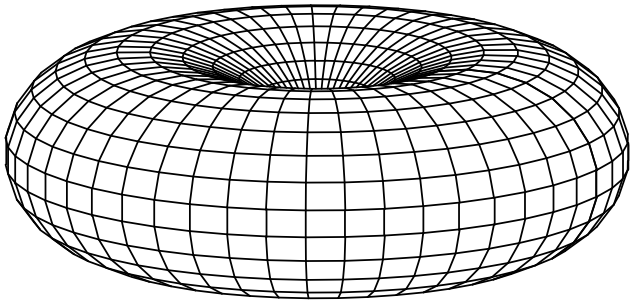

Figure 2.3: Electron density for a $4f$ electron with $m = \pm 3$ ($n = 4$, $l = 3$).

In the absence of other atoms, this orbital can be rotated freely with no change in energy. Inserting this atom into a periodic lattice introduces an additional energy term due to the Coulomb repulsion of neighbouring electron densities. To add this to the Hamiltonian (2.3), we make a transformation to the electric potential

$$V(\mathbf{r}) \mapsto V_0(\mathbf{r}) + V_{\mathrm{CF}}(\mathbf{r}). \tag{2.4}$$

The additional term is the crystal field potential. It is periodic as each atom experiences the same potential due to identical neighbour displacements in the static state (neglecting phonons). This introduces an angular dependence to the energy of this electron orbital with hard and easy axes. The angular dependence of the electron orbital is coupled to the spin degree of freedom by the spin-orbit interaction; in the

limit of large spin-orbit coupling, the spin angular momentum is rigidly coupled with the orbital moment (known as spin-momentum locking). So, when changing the magnetisation direction of a crystal by applying an external magnetic field, the electron density is rotated in the same manner. The shape of the magnetocrystalline anisotropy depends on the lattice structure and its magnitude depends on both the strength of the spin-orbit interaction and the strength of the crystal field*.

Qualitatively, the shape of the anisotropy can be determined for a given system by a thought experiment considering only the symmetry of the crystal and the sign of the effective charge density at other lattice points. In Fig. 2.4, a magnetic ion is located at the origin which is embedded in a simple cubic crystal field with negative effective charges at lattice points. The Coulomb repulsion between the electron density of the central atom and its crystal field is maximised when the orbital lies in the planes of minimum nearest-neighbour distance (the xy, yz and xz planes) which corresponds to hard spin directions along the x-, y-, and z-directions. The repulsion is minimised when the spin moment is parallel to the $\langle 111 \rangle$ directions. So, the $\langle 111 \rangle$ are easy axes. This corresponds to a cubic magnetocrystalline anisotropy. Moving from Pauli operators to classical spin vectors, the first two cubic anisotropy terms are given by

$$\varepsilon = -K_1 \left[(S_x S_y)^2 + (S_y S_z)^2 + (S_z S_x)^2 \right] - K_2 \left[S_x S_y S_z \right]^2 , \tag{2.5}$$

where ε is a single spin energy, K_i are anisotropy constants, and $S_u = \mathbf{S} \cdot \hat{\mathbf{u}}$ is a component of the classical spin vector. Assuming only one anisotropy constant is non-zero, the negative point charges in Fig. 2.4 mean that either $K_1 < 0$, or $K_2 > 0$. This simple thought experiment can be applied to any magnetic material if the site symmetries of the crystal, and electron valences are known. A rigorous symmetry-based framework for determining permitted magnetocrystalline anisotropies is discussed in Chapter 4.

2.4 Magnetic Dipole-Dipole Interactions

As discussed in Section 2.2, the exchange interaction is a many-body electronic effect mediated by the Coulomb interaction. The most fundamental purely magnetic inter-

*These are highly dependent on the nuclear charge, the magnitude of the screened charge of the crystal field, and the interatomic distance.

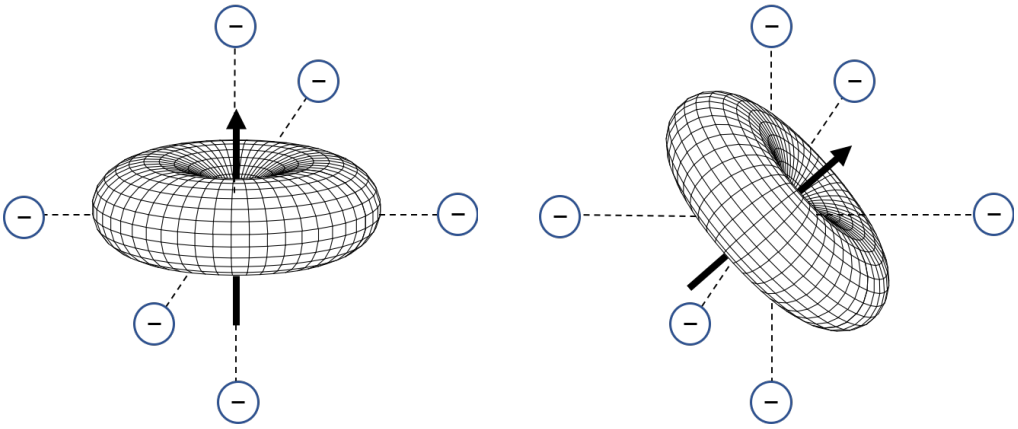

Figure 2.4: Crystal field interaction of an $|l = 3, m = \pm 3\rangle$ electron orbital with nearest neighbour cations along the principal axes. (*left*) High energy state, and (*right*) low energy state. Arrow represents the spin magnetic moment which remains parallel to the orbital moment in the limit of strong spin-orbit coupling.

action is the magnetic dipole-dipole interaction. Every magnetic moment has a dipole field, with which it interacts with other magnetic moments. This is the reason two bar magnets repel or attract dependent on their orientation. For discrete localised magnetic dipoles, the interaction is given by the following Hamiltonian

$$\mathcal{H} = -\frac{1}{2}\sum_{i\neq j}\frac{\mu_0}{4\pi}\frac{3(\boldsymbol{\mu}_i\cdot\hat{\mathbf{r}}_{ij})(\boldsymbol{\mu}_j\cdot\hat{\mathbf{r}}_{ij})-(\boldsymbol{\mu}_i\cdot\boldsymbol{\mu}_j)}{|\mathbf{r}_{ij}|^3}, \tag{2.6}$$

where μ_0 is the permeability of free space, $\boldsymbol{\mu}_i$ is the vector dipole moment of the magnetic dipole at site i, $\mathbf{r}_{ij} = \mathbf{r}_j - \mathbf{r}_i$ is the displacement vector between the moments at sites i and j, and the factor of $\frac{1}{2}$ accounts for the double counting of interactions in the summation. The dipole-dipole interaction is dependent on both the distance between two moments, as well as their alignment. In solid state systems, the magnetic moments are unpaired electron spins which are assumed to be localised on an atomic site. In this case, the magnetic moment is written as $\boldsymbol{\mu}_i = \mu_{S,i}\mathbf{S}_i$ where $\mu_{S,i}$ is the spin magnetic moment and $\mathbf{S}_i$ is the spin vector. The discrete dipole-dipole interaction is then

$$\mathcal{H} = -\frac{1}{2}\sum_{i\neq j}\frac{\mu_0\mu_{S,i}\mu_{S,j}}{4\pi}\frac{3(\mathbf{S}_i\cdot\hat{\mathbf{r}}_{ij})(\mathbf{S}_j\cdot\hat{\mathbf{r}}_{ij})-(\mathbf{S}_i\cdot\mathbf{S}_j)}{|\mathbf{r}_{ij}|^3}. \tag{2.7}$$

In crystals, the dipole-dipole interaction has two contributions; intrinsic dipole-dipole interactions and extrinsic dipole-dipole interactions. Intrinsic dipole-dipole interactions

are dependent on the symmetry of the magnetic crystal and give rise to a dipolar anisotropy which is distinct from magnetocrystalline anisotropy. Extrinsic dipole-dipole interactions are dependent on the size and shape of a sample of a magnetic crystal. In the next sections, these two sources are discussed.

2.4.1 Shape Anisotropy

Shape anisotropy is dependent only on the geometry of a magnetic material of finite size. In ferromagnets, the stray dipole field stores energy. This leads to preferred directions of magnetisation which reduce the free energy of the system. The theory of shape anisotropy in ferromagnets is well known and will not be reproduced here (see [28] or [29] for further reading). Modern research on magnetic materials for spintronic applications almost exclusively uses thin films of magnetic material. Assuming a continuous description of the magnetisation (rather than discrete, as above), the shape anisotropy of these near two-dimensional systems is given by the following energy functional

$$E = \frac{1}{2}\mu_0 M_s^2 \int_V [\mathbf{m}(\mathbf{r}) \cdot \hat{\mathbf{z}}]^2 \, d^3r, \tag{2.8}$$

where M_s is the finite temperature saturation magnetisation of the uniform ferromagnet, the integral is over the whole volume V of the ferromagnet, $\mathbf{m}(\mathbf{r})$ is the continuous reduced magnetisation field, and $\hat{\mathbf{z}}$ is the out of plane direction of the film. The shape anisotropy is minimised when the magnetisation lies in the plane of the thin film and takes the same form as a uniaxial magnetocrystalline anisotropy with $K = \frac{1}{2}\mu_0 M_s^2$.

In infinite antiferromagnets there is no stray field; magnetic moments are compensated. But, in finite sized antiferromagnets, both compensated and uncompensated magnetic surfaces and interfaces introduce an extrinsic contribution to the total dipole-dipole interaction. These are not strictly shape anisotropies but deserve discussion here. The case of uncompensated surfaces is easiest to understand; if a layered antiferromagnet is cleaved such that there is a layer of spins which are ferromagnetically aligned, then there is a small net magnetisation at the surface (see for example figure 1a of [30]) which has an energy contribution of the form of equation (2.8). Compensated interfaces are conceptually more complicated; naïvely these surfaces have a vanishing magnetic dipole field everywhere. But, by symmetry, a non-zero surface magnetisation can be induced because of the broken symmetry (see figure 1c, d of [30]), and must be induced

in linear magnetoelectric materials [31]. The small induced surface magnetisation leads to an additional extrinsic contribution to the dipole-dipole interaction–just like an uncompensated interface–which can be used to read and write the state of an antiferromagnet [32, 33]. This can explain why exchange bias occurs with similar magnitude at both compensated and uncompensated antiferromagnetic interfaces [30, 34].

2.4.2 Dipole Anisotropy

In addition to the extrinsic contributions to the dipole-dipole interaction discussed above, (infinite) magnetic crystals with non-cubic magnetic site symmetries have an anisotropic energy contribution from dipole-dipole interactions (see Fig. 2.5). We call this a dipole anisotropy to distinguish this intrinsic contribution from the extrinsic shape anisotropy. In ferromagnets, this is usually small compared to magnetocrystalline anisotropies and single sublattice ferromagnets typically have a magnetic symmetry which is close to cubic. In ferrimagnets and antiferromagnets, the changing direction of spin vectors at different sites means the symmetry is often far from cubic, and the dipole anisotropy can be large–even in the ground state. Additionally, since dipole-dipole interactions are long-range pairwise interactions, rather than local interactions (as with magnetocrystalline anisotropy), an easy-plane dipole anisotropy can break the degeneracy of antiferromagnetic spin wave branches and change their polarisation, in addition to introducing a gap in the spin wave spectrum [35]. No single-ion energy can introduce a similar effect, so calculating the discrete dipole-dipole interaction explicitly can be important when studying dynamical effects.

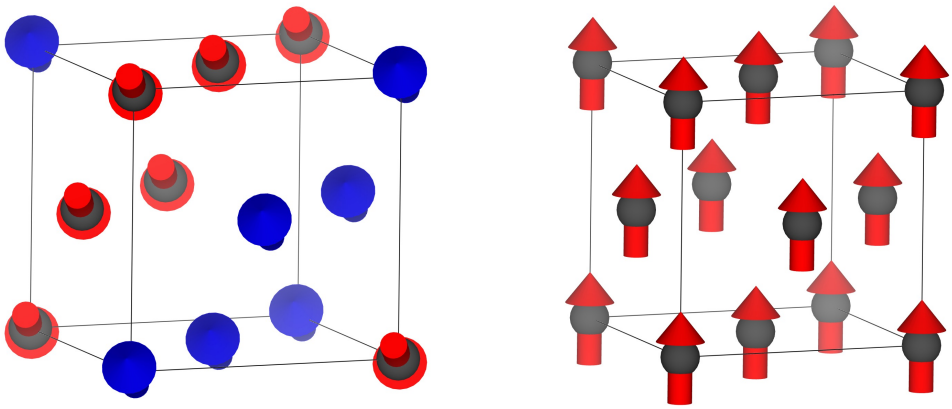

Figure 2.5: (*left*) Depiction of an antiferromagnet which has cubic crystal symmetry and non-cubic magnetic symmetry. (*right*) Depiction of a ferromagnet which has both cubic crystal and cubic magnetic symmetry. The antiferromagnet (*left*) has negligible shape anisotropy but has a non-zero intrinsic dipole anisotropy whereas the ferromagnet (*right*) has a non-zero shape anisotropy but the intrinsic dipole anisotropy vanishes.

Chapter 3

Methods

3.1 Scales of Modelling

In modern science, simulations of physical systems are increasingly playing a large role in research. Simulations aid in understanding complex phenomena that are difficult to study analytically, enable high throughput material screening without expensive experiments, and are used to help interpret experimental results. As such, there are many computational tools available to researchers which range from small scale ab-initio methods, through device-scale continuum methods. The idea of multiscale modelling is to parameterise more heavily approximated methods using less approximate methods to reduce the loss of information when going from a less- to more-coarse grained simulation.

The inclusion of temperature in most computational models is not simple. Statistical mechanics tells us that temperature is only well defined by the averaging of microscopic thermal fluctuations (ie in atomistic simulations). Temperature can be included in ab-initio methods such as time-dependent DFT (TD-DFT). But, the additional computational cost means that it is difficult to obtain good statistical sampling so these simulations have limited value. At the other end of the spectrum, stochastic thermal fields have been included in micromagnetic models to include the effect of temperature. But micromagnetism is only strictly valid at zero temperature. Micromagnetic formalisms such as those which use the Landau-Lifshitz-Bloch equation [36] attempt to resolve this but still require finite temperature values for material parameters such as the magnetisation $m(T)$, exchange stiffness $A(T)$, and transverse $\chi_\perp(T)$ and longitudinal susceptibilities $\chi_\parallel(T)$ which must be calculated using other methods [37] (mean-field approximation, atomistic spin dynamics, etc). The inclusion of stochastic fluctuations in micromagnetism should instead be thought of as a tool which introduces randomness to ensure that the micromagnetic system doesn't get stuck in local equilibria. The temperature of a micromagnetic simulation is not the same temperature that appears in statistical mechanics. The loss of microscopic degrees of freedom means the entropy of a micromagnetic simulation is distinct from the entropy of an equivalent supercell which is simulated using atomistic spin dynamics or Metropolis Monte Carlo. This is why the micromagnetic energy is usually written as a free energy which doesn't include the energy that cannot be extracted due to entropy ($F = U - TS$, TS is not available to do work). Atomistic methods like spin dynamics and Monte Carlo are

the most useful tools for calculating finite temperature properties of materials as these simulations can contain millions of atoms in an ensemble and thermal averaging can occur over nanosecond time periods. These atomistic ensemble methods are the tools used in this work.

There are three main assumptions in these atomistic methods:

1. Spins are localised on an atomic site by the Born-Oppenheimer / adiabatic approximation. This assumes that electron dynamics and spin dynamics occur on separable timescales, orders of magnitude apart.

2. Spins are approximated as classical unit vectors rather than quantum states. This means that purely quantum effects cannot be included and the method is valid at intermediate temperatures (ie incorrect at very low and very high temperatures).

3. Statistical averaging by importance sampling closely approximates the full partition function.

The above approximations are best applied to insulating magnets. The problem of quantum versus classical thermal distributions can be partially mitigated when using a quantum thermostat in spin dynamics simulations (discussed in Chapter 5).

3.2 Metropolis Monte Carlo

In principle, the whole partition function must be known to determine the thermodynamic averages. In reality, this is only calculable in very small systems. For a discrete lattice of N spins represented as classical unit vectors, the partition function is given by $2N$ integrals

$$Z = \int \mathrm{e}^{-\beta \mathcal{H}(\theta_1,\phi_1,\ldots,\theta_N,\phi_N)} d\theta_1 d\phi_1 \ldots d\theta_N d\phi_N, \tag{3.1}$$

where $\beta = 1/k_B T$, and θ_i, ϕ_i are the azimuthal and polar angles of each spin vector. The Metropolis algorithm is an example of importance sampling. The algorithm ensures that highly probable states are sampled more frequently by always accepting trial moves which are lower in energy, and higher energy moves are sampled using a Boltzmann factor to calculate the acceptance probability. States which have low probability (high energy) contribute very little to the partition function so have a low probability of being sampled. In the limit of a large number of sampled states, the set of sampled

states–which is a subset of the total states of the system–converges to the expected Boltzmann distribution of energies and represents the distribution of the complete partition function to arbitrarily high accuracy (by increasing the number of Monte Carlo steps). The degree of convergence can be measured during simulations but a fixed number of steps is usually used in practise ($> 10^5$ steps is sufficient for most systems at most temperatures). The Metropolis-Hastings algorithm can be summarised into the following steps

1. Choose a random spin $\mathbf{S}_i$.
2. Choose a trial state $\mathbf{S}_i'$.
3. Calculate the energy difference between the old state and the new state $\Delta E = E(\mathbf{S}_i') - E(\mathbf{S}_i)$.
4. Pick a random number $r \in [0, 1]$.
5. If $r \leq \exp(\min\{0, -\frac{\Delta E}{k_B T}\})$, accept the trial state. Else, reject the trial state.

The initial state of a Monte Carlo simulation is perfectly ordered. Since the system is coupled to a thermal bath of fixed temperature, energy and entropy are exchanged until the system reaches thermal equilibrium*. So, the first few steps ($\sim 10^4$) of a Monte Carlo simulation are discarded for equilibration, and the remaining steps are used for statistical averaging. In a single simulation the temperature is kept fixed, so the system is known as a canonical ensemble and the free energy is minimised. This method is useful but doesn't allow access to dynamical effects, and doesn't allow the use of different thermostats; classical statistics is built into the algorithm by using a simple Boltzmann factor. For these functionalities, we need to use a dynamical method such as atomistic spin dynamics. In this work, Monte Carlo methods are used because the Metropolis algorithm can be altered to give access to the temperature scaling of macroscopic parameters. The algorithm we use in this work is called constrained Monte Carlo [38] which is discussed in Chapter 5.

*The thermal bath is identical to an infinitely large environment, so the decrease in energy and entropy of the thermal bath due to the magnetic system is effectively zero.

3.3 Atomistic Spin Dynamics

Atomistic spin dynamics calculates the time evolution of localised classical magnetic moments on a discrete crystal lattice by the stochastic Landau-Lifshitz (LL) equation* [41], which includes a precessional torque consistent with quantum mechanics and a phenomenological damping torque. The Landau-Lifshitz equations for a canonical ensemble are written

$$\frac{\partial \mathbf{S}_i}{\partial t} = -|\gamma| \left[\mathbf{S}_i \times \mathbf{B}_i + \alpha_i \mathbf{S}_i \times (\mathbf{S}_i \times \mathbf{B}_i)\right], \tag{3.2}$$

where $\gamma = g\mu_B/\hbar$ is the gyromagnetic ratio of a free electron, α_i is the dimensionless damping constant (Table 4.5), and the local field $\mathbf{B}_i = \boldsymbol{\xi}_i - (1/\mu_{s,i})\nabla_{\mathbf{S}_i}\mathcal{H}$ contains all interactions from the Hamiltonian (4.17) and a stochastic thermal field $\boldsymbol{\xi}_i$. The LL or Landau-Lifshitz-Gilbert (LLG) equation can be used at the atomic level, as well as at the micromagnetic and macrospin levels. The equation is very successful at modelling magnetic materials, primarily because the local field $\mathbf{B}_i$, and the applied torques, can be augmented to include the effect of magnetic field pulses [42], laser pulses (using LLB) [43], as well as spintronic effects such as spin-transfer and spin-orbit torques [44].

Just like Metropolis Monte Carlo, atomistic spin dynamics samples the most probable states of the system. The formal connection with statistical mechanics can be found in work by Gyorffy [45] and standard textbooks [46]. In addition, spin dynamics can be used to study the relaxation of a system from non-equilibrium states so experiments can be replicated in a simulation, as well as allowing non-classical thermal statistics to be used (of particular interest is the Bose-Einstein thermostat, discussed in Section 5.1). The spin dynamics algorithm is a simple numerical integration of many coupled partial differential which is very easily parallelised on a computer. The implementation used in this work uses a fourth order stochastic Runge-Kutta integrator which can be deployed on both CPUs and GPUs. The ease of parallelisation means that atomistic spin dynamics can be much faster than Monte Carlo simulations when implemented on GPUs, allowing larger systems to be simulated for longer integration times, which gives better thermal statistics and higher quality results–often better than the most cutting edge

*We choose the Landau-Lifshitz form of damping, rather than the Gilbert damping [39], because the latter changes the frequency of spin waves by a factor $1/(1+\alpha^2)$. We want spin wave frequencies to be consistent with the ab-initio calculations [40].

experiments [47]. The stochastic thermal field, $\boldsymbol{\xi}$, must obey fluctuation-dissipation theorem. The fluctuation-dissipation theorem which gives Boltzmann statistics means the thermal field must have the following properties

$$\begin{aligned} \langle \xi_i^{\alpha}(t) \rangle_t &= 0 \\ \langle \xi_i^{\alpha}(t)\, \xi_j^{\beta}(t') \rangle &= \frac{2\alpha}{\mu_{\mathrm{S},i}\gamma_i} \delta_{ij}\delta_{\alpha\beta}\delta(t-t')k_B T \end{aligned} \tag{3.3}$$

where α, β are Cartesian components. The damping is included phenomenologically and its value is taken from experiments. There are many sources of damping in magnetic systems (see Fig. 3.1) but these are almost impossible to quantify without simulating the magnetic, electronic, and lattice simultaneously. So phenomenological damping parameters must be used. In most cases, this is sufficient.

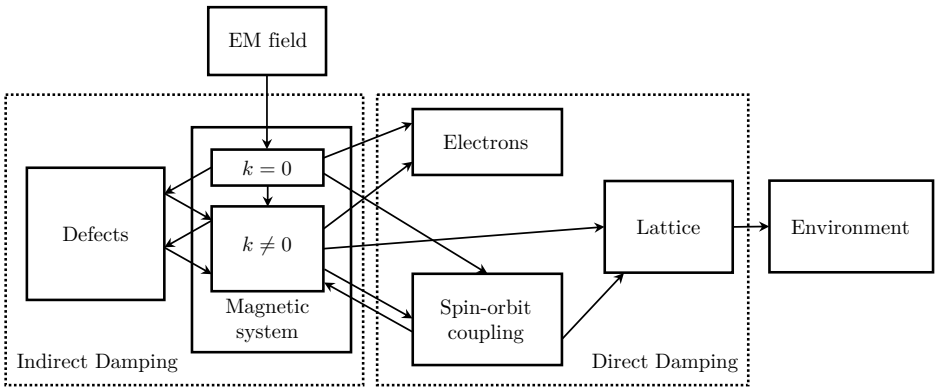

Figure 3.1: Energy transferred to and from the uniform ($k = 0$, resonant) modes of magnetic system excited by an external EM source. Sources of losses (damping) can be broadly separated into direct and indirect processes. Direct sources of damping are spin-lattice and spin-electron scattering processes where energy immediately leaves the magnetic system. Indirect sources of damping are mediated by spin-spin processes. Figure reproduced from [48].

Chapter 4

Developing Material Specific Models Using Symmetry and Multiscale Parameterisation

4.1 Outline

In this chapter we develop a framework of tools needed to create realistic models of magnetic materials. Since high performance computing is easily accessible in most universities, tools like atomistic spin dynamics and micromagnetics are commonly used by researchers as a quick and easy way to model magnetic materials and devices–a trend which has been accelerated due to the COVID-19 pandemic. The problem is that, while many different models can be tuned to match experimental results (some atomistic models even have a different crystal lattice to the material being modelled!), predictions from unrealistic models which include highly idealised interactions or include interactions which do not obey the symmetry of the magnetic crystal, will always be incomplete or incorrect when used in different contexts. Despite this, tools like atomistic spin dynamics are very important in understanding the underlying physics of antiferromagnets as the dynamics can be very complex, there can be many mechanisms which can explain a given observed phenomenon, and the microscopic degrees of freedom are not accessible experimentally due to the zero net magnetisation (though are accessible in atomistic simulations). As an example, for many-sublattice antiferromagnets, some resonance modes (eigenfrequencies) cannot be experimentally observed using macroscopic measurements of antiferromagnets because of phase cancellation of the different sublattices [49]; microscopic techniques that employ light scattering can observe these. So, these modes cannot be measured using typical experiments (without applying a forced oscillation) yet they can carry spin currents and impact the performance of antiferromagnetic devices [49]. It is therefore important that models of antiferromagnets do not alter this physics. The importance of fundamental principles such as symmetry in magnetism has been made clear by the recent discovery of altermagnetism, a new class of magnetic materials which have symmetries which are distinct from both ferromagnets and antiferromagnets. Altermagnets have zero net magnetisation like an antiferromagnet, yet the Fermi surface is spin polarised like a ferromagnet. These materials permit giant magnetoresistance (GMR), and have a strong anisotropic (k-dependent) spin Hall effects which aren't mediated by weak relativistic spin-orbit coupling–something which cannot exist in ferro-, ferri-, or anti-ferromagnets [50–55].

The rest of this chapter is outlined as follows. First, we give an introduction to NiO, an antiferromagnetic material which is usually modelled using extremely simpli-

fied interactions that don't always obey the symmetry of the magnetic crystal, despite the fact that symmetry uniquely determines the microscopic interactions which are required to stabilise its equilibrium state. Second, we describe the constraints that lattice and magnetic symmetry imposes on permitted spin Hamiltonians. Then, we discuss the use of point charge models of crystalline materials and show how it can be used to determine the dominant contributions to the magnetic anisotropy. Finally, we discuss best practices for parameterising exchange interactions in a magnetic material. Throughout this chapter, these tools will be applied to NiO, but these processes should be used to develop magnetic models of all materials.

4.2 Introduction to NiO

Above the Néel temperature, NiO has the space group $Fm\bar{3}m$. Below the Néel temperature the magnetic space group is C_c2/c [56, 57] and the corresponding magnetic point group is the non-magnetic (type I) group $\frac{2}{m}$. At low temperature, a magnetostrictive distortion reduces the non-magnetic space group to $R\bar{3}m$ [58]. The antiferromagnetic order has propagation vector $\mathbf{q} = (\frac{1}{2}, \frac{1}{2}, \frac{1}{2})$ with spins lying perpendicular to the propagation direction [57]. This means spins form alternating ferromagnetically aligned (111) sheets which are antialigned with neighbour (111) sheets (see Fig. 4.2). Within the (111) plane, spins have three-fold symmetry [59] and lie close to one of the $\langle 11\bar{2}\rangle$ directions [60–62]. The above details have a long and complicated history. Schron [63] attempted to clarify this with a very comprehensive literature review but complicates things further because their ab-initio results gives the wrong sign of the anisotropy, which gives a magnetic space group which contradicts modern experiments.

The ordering into sheets is a direct result of the exchange interaction. In idealised theories of superexchange (Goodenough-Kanamori rules [24, 64]), the nearest neighbour interaction (J_1) is small and ferromagnetic in sign because the interaction is between a Ni orbital ionically bonded to an oxygen p_x orbital, and a Ni orbital bonded to an oxygen p_y orbital (orthogonal orbitals). Whereas the next nearest neighbour interaction (J_2), is large and antiferromagnetic in sign due Ni sites attached to the same oxygen orbital (180° bond angle). The analysis of experiments and theoretical studies have often relied on two sublattice macrospin approximations which cannot include

the nearest neighbour coupling. At the atomic level however, neglecting the nearest neighbour interactions leads to four uncoupled, interpenetrating simple cubic antiferromagnetic lattices (see Fig. 4.1). This produces a model with four uncoupled Néel vectors which can deviate from one another. So, any Hamiltonian which ignores J_1 is paramagnetic as there is no global order. Including the nearest neighbour coupling is therefore essential in modelling at the atomic scale.

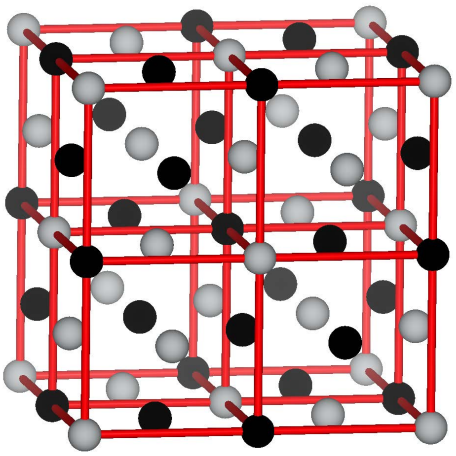

Figure 4.1: A NiO supercell. Oxygen sites are omitted. Dark atomic sites denote 'up' sites, lighter coloured sites denote 'down' sites. Red bonds show atoms connected by next nearest neighbour (J_2) exchange from a corner site (2 of the 8 sublattices). Many atoms are uncoupled.

Another nuance is that the nearest neighbour interaction couples both parallel and antiparallel pairs of spins. Because these are different sublattices, J_1 can be further split into J_{1+} and J_{1-} (see Fig. 4.2). J_{1+} denotes the exchange coupling between aligned nearest neighbours, and J_{1-} denotes the exchange coupling between antialigned nearest neighbours. In some works a single value is used for both nearest neighbour exchange couplings [65–67]. However, due to the equal strength coupling of the 4 pairs of sublattices, the nearest neighbour exchange energy is constant for all configurations of the four Néel vectors. This case is equivalent to excluding the nearest neighbour coupling because there is no energy penalty for moving one of the Néel vectors relative to the other three. Detailed analysis of the magnon spectra measured by neutron diffraction

experiments [59] and state of the art electronic structure calculations [40] show that there is a considerable splitting of the nearest neighbour exchange $\Delta J_1 = J_{1+} - J_{1-}$ with $\Delta J_1/(J_{1+} + J_{1-}) \sim 25\%$. The splitting of the nearest neighbour exchange is small compared to the antiferromagnetic next nearest neighbour exchange interaction J_2 ($\Delta J_1/J_2 \sim 1\%$) but it is still significant. J_{1+} and J_{1-} are two orders order of magnitude larger than the magnetic dipole anisotropy energy, and the splitting ΔJ_1 is a factor of ~ 30 larger than the dipole anisotropy. Therefore the effect of this exchange splitting on spin waves is larger than the effect of dipole effects at finite $\mathbf{k}$ vectors. Despite this, the splitting is usually neglected [68].

The origin of the splitting is often stated to be a small ($\sim 0.1\%$ [59]) magnetostrictive contraction of the (111) planes that vanishes at the Néel temperature and sets the direction of the antiferromagnetic ordering within a domain. This is often justified by stating that a splitting of the J_1 interaction is forbidden in a perfectly cubic crystal [69]. It is true that the non-magnetic crystal point group $(m\,\bar{3}\,m)$ does not permit this splitting. But, the *magnetic* point group of the magnetic crystal depicted in Fig. 4.2 $(2/m)$ does permit the splitting of J_1. This means that the splitting cannot be mediated by the crystal. Instead the local change in the electronic structure due to the onset of magnetism introduces the splitting. The splitting of J_1 due to the magnetic symmetry being less than cubic is seen in advanced ab-initio calculations even when the non-magnetic symmetry is cubic [40]. Simpler methods, which are known to be poor approximations of Mott insulators* such as NiO, do not observe the splitting of J_1 for the cubic atomic lattice (monoclinic magnetic symmetry) and must add the structural distortion, which reduces the non-magnetic symmetry from $m\,\bar{3}\,m$ to $\bar{3}\,m$, by hand to observe the splitting of J_1 [69] which is required for antiferromagnetic ordering. To further complicate this, it has been shown–using modern experiments which simultaneously measures magnetic and structural properties–that the magnetostrictive distortion occurs at 471K, far below the Néel temperature $T_N = 523$K [58]. This differs from the often quoted view that the distortion vanishes at the Néel temperature. There are now two cases; above 471K there is splitting, or there is not. If the splitting of J_1 persists above 471K, it will be reduced by the increase in crystal symmetry (accompanied by an increase in

*In modern literature NiO is classified as a charge-transfer insulator which differs slightly from a Mott insulator, though the difference is unimportant here [70, 71].

J_2 due to the bond angle returning to 180°), but remains sufficiently large to maintain the antiferromagnetic state. If the J_1 splitting vanishes above 471K, biquadratic exchange must stabilise the antiferromagnetic state [69]. It is likely that the difference between the two cases is smaller than the precision of any experimental data available (though biquadratic exchange was shown to be negligible in MnO, a very similar antiferromagnet [72]). Additionally, we expect the reduction of the splitting above 471K to have the same order of magnitude as the distortion ($\sim 0.1\%$). So, for our atomistic model, we choose the simplest case of vanishing biquadratic exchange, negligible structural distortion, and constant splitting of J_1 through the whole temperature range.

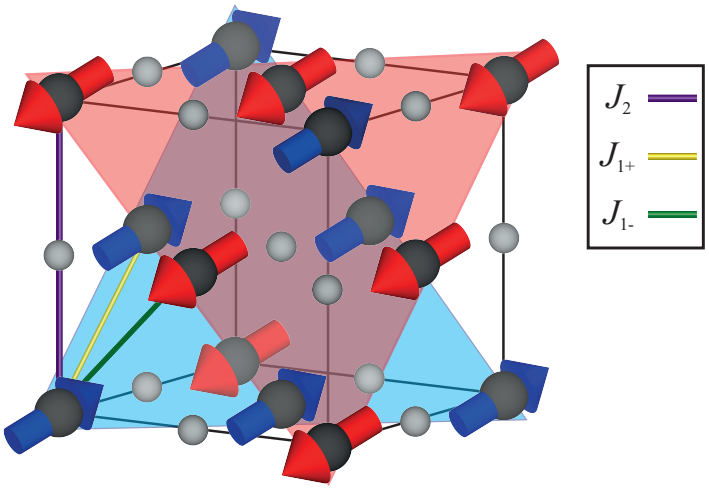

Figure 4.2: Magnetic structure of NiO. Oxygen sites are grey without vectors. Ni sites are darker spheres with spin vectors. Spins are aligned parallel within the [111] plane, which are antiparallel to neighbour planes. Green and yellow bonds show a nearest neighbour interaction, the purple bond shows a next-nearest neighbour interaction.

While the antiferromagnetic ordering into sheets is uniquely determined by exchange, the preferred direction of the spins is due to anisotropies. The ground state configuration was the subject of debate for many years [73–81], with several competing

theories [82–84]. It is now well known that the easy-plane anisotropy is due to magnetic dipole-dipole interactions. For our model of NiO, we calculate magnetic dipole-dipole interactions between distance spins without mapping the resulting dipole anisotropy onto a single-ion magnetocrystalline anisotropy. For many-ion interactions like the dipole-dipole interaction, correlations between distant spins plays an important role in the temperature dependence of the resulting anisotropy and leads to different dynamical phenomena. Analytic theories like Callen-Zener theory can, in principle, be used to calculate the temperature dependence of many-ion interactions by considering partial and full rotations of the spin system. But, this is intractable in practice. Mapping this onto a single-ion energy is an assumption that trivialises the complexities of dipole-dipole interactions.

In the next sections, we will discuss single-ion anisotropies in detail. For this, we choose to name anisotropies by the rank of the anisotropy tensor and the class of point groups which the term is unique to (uniaxial is not unique to any, this is a special case). This helps clarify the nomenclature of anisotropies. For example, a first order cubic anisotropy becomes a rank-4 cubic anisotropy (4^{th} order in direction cosines), and a first order uniaxial anisotropy becomes a rank-2 uniaxial anisotropy (quadratic in direction cosines). In NiO, there is an additional anisotropy that breaks the degeneracy of the easy-plane. Various magnetocrystalline anisotropy terms have been used to account for the preferred $\langle 11\bar{2} \rangle$ directions within the plane including a rank-6 cubic anisotropy [68], a rank-6 hexagonal anisotropy [66], and a rank-2 easy-plane anisotropy which is perpendicular to the (111) plane [59, 85]. Neumann's principle states that the symmetry of any physical property or interaction–any Hamiltonian term–must contain all the symmetry operations operations of the crystal point group. Additionally, if the crystal is magnetic, any Hamiltonian term which is mediated by the magnetic moments (dipole-dipole interaction, J_1 splitting, etc) has reduced symmetry constraints and must only contain the symmetry operations of the magnetic point group (in older literature, these non-magnetic energies are called static [86] as they are time independent). These magnetism mediated terms are often treated perturbatively [86]. In some cases, for reasons other than symmetry, these energy terms are not small and cannot be treated perturbatively. This is the case for NiO–the magnetocrystalline anisotropy is very small because the mediating oxygen ions have low nuclear charge implying vanishingly small

spin-orbit coupling but the magnetic dipole-dipole contribution is orders of magnitude larger. Magnetic dipole-dipole interactions in bulk crystals cancel whenever the magnetic symmetry is cubic, but the monoclinic magnetic point group $\frac{2}{m}$ has much lower symmetry, so the dipole contribution must be non-zero.

In any magnetic material, the symmetry of magnetocrystalline anisotropy is determined by the symmetry of the crystal field and must contain the symmetry operations of the crystal point group. The symmetry requirements of the magnetocrystalline anisotropy differs from exchange since the symmetry of exchange is determined by the symmetry of the local electronic structure which includes spin-splitting in magnetic materials. Similarly, the dipole-dipole interaction is mediated only by magnetic moments so its symmetry must contain the elements of the magnetic point group. The magnetic space group allows another magnetostrictive reduction in symmetry so that the crystal point group is $\frac{2}{m}1'$, but this has never been observed. Excluding crystalline anisotropies by symmetry is discussed in the next section. But, we will state an important result here. From Hartmann's definitions of point group generating matrices [87], and applying Neumann's principle to even rank tensors of magnetocrystalline anisotropy constants [86]*, one can show that both the rank-6 hexagonal anisotropy and rank-2 uniaxial anisotropy are forbidden for crystal point groups $m\,\bar{3}\,m$ and $\bar{3}\,m$†. Despite being able to reproduce certain experiments, these models must be incomplete and cannot represent the real system. This is justified by the difficulty in measuring the in-plane magnon mode; if this is due to a simple crystalline anisotropy, it should be measurable in all samples of similar quality, yet this is not the case. The ability to measure the low frequency mode is highly dependent on the experimental method, and the choice of experiment geometry. The $\bar{3}\,m$ generating matrix $\mathbb{M}_{10}$ forbids the hexagonal term and both generating matrices for $m\,\bar{3}\,m$ forbid the hexagonal term.

*Some ferromagnets and all ferri-/antiferro-magnets have point groups which lack spin reversal symmetry. These can permit crystal anisotropies which are given by odd-rank tensors of the direction cosines [86, 88]. These cannot be magnetocrystalline in origin (magnetoelastic coupling, dipole-dipole, etc) and generally we expect their contribution to be small in NiO.

†$\bar{3}\,m$ permits a [111] rank-2 uniaxial anisotropy but the $(1\bar{1}0)$ easy-plane term seen in the literature [59, 85, 89]

4.3 Symmetry

4.3.1 Point Groups

A crystal point group $\mathbb{P}$ is the set of rotations and reflections (operations $P \in \mathbb{P}$) which preserves all points in the crystal. This is a global property of the crystal and these operations can have a single, or many points in space where these operations can be applied and the crystal is preserved. Such sites are called centres of symmetry $\mathbf{c}$. We shall only consider crystals with centres of symmetry which are also atomic sites; these crystals are named centrosymmetric. Not all atoms in a crystal must be a centre of symmetry. The point group of a site may differ from the point group of the crystal. But, we only consider magnetocrystalline anisotropy (which is invariant under spin inversion) in NiO. In this case, the magnetic site symmetries and the crystal symmetry give the same permitted terms.

The point groups of non-magnetic crystals are split broadly into seven categories of decreasing symmetry (minimal symmetry given in parentheses): cubic (12-fold), hexagonal (6-fold), tetrahedral (4-fold), trigonal (3-fold), orthorhombic (2-fold), monoclinic (2-fold) and triclinic (1-fold / none). In total there are 32 unique non-magnetic point groups. Point groups are represented by a combination of numbers and letters which tells us directly what operations can be applied to the crystal. For example $\frac{2}{m}$ is the symbol for one of the monoclinic point groups. 2 denotes a two-fold rotation (a 180° degree rotation around some axis $\hat{\mathbf{w}}$), m denotes a mirror plane (a reflection in the plane perpendicular to $\hat{\mathbf{w}}$) and $\frac{1}{m}$ means that m can be applied to the crystal after 2 has already been applied. The only additional symbol needed to define the international symbols is an overbar (ie $\bar{2}$) which means the operation must be accompanied by space inversion, multiplying by $-\mathbb{1}$. The point group $\frac{2}{m}$ therefore has four elements: the identity $\mathbb{1}$, 180° rotation about $\hat{\mathbf{w}}$ $R_{\mathrm{w}}(\pi)$, a reflection in the uv-plane M_{w}, and space inversion $-\mathbb{1} = R_{\mathrm{w}}(\pi) \circ M_{\mathrm{w}}$ where $\hat{\mathbf{u}}$, $\hat{\mathbf{v}}$, $\hat{\mathbf{w}}$ is a basis, R is a rotation matrix, and M is a mirror matrix.

Any point group can be generated from one, two, or three matrices which we call generating matrices $\mathbb{M}$. The list of generating matrices for the 32 point groups are given in Table 4.1 and the list of generating matrices are given in Table 4.2.

These 32 non-magnetic point groups do not consider spin reversal symmetry (often called time reversal symmetry, though this is debated). If spin reversal symmetry is also considered there are 122 point groups which can be derived from the 32 non-magnetic groups. Only certain point groups are compatible with ferromagnetic, antiferromagnetic and ferrimagnetic crystals. Magnetic point groups are much more diverse than their non-magnetic counterparts and a more detailed description is out of the scope of this work. Interested readers are directed to the following sources for further reading [56, 86, 91–93]. In practice, when classifying the symmetries of magnetic crystals, the point of greatest importance is that including magnetic symmetry can only reduce the number of elements of the non-magnetic point group–it is not possible for a trigonal lattice with three-fold symmetry to have a cubic magnetic point group with four-fold symmetry.

The lattice point group of NiO is either the cubic group $m\,\bar{3}\,m$, or the trigonal point group $\bar{3}\,m$ dependent on the temperature (a reduction in symmetry occurs at 471K [58]). In both cases, the magnetic point group is the monoclinic point group $\frac{2}{m}1'$ which includes spin reversal symmetry $1'$*.

4.3.2 Neumann's Principle

Classifying the symmetry of crystals is of great importance. Symmetry can uniquely determine the physical effects that are permitted in a material; static properties like magnetocrystalline anisotropy, strain tensors and thermal expansion coefficients, dynamic properties like spin Hall effects, Peltier effect tensors and thermal conductivity, or optical properties like birefringence, Kerr effects, and second harmonic generation. To make use of the point group, we need to use Neumann's principle which states that any symmetry operation in the point group must also be a symmetry operation of any physical property of the crystal (this is also true of individual site symmetries at a microscopic level too). In maths, this means that the tensor describing a material property such as the magnetocrystalline anisotropy ρ_{ij} must be invariant under the

*Sometimes $\frac{2}{m}$ is quoted but the magnetic space group contains all the elements of $\frac{2}{m}$ as well as all the time reversed elements when combined with a translation. It is therefore accepted that the magnetic point group should be $\frac{2}{m}1'$.

Table 4.1: List of non-magnetic point groups and some of their properties. Reproduced from [87] and symbols are corrected using the Bilbao Crystallographic Server [90].

Symmetry Class	Symbol	Generating Matrices	# Elements of $\mathbb{P}$	Basis Vectors
Triclinic	1	$\mathbb{M}_0$	1	
	$\bar{1}$	$\mathbb{M}_1$	2	
Monoclinic	2	$\mathbb{M}_1$	2	
	m	$\mathbb{M}_3$	2	$\mathbf{e}_3 \| 2$ or $\mathbf{e}_3 \| \bar{2}$
	$\frac{2}{m}$	$\mathbb{M}_2$, $\mathbb{M}_3$	4	
Orthorhombic	222	$\mathbb{M}_2$, $\mathbb{M}_4$	4	$\mathbf{e}_1 \| 2$ or $\mathbf{e}_1 \| \bar{2}$
	$m\,m\,2$	$\mathbb{M}_2$, $\mathbb{M}_5$	4	$\mathbf{e}_2 \| 2$ or $\mathbf{e}_2 \| \bar{2}$
	$m\,m\,m$	$\mathbb{M}_3$, $\mathbb{M}_5$, $\mathbb{M}_6$	8	$\mathbf{e}_3 \| 2$
Trigonal	3	$\mathbb{M}_9$	3	
	$\bar{3}$	$\mathbb{M}_{10}$	6	$\mathbf{e}_1 \| 2$ or $\mathbf{e}_1 \| \bar{2}$
	$3\,2$	$\mathbb{M}_4$, $\mathbb{M}_9$	6	$\mathbf{e}_2 \perp 2$ or $\mathbf{e}_2 \perp \bar{2}$
	$3\,m$	$\mathbb{M}_5$, $\mathbb{M}_9$	6	$\mathbf{e}_3 \| 3$ or $\mathbf{e}_3 \| \bar{3}$
	$\bar{3}\,m$	$\mathbb{M}_5$, $\mathbb{M}_{10}$	12	
Tetragonal	4	$\mathbb{M}_7$	4	
	$\bar{4}$	$\mathbb{M}_8$	4	
	$4\,2\,2$	$\mathbb{M}_4$, $\mathbb{M}_7$	8	$\mathbf{e}_1 \| 2$ or $\mathbf{e}_1 \| \bar{2}$
	$\frac{4}{m}$	$\mathbb{M}_3$, $\mathbb{M}_7$	8	$\mathbf{e}_2 \| 2$ or $\mathbf{e}_2 \| \bar{2}$
	$4\,m\,m$	$\mathbb{M}_5$, $\mathbb{M}_7$	8	$\mathbf{e}_3 \| 4$ or $\mathbf{e}_3 \| \bar{4}$
	$\bar{4}\,2\,m$	$\mathbb{M}_4$, $\mathbb{M}_8$	8	
	$\frac{4}{m}\,\frac{2}{m}\,\frac{2}{m}$	$\mathbb{M}_3$, $\mathbb{M}_5$, $\mathbb{M}_7$	16	
Hexagonal	6	$\mathbb{M}_{11}$	6	
	$\bar{6}$	$\mathbb{M}_{12}$	6	
	$\bar{6}\,m\,2$	$\mathbb{M}_5$, $\mathbb{M}_{12}$	12	$\mathbf{e}_1 \| 2$ or $\mathbf{e}_1 \| \bar{2}$
	$6\,2\,2$	$\mathbb{M}_4$, $\mathbb{M}_{11}$	12	$\mathbf{e}_2 \perp 2$ or $\mathbf{e}_2 \perp \bar{2}$
	$\frac{6}{m}$	$\mathbb{M}_3$, $\mathbb{M}_{11}$	12	$\mathbf{e}_3 \| 6$ or $\mathbf{e}_3 \| \bar{6}$
	$6\,m\,m$	$\mathbb{M}_5$, $\mathbb{M}_{11}$	12	
	$\frac{6}{m}\,\frac{2}{m}\,\frac{2}{m}$	$\mathbb{M}_3$, $\mathbb{M}_5$, $\mathbb{M}_{11}$	24	
Cubic	$2\,3$	$\mathbb{M}_2$, $\mathbb{M}_{13}$	12	$\mathbf{e}_1 \| 2$
	$\bar{3}\,m$	$\mathbb{M}_2$, $\mathbb{M}_{14}$	24	$\mathbf{e}_2 \| 3$, $\mathbf{e}_3 \| 2$
	$4\,3\,2$	$\mathbb{M}_7$, $\mathbb{M}_{13}$	24	$\mathbf{e}_1 \| 4$ or $\mathbf{e}_1 \| \bar{4}$
	$\bar{4}\,3\,m$	$\mathbb{M}_8$, $\mathbb{M}_{13}$	24	$\mathbf{e}_2 \| 4$ or $\mathbf{e}_2 \| \bar{4}$
	$m\,\bar{3}\,m$	$\mathbb{M}_7$, $\mathbb{M}_{14}$	48	$\mathbf{e}_3 \| 4$ or $\mathbf{e}_3 \| \bar{4}$

Table 4.2: The generating matrices for the non-magnetic point groups and a description of its effect.

$\mathbb{M}_0 = \begin{pmatrix} 1 & 0 & 0 \\ 0 & 1 & 0 \\ 0 & 0 & 1 \end{pmatrix}$	Identity	$\mathbb{M}_1 = \begin{pmatrix} -1 & 0 & 0 \\ 0 & -1 & 0 \\ 0 & 0 & -1 \end{pmatrix}$	Space inversion
$\mathbb{M}_2 = \begin{pmatrix} -1 & 0 & 0 \\ 0 & -1 & 0 \\ 0 & 0 & 1 \end{pmatrix}$	Two-fold rotation about $\mathbf{e}_3$	$\mathbb{M}_3 = \begin{pmatrix} 1 & 0 & 0 \\ 0 & 1 & 0 \\ 0 & 0 & -1 \end{pmatrix}$	Reflection in $\mathbf{e}_1\mathbf{e}_2$-plane
$\mathbb{M}_4 = \begin{pmatrix} 1 & 0 & 0 \\ 0 & -1 & 0 \\ 0 & 0 & -1 \end{pmatrix}$	Two-fold rotation about $\mathbf{e}_1$	$\mathbb{M}_5 = \begin{pmatrix} -1 & 0 & 0 \\ 0 & 1 & 0 \\ 0 & 0 & 1 \end{pmatrix}$	Reflection in $\mathbf{e}_2\mathbf{e}_3$-plane
$\mathbb{M}_6 = \begin{pmatrix} 1 & 0 & 0 \\ 0 & -1 & 0 \\ 0 & 0 & 1 \end{pmatrix}$	Reflection in $\mathbf{e}_1\mathbf{e}_3$-plane	$\mathbb{M}_7 = \begin{pmatrix} 0 & -1 & 0 \\ 1 & 0 & 0 \\ 0 & 0 & 1 \end{pmatrix}$	Four-fold rotation about $\mathbf{e}_3$
$\mathbb{M}_8 = \begin{pmatrix} 0 & -1 & 0 \\ 1 & 0 & 0 \\ 0 & 0 & -1 \end{pmatrix}$	Four-fold inversion-rotation about $\mathbf{e}_3$	$\mathbb{M}_9 = \begin{pmatrix} -\frac{1}{2} & -\frac{\sqrt{3}}{2} & 0 \\ \frac{\sqrt{3}}{2} & -\frac{1}{2} & 0 \\ 0 & 0 & 1 \end{pmatrix}$	Three-fold rotation about $\mathbf{e}_3$
$\mathbb{M}_{10} = \begin{pmatrix} \frac{1}{2} & -\frac{\sqrt{3}}{2} & 0 \\ \frac{\sqrt{3}}{2} & \frac{1}{2} & 0 \\ 0 & 0 & -1 \end{pmatrix}$	Three-fold inversion-rotation about $\mathbf{e}_3$	$\mathbb{M}_{11} = \begin{pmatrix} \frac{1}{2} & -\frac{\sqrt{3}}{2} & 0 \\ \frac{\sqrt{3}}{2} & \frac{1}{2} & 0 \\ 0 & 0 & 1 \end{pmatrix}$	Six-fold rotation about $\mathbf{e}_3$
$\mathbb{M}_{12} = \begin{pmatrix} -\frac{1}{2} & -\frac{\sqrt{3}}{2} & 0 \\ \frac{\sqrt{3}}{2} & -\frac{1}{2} & 0 \\ 0 & 0 & -1 \end{pmatrix}$	Six-fold inversion-rotation about $\mathbf{e}_3$	$\mathbb{M}_{13} = \begin{pmatrix} 0 & 0 & 1 \\ 1 & 0 & 0 \\ 0 & 1 & 0 \end{pmatrix}$	Three-fold rotation about the [111] direction
$\mathbb{M}_{14} = \begin{pmatrix} 0 & -1 & 0 \\ 0 & 0 & -1 \\ -1 & 0 & 0 \end{pmatrix}$	Three-fold rotation about the [111] direction		

application of all the elements of a point group

$$\rho_{ij} = P_{ik}\rho_{jk}\,, \quad \forall P \in \mathbb{P}. \tag{4.1}$$

Einstein summation of repeated indices is assumed. Often physical properties can have non-negligible higher order contributions which must obey the same symmetry requirements by tensor products of the elements of the point group

$$\rho_{ijkl} = P_{im}P_{jn}\rho_{klmn}\,, \quad \forall P \in \mathbb{P}. \tag{4.2}$$

For some material properties, the lattice point group may be used; for others, the magnetic point group must be used. Magnetocrystalline anisotropy is entirely determined by the lattice crystal field. This crystal field is invariant under spin (time) reversal symmetry so the magnetocrystalline anisotropy must also be invariant under spin reversal. This means odd rank tensors vanish. This can be seen by writing an odd rank contribution in terms of the direction cosines α

$$E = \rho_{ijk}\alpha_i\alpha_j\alpha_k. \tag{4.3}$$

Each of the direction cosines must be invariant under the operation P, so

$$\rho_{ijk}\alpha_i\alpha_j\alpha_k = \rho_{ijk}P_{il}\alpha_l P_{jm}\alpha_m P_{kn}\alpha_n. \tag{4.4}$$

Since there is an odd number of copies of the point group operation P on the right hand side, and time inversion is a point group operation, we have that $\rho_{ijk}\alpha_i\alpha_j\alpha_k = (-1)^3\rho_{ijk}\alpha_i\alpha_j\alpha_k$ so $\rho_{ijk} = 0$.

4.4 Symmetry Constraints on the Magnetic Hamiltonian

4.4.1 Permitted Magnetic Anisotropies in NiO

The dominant source of magnetic anisotropy in NiO is due to dipole-dipole interactions. The result is a uniaxial easy plane anisotropy [80, 82, 83] which is very long-range (see Section 4.5.4). Whenever the magnetic symmetry is less than cubic, a non-zero dipole anisotropy exists even in infinite systems. Spin-orbit coupling is small in this material because the interstitial oxygen atoms are very light–even if the crystal field is large, the small spin-orbit coupling means the resulting magnetocrystalline anisotropy is small. The crystalline anisotropies are determined solely by the lattice symmetry, rather than

the magnetic symmetry. But, since the anisotropy is due to the configuration of magnetic moments, the resulting anisotropy must obey the symmetry of the magnetic point group $\frac{2}{m}1'$. NiO is an antiferromagnet, yet the magnetic point group is a paramagnetic point group which contains spin reversal and implies no magnetic order. The reason for this seemingly contradictory classification is because the half of the magnetic space group elements contain rotations with spin inversion (ie $2'$) must be accompanied by a translation to preserve the crystal (denoted in Seitz notation by $\{2'|\mathbf{v}\}$). The other half of the space group elements do not contain time inversion so don't need a translation from one magnetic sublattice to another (ie $\{2|\mathbf{0}\}$). Since the space group contains elements with both the point group operations 2 and $2'$, then the global magnetic point group must also contain both of these elements. This means there is more than one unique nickel site and these sites will have different point groups. The simplest case is two magnetic sublattices ($\mathrm{Ni}_\uparrow$, $\mathrm{Ni}_\downarrow$) whose point groups are separated by spin inversion $\mathbb{P}_\uparrow = 1'\mathbb{P}_\downarrow$, though more than two sublattices are possible. Unlike for magnetocrystalline anisotropy, we will not give all the permitted terms here as the dipole-dipole interactions are calculated explicitly rather than being mapped to an effective anisotropy, since dipole-dipole interactions allow complex spin wave modes [35] and have unexpected temperature dependences [94]. The symmetry does not need to be predetermined. Instead we only draw attention to the fact that a (111) easy-plane anisotropy is forbidden by the lattice point group but is permitted by the magnetic point group.

4.4.2 Permitted Crystal Anisotropies in NiO

Using equation (4.2), the permitted anisotropies can be constructed using symmetry arguments. The non-magnetic lattice of NiO has point group $m\,\bar{3}\,m$ or $\bar{3}\,m$ which are generated by matrices $\mathbb{M}_7$ and $\mathbb{M}_{14}$, and $\mathbb{M}_2$ and $\mathbb{M}_{14}$ respectively. The space group (point group operations + translations which generate the crystal) of NiO in both of these cases contains only two unique sites; one nickel site and one oxygen site which are separated by translation. This means each of the distinct magnetic sites in the magnetic crystal have identical crystal fields and experience the same magnetocrystalline anisotropy. Additionally the oxygen and nickel site have the same site point symmetry. In this case, we can use the lattice point group $m\,\bar{3}\,m$ without further analysis. For rank-2 magnetocrystalline anisotropy, we must solve the following system of matrix

equations

$$\rho_{ij} = \mathbb{M}_7^{ik}\rho_{jk}, \tag{4.5a}$$

$$\rho_{ij} = \mathbb{M}_{14}^{ik}\rho_{jk}. \tag{4.5b}$$

This reduces the allowed components of ρ_{ij} such that the only allowed anisotropy is $\rho_{00}(\alpha_1^2+\alpha_2^2+\alpha_3^2)$. By the definition of direction cosines we have $\alpha_1^2+\alpha_2^2+\alpha_3^2=1$. So, the only permitted rank-2 magnetocrystalline energy E_2 is an isotropic energy offset $E_2=\rho_{00}$. Constant energy offsets can be discarded, so rank-2 magnetocrystalline anisotropies (quadratic in α) are forbidden in cubic crystals. After applying the symmetry constraints, the permitted fourth order anisotropy energy for $m\,\bar{3}\,m$ is

$$E_4 = k_0(\alpha_1^4+\alpha_2^4+\alpha_3^4) + k_1(\alpha_1^2\alpha_2^2+\alpha_2^2\alpha_3^2+\alpha_3^2\alpha_1^2), \tag{4.6}$$

where k_1 are anisotropy constants (lower case to show the index is not related to the order). For rank-6, the permitted magnetocrystalline anisotropies are

$$\begin{aligned} E_6 = {} & k_2(\alpha_1^6+\alpha_2^6+\alpha_3^6) + k_3(\alpha_1\alpha_2\alpha_3)^2 \\ & + k_4(\alpha_1^4\alpha_2^2+\alpha_2^4\alpha_3^2+\alpha_3^4\alpha_1^2+\alpha_1^2\alpha_2^4+\alpha_2^2\alpha_3^4+\alpha_3^2\alpha_1^4). \end{aligned} \tag{4.7}$$

Using simple crystal symmetry arguments, the number of magnetocrstalline anisotropy constants to be determined has been reduced from 34 to just 5. $m\,\bar{3}\,m$ has the highest number of symmetry elements, each of which gives an additional (and distinct) equation which the anisotropy tensor must obey, so the anisotropy tensor has the fewest non-zero terms. The deviation from $m\,\bar{3}\,m$ for NiO is very small, even at zero temperature. The angles of the axes of conventional cell go from being perfectly orthogonal (90°) to making a $\sim 90.1°$ angle with one another [59]. So, the anisotropy constants of the magnetocrystalline anisotropies which are permitted by $\bar{3}\,m$ but forbidden by $m\,\bar{3}\,m$ will also be negligibly small. For completeness, the allowed anisotropies for the point group $\bar{3}\,m$ are given in Table 4.3. The direction cosines of $\bar{3}\,m$ which appear in Table 4.3 are in a different basis to the direction cosines of $m\,\bar{3}\,m$ which appear in Table 4.6, so cannot be compared without applying a transformation to a common basis. An example basis transformation is given below

$$\begin{aligned} (\alpha_1\alpha_2)^2+(\alpha_2\alpha_3)^2+(\alpha_3\alpha_1)^2 \xrightarrow{m\,\bar{3}\,m \text{ to } \bar{3}\,m} & \frac{1}{4}\left[(\alpha_1^2+\alpha_2^2)^2\right] + \frac{1}{3}\left[\alpha_3^4\right] \\ & - \frac{\sqrt{2}}{3}\left[\alpha_1\alpha_3(3\alpha_2^2-\alpha_1^2)\right]. \end{aligned} \tag{4.8}$$

Table 4.3: Permitted magnetocrystalline anisotropy terms for the non-magnetic point group $\bar{3}\,m$ in the basis where $\mathbf{e}_1 = [11\bar{2}]$, $\mathbf{e}_2 = [1\bar{1}0]$, $\mathbf{e}_3 = [111]$.

Anisotropy	Rank	Anisotropy	Rank	Anisotropy	Rank	Anisotropy	Rank
α_3^2	2	α_2^4	4	$\alpha_1^3\alpha_2^2\alpha_3$	6	$\alpha_1\alpha_2\alpha_3^4$	6
$(\alpha_1^2+\alpha_2^2)$	2	$\alpha_2^3\alpha_3$	4	$\alpha_1^3\alpha_2\alpha_3^2$	6	$\alpha_1\alpha_3^5$	6
α_1^4	4	$\alpha_2^2\alpha_3^2$	4	$\alpha_1^3\alpha_3^3$	6	α_2^6	6
$\alpha_1^3\alpha_2$	4	$\alpha_2\alpha_3^3$	4	$\alpha_1^2\alpha_2^4$	6	$\alpha_2^5\alpha_3$	6
$\alpha_1^3\alpha_3$	4	α_3^4	4	$\alpha_1^2\alpha_2^3\alpha_3$	6	$\alpha_2^4\alpha_3^2$	6
$\alpha_1^2\alpha_2^2$	4	α_1^6	6	$\alpha_1^2\alpha_2^2\alpha_3^2$	6	$\alpha_2^3\alpha_3^3$	6
$\alpha_1^2\alpha_2\alpha_3$	4	$\alpha_1^5\alpha_2$	6	$\alpha_1^2\alpha_2\alpha_3^3$	6	$\alpha_2^2\alpha_3^4$	6
$\alpha_1^2\alpha_3^2$	4	$\alpha_1^5\alpha_3$	6	$\alpha_1^2\alpha_3^4$	6	$\alpha_2\alpha_3^5$	6
$\alpha_1\alpha_2^3$	4	$\alpha_1^4\alpha_2^2$	6	$\alpha_1\alpha_2^5$	6	α_3^6	6
$\alpha_1\alpha_2^2\alpha_3$	4	$\alpha_1^4\alpha_2\alpha_3$	6	$\alpha_1\alpha_2^4\alpha_3$	6		
$\alpha_1\alpha_2\alpha_3^2$	4	$\alpha_1^4\alpha_3^2$	6	$\alpha_1\alpha_2^3\alpha_3^2$	6		
$\alpha_1\alpha_3^3$	4	$\alpha_1^3\alpha_2^3$	6	$\alpha_1\alpha_2^2\alpha_3^3$	6		

Most of the literature states that the spins lie in the $\{111\}$ planes, with preferred $\langle 11\bar{2}\rangle$ axes within these planes [59, 66, 95, 96]. Ignoring the crystal distortion, no combination of the (111) easy-plane dipole anisotropy and magnetocrystalline anisotropies which are permitted by symmetry (Table 4.6) give preferred directions of exactly $\langle 11\bar{2}\rangle$ (six-fold symmetry), and it is inconceivable that a 0.1% change in conventional bond angles could introduce a non-negligible in-plane crystal anisotropy (further justification in Section 4.5.3). This is in agreement with observations [61, 62, 97] and previous models [68], where there is a non-zero component of sublattice magnetisation parallel to [111]. The component of sublattice magnetisation parallel to [111] doesn't change the magnetic symmetry [57]. Both experimental papers and the theoretical model find non-zero out of plane components of the sublattice magnetisation. The observed deviation from (111) is incredibly small so none interpret this as having a ground state which is not $\langle 11\bar{2}\rangle$. Instead this is discarded as an artefact or experimental error. There are two additional experiments which show the three-fold symmetry more convincingly. First, Qiu *et al* [98] measured the THz emission from a (111) grown single crystal film of NiO by the inverse spin Hall effect (ISHE) signal generated in a Pt capping layer. The THz emission has three-fold symmetry upon rotating about the [111] direction

(figure 3 b-g). A similar THz time domain ellipsometry experiment [99]–which gives access to the orientation of induced dynamics–shows that, when applied to the $\sim$ 1THz mode, the induced magnetisation dynamics have three-fold symmetry, confirming the presence of a non-zero [111] component of the Néel vector.

The choice between a rank-4 cubic anisotropy, a rank-6 cubic anisotropy, a rank-6 hexagonal anisotropy, and a rank-2 easy-plane anisotropy may seem unnecessarily particular, especially when the values of the anisotropy constants can be arbitrarily chosen so that the resonant frequencies match the experimental measurement [66, 68, 85]. But, the choice of magnetocrystalline anisotropy changes the character (eigenvectors) of the magnon modes*, determines whether certain optical coupling mechanisms or magnetic transport phenomena are allowed by symmetry [99–101], and imposes certain constraints on which experimental geometries are required to observe certain magnon modes. All pump-probe experiments which measure the in-plane, $\sim$ 100GHz magnon mode have pump incidences which are not perpendicular to the [111] direction [89, 102, 103]. In work by Kampfrath [104], both pump and have propagation vectors along the (111) surface normal and the 100GHz mode is absent, and Tzschaschel [89] shows additional light polarisation selection criteria for the modes.

The choice of anisotropy also changes the relative amplitudes of known magnon modes†, it can introduce additional modes which may, or may not exist, and the choice breaks the continuous symmetry of the easy-plane in different ways introducing different possible soft modes which are no longer zero energy oscillations. So, the choice of anisotropy is important to predict which resonance modes can feasibly be measured in bulk (most modes vanish due to phase cancellation / destructive interference of the eigenoscillations) as well as to predict which experimental methods–and in which geometries–these modes can be measured.

*Only a uniaxial anisotropy appears in a linearised macrospin model. All other proposed magnetocrystalline anisotropies are highly non-linear.

†The amplitude is affected by different levels of non-linearity; a rank-2 $(1\bar{1}0)$ easy-plane anisotropy will give a much larger amplitude for the 100GHz magnon mode than a rank-6 hexagonal anisotropy because the amplitude of the mode is first order in the sublattice deflection amplitude compared to fifth order for the rank-6 anisotropy

4.4.3 Permitted Exchange Terms in NiO

The exchange interaction is complex. It is an emergent interaction in many-body systems from the combined effect of the Pauli exclusion principle and electron-electron Coulomb interactions. Exchange is also constrained by the symmetry of the crystal. Since the electron band structure is spin-split in magnetic materials, and the band structure gives information about the Coulomb interactions, then the exchange interaction must obey the symmetry of the magnetic point group. Despite this, it is generally expected that the deviation from the symmetry of the lattice is small as the contributions compatible with the magnetic symmetry are a back action on the electronic structure. Mott insulators such as NiO are an exceptional case. Electronic structure calculations such as density functional theories (DFT) which approximate electron correlations in crystals as free-electron-like (LDA, LSD, or GGA) cannot qualitatively describe Mott insulators, where deviations from free-electron behaviour creates a gap in the electronic structure. This shows that electronic correlations (magnetism) have a strong effect on the electronic structure and the magnetic back action contributions to the exchange interaction will be considerable. The reduction in (spatial) symmetry constraints by using the magnetic point group cannot introduce DMI–this requires that the interaction vectors between three neighbouring sites do not have an inversion centre [105]–but it can split the value of exchange for neighbours of different magnetic sublattices with the same interaction distance. This is the case for NiO. The next nearest neighbour interaction (J_2) couples pairs of spins which are on opposing sublattices ($J_2\mathbf{S}_\uparrow \cdot \mathbf{S}_\downarrow$), whereas the nearest neighbour interaction couples both pairs of opposing sublattices ($J_1\mathbf{S}_\uparrow \cdot \mathbf{S}_\downarrow$) and the same sublattice ($J_1\mathbf{S}_\uparrow \cdot \mathbf{S}_\uparrow$ and $J_1\mathbf{S}_\downarrow \cdot \mathbf{S}_\downarrow$). The magnetic symmetry allows the value of exchange for interactions like $\mathbf{S}_\uparrow \cdot \mathbf{S}_\downarrow$ and $\mathbf{S}_\uparrow \cdot \mathbf{S}_\uparrow$ to take different values. The cubic symmetry of the lattice in NiO is sometimes used as an argument to forbid the splitting of J_1 into J_{1+} and J_{1-} [69]*. This is not true, however, as the *magnetic* symmetry determines the allowed exchange interactions.

*A problem with reference [69] is that they say that type A and type B magnetic crystals have different lattice symmetries but have not realised that their type A and type B crystal also have different magnetic symmetries. Their depiction of type B cannot be a commensurate magnet (multiple, non-integer magnetic propagation vectors are required for order).

4.5 Parameterising the NiO Hamiltonian

Now the magnetic Hamiltonian terms that must be considered have been reduced only to terms which are permitted by symmetry, we must parameterise the Hamiltonian constants. The most important parameters for magnetic Hamiltonians are:

- Lattice parameter, a
- Spin magnetic moments, $\mu_{S,i}$
- Exchange interaction vectors and their strength, $\mathbf{r}_{ij}$ and $J_{ij}^{\alpha\beta}$
- Anisotropy constants, $K_{i,n}$
- Magnetic damping, α_i

Where the Latin subscripts i, and j are used to index spins in a supercell, the subscript n indexes the anisotropy constants (which can be different for each spin), and the Greek superscripts α, and β denote the tensor components of exchange (for symmetric Heisenberg exchange this is a scalar multiplied by the identity matrix). The next sections will describe the experimental measurements and theoretical calculations which yield the most accurate values of the above parameters*.

4.5.1 Experimental Measurements

The most accurate and reliable methods for determining lattice constants are x-ray scattering techniques. X-ray diffraction equipment exists in most experimental research groups and even tabletop apparatus is accurate enough for most applications, including measuring the 0.1° distortion in NiO. Measuring magnetic properties of antiferromagnets can be difficult but inelastic neutron scattering (INS) is a very powerful technique which gives access to structural properties (though the resolution is not as good as XRD) as well as high resolution information about the magnon spectrum. In principle, the magnon spectrum contains all the magnetic information of a system including anisotropies but the magnon gap at the Brillouin zone centre is too small to resolve in the available INS data for NiO [59]. Resonant inelastic x-ray scattering (RIXS) is another method which gives information about the magnon spectrum but its energy resolution is not as good as neutron scattering. Both of these techniques require highly specialised synchrotron facilities, but inelastic neutron scattering allows

*We exclude magnetic damping as this can vary by orders of magnitude between samples.

Table 4.4: The microscopic parameters for NiO from experimental measurements [59, 111]. Units are listed and may be different from the original reference.

Parameter	Value
a	4.17Å
J_2	-1.91 meV
J_{1+}	1.35 meV
J_{1-}	1.39 meV
μ_S	$1.60\mu_B$

exchange interactions and anisotropies to be determined with much greater accuracy than RIXS. The magnetic moment can also be difficult to measure experimentally. In principle, it can be measured using INS but this isn't available for NiO. Paramagnetic resonance techniques allow the magnetic moment to be estimated at high temperature.

In the case of NiO, there is a range of measurements available in the literature to work from: inelastic neutron scattering [59, 106, 107], RIXS [108], spherical neutron polarimetry [97], neutron diffraction [58, 74, 75, 109–111], x-ray photography [112, 113], XRD [114, 115]. Only Hutchings [59] and Betto [108] directly measure the magnetic dispersion and fit this to a magnetic Hamiltonian. Of these, only Hutchings is able to resolve the splitting in the nearest neighbour exchange–required to give the measured ground state–because of the higher energy resolution of INS. Ressouche [97] uses spherical neutron polarimetry to give the most precise confirmation of the magnetic structure of NiO (which has a small component perpendicular to the (111) plane). And, Balagurov [58] uses specialist high-resolution neutron diffraction to simultaneously measure the temperature dependence of the structural distortion and magnetic ordering, and finds that they have different transition temperatures. The magnetic moment is difficult to measure directly so is typically inferred from fitting neutron scatting data [111] and in NiO, the spin is expected to be non-half-interger because, despite being an insulator, there is significant covalency and the orbital moment is not quenched [116–118].

Using these experimental measurements, we can neglect the crystal distortion ($< 0.1°$) and an experimentally parameterised magnetic model of NiO should use the parameters listed in Table 4.4.

4.5.2 Ab-initio Calculations

NiO is a Mott insulator; spin correlations cause a strong Coulomb repulsion which creates a gap in the electronic structure. This is a problem for most DFT based methods which cannot accurately represent these systems. Some DFT methods allow a value of the Coulomb repulsion to be inputted but this requires information to be known about the system *a priori*. Quoted values for the band gap vary. An open access database using DFT states 2.30eV [119], whereas experiments range from $2.5 - 4.3$eV [120, 121]. Additionally, DFT methods which do not include the screened Coulomb interaction–including those which add in repulsion phenomenologically–do not consistently give the splitting of the nearest neighbour exchange interaction [122, 123]. These used cubic crystals but it has been known for many years that the distortion cannot completely explain the exchange splitting, so must exist even in its absence [124]. Others claim that the distortion is needed to create the splitting [69] even though their type B magnetic crystal (depicted in figure 2d) does not have the same symmetry as NiO–their magnetic crystal cannot be described by a single magnetic propagation vector so it cannot be collinear.

Instead of inferring the Coulomb repulsion (by using methods like LDA+U), it is preferable to use methods which include the effect of charge screening and correlations without this approximation. It avoids many of the problems described above. The quasi-particle self-consistent *GW* (QSGW) method is an ab-initio method which doesn't have to rely on DFT* and is parameter free [40, 125]. This method gives very good agreement with experimental measurements for parameters like spin magnetic moments, spin wave energies, and the dielectric function without artificially adding additional parameters such as the screened Coulomb interaction into the calculation, though it does not calculate lattice parameters, instead this is taken from neutron scattering experiments. Such methods are the most reliable (free of bias by the arbitrary choice / tweaking of parameters) for estimating magnetic parameters. For NiO, the values calculated using QSGW are given in Table 4.5.

At the time of writing, there are no ab-initio methods which include both relativistic effects and screened Coulomb interactions with sufficient accuracy to calculate realistic

*The implementation of QSGW in [40] uses LDA+U DFT.

Table 4.5: Microscopic Hamiltonian parameters for NiO. All parameters are taken from [40]. For exchange nn means nearest neighbour and nnn means next nearest neighbour.

Property	Symbol	Value
Spin magnetic moment	μ_S	$1.71\mu_B$
Exchange (nn $\uparrow\uparrow$)	J_{1+}	-0.77 meV
Exchange (nn $\uparrow\downarrow$)	J_{1-}	-1.00 meV
Exchange (nnn)	J_2	-14.7 meV
Lattice parameter	a	4.17Å
Cubic anisotropy constant	K	0.001 meV
Dimensionless damping	α	0.005
Dipole cutoff radius	R_{cut}	$5a$

values of the magnetocrystalline anisotropy constants in highly correlated materials such as NiO. So, we chose an ab-initio method which gives accurate parameters for exchange interactions, as these are more important than magnetocrystalline anisotropy constants.

4.5.3 Point Charge Model of Magnetic Anisotropy in NiO

In Section 4.4, we eliminated magnetocrystalline anisotropies which are forbidden by symmetry in NiO. There are no experimental measurements nor theoretical calculations which give a reasonable value for a magnetocrystalline anisotropy that isn't forbidden by symmetry, though there are cases where a crystal field with the correct symmetry has been considered. For example Battle [126] discusses a trigonal field due to nickel sites in CoO:Ni alloys and Low [127] similarly measures the trigonal crystal field splitting of nickel sites in MgO:Ni to estimate the spin-orbit coupling of nickel ions.

Without adequate measurements or calculations, the best we can do to calculate the non-negligible anisotropy terms is to use a point charge model of the crystal field. Point charge models are infrequently used because many magnetic materials of interest are metallic, so the large screening of the Coulomb interaction and highly non-local electron wavefunctions means point charge models give poor agreement [128]. Additionally, in

rare-earth materials where spin-orbit coupling is much larger than the crystal field, a point charge calculation of the crystal field is not representative of the eigenstates of the system. NiO, however, is a large band gap insulator with low spin-orbit coupling between nickel and oxygen sites so electronic and spin-orbit effects are small. Therefore we expect a point charge model to give a good estimate of the relative strength of different permissible anisotropy terms.

For our point charge model, we use a (111) oriented cubic crystal (initially with no distortion, space group $Fm\,\bar{3}\,m$), with spins lying in the (111) plane. The non-magnetic point group $m\,\bar{3}\,m$ has five anisotropy terms which are permitted by symmetry. These are given in Table 4.6.

Table 4.6: Permitted magnetocrystalline anisotropy terms for the non-magnetic point group $m\,\bar{3}\,m$ in the basis where $\hat{\mathbf{x}} = [100]$, $\hat{\mathbf{y}} = [010]$, $\hat{\mathbf{z}} = [001]$.

Anisotropy Term	Rank
$(\alpha_1^4 + \alpha_2^4 + \alpha_3^4)$	4
$(\alpha_1^2\alpha_2^2 + \alpha_2^2\alpha_3^2 + \alpha_3^2\alpha_1^2)$	4
$(\alpha_1^6 + \alpha_2^6 + \alpha_3^6)$	6
$(\alpha_1\alpha_2\alpha_3)^2$	6
$(\alpha_1^4\alpha_2^2 + \alpha_2^4\alpha_3^2 + \alpha_3^4\alpha_1^2 + \alpha_1^2\alpha_2^4 + \alpha_2^2\alpha_3^4 + \alpha_3^2\alpha_1^4)$	6

The rank-4 anisotropies are equivalent (within a constant energy offset) and can related by using the identity $\alpha_1^2+\alpha_2^2+\alpha_3^2 = 1$. We expect that the rank-6 contributions are small in comparison, but the term $(\alpha_1\alpha_2\alpha_3)^2$ has been used in the literature [68]. So, we choose to fit two anisotropy terms given by the following Hamiltonians

$$\mathcal{H} = -K_{\mathrm{c1}} \sum_i \left[(S_i^x S_i^y)^2 + (S_i^y S_i^z)^2 + (S_i^z S_i^x)^2 \right] \tag{4.9a}$$

$$\mathcal{H} = -K_{\mathrm{c2}} \sum_i \left[S_i^x S_i^y S_i^z \right]^2 . \tag{4.9b}$$

In the (111) oriented basis the Cartesian axes are given by the following crystallographic directions $\hat{\mathbf{x}} = [1/\sqrt{6},\, 1/\sqrt{2},\, 1/\sqrt{3}]$, $\hat{\mathbf{y}} = [1/\sqrt{6},\, -1/\sqrt{2},\, 1/\sqrt{3}]$, $\hat{\mathbf{x}} = [-2/\sqrt{6},\, 0,\, 1/\sqrt{3}]$.

In this basis, the rank-4 and rank-6 cubic anisotropies are

$$\begin{aligned}\mathcal{H} = -\frac{K_1}{12}\sum_i \Big[&3(S_i^x)^4 + 4\sqrt{2}(S_i^x)^3(S_i^z) + 6(S_i^x)^2(S_i^y)^2 \\ &- 12\sqrt{2}(S_i^x)(S_i^y)^2(S_i^z) + 3(S_i^y)^4 + 4(S_i^z)^4\Big],\end{aligned} \tag{4.10a}$$

$$\begin{aligned}\mathcal{H} = -\frac{K_2}{11664}\sum_i \Big[&(\sqrt{6}S_i^x - \sqrt{3}S_i^z)^2(\sqrt{6}S_i^x - 3\sqrt{2}S_i^y + 2\sqrt{3}S_i^z)^2 \\ &\times (\sqrt{6}S_i^x + 3\sqrt{2}S_i^y + 2\sqrt{3}S_i^z)^2\Big].\end{aligned} \tag{4.10b}$$

For the point charge model, we choose to only include the effect of the six interstitial first neighbour oxygen atoms–further shells of neighbours will adjust the amplitudes by a small amount and introduce additional higher rank anisotropies. The next shell consists of twelve nickel sites. The crystal field potential due to the twelve nickel sites is, at most, half the size of the potential due to the six nearest oxygen sites, and the shape of the potential due to nickel sites is inherently higher order due to a larger number of sites. Including the shell of nickel sites would introduce unnecessary complexity to a crystal anisotropy which is already very small. The displacement vectors between a nickel site at the origin and the six nearest oxygen sites are

$$\begin{aligned}\mathbf{r}_1 &= \frac{1}{2}(\mathbf{v}_3 + \mathbf{v}_1) \\ \mathbf{r}_2 &= \frac{1}{2}(\mathbf{v}_3 - \mathbf{v}_1) \\ \mathbf{r}_3 &= \frac{1}{2}(\mathbf{v}_3 - \mathbf{v}_1 - 2\mathbf{v}_2) \\ \mathbf{r}_4 &= -\frac{1}{2}(\mathbf{v}_3 + \mathbf{v}_1) \\ \mathbf{r}_5 &= -\frac{1}{2}(\mathbf{v}_3 - \mathbf{v}_1) \\ \mathbf{r}_6 &= -\frac{1}{2}(\mathbf{v}_3 - \mathbf{v}_1 - 2\mathbf{v}_2),\end{aligned} \tag{4.11}$$

where $\mathbf{v}_1 = a(\frac{\sqrt{2}}{2}, 0, 0)$, $\mathbf{v}_2 = a(-\frac{\sqrt{2}}{4}, \frac{\sqrt{6}}{4}, 0)$, $\mathbf{v}_3 = a(0, \frac{\sqrt{6}}{6}, \frac{\sqrt{3}}{3})$ and $a = 4.17$Å is the lattice parameter. Assuming the sites have opposite charge (Ni^{2+}, O^{2-}), we can write the effective crystal field interaction as a Coulomb potential

$$V_{\mathrm{CF}}(\mathbf{x}) = \sum_{i=1}^{6} \frac{-1}{|\mathbf{r}_i - \mathbf{x}|}. \tag{4.12}$$

The crystal field here is unitless. One could approximate the magnitude of the crystal field splitting by using the ionic charges Ni^{2+} and O^{2-} but this neglects the effect of

charge screening by the nuclei. To estimate the strength of the resulting magneto-crystalline anisotropy, the strength of the spin-orbit coupling and the magnitude of the orbital angular momentum of unpaired (but strongly correlated) electrons must be known. To avoid this complexity, we are only interested in the shape of the resultant anisotropy (which has the same shape as the crystal field), and the relative contributions of the permitted anisotropies. Ignoring the distortion, the point charge model gives a rank-4 cubic anisotropy (see Fig. 4.3) with a small rank-6 contribution ($\sim 2\%$ of the rank-4 energy).

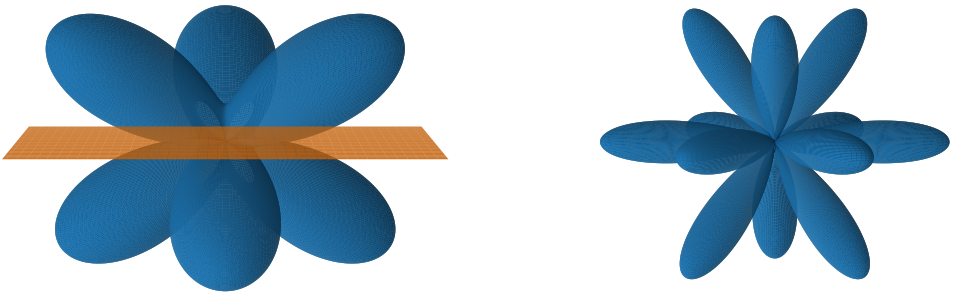

Figure 4.3: Polar energy surfaces for (*left*) a (111) oriented cubic NiO crystal from the point charge model, (right) the difference between the point charge model and optimised anisotropy Hamiltonian. The crystallographic (111) plane is depicted in orange and the axes on the right plot are 200 times smaller than the left.

Additionally, we created a point charge model which includes the contraction of crystallographic (111) planes. Hutchings [59] gave a low temperature change in bond angles of $6'$ which is equivalent to $0.1°$. We chose a much larger contraction; a 5% ($\sim 0.8°$) reduction in the distance between (111) planes so that any change in the point charge model could be resolved. The contraction was implemented by the transformation $v_3 : a(0, \frac{\sqrt{6}}{6}, \frac{\sqrt{3}}{3}) \rightarrow a(0, \frac{\sqrt{6}}{6}, 0.995\frac{\sqrt{3}}{3})$. The expressions for the displacement vectors remain the same but their numerical value changes due to the change in basis

vector $\mathbf{v}_3$. This does not preserve the volume of unit cell but, for the purpose of determining the change in magnetocrystalline anisotropy, this is unimportant as the lattice is frozen and magnetoelastic coupling is ignored.

As an aside, it may, at first glance, seem that the trigonal point group $\bar{3}\,m$ does not permit a rank-4 cubic anisotropy. It does not appear directly in Table 4.3 because the direction cosines have a different basis; $\alpha_1 = [100]$ for the cubic anisotropies in Table 4.6, and $\alpha_1 = [11\bar{2}]$ for the trigonal anisotropies in Table 4.3. But, with an appropriate rotation, the rank-4 cubic anisotropy can be written in terms of the trigonal direction cosines as

$$\begin{aligned}(\alpha_1\alpha_2)^2 + (\alpha_2\alpha_3)^2 + (\alpha_3\alpha_1)^2 \xrightarrow{m\,\bar{3}\,m \text{ to } \bar{3}\,m} &\frac{1}{4}\left[(\alpha_1^2+\alpha_2^2)^2\right] + \frac{1}{3}\left[\alpha_3^4\right] \\ &- \frac{\sqrt{2}}{3}\left[\alpha_1\alpha_3(3\alpha_2^2-\alpha_1^2)\right].\end{aligned} \tag{4.13}$$

Comparing with Table 4.3, each term in square brackets on the right hand side is admissible by $\bar{3}\,m$. So a rank-4 cubic anisotropy is a special case of the permitted $\bar{3}\,m$ terms.

Including the trigonal contraction in the point charge model is expected to introduce additional uniaxial anisotropy contributions along the [111] direction. We chose to add both a rank-2 and rank-4 uniaxial anisotropy as well as a $\bar{3}\,m$ compatible trigonal anisotropy which, in the (111) basis, are given by

$$\mathcal{H} = -K_{\mathrm{u}1}\sum_i (S_i^z)^2 \tag{4.14a}$$

$$\mathcal{H} = -K_{\mathrm{u}2}\sum_i (S_i^z)^4 \tag{4.14b}$$

$$\mathcal{H} = -K_{\mathrm{t}1}\sum_i \left[S_i^x S_i^z [3(S_i^y)^2 - (S_i^x)^2]\right]. \tag{4.14c}$$

Linear regression was performed, by hand, on the values of the rank-4 and rank-6 cubic anisotropies $k_{\mathrm{c}1}$ and $k_{\mathrm{c}2}$ for the cubic cell, and rank-2 uniaxial $k_{\mathrm{u}1}$, rank-4 uniaxial $k_{\mathrm{u}2}$ and rank-4 trigonal $k_{\mathrm{t}1}$ anisotropies for the distorted cell until the difference between the point charge model and Hamiltonian energy surface was $\sim 0.01\%$. The optimised values are given below in Table. 4.7*. The table includes the maximum energy difference $\Delta_{\max}$ between the point charge model and the anisotropy Hamiltonian. The

*Another set of optimised anisotropy constants was obtained which have similarly small difference

energy surface for the point charge model and the difference between the point charge model and anisotropy Hamiltonian for the distorted crystal are shown in Fig. 4.4 (no difference between the model and Hamiltonian can be observed by eye). Both visually and numerically this is almost identical to the cubic point charge model in Fig. 4.3, even though the distortion has been exaggerated by nearly an order of magnitude.

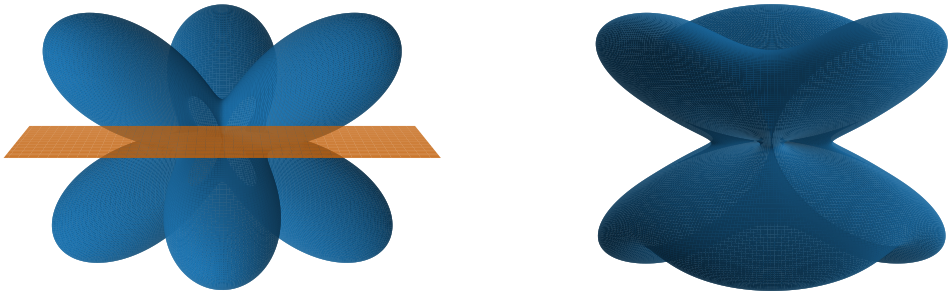

Figure 4.4: Polar energy surfaces for a (111) oriented NiO crystal including the trigonal contraction. (*left*) The point charge calculation, (*right*) the difference between the point charge model and the optimised anisotropy Hamiltonian. The crystallographic (111) plane is depicted in orange and the axes on the right plot are 200 times smaller than the left.

The anisotropy terms for the distorted crystal were chosen as the reduction in symmetry is expected to be very close to cubic with additional anisotropies compatible with the trigonal point group $\bar{3}\,m$. All values are normalised such that $k_{\mathrm{c1}} = 1$. Lowercase constants k are used as they are unitless. Hamiltonian anisotropy constants must have units of energy per spin which can be estimated from experimental measurements of the spin dynamics and crystal field splitting.

from the point charge model. These are not presented here but have a non-zero k_{u2}. It has previously been pointed out that the anisotropies here are not orthogonal, and that using spherical harmonics can be beneficial to uniquely specify the magnetocrystalline anisotropy in a material [129].

Table 4.7: Unitless anisotropy constants determined from the point charge model of NiO. The maximum difference $\Delta_{\max}$ between the point charge model and the anisotropy Hamiltonian is also included.

Anisotropy Constant	Cubic Value (k_{c1})	Trigonal Value (k_{c1})
k_{c1}	1	1
k_{c2}	0.168	0.168
k_{u1}	0	-0.107
k_{t1}	0	0.005
k_{u2}	0	0
$\Delta_{\max}$	0.0014 ($\sim 0.1\%$)	0.0055 ($\sim 0.6\%$)

The point charge model shows that the anisotropy constant for rank-6 cubic anisotropy K_{c2} is $\sim 17\%$ of the rank-4 cubic anisotropy constant K_{c1}. This may not seem negligible at first glance. But, the energy difference between maxima and minima for these two anisotropies is not 17%. The single spin energies of these anisotropies are given by

$$E_{c1} = -K_{c1}\left[(S_xS_y)^2 + (S_yS_z)^2 + (S_zS_x)^2\right] \tag{4.15a}$$

$$E_{c2} = -K_{c2}(S_xS_yS_z)^2. \tag{4.15b}$$

The pair of crystallographic directions [001] and [111] are an easy and hard axis for a spin with either a rank-4 cubic anisotropy (E_{c1}) or a rank-6 cubic anisotropy (E_{c2}). The energy difference between these two directions for each anisotropy is

$$\Delta E_{c1} = \frac{K_{c1}}{3}, \tag{4.16a}$$

$$\Delta E_{c2} = \frac{K_{c2}}{27}. \tag{4.16b}$$

So, a rank-6 cubic anisotropy would need to have an anisotropy constant 9 times larger than a rank-4 anisotropy to have the same energy barrier between easy and hard directions. Taking this into consideration, for the cubic NiO crystal with space group $Fm\bar{3}m$, the energy contribution of the rank-4 anisotropy is $|\Delta E_{c1}| = 0.\dot{3}$ and the rank-6 anisotropy contribution has $|\Delta E_{c2}| = 0.006\dot{2}$. The effect of rank-4 anisotropy is ~ 50 times larger than the effect of the rank-6 term.

4.5.4 Convergence of the Dipole-Dipole Interaction

In atomistic simulations, we calculate the magnetic dipole-dipole interaction between discrete magnetic moments directly. This is computationally very expensive and, in principle, the interaction of a magnetic moment with every other magnetic moment in the ensemble should be calculated. For a supercell which contains 24,576 magnetic moments (this is small for a simulation), there are over 600,000,000 dipole interactions which must be calculated. Since the strength of the dipole-dipole interaction is proportional to $|\mathbf{r}_{ij}|^{-3}$, we reduce the computational overhead of the dipole-dipole term by using a spherical cutoff radius; neighbours outside this radius are omitted from calculations. Fig. 4.5 shows the energy difference between the hard axis and easy plane in NiO as a function of the cutoff radius R in units of the lattice parameter $a = 4.17$Å. The cutoff radius for all simulations was chosen to be $R_{\text{cut}} = 5a$, unless otherwise stated*. This is equal to $R_{\text{cut}} = 20.85$nm. This value of the cutoff radius has good convergence of the energy difference, which means the dipole-dipole interaction in simulations of NiO has 2,122 nearest neighbours per spin (compared to 18 for exchange).

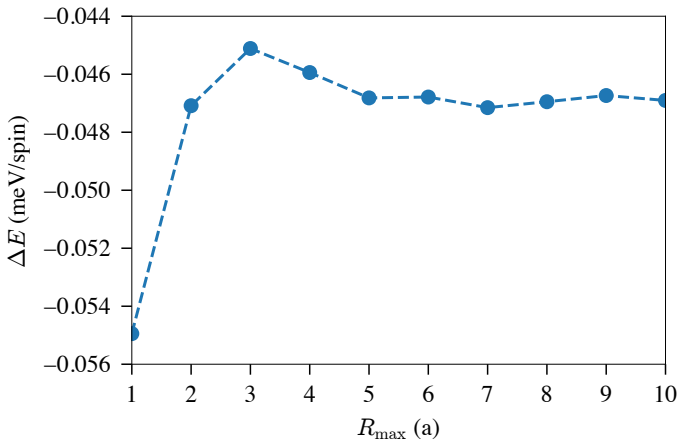

Figure 4.5: Dipole anisotropy energy difference between the Néel vector lying along $[11\bar{2}]$ and [111] against the maximum interaction distance in units of the lattice parameter.

*In very thin films and nanoparticles of NiO, the ground state is not necessarily an easy-plane, or even collinear. But in bulk-like systems, the ground state is always a collinear easy (111) plane.

4.5.5 Summary of the Magnetic Model of NiO

We choose the ab-initio parameters for the all atomistic simulations of NiO. These parameters give the best agreement with experiments and are the least sensitive to choices made in experimental measurement and/or fitting. It is also much newer than the best neutron diffraction experiments by Hutchings in 1972 [59]. The total magnetic Hamiltonian is

$$\begin{aligned}\mathcal{H} = &-\frac{1}{2}\sum_{i,j} J_{ij}\mathbf{S}_i \cdot \mathbf{S}_j \\ &-\frac{1}{2}\sum_{i\neq j}\frac{\mu_0\mu_{S,i}\mu_{S,j}}{4\pi}\frac{3(\mathbf{S}_i\cdot\hat{\mathbf{r}}_{ij})(\mathbf{S}_j\cdot\hat{\mathbf{r}}_{ij})-(\mathbf{S}_i\cdot\mathbf{S}_j)}{|\mathbf{r}_{ij}|^3} \\ &-\sum_i K_i\left[(S_i^{\mathrm{u}}S_i^{\mathrm{v}})^2+(S_i^{\mathrm{v}}S_i^{\mathrm{w}})^2+(S_i^{\mathrm{w}}S_i^{\mathrm{u}})^2\right],\end{aligned} \tag{4.17}$$

where the unit vectors $\hat{\mathbf{u}}$, $\hat{\mathbf{v}}$, $\hat{\mathbf{w}}$ are given by $\hat{\mathbf{u}} = [1/\sqrt{6},\, 1/\sqrt{2},\, 1/\sqrt{3}]$, $\hat{\mathbf{v}} = [1/\sqrt{6},\, -1/\sqrt{2},\, 1/\sqrt{3}]$, and $\hat{\mathbf{w}} = [-2/\sqrt{6},\, 0,\, 1/\sqrt{3}]$. The microscopic material parameters used in all atomistic simulations are given in Table 4.5.

By considering both the lattice and magnetic symmetries of NiO, we have created a spin Hamiltonian which obeys Neumann's principle and is commensurate with global antiferromagnetic ordering. The material parameters and exchange interactions were then parameterised using both high resolution experimental measurements (Table 4.4) and carefully selected ab-initio methods (Table 4.5)–the difference in material parameters between these two are small so we can be confident that the model accurately reflects reality. The relative strengths of the magnetocrystalline anisotropy constants were estimated using a point charge model of the crystal field which unequivocally shows that there is a non-zero (albeit very small) out of plane component of the sublattice magnetisation. Since no reliable measurements or calculations of the strength of the leading order magnetocrystalline anisotropy are available in the literature, a simple order of magnitude estimation from the magnitude of the measured out of plane sublattice magnetisation is used* [60]. Aside from this, the model presented has no parameters which are altered to agree with experiment. The tools presented above

*In Chapter 6, we analyse the eigenfrequencies of NiO in the linear approximation and find that the magnetocrystalline anisotropy doesn't introduce any additional eigenmodes so the anisotropy constant cannot be estimated from the low frequency mode.

are very powerful and a similar process should be used to create models of magnetic materials to ensure the model is realistic, is not forbidden by symmetry, and can be used to confidently predict the microscopic behaviour of magnetic materials which is especially important in antiferromagnets.

Chapter 5

Thermodynamics of NiO

5.1 Thermostats

In atomistic spin dynamics calculations, the stochastic thermal field must obey fluctuation dissipation theorem. The stochastic thermal field $\boldsymbol{\xi}_i(t)$–which is often called a thermostat–is defined by its correlations. These are

$$\langle \xi_i^{\alpha}(t) \rangle_t = 0 \tag{5.1a}$$

$$\langle \xi_i^{\alpha}(t)\, \xi_j^{\beta}(t') \rangle = \frac{2\alpha}{\mu_{\mathrm{S},i}\gamma_i} \delta(i,j)\delta(\alpha,\beta)\delta(t,t')\varphi(f,T), \tag{5.1b}$$

where α, β are Cartesian directions and $\varphi(f,T)$ is the power spectrum of the thermal noise. Most atomistic spin dynamics codes use classical, white thermal noise. This means that there are a similar number of $\mathbf{k} = 0$ spin waves and Brillouin zone edge spin waves. Since magnons are approximately bosons*, the power spectrum of the thermal noise should follow a Bose-Einstein distribution, even when spin is not quantised [131, 132]. This method was first applied to molecular dynamics [133] and has since been applied to spin dynamics [132]. By using Planck statistics, we populate thermal spin waves such that the there are many more low energy spin waves than high energy ones. The white and Planck power spectral functions $\varphi(f,T)$ are given by†

- Classical $\varphi_{\mathrm{cl}}(f,T) = k_B T$
- Semi-classical $\varphi_{\mathrm{q}}(f,T) = hf/\exp(hf/k_B T)$.

When φ_{q} is used, as in Fig. 5.1, analytic theories such as Bloch's law [130, 134, 135]–which shows that the decrease in the saturation magnetisation due to temperature in a ferromagnet is proportional to $T^{3/2}$–are recovered in simulations without any fitting or temperature rescaling as seen in other work [131, 136]. When temperature is rescaled, Bloch's law can be recovered from simulations with white noise, but the incorrect population of spin waves across the Brillouin zone will have strange effects on spin wave interactions and the temperature dependence of other observables such as the spin wave

*Magnon states (Holstein-Primakoff operators) are not perfectly orthogonal so cannot be perfectly bosonic [130]. The truncation of the binomial expansion of Holstein-Primakoff operators to linear in boson operators is an approximation ie $\sqrt{2S}\left(1 - \frac{1}{2S}\hat{a}_i^{\dagger}\hat{a}_i\right)^{1/2}\hat{a}_i \approx \sqrt{2S}\hat{a}_i$

†There are many equivalent nomenclatures for these two cases. For classical statistics, one will often see the following terms used; white noise, Boltzmann statistics, Maxwell-Boltzmann distribution, equipartition, Gaussian thermal noise, Johnson-Nyquist noise, Rayleigh-Jean law. For quantum boson statistics, the following are used; coloured noise, Planck statistics, Bose-Einstein distribution, energy quantisation, etc.

stiffness, anisotropy and damping. In Fig. 5.1, the breakdown of Bloch's law can be seen at high temperature and is discussed in Section 5.2. As predicted by quantum theory, the thermodynamics of a simulation using a quantum thermostat becomes dependent not only on the values J_{ij}, but also on the spin magnetic moment μ_S (or the spin quantum number S for truly quantum systems). This additional degree of freedom means it is even more important to carefully parameterise the Hamiltonian of the system when using a quantum thermostat.

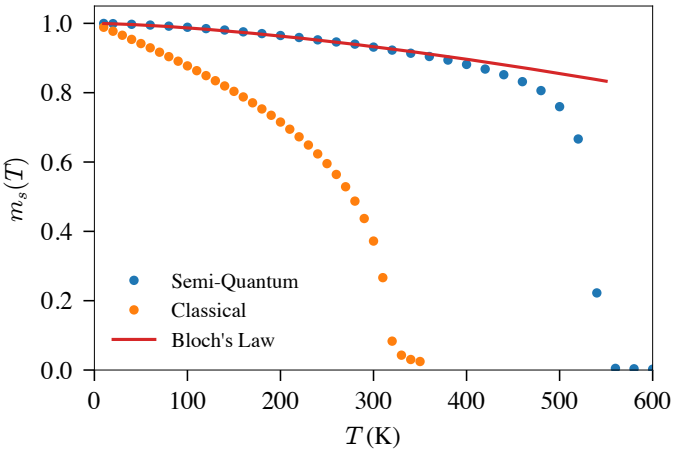

Figure 5.1: The temperature dependence of the magnetisation of a simple cubic ferromagnet with uniaxial magnetocrystalline anisotropy ($J_1 = 3 \times 10^{-21}$J, $K = 1 \times 10^{-23}$J, $\mu_S = 1\mu_B$ and $a = 3$Å) using atomistic spin dynamics. Calculations using both the classical and quantum thermostat are included. The curve is the analytic expression for Bloch's law (5.3).

This is not a perfect method. In the limit of low damping, this implementation of coloured noise breaks fluctuation-dissipation theorem. A different implementation, which requires two magnetic damping parameters [137], introduces a 'memory' of previous states to ensure fluctuation-dissipation theorem is obeyed–though the idea of a memory in the thermal fluctuations of quantum systems isn't new [138–140]. In practice, $\alpha > 10^{-3}$ is sufficient to ensure fluctuation-dissipation theorem is obeyed–this is small for most metals but is large compared to insulators like YIG [141] and NiO [142].

It is important to discuss the limitations of using coloured thermostats to introduce quantum effects into classical systems. By using a quantum thermostat we have excellent quantitative agreement with experiments for temperatures away from absolute zero and away from the critical temperature. Since this is a classical method, purely quantum effects such as superposition, tunnelling and zero point fluctuations are not observed. And, since this is still a three-dimensional Heisenberg model, we have not changed the universality class, so observe a classical scaling exponent [143, 144]*. When using methods like atomistic spin dynamics for multiscale materials specific modelling we are often working on time-, temperature-, and length-scales where these quantum effects are not important. Instead, we care about macroscopic observables such as the magnetisation, or thermodynamic effects like spin wave softening, and linewidth broadening so that we can explain and/or predict the behaviour of devices at this scale. In this case, correctly populating the spin wave spectrum so that the magnetisation and magnon-magnon scattering cross-sections are quantitative compared to experiments is sufficient. If quantum effects must be included then quantum Monte Carlo simulations must be used which are limited to ∼100 atoms (this is a nondeterministic polynomial complexity problem [146]) or two-dimensional models [147], instead of the hundreds of thousands or millions of spins that can be accessed using three-dimensional atomistic spin dynamics.

5.2 Sublattice Magnetisation

The sublattice magnetisation of an antiferromagnet has a different temperature dependence to ferromagnets. Ferromagnets have quadratic dispersions so follow Bloch's law [134]. Bloch's law has a very simple premise–each magnon is a delocalised spin flip so the finite temperature magnetisation is related to the total number of magnons. The number of occupied magnon states can be calculated analytically by a small k approximation and using Bose statistics to estimate the magnetisation. Though the theory was originally derived by Bloch, Dyson [130] created the modern spin wave theory of magnetic materials, giving very comprehensive consideration of the effects of spin wave occupations, the shape of the spectrum and the non-orthogonality of magnon states (non-bosonic contributions); a second article was published at the same time applying

*Though the critical exponents of real materials can be closer to the 3-dimentional Heisenberg model than the 3-dimensional Ising model (see figure 7 of [145], for example).

this theory to a simple anisotropic ferromagnet [135]. This is a generalised Bloch's law and introduced a number of higher order terms, but these are rarely used. For a bulk isotropic ferromagnet with conventional lattice parameter a, spin magnetic moment per atom μ_S, and only contains nearest neighbour exchange of strength J in a small magnetic field applied $\mathbf{H} = H_0\hat{\mathbf{z}}$, the Hamiltonian is

$$\mathcal{H} = -\frac{1}{2}\sum_{i,j} J_{ij}\mathbf{S}_i \cdot \mathbf{S}_j - \mu_0\mu_S \sum_i S_i^z H_0, \tag{5.2}$$

and, assuming the applied field is small, Bloch's law is given by

$$m_z(T) = \left\langle \sum_i S_i^z \right\rangle = 1 - \frac{g\mu_B}{\mu_S}\frac{\nu_{\text{WS}}\Gamma(3/2)\zeta(3/2)}{4\pi^2}\left(\frac{k_B T}{J\mu_S a^2/g\mu_B}\right)^{\frac{3}{2}} \tag{5.3}$$

where g is the Landé-g factor*, Γ is the gamma function, and ζ is the Riemann zeta function. This comes from a direct evaluation of the magnon number operator $\langle\langle \hat{n}_{\mathbf{k}}\rangle_{\mathbf{k}}\rangle_T$ in the low temperature limit. The number operator for magnons is related to the thermal noise power by $\langle \hat{n}_{\mathbf{k}}\rangle_T = \langle \varphi_{\text{q}}(f,T)\rangle_T$. The noise power is evaluated numerically and we do not take the low temperature limit (as in Bloch's law). Therefore, simulations using a quantum thermostat include all higher order effects, and results are quantitative to higher temperatures where the quantisation of spin plays determines the critical exponents of the system; since the spins in our simulations are continuous unit vectors, these still belong to the classical Heisenberg model universality class. For antiferromagnets, however, the linear dispersion means that the low temperature approximation of the magnon number $\langle \hat{n}_{\mathbf{k}}\rangle_{\mathbf{k}}$ has a different expression. This is a little known fact in the field and researchers either assume Bloch's law is valid in antiferromagnets, or a Brillouin function is used to estimate the sublattice $m_s(T)$† [142]. The antiferromagnetic analogue to Bloch's law was derived by Kubo [148] which gives a quadratic temperature dependence of the sublattice/staggered magnetisation. In Appendix D we derived the exchange magnon Hamiltonian for NiO including both nearest and next nearest exchange, and the exchange splitting. We reproduce a few steps here for the derivation

*This form of Bloch's law is for classical spins. For the quantum case, $\mathbf{S}_i \cdot \mathbf{S}_j \to \hat{S}_i^x\hat{S}_j^x + \hat{S}_i^y\hat{S}_j^y + \hat{S}_i^z\hat{S}_j^z$ so one must multiply the second term by S^2 (not $S(S+1)$).

†We use $m_s(T)$ to distinguish between the absolute value $|\mathbf{m}(T)| = \left(\sum_i (-1)^i \mathbf{S}_i\right) \cdot \left(\sum_i (-1)^i \mathbf{S}_i\right)$ and by taking some quantisation axis (ie $\hat{\mathbf{z}}$) to measure the saturation $m_s(T) = \sum_i (-1)^i (\mathbf{S}_i \cdot \hat{\mathbf{z}})$. Both Bloch's law and Kubo's expression for antiferromagnets are only valid with respect to a quantisation axis because of the uncertainty principle's stipulation that $\hat{S}_x$, $\hat{S}_y$ and $\hat{S}_z$ cannot simultaneously be measured in a quantum system.

of a modified Kubo T^2 law. Ignoring zero point fluctuations (atomistic simulations are classical so we do not observe this), we begin with the following form of the the second order magnon Hamiltonian operator

$$\hat{\mathcal{H}}^{(2)} = \sum_{\mathbf{k}} A_{\mathbf{k}} \left(\hat{a}^{\dagger}_{\mathbf{k}} \hat{a}_{\mathbf{k}} + \hat{b}^{\dagger}_{\mathbf{k}} \hat{b}_{\mathbf{k}^{\dagger}} \right) + B_{\mathbf{k}} \left(\hat{a}_{\mathbf{k}} \hat{b}_{\mathbf{k}} + \hat{a}^{\dagger}_{\mathbf{k}} \hat{b}^{\dagger}_{\mathbf{k}} \right), \tag{5.4}$$

where

$$A_{\mathbf{k}} = -Sz[\mathcal{J}_{1+}(\gamma^{+}_{\mathbf{k}} - 1) + \mathcal{J}_{1-} + \mathcal{J}_2], \tag{5.5a}$$

$$B_{\mathbf{k}} = -Sz[\mathcal{J}_{1-}\gamma^{-}_{\mathbf{k}} + J_2\gamma^{(2)}_{\mathbf{k}}], \tag{5.5b}$$

$$\gamma^{+}_{\mathbf{k}} = \frac{1}{3}\left[\cos\left(\frac{a}{2}(k_x + k_y)\right) + \cos\left(\frac{a}{2}(k_y + k_z)\right) + \cos\left(\frac{a}{2}(k_x - k_z)\right)\right], \tag{5.5c}$$

$$\gamma^{-}_{\mathbf{k}} = \frac{1}{3}\left[\cos\left(\frac{a}{2}(k_x - k_y)\right) + \cos\left(\frac{a}{2}(k_y - k_z)\right) + \cos\left(\frac{a}{2}(k_z + k_x)\right)\right], \tag{5.5d}$$

$$\gamma^{(2)}_{\mathbf{k}} = \frac{1}{3}\left[\cos\left(k_x a\right) + \cos\left(k_y a\right) + \cos\left(k_z a\right)\right], \tag{5.5e}$$

$\mathcal{J} = \frac{J}{S^2}$ are the exchange interaction strengths*, $z = 6$ is the number of neighbours for each exchange interaction, $\hat{a}^{\dagger}_{\mathbf{k}}$ and $\hat{b}^{\dagger}_{\mathbf{k}}$ are the creation operators for bosonic excitations which are localised on the $\uparrow$ and $\downarrow$ sublattices respectively, $\hat{a}_{\mathbf{k}}$ and $\hat{b}_{\mathbf{k}}$ are the corresponding annihilation operators. All other material parameters are given in Table 4.5. There are off-diagonal terms in the above Hamiltonian which means the localised magnons of the two sublattices are coupled. We wish to rewrite this in the form

$$\hat{\mathcal{H}}^{(2)} = hf_{\mathbf{k}}(\hat{\alpha}^{\dagger}_{\mathbf{k}}\hat{\alpha}_{\mathbf{k}} + \hat{\beta}^{\dagger}_{\mathbf{k}}\hat{\beta}_{\mathbf{k}}), \tag{5.6}$$

where $hf_{\mathbf{k}}$ are the linearised magnon energies, $\hat{\alpha}^{\dagger}_{\mathbf{k}}$ and $\hat{\beta}^{\dagger}_{\mathbf{k}}$ are the creation operators of the two linearised magnons, and $\hat{\alpha}_{\mathbf{k}}$ and $\hat{\beta}_{\mathbf{k}}$ are the corresponding annihilation operators. The excitations described by α, β are not localised on a sublattice. Instead these are linearised/diagonalised using a Bogoliubov transformation which is $\mathbf{k}$-dependent. We choose the following form of the Bogoliubov transformation

$$\begin{bmatrix} \hat{a}_{\mathbf{k}} \\ \hat{b}^{\dagger}_{-\mathbf{k}} \end{bmatrix} = \begin{bmatrix} u_{\mathbf{k}} & -v_{\mathbf{k}} \\ -v_{\mathbf{k}} & u_{\mathbf{k}} \end{bmatrix} \begin{bmatrix} \hat{\alpha}_{\mathbf{k}} \\ \hat{\beta}^{\dagger}_{-\mathbf{k}} \end{bmatrix} \tag{5.7}$$

where $u_{\mathbf{k}} = [(A_{\mathbf{k}} + hf_{\mathbf{k}})/2hf_{\mathbf{k}}]^{1/2}$, $v_{\mathbf{k}} = [(A_{\mathbf{k}} - hf_{\mathbf{k}})/2hf_{\mathbf{k}}]^{1/2}$, and $hf_{\mathbf{k}} = \sqrt{A^2_{\mathbf{k}} - B^2_{\mathbf{k}}}$. To calculate the reduction in sublattice magnetisation due to temperature, we must

*We write the exchange like this to ensure agreement with our classical definitions of the exchange Hamiltonian. In other chapters calligraphic exchange constants are used for macroscopic parameters.

find expressions for the $\hat{S}_z$ operators on the $\uparrow$ and $\downarrow$ sublattices in terms of α and β operators. Using the above transformation and the canonical commutation relations, these are given by

$$\hat{S}_z^{\uparrow} = N_{\uparrow}S - \sum_{\mathbf{k}} \hat{a}_{\mathbf{k}}^{\dagger}\hat{a}_{\mathbf{k}} = NS - \sum_{\mathbf{k}} \left(u_{\mathbf{k}}^2 \hat{\alpha}_{\mathbf{k}}^{\dagger}\hat{\alpha}_{\mathbf{k}} + v_{\mathbf{k}}^2 \hat{\beta}_{-\mathbf{k}}^{\dagger}\hat{\beta}_{-\mathbf{k}} \right) \tag{5.8a}$$

$$\hat{S}_z^{\downarrow} = N_{\downarrow}S - \sum_{\mathbf{k}} \hat{b}_{\mathbf{k}}^{\dagger}\hat{b}_{\mathbf{k}} = NS - \sum_{\mathbf{k}} \left(v_{\mathbf{k}}^2 \hat{\alpha}_{-\mathbf{k}}^{\dagger}\hat{\alpha}_{-\mathbf{k}} + u_{\mathbf{k}}^2 \hat{\beta}_{\mathbf{k}}^{\dagger}\hat{\beta}_{\mathbf{k}} \right). \tag{5.8b}$$

Since the magnon Hamiltonian (5.4) can be written as a symmetric matrix, both sublattices have the same energies and occupations. So, the sublattice magnetisations and the Néel vector have the same temperature dependence (this is not true for ferrimagnets) which can be calculated by counting the number of thermal magnons. We now want to move back to classical spins while retaining the boson number operators $\langle \sum_{\mathbf{k}} \hat{\alpha}_{\mathbf{k}}^{\dagger}\hat{\alpha}_{\mathbf{k}} \rangle = \langle \sum_{\mathbf{k}} \hat{\beta}_{\mathbf{k}}^{\dagger}\hat{\beta}_{\mathbf{k}} \rangle = \langle \sum_{\mathbf{k}} \hat{n}_{\mathbf{k}} \rangle$ which, in combination with ignoring zero point fluctuations, becomes equivalent to numerical atomistic spin dynamics with a quantum thermostat. Moving from quantised magnons to classical spin waves looks like a simple transformation but has a few consequences which aren't often made explicit. We often think of the Heisenberg model in terms of classical spin vectors of unit length $\mathbf{S}$ but in atomistic spin dynamics these are actually magnetic moments $\boldsymbol{\mu} = \mu_S \mathbf{S}$. So, the (quantum) spin angular momentum S must be transformed to a classical magnetic moment using $g\mu_B S = \mu_S$*. This means that classical spin waves carry spin angular momentum $\mu_{\mathrm{SW}} = \mu_S$, and we retain the normalisation factor $1/NS$ in Bloch's law ($m_s(T) = 1 - (1/NS)\langle \hat{n}_{\mathbf{k}} \rangle$), even in the classical case. Moving to classical magnetic moments from quantised spins also justifies the absence of zero point fluctuations since a classical equation of motion with a classical Hamiltonian and classical spins always has the trivial ground state of perfectly aligned moments with no fluctuations.

Returning to the derivation of a modified Kubo T^2 law, the finite temperature Néel vector for classical magnetic moments (quantum operators become functions) is given

*One may initially think the transformation should use the total spin angular momentum $|S| = \sqrt{S(S+1)}$ but we have intentionally used the operator $\hat{S}^z$ which is given (with respect to some ground state $|0\rangle$) by $\hat{S}^z|0\rangle = S|0\rangle$. Therefore the transformation from quantised spin to classical spin angular momentum is given by $S \rightarrow \mu_S/g\mu_B$.

by

$$\begin{aligned} l_s(T) &= \left\langle \frac{1}{N}\sum_i (-1)^i S_i^s \right\rangle = \frac{1}{2}\left\langle \frac{1}{N_\uparrow}\sum_{i\in\uparrow} S_i^s \right\rangle - \frac{1}{2}\left\langle \frac{1}{N_\downarrow}\sum_{j\in\downarrow} S_j^s \right\rangle \\ &= 1 - \frac{g\mu_B}{\mu_S}\Big[\frac{1}{2N_\uparrow}\left\langle\left\langle u_{\mathbf{k}}^2\alpha_{\mathbf{k}}^\dagger\alpha_{\mathbf{k}} + v_{\mathbf{k}}^2\beta_{-\mathbf{k}}^\dagger\beta_{-\mathbf{k}} - u_{\mathbf{k}}v_{\mathbf{k}}\left(\hat{\alpha}_{\mathbf{k}}^\dagger\hat{\beta}_{-\mathbf{k}} + \hat{\alpha}_{\mathbf{k}}\hat{\beta}_{-\mathbf{k}}\right)\right\rangle\right\rangle \\ &\quad + \frac{1}{2N_\downarrow}\left\langle\left\langle v_{\mathbf{k}}^2\alpha_{-\mathbf{k}}^\dagger\alpha_{-\mathbf{k}} + u_{\mathbf{k}}^2\beta_{\mathbf{k}}^\dagger\beta_{\mathbf{k}} - u_{\mathbf{k}}v_{\mathbf{k}}\left(\hat{\alpha}_{\mathbf{k}}\hat{\beta}_{-\mathbf{k}} + \hat{\alpha}_{\mathbf{k}}\hat{\beta}_{-\mathbf{k}}\right)\right\rangle\right\rangle\Big] \\ &= 1 - \frac{g\mu_B}{N\mu_S}\left\langle\left\langle\left(u_{\mathbf{k}}^2 + v_{\mathbf{k}}^2\right)n_{\mathbf{k}}\right\rangle\right\rangle, \end{aligned} \tag{5.9}$$

where $N = N_\uparrow + N_\downarrow$ is the total number of magnetic moments, the quantisation axis s for NiO is the easy plane*, $u_{\mathbf{k}}^2 + v_{\mathbf{k}}^2 = |A_{\mathbf{k}}/hf(\mathbf{k})|$, and the inner and outer angle brackets denote the sum over $\mathbf{k}$ and thermal average, respectively.

Using equations (5.5), (5.6), and (5.7), the classical spin wave spectrum for our model of NiO is†

$$hf(\mathbf{k}) = \frac{g\mu_B\sqrt{z}}{\mu_S}\sqrt{\left[J_{1+}(\gamma_+(\mathbf{k}) - 1) + J_{1-} + J_2\right]^2 - \left[J_{1-}\gamma_-(\mathbf{k}) + J_2\gamma_2(\mathbf{k})\right]^2}, \tag{5.10}$$

where $z = 6$ is the number of neighbours for all three exchange interactions, and $\gamma(\mathbf{k})$ are the continuous structure factors in the limit of an infinite crystal. The remainder of the derivation is very similar to Bloch's law; take the small-k limit for spin waves to obtain a linear spin wave spectrum (quadratic in Bloch's law), then compute the generalised Watson integral [149] using substitution. The above expression is more complex than those used previously as it includes the nearest neighbour interaction (and its splitting). The additional mathematical complexity in our final expression for $l_s(T)$ is expected to give better agreement with experiments and our numerical

*Since the temperature dependence is independent of the anisotropy we were free to choose the z-direction as the quantisation axis but in practise the quantisation axis can in fact be a plane. The only requirement by the uncertainty principle on the derivation is a pair of orthogonal measurements which are usually taken to be $\hat{S}_z$ and $|S|^2 = S(S+1)$.

†In addition to removing the quantisation of spin, we have also removed the quantisation of $\mathbf{k}$ which is equivalent to the assumption of an infinite system. In an atomistic simulations we have a discrete lattice with a finite number of atomic sites so $\mathbf{k}$ is, in fact, quantised.

simulations. In the small-k limit the spectrum becomes

$$hf(\mathbf{k}) \approx \frac{g\mu_B}{\mu_S} a \Big[2J_2(J_2+J_{1-})|\mathbf{k}|^2 + J_{1-}(J_2+J_{1-})(|\mathbf{k}|^2 - k_xk_y - k_yk_z + k_zk_x) + J_{1+}(J_2+J_{1-})(|\mathbf{k}|^2 + k_xk_y + k_yk_z - k_zk_x) \Big]^{1/2}. \tag{5.11}$$

The inclusion of the split nearest neighbour interaction introduces some anisotropy to the dispersion relation. But, we can safely ignore this since terms like k_xk_y are odd and vanish in the generalised Watson integral. Now we have

$$\begin{aligned} hf(\mathbf{k}) &= \frac{g\mu_B}{\mu_S}\sqrt{(J_2+J_{1-})(2J_2+J_{1-}-J_{1+})}|k|a \\ &= D|k|, \end{aligned} \tag{5.12}$$

where $D = \frac{g\mu_B a}{\mu_S}\sqrt{(J_2+J_{1-})(2J_2+J_{1-}-J_{1+})}$ is the spin wave stiffness. The factor $u_{\mathbf{k}}^2 + v_{\mathbf{k}}^2$ in equation (5.9) was introduced by the Bologliubov transformation and is k-dependent; in the classical, small-k limit it is proportional to $1/|\mathbf{k}|$. So, we define the constant λ by the relation $u_{\mathbf{k}}^2 + v_{\mathbf{k}}^2 \approx \lambda/|\mathbf{k}|$. In the small-$k$ limit, λ is

$$\lambda \approx \frac{\sqrt{6}|J_2+J_{1-}|}{a\sqrt{(J_2+J_{1-})(2J_2+J_{1-}-J_{1+})}}. \tag{5.13}$$

The reduction of the staggered magnetisation at finite temperature $\Delta l_s(T) = 1 - l_s(T)$, can be calculated by substituting $u_{\mathbf{k}}^2 + v_{\mathbf{k}}^2 \approx \lambda/|\mathbf{k}|$ into equation (5.9), and replacing the number operator with a generalised Watson integral. This gives

$$\begin{aligned} \Delta l_s(T) &= \frac{g\mu_B}{\mu_S}\frac{\nu_{\mathrm{WS}}}{(2\pi)^3}\int_{k=0}^{k_{\max}}\int_{\theta=0}^{\pi}\int_{\phi=0}^{2\pi}\left(\frac{\lambda}{k}\right)\frac{k^2\sin\theta}{\mathrm{e}^{Dk/k_BT}-1}\,\mathrm{d}\phi\,\mathrm{d}\theta\,\mathrm{d}k \\ &= \frac{g\mu_B}{\mu_S}\frac{\nu_{\mathrm{WS}}\lambda}{(2\pi)^3}\int_{k=0}^{k_{\max}}\int_{\theta=0}^{\pi}\int_{\phi=0}^{2\pi}\frac{k\sin\theta}{\mathrm{e}^{Dk/k_BT}-1}\,\mathrm{d}\phi\,\mathrm{d}\theta\,\mathrm{d}k, \end{aligned} \tag{5.14}$$

where $\nu_{\mathrm{WS}} = a^3/4$ is the Wigner-Seitz volume. By using the substitution $x = Dk/k_BT$ and integrating from $x = 0$ to ∞, the staggered magnetisation is given by

$$l_s(T) = 1 - \frac{g\mu_B\nu_{\mathrm{WS}}\lambda}{12\mu_S}\left(\frac{k_BT}{D}\right)^2. \tag{5.15}$$

Including all three exchange terms, the reduction in staggered magnetisation is $\Delta l_s(T) \approx 5.08\times10^{-7}\,T^2$. By neglecting the J_1 contributions in the analytic calculation, the reduction in staggered magnetisation is $\Delta l_s(T) \approx 5.31\times10^{-7}\,T^2$. For a two sublattice model

(ignoring the problem of four uncoupled sublattices), the nearest neighbour interactions stabilise the magnetisation against thermal fluctuations. Though the difference is small ($\sim 4\%$). But, as discussed in Chapter 4, the nearest neighbour splitting is required for an antiferromagnetic state to be the equilibrium state at all temperatures. Similar to Dyson's treatment for ferromagnets, there are higher order corrections that can be included into the theory. For ferromagnets, the first order approximation is proportional to $T^{3/2}$, higher order corrections due to the shape of the spectrum are proportional to $T^{3/2+n}$ where n indexes the correction to the shape of the spectrum, and the lowest correction due to spin wave interactions is proportional to T^4. In antiferromagnets, the series can be written in a similar way, but is both qualitatively and quantitatively different; the first order approximation is proportional to T^2, corrections due to the shape of the spectrum are proportional to $T^{2(1+n)}$, and the first correction due to spin wave interactions is proportional to T^6 [150].

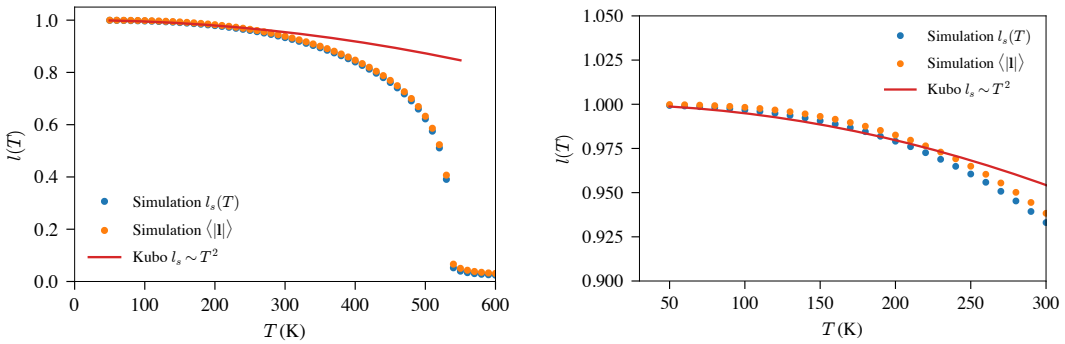

Figure 5.2: Comparison of Kubo's T^2 scaling from Eq (5.15) including both nearest neighbour and next nearest neighbour exchange and atomistic spin dynamics with a quantum thermostat. Both $\langle|\mathbf{l}|\rangle$ and $l_s(T) = \langle(1/N)\sum_i(-1)^i\mathbf{S}_i^{\perp}\rangle$ are plotted, and $\perp$ denotes the in-plane component of the spin moment.

In older literature, there were various discussions and speculations on the applicability of magnon theories on antiferromagnets because of zero point fluctuations in addition to the typical problems of non-orthogonal states and truncation of Holstein-Primakoff operators [148, 150, 151] which led to the use Schwinger boson mean-field (SBMF) theory which writes spin operators exactly Schwinger bosons instead of an approximate Taylor expansion of Holstein-Primakoff operators [152]. This theory is

applicable throughout the whole temperature range and doesn't require an ordered equilibrium state. But, the theory is applied numerically using Green's functions so doesn't yield easy to use analytic power laws in temperature. This means it is usually confined to highly anisotropic low dimensional systems [152] and systems with complex equilibrium states such as spin glasses, which aren't well described by spin wave theories [153].

Using linear spin wave theory, we now have an analytic expression to compare our numeric results with. We can't comment on the applicability of magnon theories on truly quantum systems, but we can compare the first order theory with the calculated temperature dependence from spin dynamics simulations using the quantum thermostat*. The simulations evaluate the full spin wave Hamiltonian–not simply the second order contribution–and includes the full shape of the spin wave spectrum instead of a linear approximation. In general, we expect first order theories of antiferromagnets to be slightly worse approximations than for ferromagnets because the system is inherently more 'quantum' (ie zero point fluctuations). It can be seen from the low temperature data of Fig. 5.2 that, at low temperatures, both $\langle|\mathbf{l}|\rangle$ and $l_s(T)$ lie above the analytic theory. This is in contrast to Fig. 5.1 where the simulation calculated $m(T)$ for an isotropic ferromagnet always lie below the analytic expression for Bloch's law. This is likely due to the relatively strong anisotropy in NiO. The effect of anisotropy can be included in the theory [148, 154]; the effect on the spin wave stiffness is negligible. But, at very low temperatures, the $>$ 1THz magnon gap introduced by the anisotropy prevents the occupation of low-k magnons, stabilising the sublattice magnetisation from thermal fluctuations. The effect of magnon freezing persists to temperatures much greater than the effective temperature of the gap (see figure 1 of Eisele [154]). The deviations from the simple theory are small enough that calculating a more complex expression will give no new insight into the system. Even if the effect of anisotropy was included in the theory, it is expected that $\langle|\mathbf{l}|\rangle$ will still lie above the theory because of the requirement from quantum mechanics that a quantisation axis/plane must be chosen.

Since the numerical calculations and analytic expression are derived from identical models of NiO, we can confidently say that the first order approximation of the tem-

*NiO is expected to be well described by spin wave theories.

perature dependence of staggered magnetisation should only be used for temperatures less than $\sim$ 40% of the Néel temperature–in metals, the agreement between experiments and spin wave theory is expected to break down at lower temperatures. In a typical ferromagnet, Bloch's law to first approximation can be applied up to $\sim$ 60% of the Curie temperature (at least for our generic simple cubic ferromagnet 5.1). For completeness, a comparison between the classical and quantum thermostat is given in Fig. 5.3.

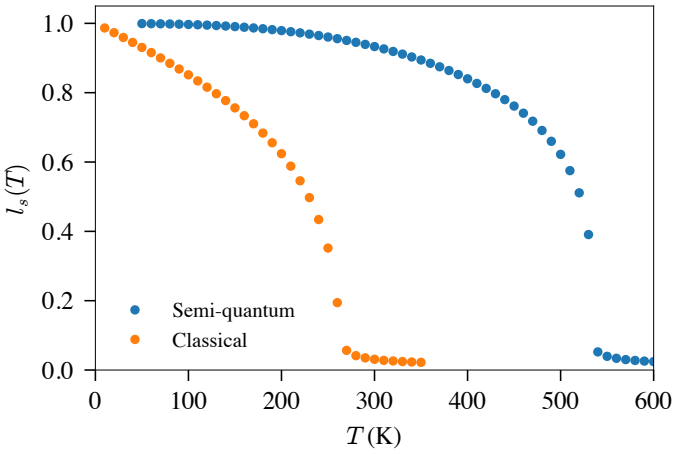

Figure 5.3: The temperature dependence of the staggered magnetisation calculated using atomistic spin dynamics. Calculations using both the classical and quantum thermostat are included.

Comparing with experimental measurements of the magnetisation is of more practical interest so that material and device properties can be predicted. The experimentally measured Néel temperature is $T_N = 523$K [58]. Our model gives excellent agreement, the Néel temperature of the semi-quantum simulation is $T_N \approx 535$K–typical spin dynamics simulations, which use Boltzmann statistics, have Néel temperatures of around half the experimental value. Fig 5.4 shows the $m_s(T)$ curves for both single crystal and powder samples. As expected, the powder samples are significantly different from the semi-quantum simulation. Here the simulated supercell is larger than the average particle sizes of the powder samples. Since the dipole-dipole interaction is very long range (convergence for $R_{\text{cut}} > 20$Å), and spin-lattice coupling is large [155, 156],

finite size effects are more prominent in the experiment than the simulation. For single crystals (Fig 5.4 (*left*)), there is a lack of data at cryogenic temperatures and the deviations from the simulation at these temperatures highlights the failure of thermostating at high temperatures. In Section 5.5, we show quantitative agreement through the temperature range $50 - 450$K. The experimental data used in Section 5.5 is shown in Fig 5.5. Despite the data of Moriyama and Van Doorn being taken over 40 years apart, and on different single crystal samples, the shapes of the temperature dependences are almost identical.

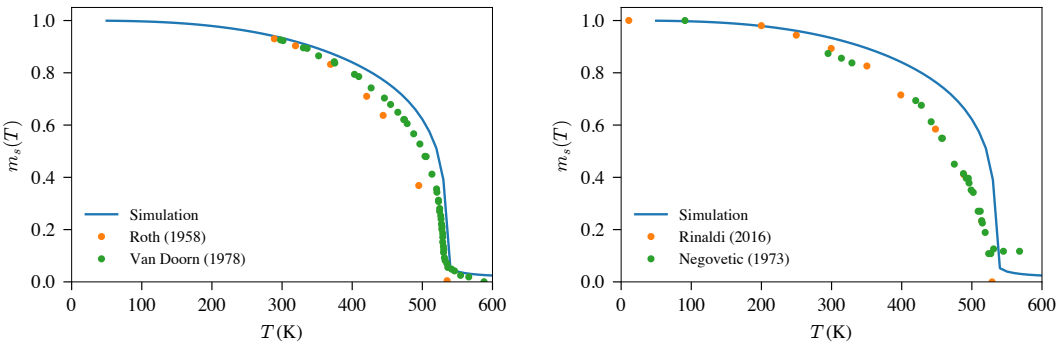

Figure 5.4: Temperature dependence of the sublattice magnetisation in NiO. Both include the semi-quantum atomistic simulation in addition to neutron diffraction experiments on (*left*) single crystal samples, and (*right*) powder samples. Experimental data is taken from Roth [75], Van Doorn [107], Rinaldi-Montes [157], and Negovetic [158].

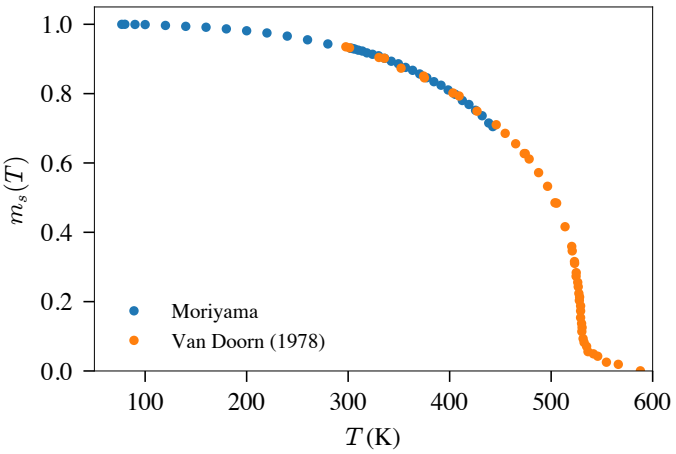

Figure 5.5: Comparison of the temperature dependence of resonant frequency (Moriyama) and the Van Doorn. Data from Moriyama is a private communication, the method and crystal details can be found here [142].

5.3 Anisotropy

5.3.1 Callen-Zener

Callen-Zener theory [159, 160] has been very successful in both experiments and numerical models at describing the temperature dependence of macrospin single-ion anisotropy constants in magnetic materials [38, 161–163]. The theory is applicable to both ferromagnetic and antiferromagnetic ordering in any material where the anisotropy can be considered as a perturbation to the exchange Hamiltonian. In materials where the anisotropy is two-ion, or is of the same order of magnitude as the exchange, and in metallic magnets where the anisotropy is highly non-local, the theory breaks down [164–168]. The paper of H. Callen and E. Callen [159] gives a comprehensive overview of the complicated history of finite temperature theories of anisotropy and generalises Zener's 1954 derivation [160] which rewrites magnetocrystalline (single-ion) anisotropies with anisotropy constants K_i in terms of spherical harmonics $Y_l^m(\theta, \phi)$ (effectively a different basis) where l is the azimuthal quantum number (quanta of orbital angular momentum), m is the magnetic quantum number (projection of l along a quantisation axis) with anisotropy constants κ_j. l can only take even values because of spin inversion symmetry of the mediating lattice (as in Section 4.4). Zener shows that

the temperature dependence of these anisotropy terms can be written as the thermal average of equilibrium spin fluctuations $m_s(T)$ about the spherical harmonic $\langle Y_l^0(\theta)\rangle$. This is independent of the shape of $m_s(T)$, and it is independent of whether the underlying physics is classical or quantum–it simply accounts for the curvature of the anisotropy $Y_l^m(\theta,\phi)$ by calculating integrals of the form

$$\frac{\kappa(T)}{\kappa(0)} = \frac{\int Y_l^m(\theta,\phi)\, e^{-\mathcal{H}/k_BT}\,\mathrm{d}\theta\mathrm{d}\phi}{\int e^{-\mathcal{H}/k_BT}\,\mathrm{d}\theta\mathrm{d}\phi}. \tag{5.16}$$

The integrals can, in principle, be calculated in the basis of K_i. But, the mathematical evaluation does not have an obvious analytic solution. The purpose of Chapter 7 is to create a new framework where the curvature of anisotropies (and even exchange) can be calculated in numeric simulations using simple thermal averages of functions of the order parameter, in equilibrium, and free from constraints or complicated sampling methods. The inability to work in the basis of Cartesian magnetocrystalline anisotropies with constants K_i means Callen-Zener theory is rarely used outside of the often quoted m^3 and m^{10} scaling of rank-2 uniaxial anisotropy and rank-4 cubic anisotropy respectively.

5.3.2 Constrained Monte Carlo

The constrained Monte Carlo (CMC) method is a specialist Monte Carlo algorithm which calculates the temperature dependence of anisotropies in magnetic systems [38]. The method constrains the direction of the order parameter using a biased Metropolis Monte Carlo algorithm; there is no fictitious field imposing the constraint so the shape of free energy landscape and the scaling of the pseudo-equilibrium free energy are preserved*. The constraint leads to a persistent (non-zero) torque, $\mathbf{T}$, on the order parameter $\hat{\mathbf{l}}$, $\mathbf{T} = -\hat{\mathbf{l}} \times \partial\mathcal{F}/\partial\hat{\mathbf{l}}$. The free energy difference along a path between two staggered magnetisation states can then be calculated as

$$\mathcal{F}(\hat{\mathbf{l}}) = \mathcal{F}(\hat{\mathbf{l}}_0) + \int_{\hat{\mathbf{l}}_0}^{\hat{\mathbf{l}}} (\hat{\mathbf{l}}' \times \mathbf{T})\ \ \mathrm{d}\hat{\mathbf{l}}', \tag{5.17}$$

where $\hat{\mathbf{l}} = \frac{1}{N}\sum_i^N \mathcal{R}_i\hat{\mathbf{m}}_i$ is the staggered magnetisation. The staggered magnetisation applies a rotation $\mathcal{R}_i$ to each magnetic sublattice $\hat{\mathbf{m}}_i$ in the system so that all sub-

*The pseudo-equilibrium requires that the anisotropy is sufficiently small such that the temperature dependence is dominated by exchange. This is the same requirement as Callen-Zener theory.

lattice magnetisations align parallel; for a collinear antiferromagnet this is the Néel vector. $\hat{\mathbf{l}}_0$ is the direction of the order parameter at some initial direction, the easy axis for example, and $\mathbf{T} \equiv \mathbf{T}(\hat{\mathbf{l}}')$ is the torque acting on the staggered magnetisation. The anisotropic contribution to Hamiltonian energy has the same scaling as the torque, so the thermal average of the torque is calculated at a point of maximal torque for multiple temperatures to determine the anisotropy scaling. For an easy-plane anisotropy maximum torque is 45° from the easy-plane. The anisotropy scaling is usually written as a power law of the order parameter $l_s(T)$,

$$\frac{K(T)}{K(0)} = \left(\frac{l_s(T)}{l_s(0)}\right)^{\alpha}. \tag{5.18}$$

We apply this method here to calculate the torque $\boldsymbol{\tau}_i$ experienced by the magnetisation $\mathbf{m}_i$ of sublattice i, due to the dipole anisotropy, for a given microstate by the following sum over magnetic moments

$$\boldsymbol{\tau}_i = -\sum_{j}^{N_i} \mathbf{S}_j \times \frac{\partial \mathcal{H}}{\partial \mathbf{S}_j}, \tag{5.19}$$

where j are indices for spins in sublattice i*. The total torque on the order parameter $\boldsymbol{\tau}$ for a microstate in NiO is then $\boldsymbol{\tau} = \sum_{i=1}^{8}(-1)^i \boldsymbol{\tau}_i$ and the expectation value of the torque $\mathbf{T}$ is given by the thermal average $\mathbf{T} = \langle \boldsymbol{\tau} \rangle$.

This Monte Carlo method cannot use the quantum thermostat–in fact there is no thermostat. Instead a classical Boltzmann function determines the thermodynamics so it is equivalent to spin dynamics with white noise. But, since in Section 5.3.1 we noted that the Callen-Zener theory is independent of the details of the thermodynamics used, the magnetisation scaling of the effective macrospin anisotropy constant is still valid ie $K(m_s)$ is valid for any $m_s(T)$†.

We apply constrained Monte Carlo to the dipole anisotropy in NiO and fit a power law of the saturation sublattice magnetisation. The dipole anisotropy is found to scale as the second power of the sublattice magnetisation, $K_{\text{dip}} \sim m_S^2(T)$, where K_{dip} is

*In systems with multiple sources of anisotropy, like NiO, the torque is calculated per Hamiltonian term.

†We also show later in Fig. 7.8 that the constraint in constrained Monte Carlo changes the shape of $m_s(T)$ compared to a system without any constraints using Metropolis Monte Carlo.

the effective macrospin uniaxial anisotropy constant (see Fig. 5.6). Deviations from $K_{\text{dip}} \sim m_S^2(T)$ can only be seen using logarithmic axes and occur for $m_s(T) < 0.1$, at which point the observed magnetisation is likely a remanent of the constraint rather than true magnetic order.

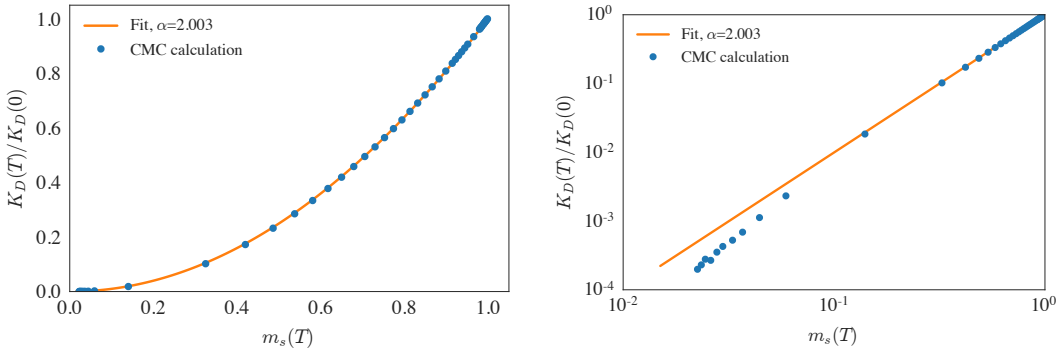

Figure 5.6: The effective dipole anisotropy strength in NiO as a function of the finite temperature sublattice magnetisation. (*right*) has logarithmic axes.

The dominant dipole anisotropy in NiO is very non-local. Holstein and Primakoff [169] showed that–using magnon theories similar to those used in Section 5.2–in the absence of correlations between distant neighbours, and to second order in magnon number operators, the dipolar anisotropies scale as m^2. The absence of correlations permits the splitting of the thermal average of a pair of localised magnon number operators $\langle \hat{n}_i \hat{n}_j \rangle$ into $\langle \hat{n}_i \rangle \langle \hat{n}_j \rangle$. This requires that localised magnons are distant from one another–or that only $k = 0$ modes are appreciably occupied. In NiO, since the four interpenetrating simple cubic antiferromagnetic sublattices are only weakly coupled by the nearest neighbour splitting $\Delta J_1 \sim 0.7$meV/spin, correlations between the sublattices will be small. This magnetisation scaling is the same as shape anisotropy in non-spherical ferromagnets where the long range dipole interactions are uncorrelated. If correlations are important, then $\langle \hat{n}_i \hat{n}_j \rangle < \langle \hat{n}_i \rangle \langle \hat{n}_j \rangle$ and the magnetisation scaling exponent is less than two, as is the case for Cr_2O_3 [94]. To further justify the m^2 scaling, we calculated an analytic expression for the dipole-dipole interaction in the limit of an infinite system by applying a Poisson summation to an infinite two-dimensional (111) sheet of NiO, then sum over neighbouring sheets. The expression is derived for spin vectors aligned along [111], and along directions within the (111) plane. The difference between an in

plane, and out of plane, direction is taken to evaluate the zero temperature anisotropy strength. The detailed derivation is given in Appendix C. The final expression for the zero-temperature energy difference between the hard-axis and easy-plane is

$$\begin{aligned}\Delta E = -\frac{176\sqrt{2}\pi\mu_0\mu_S^2}{3a^3}\sum_{n=-\infty}^{\infty}(-1)^n\Bigg[\sum_{k=1}^{\infty}k\cos\left(k\mathbf{b}_1\cdot\mathbf{R}_n\right)\mathrm{e}^{-Ck|\mathbf{R}_n\cdot\hat{\mathbf{z}}|} \\ + \frac{8}{11}\sum_{l=1}^{\infty}l\cos\left(l\mathbf{b}_2\cdot\mathbf{R}_n\right)\mathrm{e}^{-Cl|\mathbf{R}_n\cdot\hat{\mathbf{z}}|} + \sum_{\pm}\sum_{k,l=1}^{\infty}\frac{2k^2\pm kl+l^2}{\sqrt{k^2\pm kl+l^2}} \\ \times\cos\left((k\mathbf{b}_1\pm l\mathbf{b}_2)\cdot\mathbf{R}_n\right)\mathrm{e}^{-C\sqrt{k^2\pm kl+l^2}|\mathbf{R}_n\cdot\hat{\mathbf{z}}|}\Bigg]\end{aligned} \tag{5.20}$$

where $C = 8\sqrt{6}\pi/(3a)$ with a as the lattice parameter, μ_0 is the permeability of free space, n indexes the layers of [111] ordered sheets, k and l are harmonic indices, $\mathbf{R}_n = n\mathbf{v}_3$ is the vector position of an atom in the n-th sheet, $\mathbf{v}_3 = a(0, \sqrt{6}/6, \sqrt{3}/3)$, and $\mathbf{b}_1 = (4\pi/a)(1/\sqrt{2}, 1/\sqrt{6})$, $\mathbf{b}_2 = (4\pi/a)(0, 2/\sqrt{6})$ are reciprocal lattice vectors. The sum over harmonics in reciprocal space converges very quickly. Summing over $n \in [-3, 3]$, $k, l \in [1, 3]$ compared with summing over more than 10 layers (above and below) and 10 harmonics gives a difference of only 0.001%. The value for the energy difference using equation (5.20) is $\Delta E = -0.04652$ meV/spin, and the direct summation over spins within a radius of $5a$ gives $\Delta E = -0.04695$ meV/spin. The difference between these two methods is less than 1%.

The prefactor in equation (5.20) contains μ_S^2 and its coefficient is a sum over k-vectors*. At finite temperature, we take the mean-field approximation such that $\langle\mu_S^2\rangle = [\mu_S m_s(T)]^2$, where each magnetic moment is reduced by the value of the reduced magnetisation, we reproduce the scaling we find numerically. This means that the dipole anisotropy in NiO behaves in a similar way to the shape anisotropy in a thin film ferromagnet. Intuitively this makes sense. The magnetic structure of NiO is composed of antialigned two-dimensional ferromagnets (an atomically thin synthetic antiferromagnet), each of which has a stray dipole field that interacts with neighbouring ferromagnetic sheets.

*For the case of Cr_2O_3, because of symmetry, it is unlikely that the dipole-dipole interaction can be written in such a simple way.

5.4 Spin Wave Stiffness

The spin wave stiffness, D, was introduced in Section 5.2. It is the k-independent coefficient of the magnon spectrum in the small-k limit. The spin wave stiffness is temperature dependent–at finite temperatures the spin wave spectrum is said to soften. This is true of other quasiparticle excitations like phonons, plasmons, and excitons. Softening due to temperature is often ignored outside of magnetism because its effect is very weak (see [170] for phonons).

Similar to the magnetisation, a first approximation of the temperature dependence of the spin wave stiffness can be derived analytically by using non-linear magnon theories. Dyson's rigorous non-Holstein-Primakoff theory of spin waves briefly discusses this (see equation (111) of [130]) but the complicated theory makes any physical interpretation of the results difficult. The first simple explanation of softening instead came later from Keffer and Loudon [171]. They realised that the softening of the spin wave stiffness due to temperature must be related to the total energy of magnons per spin angular momentum* ('per spin angular momentum' implies we retain the normalisation of $1/NS$ like in Bloch's law). We make a small adjustment to this interpretation here (in line with modern understanding) by saying that the whole magnon spectrum is renormalised, rather than simply the spin wave stiffness†. In other research fields this is called a magnon pressure, an attractive force between magnons, or the temperature dependence of the effective chemical potential (magnochemical potential) which includes kinetic energy‡. For a ferromagnet, the finite temperature spin wave spectrum

*Since the Hamiltonians considered in this project contain only magnetic terms (frozen lattice and frozen electrons), the change in internal energy due to temperature is only due to spin waves ie the total magnon energy $\epsilon(T)$ is equal to $\Delta U(T) = U(0) - U(T)$.

†Keffer and Loudon [171] give a very clear classical interpretation using localised spin waves; it is easier to add a spin wave to a magnetic site when the instantaneous non-equilibrium position deviates from the ground state due to an existing spin wave. This picture is the same as pushing a broken down car–it's easier to push along the road once it is already moving.

‡The intrinsic chemical potential of magnons is zero because its rest mass is zero. But, thermal magnons have an average kinetic energy which is temperature dependent because of their number and their interactions; this is the extrinsic chemical potential. Examples of other external chemical potentials include gravitational potential energy, the energy at the Fermi level (electrostatic energy) for electrons, or the energy of mobile magnetic particles in magnetic fields[172].

is given by

$$\langle hf_{\mathbf{k}} \rangle = hf_{\mathbf{k}} \left[1 - \frac{g\mu_B}{N\mu_S} \langle (1-\gamma_{\mathbf{k}})\hat{n}_{\mathbf{k}} \rangle \right], \tag{5.21}$$

where the single angle bracket is a thermal average. This expression, and the idea of magnon softening, is well known in the neutron scattering community as it is used to extrapolate low temperature measurements of exchange interactions to zero temperature values [173]. The derivation of the above expression is very involved, so we will not reproduce it here [174–178]. But, the simplest case is of a Hartree-Fock renormalisation where four-magnon operators can be approximated by two non-interacting pairs, or equivalently a one-loop self-energy Feynman diagram (no scattering) [179]. Evaluating the above magnon renormalisation for a simple cubic ferromagnet is easy. Transforming to classical magnetic moments, we have

$$\langle hf(\mathbf{k}) \rangle = hf(\mathbf{k}) \left[1 - \frac{g\mu_B \nu_{\mathrm{WS}}}{\mu_S} \frac{\Gamma(5/2)\zeta(5/2)}{4\pi^2} \left(\frac{k_B T}{J\mu_S a^2/g\mu_B} \right)^{\frac{5}{2}} \right]. \tag{5.22}$$

The above $T^{5/2}$ scaling only applies for insulating ferromagnets. In conductors, there is an additional term proportional to T^2 which can be dominant at very low temperatures [180, 181]*. Just like Bloch's law, the temperature dependence of the spin wave softening in an antiferromagnet is different due to the linear dispersion. The algebra for an antiferromagnet is much more complex. But, in the end, the only adjustment moving from a one-sublattice ferromagnet to a two-sublattice antiferromagnet is to include the Bogoliubov transformation. For a two sublattice antiferromagnet, the first order approximation of the finite temperature spin wave spectrum is then [150, 182, 183]

$$\langle hf(\mathbf{k}) \rangle = hf(\mathbf{k}) \left[1 - \frac{g\mu_B}{2N\mu_S} \left\langle \frac{\hat{n}_{\mathbf{k}}}{(u_{\mathbf{k}}^2 + v_{\mathbf{k}}^2)} \right\rangle \right] \tag{5.23}$$

where the factor 2 accounts for the double counting of magnons. Evaluating this for NiO, and moving to classical spin waves, we get

$$\langle hf(\mathbf{k}) \rangle = hf(\mathbf{k}) \left[1 - \frac{g\mu_B \nu_{\mathrm{WS}} \pi^4}{15(2\pi)^2 \mu_S \lambda} \left(\frac{k_B T}{D} \right)^4 \right], \tag{5.24}$$

*Izuyama and Kubo [181] derive magnon, phonon, and electron contributions to the softening in ferromagnets. The T^2 term is electronic in origin and two terms are proportional to $T^{5/2}$: one electronic and one magnetic. Stringfellow [180] shows that this leads to an *increase* of the stiffness proportional to $T^{5/2}$.

where $D = \frac{g\mu_B a}{\mu_S}\sqrt{(J_2 + J_{1-})(2J_2 + J_{1-} - J_{1+})}$, and λ is again given by

$$\lambda = \frac{\sqrt{6}|J_2 + J_{1-}|}{a\sqrt{(J_2 + J_{1-})(2J_2 + J_{1-} - J_{1+})}}. \tag{5.25}$$

We can test the validity of this theory by running numerical atomistic spin dynamics simulations of NiO using the quantum thermostat. The spin wave spectrum is the space and time Fourier transformation of the spin correlation function. This representation is often called the dynamic structure factor $\mathcal{S}^{\alpha\beta}(\mathbf{k}, f)$ (α and β denote Cartesian directions of spin components). For a large system in thermal equilibrium, the dynamic structure factor is often written as

$$\mathcal{S}^{\alpha\beta}(\mathbf{k}, f) = \frac{1}{\sqrt{2\pi}}\frac{1}{N}\sum_{i=1}^{N}\sum_{j\neq i} \mathrm{e}^{\mathrm{i}\mathbf{k}\cdot\mathbf{r}_{ij}} \int_{-\infty}^{\infty} \mathrm{e}^{\mathrm{i}(2\pi f)t} \left\langle S^{\alpha}(\mathbf{r}_i, 0), S^{\beta}(\mathbf{r}_j, t)\right\rangle \mathrm{d}t \tag{5.26}$$

where N is the number of localised magnetic moments, $\mathbf{r}_{ij} = \mathbf{r}_j - \mathbf{r}_i$ is the displacement vector between magnetic moments i and j, S^{α} is the α component of the classical spin vector, and angle brackets denotes the thermal average of correlations, $\left\langle S^{\alpha}(\mathbf{r}_i, 0), S^{\beta}(\mathbf{r}_j, t)\right\rangle = \left\langle S^{\alpha}(\mathbf{r}_i, 0)S^{\beta}(\mathbf{r}_j, t)\right\rangle - \left\langle S^{\alpha}(\mathbf{r}_i, 0)\right\rangle\left\langle S^{\beta}(\mathbf{r}_j, t)\right\rangle$ [184, 185]. To avoid the confusion of thermal (time) averages inside a time integral, we prefer the following definition [186]

$$\mathcal{S}^{\alpha\beta}(\mathbf{k}, f) = \frac{1}{2\pi N}\lim_{t_{\max}\to\infty}\int_0^{t_{\max}} \mathrm{e}^{\mathrm{i}(2\pi f)\tau}\left[\frac{1}{t_{\max}}\int_0^{t_{\max}} \rho^{\alpha}(\mathbf{k}, t)\rho^{\beta}(\mathbf{k}, t+\tau)\mathrm{d}t\right]\mathrm{d}\tau, \tag{5.27}$$

where $\rho^{\alpha}(\mathbf{k}, t) = \sum_{i=1}^{N} \mathrm{e}^{\mathrm{i}\mathbf{k}\cdot\mathbf{r}_i} S_i^{\alpha}(t)$. Since the above definition is a convolution integral and includes the limit that $t_{\max} \to \infty$, rather than an explicit integral over infinite time, the connection with numerical methods is clear; convolutions are easily calculated in discrete time numeric simulations using fast Fourier transforms or periodogram methods used in signal processing. Additionally, the limit makes the requirement of well-converged thermal statistics clear.

Figure 5.7 shows two finite temperature spectra of NiO. The spin wave softening can be seen by the bare eye. To extract the temperature dependence of the spectrum, we take the peak intensity of the spectrum at each point in k-space and fit the resultant spectrum to equation (5.10), using temperature dependent exchange parameters. The

fitting equation is

$$hf_{\mathbf{k}}(T) = \frac{g\mu_B\sqrt{z}}{\mu_S}\Bigg[\Big(J_{1+}(T)(\gamma^{+}_{\mathbf{k}}-1)+J_{1-}(T)+J_2(T)\Big)^2 - \Big(J_{1-}(T)\gamma^{-}_{\mathbf{k}}+J_2(T)\gamma^{(2)}_{\mathbf{k}}\Big)^2\Bigg]^{\frac{1}{2}}, \tag{5.28a}$$

$$\gamma^{+}_{\mathbf{k}} = \frac{1}{3}\left[\cos\left(\frac{a}{2}(k_x+k_y)\right)+\cos\left(\frac{a}{2}(k_y+k_z)\right)+\cos\left(\frac{a}{2}(k_x-k_z)\right)\right], \tag{5.28b}$$

$$\gamma^{-}_{\mathbf{k}} = \frac{1}{3}\left[\cos\left(\frac{a}{2}(k_x-k_y)\right)+\cos\left(\frac{a}{2}(k_y-k_z)\right)+\cos\left(\frac{a}{2}(k_z+k_x)\right)\right], \tag{5.28c}$$

$$\gamma^{(2)}_{\mathbf{k}} = \frac{1}{3}\left[\cos\left(k_x a\right)+\cos\left(k_y a\right)+\cos\left(k_z a\right)\right]. \tag{5.28d}$$

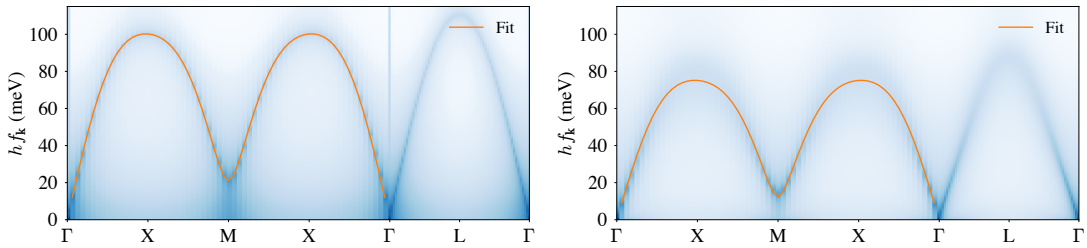

Figure 5.7: Thermal spin wave spectra at $T = 40$K (*left*) and $T = 500$K (*right*) for NiO calculated using atomistic spin dynamics. Γ is the Brillouin zone centre, M is the point $\mathbf{k} = [0, \frac{2\pi}{a}, 0]$, and $L = [\frac{\pi}{a}, \frac{\pi}{a}, \frac{\pi}{a}]$ with respect to the primitive lattice vectors. The magnetic Brillouin zone is twice the size of the non-magnetic zone because the primitive cell contains two magnetic Ni atoms. Orange curves are the finite temperature fitting

The temperature dependence of the extracted curves is given in Fig. 5.8. The data chosen for fitting was taken along the path $\Gamma \to M$ as this is sensitive to J_2, J_{1-}, and J_{1-}. The path $\Gamma \to L$ is independent of J_{1+}, so $J_{1+}(T)$ cannot be determined using this path. All three effective exchange terms have the same temperature dependence. The spin wave spectrum is very weakly temperature dependent; at $\sim 95\%$ of the critical temperature we have $hf_{\mathbf{k}}(500\text{K}) \approx 0.76hf_{\mathbf{k}}(0\text{K})$. The thermal spin wave spectrum from atomistic spin dynamics includes all elastic and inelastic spin wave interactions, and conserves the total length of spin vectors (total angular momentum) so includes a kinematic interaction*, not simply the Hartree-Fock renorm-

*The connection with the kinematic interaction in Dyson's quantum treatment is not clear.

alisation given by equation (5.24). So, it is surprising that the leading order approximation from spin wave theory, (5.24), gives such close agreement with the numeric calculations. Additionally, if the J_1 terms are not included in equation (5.24), the spin wave stiffness is predicted to drop off much quicker than is observed; including J_1, equation (5.24) gives $hf_{\mathbf{k}}(T)/hf_{\mathbf{k}}(0) \approx 3.69 \times 10^{-12}\, T^4$. Whereas ignoring J_1 gives $hf_{\mathbf{k}}(T)/hf_{\mathbf{k}}(0) \approx 4.40 \times 10^{-12}\, T^4$. Fig. 5.9 shows a spectrum above T_N. The spectrum can still be observed, but the peak extraction of the spectrum becomes difficult. No extra information would be gained by fitting above T_N, though correlations have been measured experimentally in ferromagnets [187]. The expression derived for the temperature dependence of the spectrum agrees to very high temperatures $\sim 95\% T_N$. This is in contrast to the expression for the magnetisation which only agrees to $\sim 40\%$*. Since the spin wave interactions are weak–demonstrated by the weak temperature dependence of the spectrum–then the additional terms which have a non-negligible contribution to the temperature dependence of the sublattice magnetisation must be the corrections to the spectrum shape, as well as the kinematic term which limits the total angular momentum carried by classical spin waves in the system to $\frac{2\mu_S}{g\mu_B} N$ (up to $2NS$ magnons in the quantum case).

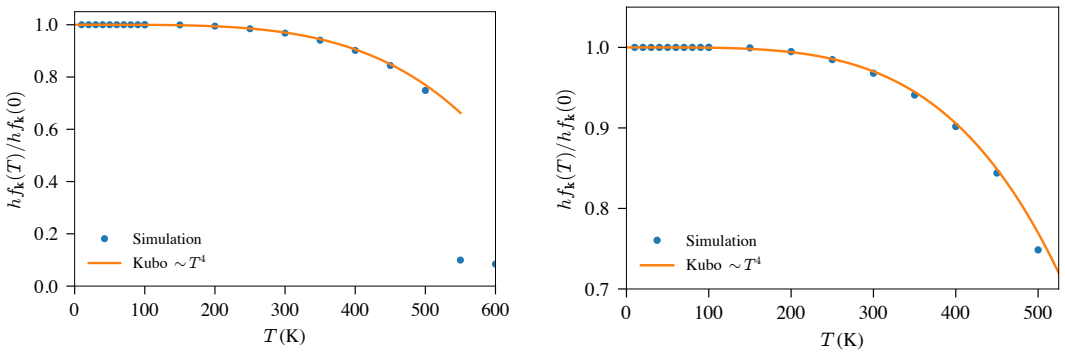

Figure 5.8: The temperature dependence of the thermal spin wave spectra for NiO. Both panels show the same data with different axis limits.

*Self-consistent methods have been shown to obtain very close agreement with experiments for both the magnetisation and spin wave energies in MnO, another antiferromagnet which is described by the same spin Hamiltonian [177].

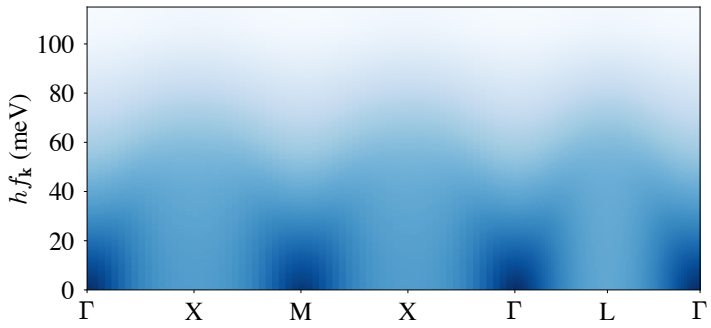

Figure 5.9: A spin wave spectrum of NiO above T_N at 600K. The spectrum is not flat so magnetic correlations persist above T_N.

5.5 Resonance and Damping

The work of this section was carried out while the author was a JSPS (Japan Society for the Promotion of Science) summer fellow in collaboration Takahiro Moriyama at the group of Teruo Ono in the Department of Materials Chemistry, Kyoto University. Moriyama provided experimental measurements of the temperature dependent frequency of the $\sim$ 1THz resonance mode, as well as the temperature dependence of its linewidth (effective macrospin Gilbert damping) in a 0.45mm thick single crystal slab of NiO. The sample and method are identical to those in the reference [142]. Experimental details will be briefly discussed here–a thorough discussion on experimental measurements of AFMR is discussed in the next chapter. Modern experimental measurements of magnetisation dynamics in antiferromagnets use THz time-domain spectroscopy (THz-TDS), and various pump-probe spectroscopy methods [89, 100, 103]; Raman scattering, Brillouin light scattering (BLS) and infrared (IR) absorption techniques are used in older literature on antiferromagnets [68, 188–190]. These methods measure slightly different phenomena in an antiferromagnet, and the distinction can become important when studying the fundamental properties of a material. The data presented here uses a continuous wave (cw) THz spectroscopy measurement; this is simply infrared absorption by NiO (which is sensitive to free oscillations), but the creation of the THz radiation uses photomixing [191] instead of a tuneable laser source*.

*At the time of writing, there are very few THz lasers, none are commercially available. Advances have been made using semiconductor lasers [192], otherwise free electron laser sources which use expensive particle accelerators must be used [193].

A pair of tuneable lasers operating at different frequencies (in the near-infrared range $\sim$ 350THz) are combined to produce a laser with a tuneable beating frequency in the far-infared range (0THz–2THz). After the photomixed radiation is passed through the sample, absorption is detected by a second photomixer and detector which is sensitive to the change in frequency mixing of the incident and output radiation. For single crystal samples, interference between the incident and backscattered beam, known as Fabry-Perot interference, must be removed to obtain the magnetic absorption [142]. The processed data provided by Moriyama is shown in Fig. 5.10.

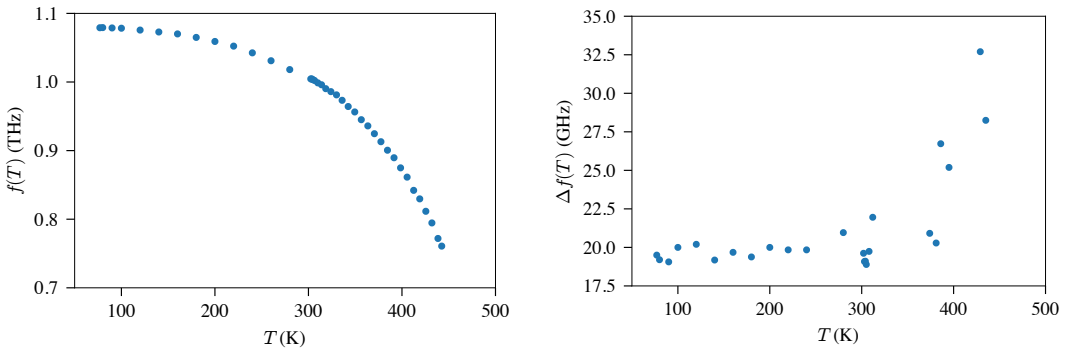

Figure 5.10: The temperature dependence of the resonant frequency (*left*) and its linewidth (*right*) in a bulk single crystal of NiO measured experimentally by continuous wave THz spectroscopy.

The resonant dynamics of antiferromagnets can be difficult to measure in bulk samples. Microwave resonance experiments on thin films, or surface sensitive spin-pumping experiments can be used. But, as seen in section 5.2, the temperature dependence of magnetic properties of thin films and nanoparticles can be significantly different from bulk samples. Light scattering techniques have been used on bulk samples of NiO, but the large amplitude of lattice dynamics makes analysis difficult [188, 189]. Similarly, optical absorption techniques have been used [190]. But, until recently, high resolution and low noise measurements of dynamics in the THz gap have been absent. Despite this, the temperature dependence of resonance in NiO has been of scientific interest for decades [190, 194]. Studying thermal magnetisation dynamics is much easier using computational methods. The calculation of the dynamic structure factor in the previous section gives access to the resonant dynamics of the system. But, the con-

volution methods used to calculate the spin wave spectrum in simulations don't give sufficiently high energy resolution to accurately extract the gap at $k = 0$. Instead, we use a much simpler method. The atomistic simulations contain eight sublattices (a pair for each coupled simple cubic antiferromagnet). The magnetisation of each sublattice α at time t, given by $\mathbf{m}_\alpha(t) = (1/N_\alpha)\sum_{i\in\alpha}\mathbf{S}_i$, is written to a file at a given interval Δt. The time between writing to the file is chosen to balance frequency resolution and total time of the simulation*. The Nyquist frequency, $f_{\max}$, is the maximum frequency that can be sampled for a given Δt, and is given by

$$f_{\max} = \frac{1}{2\Delta t}. \tag{5.29}$$

To choose Δt, we need to know the frequency that we wish to sample. The resonance frequency for a two sublattice macrospin model of NiO at zero temperature is given by†

$$f_0 = \frac{2|\gamma|}{\mu_S}\sqrt{z(J_2 + J_{1-})K_{\mathrm{u}}}, \tag{5.30}$$

where $|\gamma| = 2.80 \times 10^{10}\mathrm{s}^{-1}\mathrm{T}^{-1}$ is the gyromagnetic ratio of an electron, and $K_{\mathrm{u}} = -0.04695\mathrm{meV}$ is the effective strength of the dipole anisotropy at zero temperature for the atomistic model. This gives a resonant frequency of $f_0 \approx 1.19\mathrm{THz}$. Therefore we choose $\Delta t = 125\,\mathrm{fs}$ giving a Nyquist frequency of $f_{\max} = 4\,\mathrm{THz} \gg 1.19\,\mathrm{THz}$. The power spectrum of resonant dynamics is calculated from the magnetisation time series using Welch's method. Welch's method is a periodogram method for estimating the power spectral density of a signal. Welch's method is advantagous over a windowed FFT; a windowed FFT is insensitive to signals at the edges of the window, so useful information is lost. Welch's method splits a signal into smaller overlapping subsets of the original signal. A windowed FFT is calculated for each overlapping segment, then Welch's method averages these segments. The overlap ensures that the data at the edges of the window of each segment are well sampled, reducing the loss of information. This method sacrifices some frequency resolution for an increased signal to noise ratio. The reduced noise is not due to smoothing, but is a result of the geometrical averaging of the time series, and the noise/resolution are tuned by changing the length of the segments. The lineshape of the resonance mode is expected to be approximately

*These simulations run on GPUs and the process of writing to file requires slow memory synchronisation between the GPU and CPU, so minimising the number of file writes speeds up computation.

†The result is stated here, it is derived in the next chapter (Chapter 6). The effect of J_{1+} is ignored in a two sublattice model so the resonance in atomistic simulations differs from this result.

Lorentzian since the lineshape of the dynamic susceptibility is Lorentzian [142]; though the lineshape of the resonance becomes asymmetrical in systems where the magnon lifetime is frequency dependent (as with the quantum thermostat*) [140, 195, 196]. In addition to the resonance peak, spectral leakage from the thermostat can be observed in the magnetisation dynamics which is given by the Bose-Einstein distribution. Therefore, we choose a fitting function for the Fourier transform of a component of a sublattice magnetisation $m(f) := \mathcal{FT}[m(t)]$, which includes both a Lorentzian peak and a Bose-Einstein background. The fitting function is given by

$$m(f) = \frac{A_1}{\pi} \frac{\sigma}{(f - f_0)^2 - \sigma^2} + \frac{A_2\, hf}{\mathrm{e}^{hf/k_B T} - 1}, \tag{5.31}$$

where A_1 is the Lorentzian amplitude, 2σ is the full width at half maximum (FWHM) of the Lorentzian and $\sigma = \Delta f$ is the linewidth, f_0 is the peak centre of the Lorentzian, A_2 is the amplitude of the Bose-Einstein background, T is fixed to the temperature of the simulation being fitted. Fig. 5.11 shows an example of the fitted magnetisation dynamics.

The lowest temperature measurement of the resonant mode by Moriyama was 1.07(91)THz at 77K; at 50K the resonant frequency extracted from a simulation was 1.16(22)THz. The Néel temperature of the sample used by Moriyama wasn't measured and the Néel temperature of the simulation model using the quantum thermostat was between 530K and 540K. To compare the shape of temperature dependence of f, we want to ignore the small differences in low temperature values of f and small differences in the Néel temperature. So, we show normalised in the next figures. Fig. 5.12 shows the temperature dependence of the resonant mode measured experimentally and from simulations using a quantum thermostat when both frequency and temperature are normalised. Both curves show excellent agreement through the measured temperature range. And, unlike the experimental measurements of $m(T)$ (Fig. 5.4), these measurements of $f(T)$ aren't complicated by finite size effects or limited by experimental accuracy.

The resonant frequency in NiO has a very similar temperature dependence to the sublattice magnetisation. The reason for this can be shown simply using Eq. 5.30.

*In spin dynamics simulations with a classical thermostat, asymmetry is still observed, though smaller than when using the quantum thermostat.

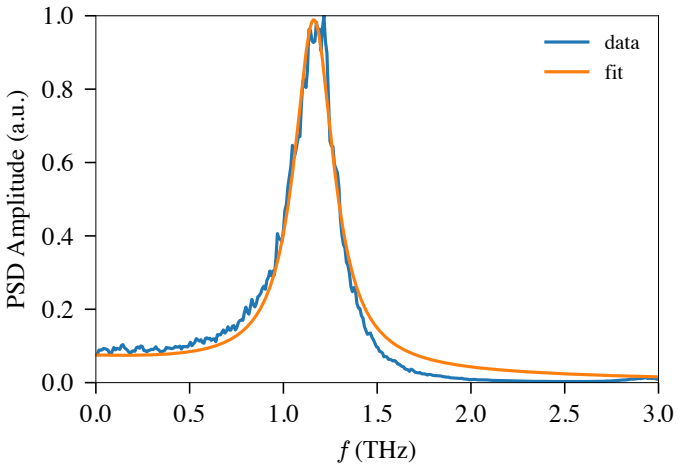

Figure 5.11: Example power spectral density (PSD) of the magnetisation dynamics of NiO from an atomistic simulation at $T = 50$K. The orange curve is fitted using equation (5.31). Asymmetric deviations from the fitted Lorentzian lineshape can be seen by eye.

Replacing zero temperature macroscopic constants with finite temperature constants, we have

$$f(T) = \frac{2|\gamma|}{\mu_S}\sqrt{z(J_2(T) + J_{1-}(T))K_{\mathrm{u}}(T)}. \tag{5.32}$$

As shown in the previous section, the spin wave stiffness is very weakly temperature dependent, so can be ignored. $K_{\mathrm{u}}(T)$, however varies as $m(T)^2$. Making the substitutions $\{J_2(T),\, J_{1-}(T),\, K_{\mathrm{u}}(T)\} \approx \{J_2(0),\, J_{1-}(0),\, K_{\mathrm{u}}(0)m(T)^2\}$ then

$$f(T) = \frac{2|\gamma|m(T)}{\mu_S}\sqrt{z(J_2(0) + J_{1-}(0))K_{\mathrm{u}}(0)}, \tag{5.33}$$

Or $f(T)/f(0) \approx m(T)$. Fig 5.14 shows the normalised temperature dependence of both the resonant frequency and magnetisation, and confirms that they have the same temperature scaling.

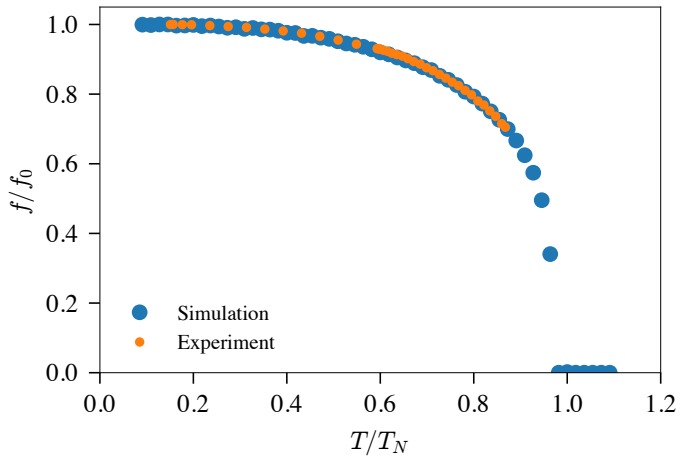

Figure 5.12: (blue points) Spin dynamics calculated resonant frequency normalised to the estimated Néel temperature (540K) and the resonant frequency at 50K (1.16THz). (orange points) Experimental measurements of the resonant frequency normalised to the estimated Néel temperature (500K) and the resonant frequency at 77K (1.08THz).

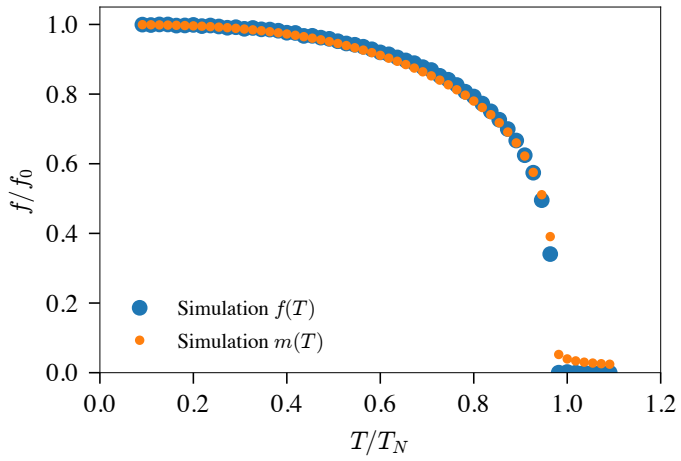

Figure 5.14: Curves normalised to $T_N = 540$K for: (blue points) spin dynamics calculated resonant frequency normalised to the resonant frequency at 50K (=1.16THz), (orange points) spin dynamics calculated sublattice magnetisation against temperature.

Now we have confirmed the semi-quantum model of NiO gives quantitative information about the temperature dependence of the resonant frequency, we can use

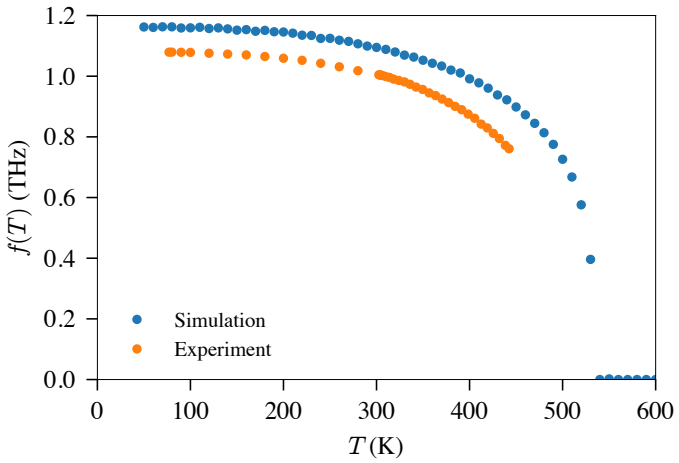

Figure 5.13: (blue points) Spin dynamics calculated resonant frequency. (orange points) Experimental measurements of the resonant frequency.

it–in combination with the experimental measurements–to discern new information that isn't accessible in either observation alone. In the simulations, only the magnetic degrees of freedom are modelled; in experiments every degree of freedom (magnetic, lattice, electronic, environment) can influence magnetic measurements. In particular, non-magnetic (direct) sources of damping are almost impossible to disentangle from magnetic (indirect) sources of damping in experiments. By comparing both measures of the linewidth, we can distinguish the direct and indirect sources of temperature dependent damping in NiO. The direct sources of damping in NiO are quite simple. Spin-electron losses are small because of the large band gap in NiO, so direct damping is dominated by spin-lattice processes. To begin, let $\alpha_{\text{sim}}(T)$ and $\alpha_{\text{exp}}(T)$ denote the effective (macrospin) finite temperature Gilbert damping measured in simulations and in experiments, respectively. We can write the simulation Gilbert damping as

$$\alpha_{\text{sim}}(T) = \alpha_0 f_M(T), \tag{5.34}$$

where α_0 is the microscopic Gilbert damping (temperature independent) and $f_M(T)$ is the temperature dependence of losses due to indirect damping processes (magnon-magnon interactions). The experimentally measured temperature dependent damping can be written as

$$\alpha_{\text{exp}}(T) = \alpha_M f_M(T) + \alpha_P f_P(T) + \alpha_E f_E(T), \tag{5.35}$$

where α_M is the zero temperature value of Gilbert damping due to indirect magnon-magnon processes, α_P is the zero temperature damping due to magnon-phonon interactions, α_E is the zero temperature damping due to magnon-electron interactions, and $f_P(T)$, $f_E(T)$ are their temperature dependences. Since NiO is a large band gap insulator, below the Néel temperature, we can make the approximation $\alpha_E = 0$ (3eV band gap$\approx 35,000$K). This reduces (5.35) to

$$\alpha_{\text{exp}}(T) = \alpha_M f_M(T) + \alpha_P f_P(T). \tag{5.36}$$

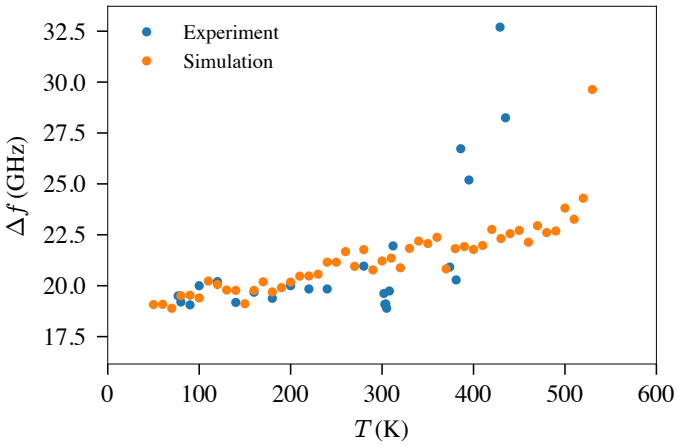

Figure 5.15: Curves for the effective (macrospin) temperature dependent Gilbert damping extracted from the linewidth of the resonant mode measured using (*blue*) semi-quantum simulations, and (*orange*) experiments.

Fig. 5.15 shows the temperature dependence of the effective Gilbert damping calculated from both simulations and experiments. Up to $\sim$ 400K both sets of data show excellent agreement. Below 400K, both experiments and simulations show a weak linear increase in the effective damping with temperature. Since the linear increase is observed in both data, we attribute this to indirect magnon-magnon losses ($f_M(T)$); magnon-phonon are approximately constant below 400K. Therefore, at low temperature, we can say that $f_M(T) = C_1 T$ and can estimate the magnitude of α_M from α_0. The fit is shown in Fig. 5.16.

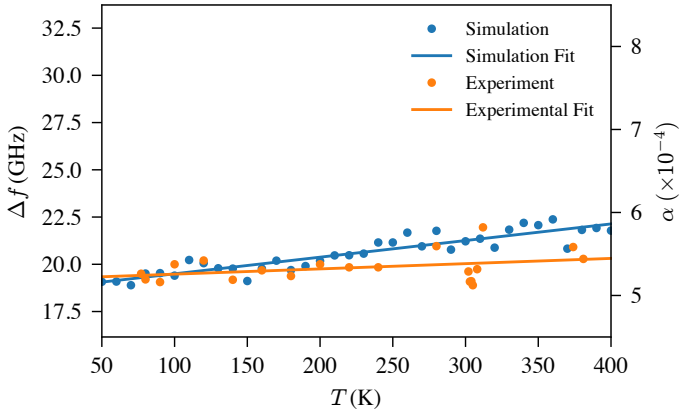

Figure 5.16: Data shown in Fig. 5.15 including linear fits to values below 400K.

The values of the fit give $\alpha_{\text{sim}}(T < 400\text{K}) = 1.76\alpha_0 T$ and $\alpha_{\text{sim}}(T < 400\text{K}) = 2.78 \times 10^{-4} T$. The assumption that the constant $C_1 = 1.76$ is applicable to both simulations and experiments requires that magnon-magnon interactions are calculated quantitatively in simulations when using the quantum thermostat, and that magnon-phonon contributions to the temperature dependence are negligible in this temperature range. Given the quantitative agreement of all other temperature dependent parameters with experimental values shown in this chapter, the former assumption is valid; the latter assumption will be discussed shortly. We can then equate the ratio of the damping constants α_M and α_0 with the ratio of the fitted gradients,

$$\frac{\alpha_M}{\alpha_0} = \frac{2.78 \times 10^{-4}}{17.6\alpha_0}, \tag{5.37}$$

which gives $\alpha_M \approx 1.6 \times 10^{-4}$. The remainder of the damping in experiments is due to direct magnon-phonon losses, such that $\alpha_P \approx 3.4 \times 10^{-4}$. We will not attempt to estimate $f_P(T)$, but this simple analysis is the first estimation of direct and indirect sources of damping in a single crystal sample of NiO.

There are two phonon modes in NiO; the transverse optical (TO) and longitudinal optical (LO) modes. Aytan *et al* [197] measured the TO and LO phonon modes at 12.1 and 17.6THz, respectively*. Disentangling the losses through each of these phonon modes is outside the scope of this work but it is worth noting that the effective temper-

*Data reproduced in the following reference which is easier to extract the relevant frequencies [198].

atures of the TO and LO mode are approximately 580 and 850K, respectively. Given the high effective temperatures of these modes, we postulate that the reason we are able to ignore magnon-phonon losses below 400K is because the phonon population is sufficiently low at these temperatures that the magnon-phonon interaction cross section is negligible. At 400K, the phonon population rapidly increases as the exponent in the Boson number operator approaches unity and is accompanied by an increase in the magnon-phonon interaction cross section.

5.6 Conclusion

In this chapter, it has been shown that by using the carefully parameterised model of NiO from Chapter 4 and specialist semi-quantum spin dynamics, it is possible to gain a quantitative understanding of complex magnetic materials without post-processing. The very close agreement between experiments, semi-quantum simulations, and analytic theory for the thermodynamic parameters presented here validates the use of Bose-Einstein thermostats in numerical calculations to predict the finite temperature behaviour of magnetic materials. All implementations of spin dynamics should use Bose-Einstein thermostats as a standard tool to better align the results of simulations with experiments. It has been shown that the dipole anisotropy has a temperature scaling consistent with shape anisotropy, which differs from the scaling expected from Callen-Zener theory when using a magnetocrystalline anisotropy with the same shape. New equations have been derived for the temperature dependence of the spin wave stiffness in NiO, which show excellent agreement with both simulations and experiments. The most significant result from this chapter is that we have used high precision experiments and simulations to separate direct and indirect contributions to the magnetic damping in NiO which allows a more thorough understanding of losses in magnetic systems which can be used to guide device engineering and has been missing from the literature.

Chapter 6

Dynamics in NiO

6.1 Fundamentals of Antiferromagnetic Resonance

Before discussing antiferromagnetic resonance (AFMR), it is useful to first understand how ferromagnetic resonance (FMR) is measured. In thin film ferromagnets, the most common FMR experiments [199, 200] use a vector network analyser (VNA) to generate and detect radio frequency (RF) AC electrical currents which are passed through a metallic co-planar waveguide (CPW) to generate propagating EM radiation (B-field and E-field) which is selectively absorbed by the ferromagnet. There are then three modes of operation; the first has no static external magnetic field, whereas the other two have a uniform static applied magnetic field from a Helmholtz coil or split-pair superconducting magnet. The three modes are

1. The frequency of the RF radiation is swept through some range and the absorbed power is measured. The peak absorption corresponds to the natural frequency of the ferromagnet.

2. The external field strength is held constant and the RF current is swept to find the peak absorption.

3. The frequency of RF radiation is held fixed and the magnetic field strength is swept through some range. Peak absorption occurs when the natural frequency of the ferromagnet is equal to the RF frequency.

The first case of external field-free measurements requires two anisotropies in the ferromagnet to create a gap in the magnon spectrum [201], and the ferromagnet is not necessarily saturated, so allows non-equilibrium switching dynamics to be studied [202]. For simple ferromagnets, an external magnetic field is required to introduce a gap. So, the second or third operating modes must be used to observe a peak. VNA-FMR experiments are limited by the maximum frequency that the VNA can generate and detect; typically they have maximum operating frequencies of $\sim$ 100GHz [203]. Another common FMR technique uses an optical cavity rather than electrical contacts, and the experimental equipment is identical to electron spin resonance (ESR) / electron paramagnetic resonance (EPR). Instead of using a CPW to electrically generate RF EM radiation, a sample is inserted into a cavity which spatially confines EM radiation of specific frequency (often a few fixed frequencies [204]) that is shone onto it. This method requires an external magnetic field which is swept through a range of field

strengths. For a given magnetic field strength, some optical radiation is absorbed by the ferromagnet, the rest is reflected, and the absorbed power is measured. This optical method can operate at higher frequencies than VNA-FMR ($\sim$ 270GHz [205]) but has a poorer signal-to-noise ratio [200]. Pulsed inductive microwave magnetometry (PIMM) is a another non-equilibrium driven technique [199, 202]. Because of the frequency constraints, FMR techniques cannot be used to measure AFMR in antiferromagnets of technological interest which have high Néel temperatures*, and high natural frequencies†.

Experimental techniques used to measure AFMR are usually optical, rather than electrical‡, because of the THz gap–non-linear crystals such as GaAs can be used to generate and detect THz EM radiation but electrical technologies cannot reach these frequencies. Experimental techniques which measure the dynamics of an antiferromagnet can be broadly separated into two categories; those that measure free oscillations, and those that measure driven oscillations. Driven experiments can then be further divided into near-equilibrium and non-equilibrium measurements§. A summary of these techniques is given in Table 6.1.

Experiments which directly measure the free dynamics of the system (also called the normal modes, natural frequencies, or eigenfrequencies) include techniques which are similar to conventional FMR measurements where the absorbed power of EM radiation is measured, as well as optical scattering techniques where individual photons create or absorb thermal magnons. Driven dynamics are measured by inducing–sometimes large–perturbations to the antiferromagnetic order, and measure the relaxation from the perturbed state to the equilibrium state. Fundamentally, these two categories are measuring different properties of the material; non-driven experiments are measuring the thermal eigenstates of the system, and driven experiments measure the relaxation of forced oscillations which, by definition, are not eigenoscillations. This difference is clear in macrospin theories of magnetic resonance which yield different expressions for

*Some examples of ESR measurements of AFMR are given here [206, 207]

†Some techniques can be used at very high frequencies but these can only be used on powder samples [208]

‡Although the first measurement of AFMR used ESR [209, 210].

§Zhang [211] gives a good summary of of near-equilibrium and non-equilibrium pump-probe techniques in the context of ferroelectrics.

Table 6.1: Experimental techniques used to measure AFMR. The methods are separated into those that measure free and driven oscillations. Driven techniques are further divided into near-equilibrium and non-equilibrium techniques.

Free Oscillations	Driven Oscillations	
	Near-Equilibrium	Non-Equilibrium
IR absorption [190]	THz-TDS [99, 103]	Pulsed field, optical detection [94, 212]
Raman scattering [68, 189]	OPOP [89, 102, 103]	OPOP [89, 102, 103]
BLS [188]	VNA-AFMR [213]	Quasi-optical backward-wave-oscillator [214, 215]
cw-THz spectroscopy [142, 216]	THz pump Faraday probe [217]	THz pump Faraday probe [217]
	OPTP [218]	OPTP [218]
		TPOP [100]
		ISRS[a] [99, 219, 220]

[a]ISRS is sometimes called THz-TDS [219] but the excitation is highly non-equilibrium stimulated Raman scattering [220].

the frequencies of free and forced oscillations [221, 222]. The differences in frequencies are negligible for small driving amplitudes, but can vary drastically above a threshold amplitude (see for example figure 9.2 of [222]). Here we will state the result for a zero temperature two sublattice macrospin model of NiO, the result is derived in Section 6.2. For a two sublattice ($n = 2$) fcc antiferromagnet with only next nearest neighbour exchange interactions (J_2, $z = 6$ neighbours) and easy-plane anisotropy of strength K_u, the frequency of free oscillations is given by $f_0 = \frac{2|\gamma|}{\mu_S}\sqrt{zK_\mathrm{u}\left[J_2 + J_{1-}\right]}$, whereas the frequency of forced oscillations using an out of plane, linearly polarised AC magnetic field is given by $f_\mathrm{AC} = \frac{2|\gamma|}{\mu_S}\sqrt{K_\mathrm{u}\left(z\left[J_2 + J_{1-}\right] - K_\mathrm{u}\right)}$. The zero temperature material parameters for NiO are $J_2 = -14.7\mathrm{meV}$, $K_\mathrm{u} = -0.04695\mathrm{meV}$, and $\mu_S = 1.71\mu_B$ which

gives the following frequencies

$$f_0 \approx 1.1887\text{THz} \tag{6.1a}$$

$$f_{\text{AC}} \approx 1.1884\text{THz}. \tag{6.1b}$$

A difference of less than 0.03% is indeed negligible*. But, in antiferromagnets with many sublattices and highly non-linear energy terms like a cubic anisotropy, this difference can determine which characteristic frequencies of the system can be measured by a given experimental technique, and in which geometries (see for example section 3.2.1 and 3.2.2 of [49]). Other complexities like parametric excitations and frequency mixing become important in driven experiments which use broadband THz pulses or large driving amplitudes, where non-linear oscillations couple to resonant modes [222, 224–226].

For NiO, the most comprehensive experimental measurements of free oscillations are by Grimsditch [68, 188, 189], where both Raman and Brillouin light scattering (BLS) were used to measure the magnon modes. A total of five modes were measured: 30GHz, 120GHz, 390GHz, 1.14THz, and 1.29THz. It is important to note that the 1.29THz mode was attributed to surface magnons in earlier work [227–229]; in Section 6.3 we argue this mode can exist in bulk, however. Light scattering techniques are very useful for studying the free oscillations of antiferromagnets as all magnon modes can be measured by using a combination of two techniques, one of which is sensitive to Raman active modes, and the other to infra-red (IR) active modes. Aside from the comprehensive measurements of Grimsditch, the literature on resonance in NiO is convoluted. Take, for example, articles by Kampfrath *et al* [104] and Satoh *et al* [102] (the papers have some shared authors and were published in the same year). Both Kampfrath and Satoh use a pump-probe technique but Kampfrath measures a single magnon mode at $\sim$ 1THz, whereas Satoh measures two modes at 1.07THz and 140GHz. There were three difference between these pump-probe experiments:

1. Kampfrath used a THz-frequency pump; Satoh used an optical-frequency pump.
2. Kampfrath used linearly polarised pump and probe beams; Satoh used circularly polarised pump and a linearly polarised probe.

*In metallic or half-metallic magnets, electron heating in OPTP experiments results in electron heating and far from equilibrium spin dynamics which is not included in the above equatioins [223].

3. The experiment of Kampfrath had pump and probe co-propagating along the [111] direction. In Satoh's, the probe propagated along [111] but the pump propagation vector had a 7° angle with [111]. Additionally, Satoh chose a T-domain where spins are aligned within the $(1\bar{1}1)$, not aligned perpendicular to the sample surface (111).

Any of these differences could feasibly create the necessary conditions for exciting and observing the lower frequency mode. We neglect the first difference immediately because the difference in frequency only changes the absorbed power; Kampfrath calculates that the absorbed power will heat the NiO volume by less than 10μK, and Satoh justifies a non-thermal origin by showing that both modes reverse the rotation angle of the beam upon reversing the pump helicity (a unidirectional dependence must be magnetic in origin), as well as estimating that one pump photon is absorbed per 10^4 Ni atoms in the 100μm spot (we estimate this to be $\sim$ 1K per Ni site). We can also neglect the difference in pump polarisation as the origin; THz absorption measurements using circularly polarised light by Moriyama *et al*[*], which had a propagation vector along [111] did not observe any modes between 98GHz and the high frequency mode at 1.09THz for both single crystal, and polycrystalline, samples of NiO [142]. A low frequency mode was also missing from thin film measurements using the same method [216]. From this, we can assume circularly polarised light propagating along [111] cannot excite the mode at $\sim$ 140GHz. The mode at $\sim$ 140GHz must've been observable by Satoh because of the chosen propagation vectors of the pump and probe with respect to the spin orientation. T-domains in single crystals of NiO have dimensions $\sim 100\mu$m and S-domains, which originate from the small magnetocrystalline anisotropy, have dimensions $\lesssim 1\mu$m [230]. The probe spot size of 40μm in Satoh's experiment will cover many S-domains so samples spins which point along [121] (almost parallel to the pump propagation vector [111]), and spins aligned with $[10\bar{1}]$ (perpendicular to [111]). By conservation of momentum, the absorbed optical radiation must include a component out of the $(1\bar{1}1)$ plane which excites the $\sim$ 140GHz mode. It is likely that this mode is thermally excited but the destructive interference of the amplitudes on different pairs of sublattices means it cannot be observed by an excitation propagating perpendicular to the easy plane[†].

[*]This is a free oscillation method, cw-THz spectroscopy.

[†]Bossini [231] reaches a similar conclusion, though the 140GHz mode is an eigenfrequency of the

There are other similar cases where different numbers of modes have been observed using the same technique. An inexhaustive collection of experiments is given in Table 6.2.

Table 6.2: Some experimental measurements of AFMR in NiO. Grimsditch's measurements [68, 188, 189] are used to label the resonances f_1 through f_5. Experiments are ordered by the dynamics they measure: free oscillations, near-equillibrium driven oscillations, then non-equilibrium driven oscillations. Pre-2000 measurements of free oscillations using IR absorption [190, 194] and Raman spectroscopy [227] are included last because of the low resolution and sensitivity of the experiments.

Measurement technique(s)	f_1	f_2	f_3	f_4	f_5	f_6
BLS[1] + Raman[2] [68]	30GHz[1]	120GHz[1]	—	390GHz[1]	1.14THz[2]	1.29THz[2]
OPTP[3] + THz-TDS[4] [103, 232]	—	100GHz[3]	—	500GHz[4]	1.10THz[3,4]	1.30THz[3]
OPOP [89, 102]	—	140GHz	—	—	1.07THz	—
TPOP [100]	—	—	230GHz[a]	—	1.00THz	—
TPOP [104]	—	—	—	—	1.00THz	—
ISRS [99]	—	—	—	$\sim$ 400GHz[b]	1.00THz	—
ISRS [219]	—	—	—	—	1.00THz	—
ISRS [233]	—	—	—	—	1.00THz	—
ISRS [234]	—	—	—	—	1.00THz	—
IR Absorption [194]	—	—	—	—	1.10THz	—
IR Absorption [190]	—	—	—	—	1.09THz	—
Raman [227]	—	—	—	—	1.13THz	1.31THz

[a] Inferred from the sum-frequency and difference-frequency signals at 0.77THz and 1.23THz.
[b] Not reported but visible in figure 3c.

From the above table, it is clear that the further from equilibrium the system is, the fewer magnon modes are measurable. Though, this is likely a combination of the relative amplitude of f_4 being much larger than other modes far from equilibrium because of the higher density of states of the Kittel mode compared to other non-linear modes, as well

system (we disagree) using a magnetocrystalline anisotropy which is fobidden by symmetry and requires multiple T domains to be observed (see discussion below figure 4).

as the phase cancellation of sublattices with opposite deflections for f_2. Additionally, as the distance from equilibrium in a measurement increases, the frequency of f_4 decreases due to the reduction of the effective macrospin exchange and dipole anisotropy field in the non-equilibrium state*. This is not a new idea, Stremoukhov *et al* [236] have shown analytically that the measured resonance in THz pump-ISHE probe experiments is dependent both on the pump frequency and the oscillation amplitude (see also [237]). In the rest of this chapter we use the model developed in Chapter 4 in both the macrospin approximation, and numerical calculations of the thermal dynamics using atomistic spin dynamics to elucidate the origin of the measured modes f_1, ..., f_6.

6.2 Linearised Macrospin Models

The coupled Landau-Liftshiz-Gilbert equation for multiple magnetic sublattices, indexed by i, in an effective magnetic field is typically written in the following form

$$\dot{\mathbf{M}}_i = -\gamma \mathbf{M}_i \times \mathbf{H}_i + \frac{\alpha}{M_{i,s}} \left(\mathbf{M}_i \times \dot{\mathbf{M}}_i \right), \tag{6.2}$$

where $\mathbf{M}_{A,B}$ is the sublattice magnetisation vector of sublattice A and B, M_s is the saturation magnetisation (with $M_{A,s} = M_{B,s} = M_s$), γ is the gyromagnetic ratio of an electron, $\mathbf{H}_i$ is the effective field, α is the dimensionless damping parameter. We use the LLG equation here because it is simpler to manipulate algebraically, and the linewidth takes the typical Lorentzian form. The atomistic calculations use the LL equation, however (a simple transformation of γ and α moves from one equation to the other). To simplify calculations, we choose to rewrite the LLG equation such that parameters are normalised to single spin values, rather than per volume typically used in experiment. This reduced form of the LLG equation is

$$\dot{\mathbf{m}}_{A,B} = \frac{\gamma}{M_s} \mathbf{m}_{A,B} \times \mathbf{h}_{A,B} - \alpha \left(\mathbf{m}_{A,B} \times \dot{\mathbf{m}}_{A,B} \right), \tag{6.3}$$

where $\mathbf{m}$ are the unit magnetisation vectors, and $\mathbf{h} = -\mu_0 \mu_S \mathbf{H}_{\text{eff}} = \frac{\partial \mathcal{H}}{\partial \mathbf{m}}$ is the reduced field, which has units of Tesla. We repeat the atomistic Hamiltonian here for easy comparison

*Bowlan [235] shows, in sections 3.1 and 3.2, that the induced THz dynamics in OPTP experiments on antiferromagnetic insulators is by spin-lattice thermalisation (phonons initially excited) which modulates the exchange interactions.

$$\begin{aligned}\mathcal{H} = &-\frac{1}{2}\sum_{i,j} J_{ij}\mathbf{S}_i\cdot\mathbf{S}_j \\ &-\frac{1}{2}\sum_{i\neq j}\frac{\mu_0\mu_{S,i}\mu_{S,j}}{4\pi}\frac{3(\mathbf{S}_i\cdot\hat{\mathbf{r}}_{ij})(\mathbf{S}_j\cdot\hat{\mathbf{r}}_{ij})-(\mathbf{S}_i\cdot\mathbf{S}_j)}{|\mathbf{r}_{ij}|^3} \\ &-\sum_i K_i\left[(S_i^{\mathrm{u}}S_i^{\mathrm{v}})^2+(S_i^{\mathrm{v}}S_i^{\mathrm{w}})^2+(S_i^{\mathrm{w}}S_i^{\mathrm{u}})^2\right],\end{aligned} \tag{4.17}$$

where the unit vectors $\hat{\mathbf{u}}$, $\hat{\mathbf{v}}$, $\hat{\mathbf{w}}$ are given by $\hat{\mathbf{u}} = [1/\sqrt{6}, 1/\sqrt{2}, 1/\sqrt{3}]$, $\hat{\mathbf{v}} = [1/\sqrt{6}, -1/\sqrt{2}, 1/\sqrt{3}]$, $\hat{\mathbf{w}} = [-2/\sqrt{6}, 0, 1/\sqrt{3}]$. The microscopic material parameters used in all atomistic simulations, unless otherwise stated, are given in Table 4.5.

6.2.1 Two Sublattice Model

The free energy functional for a two sublattice macrospin model of NiO from the Hamiltonian 4.17, plus an external driving field is

$$\begin{aligned}\mathcal{F} = &-(\mathcal{J}+\mathcal{A})\hat{\mathbf{m}}_1\cdot\hat{\mathbf{m}}_2 \\ &-K_{\mathrm{u}}\sum_{i=1,2}(\hat{\mathbf{m}}_i\cdot\hat{\mathbf{z}})^2 \\ &-K_{\mathrm{c}}\sum_{i=1,2}\left[(m_i^{\mathrm{u}}m_i^{\mathrm{v}})^2+(m_i^{\mathrm{v}}m_i^{\mathrm{w}})^2+(m_i^{\mathrm{w}}m_i^{\mathrm{u}})^2\right] \\ &-\mu_S\mathbf{B}_{\mathrm{ext}}(t)\cdot[\hat{\mathbf{m}}_1+\hat{\mathbf{m}}_2],\end{aligned} \tag{6.4}$$

where $\hat{\mathbf{m}}_i$ are sublattice magnetisation vectors of unit length, $\mathcal{J}$ is the next nearest neighbour exchange coupling, $\mathcal{A}$ is the antiparallel nearest neighbour exchange coupling (related to J_{1-}), K_{u} is the easy-plane energy (must be calculated from the atomistic dipole-dipole interaction), K_{c} is the cubic anisotropy energy, $\mathbf{B}_{\mathrm{ext}}(t)$ is the external driving field, the unit vectors $\hat{\mathbf{u}}$, $\hat{\mathbf{v}}$, $\hat{\mathbf{w}}$ and the magnetisation components m_i^{u}, m_i^{u}, m_i^{w} have the same definition as the atomistic Hamiltonian (4.17). The zero temperature value of these parameters are given in Table 6.3 (notice that the parallel nearest neighbour exchange J_{1+} does not appear in the free energy functional).

In the absence of an external AC magnetic driving field and assuming equilibrium (no damping) and choosing the equilibrium sublattice magnetisations as $\mathbf{m}_i = [m_i^{\mathrm{u}}, m_i^{\mathrm{v}}, m_i^{\mathrm{w}}] = [(-1)^i, m_i^{\mathrm{v}}(t), m_i^{\mathrm{w}}(t)]$. The matrix representation of the linearised

Table 6.3: Algebraic and numeric values of the parameters found in the two sublattice free energy functional for NiO when mapped from the atomistic Hamiltonian. $z = 6$ is the number of neighbours for the atomistic exchange interactions given by exchange constants J_2, J_{1+} and J_{1-}.

Symbol	Atomistic Expression	Numeric Value
$\mathcal{J}$	zJ_2	-88.2 meV
$\mathcal{A}$	zJ_{1-}	-6.0 meV
$\mathcal{P}$	zJ_{1+}	$4,62$ meV
K_u	—	-0.04695 meV
K_c	K	0.001 meV

coupled LLG equations are given by

$$\begin{bmatrix} \dot{m}_1^\mathrm{v} \\ \dot{m}_1^\mathrm{w} \\ \dot{m}_2^\mathrm{v} \\ \dot{m}_2^\mathrm{w} \end{bmatrix} = \frac{\gamma}{\mu_S} \begin{bmatrix} 0 & \mathcal{J}+\mathcal{A}+\frac{K_\mathrm{c}}{3}+2K_\mathrm{u} & 0 & \mathcal{J}+\mathcal{A} \\ -\mathcal{J}-\mathcal{A} & 0 & -\mathcal{J}-\mathcal{A} & 0 \\ 0 & -\mathcal{J}-\mathcal{A} & 0 & -\mathcal{J}-\mathcal{A}-\frac{K_\mathrm{c}}{3}-2K_\mathrm{u} \\ \mathcal{J}+\mathcal{A} & 0 & \mathcal{J}+\mathcal{A} & 0 \end{bmatrix} \begin{bmatrix} m_1^\mathrm{v} \\ m_1^\mathrm{w} \\ m_2^\mathrm{v} \\ m_2^\mathrm{w} \end{bmatrix} \tag{6.5}$$

The components of sublattice magnetisation containing v are in the easy plane, whereas those containing w are out of plane. From the above matrix equation, the resonant frequencies are given by the eigenvalues of the resonance matrix. Solving for these gives a single mode with eigenfrequency

$$f_5 = \frac{\sqrt{6}\gamma\sqrt{(\mathcal{J}+\mathcal{A})\,(K_\mathrm{c}+6K_\mathrm{u})}}{3\mu_S}, \tag{6.6}$$

with two eigenvectors (polarisations of the eigenmode) which are given by

$$\boldsymbol{\nu}_1 = \begin{bmatrix} \frac{\mathrm{i}\sqrt{6}\sqrt{(\mathcal{J}+\mathcal{A})(K_\mathrm{c}+6K_\mathrm{u})}}{6(\mathcal{J}+\mathcal{A})} \\ 1 \\ \frac{\mathrm{i}\sqrt{6}\sqrt{(\mathcal{J}+\mathcal{A})(K_\mathrm{c}+6K_\mathrm{u})}}{6(\mathcal{J}+\mathcal{A})} \\ -1 \end{bmatrix}, \tag{6.7}$$

and

$$\boldsymbol{\nu}_2 = \begin{bmatrix} \frac{\mathrm{i}\sqrt{6}\sqrt{(\mathcal{J}+\mathcal{A})(K_\mathrm{c}+6K_\mathrm{u})}}{6(\mathcal{J}+\mathcal{A})} \\ -1 \\ \frac{\mathrm{i}\sqrt{6}\sqrt{(\mathcal{J}+\mathcal{A})(K_\mathrm{c}+6K_\mathrm{u})}}{6(\mathcal{J}+\mathcal{A})} \\ 1 \end{bmatrix}. \tag{6.8}$$

The numeric values are $f_5 = 1.19\text{THz}$, $\boldsymbol{\nu}_1 = [-0.022\text{i}, 1, -0.022\text{i}, -1]$, and $\boldsymbol{\nu}_2 = [-0.022\text{i}, -1, -0.022\text{i}, 1]$. These are left- and right-handed elliptically (almost linearly) polarised AFMR modes. In the absence of the cubic anisotropy, these are identical to two decimal places and the expression for the resonant frequency reduces to $\frac{2\gamma\sqrt{-JK_\text{u}}}{\mu_S}$.

6.2.2 Eight Sublattice Model

To show, unequivocally, that there is only a single resonant mode in a linearised model of NiO, we repeat the calculation in the extreme case that all eight magnetic sublattices have distinct dynamics. The free energy functional for an eight sublattice model of NiO is given by

$$\begin{aligned}\mathcal{F} = &-\frac{\mathcal{J}}{4}\sum_{i=1}^{4}[\hat{\mathbf{m}}_{i+}\cdot\hat{\mathbf{m}}_{i-}] - \frac{\mathcal{A}}{12}\sum_{i=1}^{4}\sum_{j\neq i}[(\hat{\mathbf{m}}_{i+}\cdot\hat{\mathbf{m}}_{j-}) + (\hat{\mathbf{m}}_{i-}\cdot\hat{\mathbf{m}}_{j+})] \\ &- \frac{\mathcal{P}}{12}\sum_{i=1}^{4}\sum_{j\neq i}[(\hat{\mathbf{m}}_{i+}\cdot\hat{\mathbf{m}}_{j+}) + (\hat{\mathbf{m}}_{i-}\cdot\hat{\mathbf{m}}_{j-})] - K_u\sum_{i=1}^{4}\sum_{\pm}(\hat{\mathbf{m}}_{i\pm}\cdot\hat{\mathbf{z}})^2 \\ &- K_c\sum_{i=1}^{4}\sum_{\pm}\left[(\mathrm{m}^{\mathrm{u}}_{i\pm}\mathrm{m}^{\mathrm{v}}_{i\pm})^2 + (\mathrm{m}^{\mathrm{v}}_{i\pm}\mathrm{m}^{\mathrm{w}}_{i\pm})^2 + (\mathrm{m}^{\mathrm{w}}_{i\pm}\mathrm{m}^{\mathrm{u}}_{i\pm})^2\right],\end{aligned} \tag{6.9}$$

where fractional coefficients account for the overcounting of microscopic exchange interactions in the macrospin model; overcounting is necessary to couple the sublattices correctly. The resulting matrix form of the coupled LLG equations must be represented by a square matrix of dimension 16. The matrix was calculated using a computer

algebra system (SymPy), rather than by hand. The matrix is given below

$$\frac{\gamma}{\mu_S}\begin{bmatrix}
0 & -\frac{\mathcal{A}}{4}-\frac{\mathcal{J}}{4}+\frac{\mathcal{P}}{4} & 0 & C & 0 & \frac{\mathcal{A}}{12} & 0 & \frac{\mathcal{P}}{12} & 0 & \frac{\mathcal{A}}{12} & 0 & \frac{\mathcal{P}}{12} \\
\frac{\mathcal{J}}{4} & 0 & -C & 0 & \frac{\mathcal{A}}{12} & 0 & -\frac{\mathcal{P}}{12} & 0 & \frac{\mathcal{A}}{12} & 0 & -\frac{\mathcal{P}}{12} & 0 \\
0 & -\frac{\mathcal{J}}{4} & 0 & \frac{\mathcal{A}}{4}+\frac{\mathcal{J}}{4}-\frac{\mathcal{P}}{4} & 0 & -\frac{\mathcal{A}}{12} & 0 & \frac{\mathcal{P}}{12} & 0 & -\frac{\mathcal{A}}{12} & 0 & \frac{\mathcal{P}}{12} \\
C & 0 & -\frac{\mathcal{J}}{4} & 0 & -\frac{\mathcal{A}}{12} & 0 & \frac{\mathcal{P}}{12} & 0 & -\frac{\mathcal{A}}{12} & 0 & \frac{\mathcal{P}}{12} & 0 \\
0 & \frac{\mathcal{J}}{4} & 0 & -\frac{\mathcal{A}}{4}-\frac{\mathcal{J}}{4}+\frac{\mathcal{P}}{4} & 0 & \frac{\mathcal{A}}{12} & 0 & -\frac{\mathcal{P}}{12} & 0 & \frac{\mathcal{A}}{12} & 0 & -\frac{\mathcal{P}}{12} \\
-\frac{\mathcal{A}}{4}-\frac{\mathcal{J}}{4}+\frac{\mathcal{P}}{4} & 0 & \frac{\mathcal{A}}{12} & 0 & -\frac{\mathcal{P}}{12} & 0 & \frac{\mathcal{A}}{12} & 0 & -\frac{\mathcal{P}}{12} & 0 & \frac{\mathcal{A}}{12} & 0 \\
0 & -\frac{\mathcal{J}}{4} & 0 & \frac{\mathcal{A}}{4}+\frac{\mathcal{J}}{4}-\frac{\mathcal{P}}{4} & 0 & -\frac{\mathcal{A}}{12} & 0 & \frac{\mathcal{P}}{12} & 0 & -\frac{\mathcal{A}}{12} & 0 & \frac{\mathcal{P}}{12} \\
\frac{\mathcal{P}}{12} & 0 & -\frac{\mathcal{A}}{12} & 0 & C & 0 & -\frac{\mathcal{J}}{4} & 0 & \frac{\mathcal{A}}{4}+\frac{\mathcal{J}}{4}-\frac{\mathcal{P}}{4} & 0 & -\frac{\mathcal{A}}{12} & 0 \\
0 & \frac{\mathcal{P}}{12} & 0 & -\frac{\mathcal{A}}{12} & 0 & \frac{\mathcal{P}}{12} & 0 & -\frac{\mathcal{J}}{4} & 0 & \frac{\mathcal{A}}{12} & 0 & \frac{\mathcal{P}}{12} \\
\frac{\mathcal{A}}{12} & 0 & -\frac{\mathcal{P}}{12} & 0 & -C & 0 & \frac{\mathcal{A}}{12} & 0 & -\frac{\mathcal{P}}{12} & 0 & \frac{\mathcal{A}}{12} & 0 \\
0 & -\frac{\mathcal{A}}{12} & 0 & \frac{\mathcal{P}}{12} & 0 & \frac{\mathcal{J}}{4} & 0 & \frac{\mathcal{A}}{4}+\frac{\mathcal{J}}{4}-\frac{\mathcal{P}}{4} & 0 & -\frac{\mathcal{A}}{12} & 0 & \frac{\mathcal{P}}{12} \\
\frac{\mathcal{P}}{12} & 0 & -\frac{\mathcal{A}}{12} & 0 & \frac{\mathcal{P}}{12} & 0 & -\frac{\mathcal{J}}{4} & 0 & -\frac{\mathcal{A}}{4}-\frac{\mathcal{J}}{4}+\frac{\mathcal{P}}{4} & 0 & \frac{\mathcal{A}}{12} & 0 \\
0 & \frac{\mathcal{P}}{12} & 0 & -\frac{\mathcal{A}}{12} & 0 & \frac{\mathcal{P}}{12} & 0 & -\frac{\mathcal{A}}{12} & 0 & \frac{\mathcal{P}}{12} & 0 & -\frac{\mathcal{A}}{12} \\
0 & -\frac{\mathcal{A}}{12} & 0 & \frac{\mathcal{P}}{12} & 0 & -\frac{\mathcal{A}}{12} & 0 & \frac{\mathcal{P}}{12} & 0 & -\frac{\mathcal{A}}{12} & 0 & \frac{\mathcal{P}}{12} \\
\frac{\mathcal{A}}{12} & 0 & -\frac{\mathcal{P}}{12} & 0 & \frac{\mathcal{A}}{12} & 0 & -\frac{\mathcal{P}}{12} & 0 & \frac{\mathcal{A}}{12} & 0 & -\frac{\mathcal{P}}{12} & 0
\end{bmatrix} \tag{6.10}$$

where $C = \frac{\mathcal{A}}{4} + \frac{\mathcal{J}}{4} + \frac{K_c}{24} + \frac{K_u}{4} - \frac{\mathcal{P}}{4}$. Computing the eigenvalues and eigenvectors of this matrix symbolically would take a very long time and is unnecessary for our purpose. A numeric calculation is sufficient to show that, in the linearised approximation, there are no eigenfrequencies below 1THz. Using a numeric solver in SymPy, the following

eigenfrequencies are obtained

$$\begin{aligned} f_5 &= 1.19\text{THz} \\ \lambda &= 5.06\text{THz} \\ \lambda' &= 5.19\text{THz}, \end{aligned} \tag{6.11}$$

Indexed frequencies like f_5 correspond to experimentally measured modes in Table 4.4, other eigenvalues are denoted by λ. The eigenvectors of the 1.19THz mode are almost identical to the numeric values of the two sublattice model. As before, no resonance frequencies below 1THz are calculated. Since the 140GHz mode has been observed using experiments which measure free oscillations, this mode must arise from the non-linear terms in the LLG equation; either due to the nonlinear nature of the cubic anisotropy, or it is a second order term due to exchange/dipole interactions mediated by damping*. This highlights the failure of first order, linear approximations to the dynamics of simple antiferromagnets. Instead of introducing arbitrary anisotropy terms so that additional modes appear in the solutions of linearised equations of motions, more advanced analytic techniques [222, 226] or numerical spin dynamics simulations (Section 6.3 should be used. Additionally, linear model should be used with caution when studying more complex materials.

6.3 Spin Dynamics

By using atomistic spin dynamics, rather than linearised macrospin models, we can observe all linear and nonlinear modes of the system; it isn't possible to determine an analytic expression for the modes. But, by comparing with the analytic expressions above and other similar Hamiltonians, it's possible to infer the origin of these modes. In this section three Hamiltonians are used, all of which include the splitting of the nearest neighbour interaction, and all of which use $\alpha = 5 \times 10^{-4}$–this is an order of magnitude lower than in the previous chapter to ensure nonlinear modes are not overdamped. The first Hamiltonian omits the cubic anisotropy and replaces the dipole-dipole interaction with a single-ion uniaxial magnetocrystalline anisotropy of the same strength as the easy-plane dipole anisotropy ($\Delta E = -0.04695$ meV/spin). This Hamiltonian is labelled

*The coupled macrospin LLG equations for an antiferromagnet inherently give rise to inertial dynamics of the Néel vector, even in the absence of damping [238].

$\mathcal{H}_{\mathrm{u}}$ and is given by

$$\mathcal{H}_{\mathrm{u}} = -\frac{1}{2}\sum_{i,j} J_{ij}\mathbf{S}_i \cdot \mathbf{S}_j - \sum_i K_{\mathrm{u}} \left[S_i^{\mathrm{u}}\right]^2, \tag{6.12}$$

The next Hamiltonian, labelled $\mathcal{H}_{\mathrm{dip}}$, omits the cubic anisotropy, and includes the dipole-dipole interaction with a reduced cutoff radius $R_{\mathrm{cut}} = 3a$, rather than $5a$. $\mathcal{H}_{\mathrm{dip}}$ is given by

$$\begin{aligned}\mathcal{H}_{\mathrm{dip}} = &-\frac{1}{2}\sum_{i,j} J_{ij}\mathbf{S}_i \cdot \mathbf{S}_j \\ &-\frac{1}{2}\sum_{i\neq j} \frac{\mu_0 \mu_{S,i}\mu_{S,j}}{4\pi} \frac{3(\mathbf{S}_i \cdot \hat{\mathbf{r}}_{ij})(\mathbf{S}_j \cdot \hat{\mathbf{r}}_{ij}) - (\mathbf{S}_i \cdot \mathbf{S}_j)}{|\mathbf{r}_{ij}|^3},\end{aligned} \tag{6.13}$$

The final Hamiltonian, $\mathcal{H}_{\mathrm{dip,c}}$ includes the dipole-dipole interaction with reduced cutoff radius of $3a$, and the cubic anisotropy. It is given by

$$\begin{aligned}\mathcal{H}_{\mathrm{dip,c}} = &-\frac{1}{2}\sum_{i,j} J_{ij}\mathbf{S}_i \cdot \mathbf{S}_j \\ &-\frac{1}{2}\sum_{i\neq j} \frac{\mu_0 \mu_{S,i}\mu_{S,j}}{4\pi} \frac{3(\mathbf{S}_i \cdot \hat{\mathbf{r}}_{ij})(\mathbf{S}_j \cdot \hat{\mathbf{r}}_{ij}) - (\mathbf{S}_i \cdot \mathbf{S}_j)}{|\mathbf{r}_{ij}|^3} \\ &-\sum_i K_i \left[(S_i^{\mathrm{u}} S_i^{\mathrm{v}})^2 + (S_i^{\mathrm{v}} S_i^{\mathrm{w}})^2 + (S_i^{\mathrm{w}} S_i^{\mathrm{u}})^2\right],\end{aligned} \tag{6.14}$$

For $\mathcal{H}_{\mathrm{u}}$, the omission of the cubic anisotropy allows us to determine whether any of the modes f_1, ..., f_6 are mediated by the cubic anisotropy. If all modes can be observed in a simulation using $\mathcal{H}_{\mathrm{u}}$, then the modes which aren't predicted by the linearised macrospin models must arise from nonlinear processes involving exchange and the easy-plane anisotropy which are mediated by damping. In this case, an analytic derivation of these modes must include damping in a macrospin model but can ignore the small magnetocrystalline anisotropy. Additionally, the choice of a uniaxial magnetocrystalline anisotropy was made to reduce the computational cost of simulations; including dipole-dipole interactions with $R_{\mathrm{cut}} = 5a$ for a large supercell of $[32 \times 32 \times 8]$ unit cells each containing 24 Ni atoms* meant that a 48 hour simulation using a Tesla V100 GPU had a total integration time of ~ 0.045ns. Such a short integration time doesn't give sufficiently low noise to resolve the low frequency modes (100GHz corresponds to an oscillation period of 0.01ns). Using a magnetocrystalline uniaxial anisotropy means that the temperature dependence of the observed modes will be incorrect–especially

*This equates to 196,608 spins. Typical spin dynamics simulations contain at least $10,000$ spins to eliminate finite size effects [239].

those which are strongly dependent on the effective macrospin anisotropy constant (ie the 1.19THz Kittel mode). But, at low temperature, this is sufficient to determine whether a mode can be observed without the cubic anisotropy.

6.3.1 Hamiltonian Validation

The full Hamiltonian (4.17) has complex $k = 0$ dynamics, and it has been shown that the dipole-dipole interactions affect both $k = 0$ and $k \neq 0$ spin waves [35]. To ensure that substituting the dipole-dipole anisotropy with a uniaxial magnetocrystalline anisotropy of the same strength is valid, we must first compare the dynamics of simulations using Hamiltonians $\mathcal{H}_{\text{dip}}$ and $\mathcal{H}_{\text{u}}$. Fig. 6.1 shows the power spectrum of the total in plane magnetisation m^{IP} using $\mathcal{H}_{\text{u}}$, $\mathcal{H}_{\text{dip}}$, and $\mathcal{H}_{\text{dip,c}}$. The time series of the total in plane magnetisation is calculated by the following equation

$$m^{\text{IP}}(t) = \frac{1}{8}\sum_{i=1}^{8} m_i^{\text{IP}}(t) = \frac{1}{8}\sum_{i=1}^{8}\sqrt{[m_i^{\text{u}}(t)]^2 + [m_i^{\text{v}},(t)]^2}. \tag{6.15}$$

The sublattice magnetisation at a given time is calculated by the usual sum over the ensemble. The three plots of Fig. 6.1 are almost identical; all modes are present in all three, and their relative amplitudes are very similar. Although $\mathcal{H}_{\text{u}}$ has much lower noise and there are small deviations in the peak centres due to the poor convergence of the dipole-dipole interaction when using $R_{\text{cut}} = 3a$. Nevertheless, for studying fixed, low temperature dynamics, $\mathcal{H}_{\text{u}}$, $\mathcal{H}_{\text{dip}}$, and $\mathcal{H}_{\text{dip,c}}$ can be used interchangeably. This simple comparison shows that we are able to reproduce all modes of interest using any of these three Hamiltonians (at least for m^{IP}); the $k = 0$ dynamics are robust against the addition of the small cubic anisotropy, and exchange-dipole spin waves are unimportant.

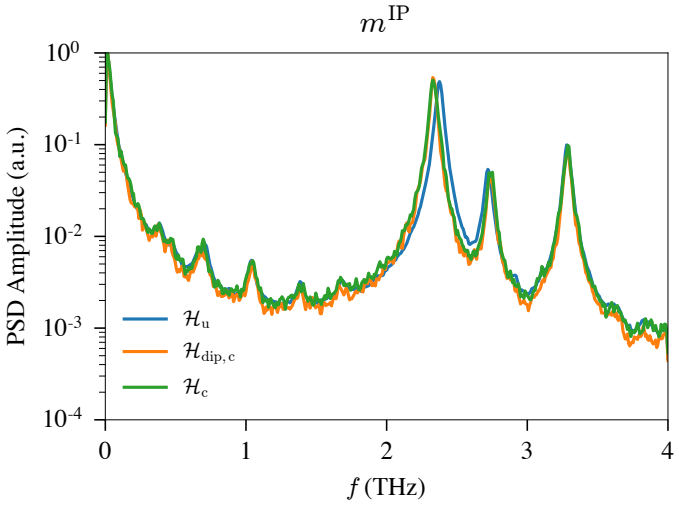

Figure 6.1: Power spectra of the total in plane magnetisation of NiO at 100K using Hamiltonians $\mathcal{H}_{\mathrm{u}}$, $\mathcal{H}_{\mathrm{dip}}$, and $\mathcal{H}_{\mathrm{dip,c}}$. Due to the difference in computational difficulty of the Hamiltonians, the total simulation times were 101ns, 7.7ns, and 9.2ns respectively.

6.3.2 Discussion

In this section, we aim to show that all of the experimentally measured modes in Table 6.2 can be observed in simulations which don't include a cubic anisotropy. And, we aim to show that the combination of components of sublattice magnetisations required to observe these modes are available experimentally (experiments are not sensitive to single sublattice magnetisation dynamics, for example). Modes will be indexed using the same frequencies as in Table 6.2 (f_1, ..., f_6), plots will be shown on a logarithmic scale to ensure low amplitude modes are not overlooked, all simulations use the quantum thermostat to ensure the relative amplitude of $k = 0$ and $k \neq 0$ modes is large (as expected in a real sample), and all simulations output the magnetisation every 0.125ps giving a Nyquist frequency of 4THz.

A natural starting point is to consider the characteristic frequencies of a single sublattice $\mathbf{m}_i$. This is not experimentally measurable, but gives information about the most fundamental characteristic frequencies of the system. Fig. 6.2 shows the spectral density of the out of plane component of a single sublattice magnetisation, m_{1+}^{OOP}. There are two characteristic frequencies at 1.19 and 2.81THz; all eight sublattices have the same

peak centres. The in plane dynamics (shown in Fig. 6.3) are much more complicated. To reduce noise in the spectral density, Fig. 6.3 shows the average spectral density of all sublattices; the average of the magnetisation time series ($m^{\alpha}(t) = \frac{1}{8}\sum_{i=1}^{8} m_i^{\alpha}(t)$) causes interference between modes of different sublattices (which have different polarisations, even for the same frequency mode). But, the average in frequency space ($\frac{1}{8}\sum_{i=1}^{8} \mathcal{FFT}\{m_i^{\alpha}\}$) does not. This spectral averaging increases signal-to-noise and ensures that observed peaks in the spectrum are characteristic frequencies of the system, rather than noise. The characteristic frequencies of the in plane sublattice dynamics (up to 2.5THz) are: $\sim$ 310GHz, $\sim$ 675GHz, $\sim$ 1.04THz, $\sim$ 1.62THz, $\sim$ 2.38THz. These characteristic frequencies don't correspond to the frequencies observed experimentally but strongly indicates that the dynamics of NiO (even when excluding the cubic anisotropy and exchange-dipole spin waves) cannot be understood by linearised models.

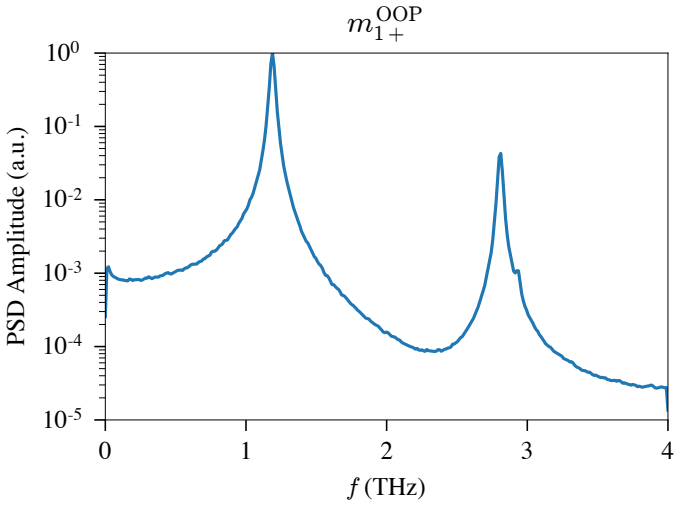

Figure 6.2: The spectral density of the out of plane component of a single sublattice magnetisation for a simulation using $\mathcal{H}_{\mathrm{u}}$.

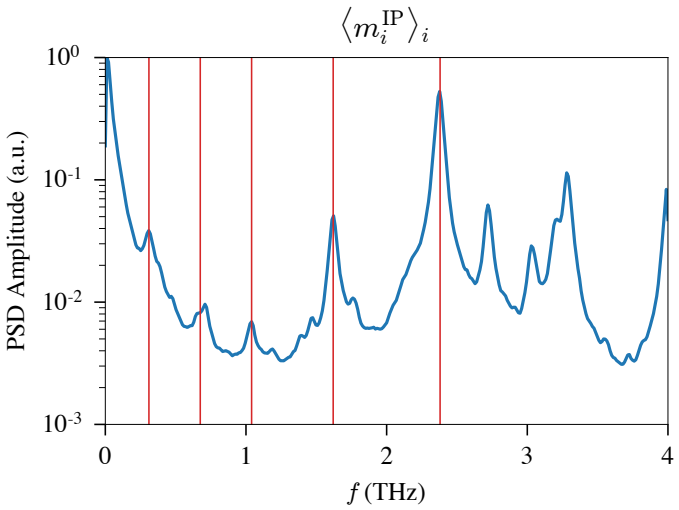

Figure 6.3: The spectral density of the in plane component of sublattice magnetisation (averaged across all sublattices) for a simulation using $\mathcal{H}_{\mathrm{u}}$. Vertical red lines are placed at 310GHz, 675GHz, 1.04THz, 1.62THz and 2.38THz.

The simplest, highest amplitude mode in NiO is the Kittel mode; this is the frequency at which the out of plane component of the total Néel vector ($l^{\mathrm{OOP}} = \frac{1}{8}\sum_{i=1}^{8}(-1)^i l_i^{\mathrm{OOP}}$) oscillates. In the previous chapter we showed that, at zero temperature, our atomistic model of NiO gives $f_5 = 1.19$THz. Fig. 6.4 shows that the out of plane component of the total Néel vector only has a single mode and that the out of plane component of total magnetisation has no modes in equilibrium; well calibrated experiments in geometries which are only sensitive to out of plane dynamics can only measure one mode (such as those by Moriyama [142]). The absence of any modes in the power spectrum of m^{OOP} means that both the 1.19THz and 2.81THz modes seen in a single sublattice (Fig. 6.2) destructively interfere in the summation of sublattices; inter-sublattice coupling via the split nearest neighbour exchange determines the relative polarisation of these modes which leads to the constructive/destructive interference for the total magnetisation and total Néel vector, respectively.

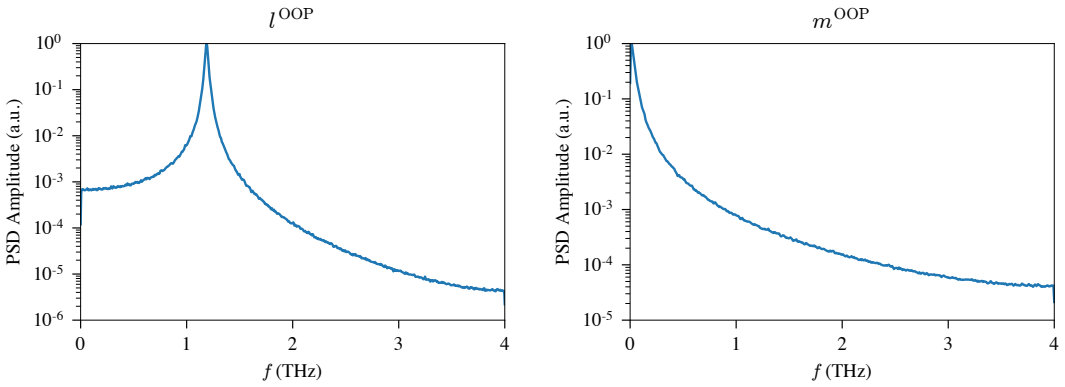

Figure 6.4: The spectral density of the out of plane component of the total Néel vector (*left*) and total magnetisation (*right*) for a simulation using $\mathcal{H}_{\mathrm{u}}$.

Now we consider the in plane dynamics of the total Néel vector. All contributions from the total Néel vector and total magnetisation are experimentally accessible. But, the dynamics of the total Néel vector have much higher amplitude than the total magnetisation because, in equilibrium, real samples will be almost perfectly compensated. Fig. 6.5 shows the PSD of l^{IP}. Two modes are immediately identifiable at 1.19 and 2.26THz. If this were a nonequilibrium or driven experiment which included a large field pulse or tuneable AC driving field similar to Baierl [100], we may ascribe the 2.26THz mode to the second harmonic of the Kittel mode. But, in this equilibrium spin dynamics simulation, there is no mechanism for the second harmonic to be excited so this must be a $k = 0$ spin wave whose amplitude is too low to be measured experimentally. This is irrelevant to device applications, but may need to be considered in very high sensitivity light scattering experiments.

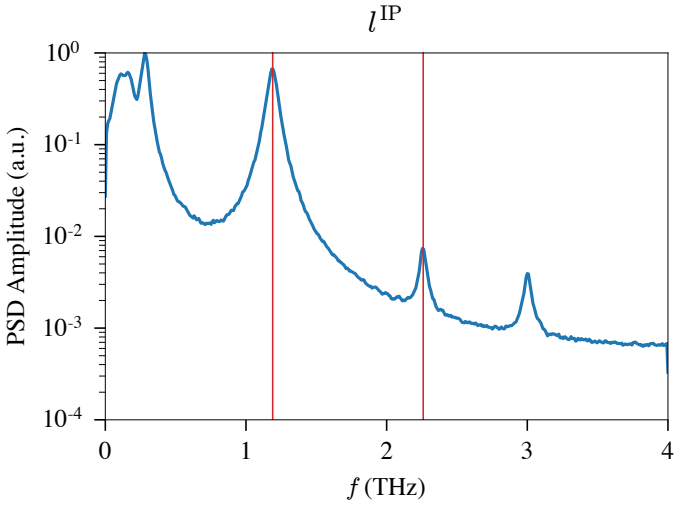

Figure 6.5: The spectral density of the in plane component of the total Néel vector for a simulation using $\mathcal{H}_{\mathrm{u}}$. Vertical red lines are placed at 1.19THz, and 2.26THz.

The low frequency peaks in Fig. 6.5 require more detailed consideration; Fig 6.6 shows the low frequency data, four modes can be resolved: $\sim$ 20GHz, 110GHz, 160GHz, and 280GHz. The lowest frequency mode is consistent with f_1 measured by Grimsditch [68], though this mode could be due to spectral leakage. Due to computational constraints, it isn't possible to more clearly resolve such low frequency dynamics. Although spectral leakage from the thermostat always appears in simulations as a monotonic decrease in amplitude except for PSD($f = 0$) (see m^{OOP} in Fig. 6.4). The amplitude at $f = 0$ is lower than the first frequency bin because Welch's method reduces the sensitivity to constant time offsets (ie at $f = 0$); this is a severe limitation of a typical FFT method. Since Fig. 6.6 shows a monotonic *increase* between $f = 0$ and $f = 0.05$THz, we deduce that there is a mode at low frequency. But, the resolution at low frequency is not high enough to obtain a good estimate of the frequency. A similar conclusion could be drawn from the two modes at 110GHz and 160GHz. Rather than two distinct peaks, it's possible that these are a single broad peak of frequency 135GHz because of the poor sampling of low frequency dynamics. Discounting this technicality, these two modes are consistent with the low frequency mode f_2 (measured experimentally between 100 and 140GHz) which is often associated with an additional magnetocrystalline anisotropy. There is no additional anisotropy present in

this model, so previous interpretations miss key physics in this material (leading to the use of forbidden Hamiltonian terms). Further, the mode at 280GHz can be mapped onto f_3 which has been inferred from the sum- and difference-frequencies measured by Baierl [100].

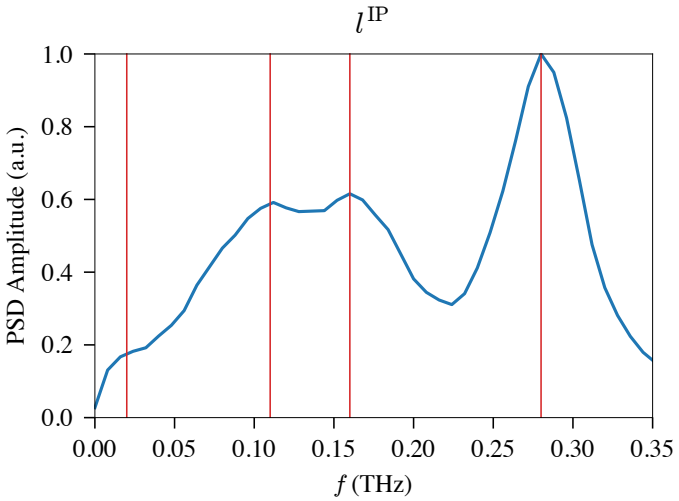

Figure 6.6: The spectral density of the in plane component of the total Néel vector for a simulation using $\mathcal{H}_{\mathrm{u}}$. Vertical red lines are placed at 20GHz, 110GHz, 160GHz, and 280GHz.

We have now identified the measured resonance modes f_1, f_2, f_3, and f_5 in a simulation of NiO which includes only a uniaxial anisotropy and exchange. Aside from the Kittel mode, f_5, these resonant frequencies are due to nonlinear dynamical processes which are mediated by the intersublattice coupling and damping*. The remaining modes can be observed by considering the in plane component of the total magnetisation seen in the Section 6.3.1. The spectral density of the in plane component of the total magnetisation is shown in Fig. 6.7. Five low amplitude modes are highlighted which have frequencies: 385GHz, 680GHz, 1.04THz, 1.38THz, and 1.68THz. The 1.68THz peak is likely f_6, which is strongly temperature dependent and has been measured to merge with the Kittel mode at ~ 250K [68, 103]. The present model slightly overestim-

*These modes disappear in simulations which have small supercells, when damping is large and when the classical thermostat is used. This strongly suggests a highly nonlinear process which is very easily damped.

ates the frequency of the Kittel mode and has a large splitting of the nearest neighbour exhange J_1. It is likely that this mode is mediated by the splitting which, in the present model, may be larger than in real samples. Alternatively, the coupling of spin waves in different S-domains within a T-domain, or the domain dynamics, at elevated temperatures could explain the observed merging of f_5 and f_6. The 1.04 and 1.38THz peaks are evenly spaced at either side of the Kittel mode (-0.15GHz and $+0.19$THz, respectively). Baierl [100] noted that their nonequilibrium measurement of the Kittel mode (1.00THz) had shoulders at 0.77 and 1.23THz which they ascribed to the mixing (sum-frequency and difference-frequency) of in plane and out of plane modes. It is reasonable to assume that the shoulders observed in the experiment are the same as those measured here, and the mixing is between the Kittel mode f_5 and the nonlinear f_2 mode at ~ 160GHz ($1.19 - 0.16 = 1.03$THz). We do not observe the mixing frequencies in the spectrum of the Néel vector because the amplitude of the Kittel mode is orders of magnitude larger than the mixing frequencies in equilibrium, but experiments which strongly excite the system out of equilibrium are able to measure this. The peaks at 385 and 680GHz are not easily reconciled with experimental measurements, though f_4 has been measured in a wide frequency range, anywhere from 390GHz to 500GHz (see Table 6.2). In particular, Kohmoto [103] measures a very broad feature in the THz-TDS transmittance which is centred around 500GHz*. Taking the mean of the two frequencies, 385 and 680GHz, we arrive at a centre average of ~ 440GHz which is near the middle of the experimentally measured values.

*The lowest frequency measurable in their THz-TDS experiment is around 300GHz. So, it is possible that two modes are present but the experiment doesn't have sufficient sensitivity at low frequency.

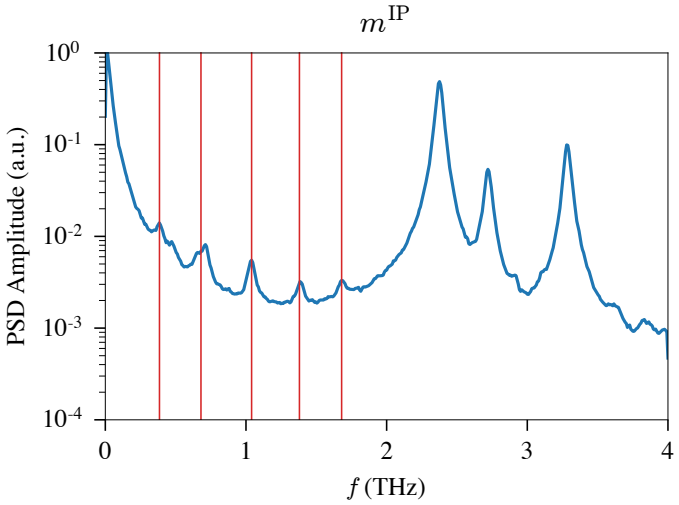

Figure 6.7: The spectral density of the in plane component of the total magnetisation for a simulation using $\mathcal{H}_{\mathrm{u}}$. Vertical red lines placed at 385GHz, 680GHz, 1.04THz, 1.38THz, and 1.68THz.

In an experimental measurement, the sample will contain inhomogeneities and the sample area which is probed by the measurement will contain multiple domains*, as considered experimentally by Higuchi [99]. We can apply some simple post-processing to our simulation data to emulate sublattice mixing in neighbouring domains. The eight sublattices are labelled $\mathbf{m}_{1+}$, $\mathbf{m}_{1-}$, $\mathbf{m}_{2+}$, $\mathbf{m}_{2-}$, $\mathbf{m}_{3+}$, $\mathbf{m}_{3-}$, $\mathbf{m}_{4+}$, and $\mathbf{m}_{4-}$. In a two sublattice model all + sublattices are equivalent and the − sublattices are antiparallel. The calculation of the Néel vector time series is

$$\mathbf{l}(t) = \frac{1}{8}\sum_{i=1}^{8}(-1)^{i}\mathbf{m}_{i}(t). \tag{6.16}$$

Having multiple domains within the spot size of an experiment means there is an unequal mixing of these sublattices. We can include a multiplier to each sublattice, ensuring there is an equal mixture of + and − sublattices so the sampled dynamics are compensated. Four random multipliers were chosen between 0.9 and 1.1 which sum to four. These are applied to the sublattices. The equation for the mixed Néel vector is

*Even if a single T-domain is chosen, there is no known procedure to produce an S-domain large enough to measure a single domain.

then

$$\begin{aligned}\mathbf{l}'(t) = \frac{1}{8}\big[&1.07\mathbf{m}_{1+}(t) - 0.93\mathbf{m}_{1-}(t) + 0.90\mathbf{m}_{2+}(t) - 1.10\mathbf{m}_{2-}(t) + 1.07\mathbf{m}_{3+}(t) \\ &- 0.90\mathbf{m}_{3-}(t) + 0.93\mathbf{m}_{4+}(t) - 1.10\mathbf{m}_{4-}(t)\big].\end{aligned} \tag{6.17}$$

This is a crude approximation of the effect of domains. But, in our case, we are only interested in the interference of the eigenoscillations of the eight sublattices, so this simple convolution of the sublattice dynamics is sufficient. The spectral density of the in plane component of $\mathbf{l}'$ is shown in Fig. 6.8. Modes f_1, f_2, f_3, f_5, and f_6 can be seen on the plot which doesn't use a logarithmic scale, so these modes have a large (experimentally accessible) amplitude. The missing f_4 mode has very low amplitude and can be seen in Fig. 6.9. It is surprising that this mode has been measured experimentally given its small amplitude but we can attribute this mode to a non-zero magnetisation, suggesting that experimental methods are highly non-equilibrium. Higuchi [99] measured two modes in addition to the Kittel mode at $\sim$ 400GHz and $\sim$ 800GHz (see figure 3c) using stimulated Raman scattering but these were not discussed in the main text.

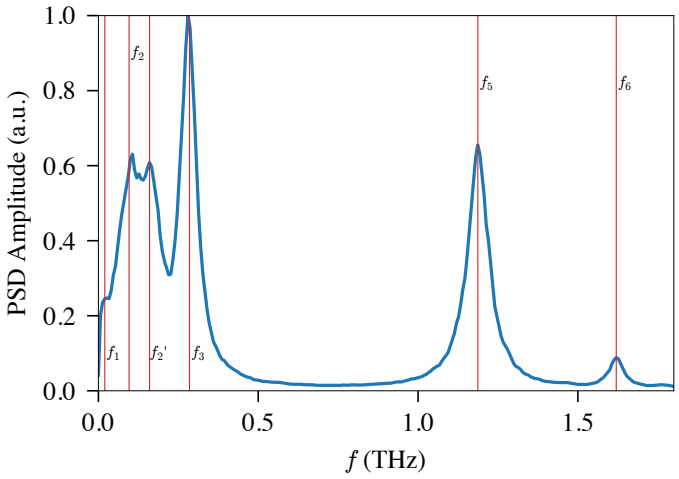

Figure 6.8: The spectral density of the in plane component of the convoluted Néel vector for a simulation using $\mathcal{H}_{\mathrm{u}}$. Vertical red lines placed at $f_1 = 20$GHz, $f_2 = 100$GHz, $f_2' = 160$GHz, $f_3 = 285$GHz, $f_5 = 1.19$THz, and $f_6 = 1.62$THz.

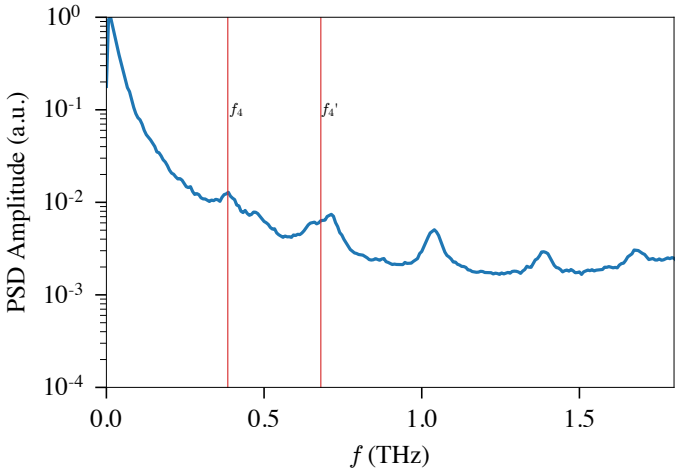

Figure 6.9: The spectral density of the in plane component of the convoluted magnetisation $\mathbf{m}'$ for a simulation using $\mathcal{H}_{\mathrm{u}}$. Vertical red lines placed at $f_4 = 385$GHz and $f_4' = 680$GHz.

The convolution carried out here shows that under realistic experimental conditions, where inhomogeneities and unequal numbers of domains leads to imperfect mixing of sublattice magnetisations, all of the modes which have been reported in the literature can be understood by a simple model containing only exchange and uniaxial anisotropy but which must include nonlinear dynamics through damping. Including additional anisotropies is an incorrect interpretation of the physics of this material.

Chapter 7

Thermodynamic Stability

7.1 Introduction

The finite temperature parameterisation of micromagnetic and macrospin models of magnetic materials is often approached in an *ad-hoc* manner. Material parameters such as the exchange stiffness A, anisotropy constants K, and DMI strength are tweaked so that simulations and analytic models agree with a single reference point of the physical system, such as the domain wall width* Usually this tweaking doesn't involve any sanity checks against experimental values of material parameters, or calculating other metrics (such as resonance frequencies). This leads to computer simulations which are said to be representative of samples which have been measured experimentally, but uses unrealistic input values for material properties. There are a few reasons why the finite temperature parameterisation of continuum models–specifically exchange stiffness and DMI strength–from atomistic models and experiments isn't treated rigorously:

1. Direct experimental measurements of exchange stiffness and DMI are difficult and require complex multi-step experimental procedures which requires a large degree of approximation in the analysis of experiments [240–244].

2. The experimental method chosen to measure the same macroscopic parameter in the same material can heavily influence the measured temperature dependence. Niitsu [245] has collected temperature dependent exchange stiffness measurements from the literature in elemental Fe and Ni (figures 2 and 3) which highlights this issue.

3. There are many publications which report conflicting expressions for the same parameter in similar materials. For example, see Niitsu [245] for exchange stiffness or the the following references for the helicity modulus (discussed in Section 7.3.2) [246–255].

4. There are insufficient computational methods to directly investigate micromagnetic quantities. Constrained Monte Carlo [38] is a very useful tool but can only measure anisotropic terms, not leading order energies like the exchange stiffness. Some publications, such as Moreno [256], resort to fitting domain walls which

*Often domain walls are too small to resolve using microscopy techniques so the width of a domain is used which has a stronger and more complex dependence on material parameters and inhomogeneities.

are forced into the system by including antiperiodic boundary conditions*, under the assumption that $K(T)$ exactly follows the Callen-Callen scaling within the domain wall. In atomistic simulations, all microscopic degrees of freedom are accessible so it should be possible to evaluate finite temperature macroscopic parameters without this type of inference.

5. Naming conventions in magnetism means that distinct material properties such as exchange stiffness A and spin wave stiffness D, are used interchangeably. This means their temperature dependences are also confounded [145, 257].

6. The fields of thermodynamics and statistical mechanics were established before modern magnetism, so a lack of magnetism-specific language and literature means the barrier to entry is high†–most literature is written in terms of fluids and gases so astronomers, biophysicists, and engineers benefit from well developed frameworks for studying thermal properties in their fields. Additionally, magnon theories such as those used in Chapter 5 are often thought of as complete theories of the thermodynamics of magnetic materials.

7. The increased availability of computing resources within universities (especially GPUs) means tools like micromagnetism are widely used by both researchers experienced in magnetism, and those new to the field. Coupled with the increased pressure from academic journals to include computational modelling in publications, it is easy (and often encouraged) to include micromagnetic models regardless of how realistic the are.

These problems become very important in complex systems with many competing energy terms which can lead to spin reorientation transitions [258], Morin transitions [259], and multiple magnetic phase transitions in chiral magnets [260]. A thermodynamic understanding of magnetisation textures like skyrmions is vital for material exploration and device engineering, but the complexity of the Hamiltonians of skyrmion

*Antiperiodic boundary conditions are expected to introduce strange artificial interactions because of spin waves propagating across these mirror boundaries, and pinning introduced at the supercell edges is already known to change $m(T)$. In general, forcing domain walls into a computer simulation has unknown effects the on free energy landscape.

†Even the most fundamental ideas such as the difference between free and internal energy are poorly understood and evoke strong opinions in the magnetism community.

hosting materials means computational methods must be able to deconvolve the temperature dependence of these competing energy terms to gain useful insights. Methods currently available to researchers do not have the specificity for these use cases. In the case of exchange, some efforts have been made to use atomistic numerical models to calculate these macroscopic properties of magnetic materials [38, 256, 261–264] but these methods often require fitting and the use of assumptions. In this chapter we aim to solve some of these issues by developing a theoretical framework for calculating the temperature dependence of macroscopic magnetic properties (effective anisotropy constants, effective exchange constants, etc) from simple thermal averages which are independent of the method used to evaluate them–analytic mean field approximations, spin wave theories, or numerical atomistic models (both quantum and classical). We name these parameter-specific thermal averages stability coefficients after the work of Debenedetti [265]. Stabilty coefficients are derived from the fundamental principles of thermodynamics, and are independent of magnetism. The underlying principles are not new, but the connection between stability coefficients and multiscale parameterisation from statistical ensembles has never been made.

The chapter is outlined as follows. First, we describe some specific cases in magnetism where the above problems have led to inaccuracies in the literature. Next, we rewrite main postulates and results of classical thermodynamics using language which is independent of liquids, gases, and molecules, as well as giving key examples applied to modern magnetism*. Then, we discuss the geometric interpretation of thermodynamics and state some results from differential geometry. Finally, we derive *stability coefficients* which allow us to express the finite temperature internal energy of any parameter, from any macroscopic/mean field description of a thermodynamic ensemble, in terms of simple expectation values of microscopic parameters. The internal energy stability coefficients are related to the free energy stability coefficients by a simple integral (the Gibbs-Helmholtz equation). We derive the stability coefficients for a rank-2 uniaxial magnetocrystalline anisotropy and the exchange stiffness in a micromagnetic

*Modern magnetism here means mesoscale magnetic devices; thin films of ferromagnets, ferrimagnets and antiferromagnets which can be used for computing and memory devicese. This is in contrast to other literature on the thermodynamics of magnetic materials which typically describes bar magnets in electric fields, hysteresis of permanent magnets in terms of reversible and irreversible processes, and which completely fails to describe antiferromagnets.

model of ferromagnetism.

7.1.1 Measuring Exchange Stiffness

Without rigorous theoretical language and tools, experiments cannot be designed to measure the thermodynamic property that was intended. A perfect example of this is exchange stiffness, A. The spin wave stiffness, D, is the coefficient of the spin wave spectrum in the small-k limit $\langle hf \rangle \approx D(T)k^2$ (for a ferromagnet). A spin wave is a dynamical excitation with an instantaneous (in time) deviation from the magnetisation direction which is neither fixed, nor an equilibrium value. It is a free eigenoscillation of the system. The exchange stiffness A, on the other hand, is related to the energy required to twist the magnetisation (not individual spins); it is a static solution of the free energy functional which is a stable equilibrium state of a ferromagnet. The existence of domain walls, or twists in the magnetisation, do not require dynamics. Despite this, researchers often compare the temperature dependence of these two distinct properties [145, 257]. This comes from the comparison of the zero temperature expressions for these properties*:

$$A(T=0) = \frac{1}{3} \sum_{\alpha=x,y,z} \left[\frac{1}{4} \frac{1}{N\nu_{\mathrm{WS}}} \sum_{i,j} J_{ij} r_{ij}^{\alpha} r_{ij}^{\alpha} \right], \tag{7.1a}$$

$$D(T=0) = \frac{1}{3N} \sum_{i,j} \frac{|\gamma|}{\mu_{S,i}} J_{ij} |\mathbf{r}_{ij}|^2, \tag{7.1b}$$

where the summation is over all spins in the lattice, N is the total number of spins, ν_{WS} is the volume of the Wigner-Seitz cell, γ is the gyromagnetic ratio, and $\mathbf{r}_{ij} = \mathbf{r}_j - \mathbf{r}_i$ is the displacement vector between two spins. For a simple cubic ferromagnet with a single magnetic sublattice, these reduce to

$$A(T=0) = \frac{J}{2a}, \tag{7.2a}$$

$$D(T=0) = \frac{2|\gamma|}{\mu_S} J a^2. \tag{7.2b}$$

*Note that we differ from other references because we explicitly use a classical Hamiltonian for both calculations.

The zero temperature relationship between these two parameters is then

$$A_0 = \frac{1}{4}\frac{D_0}{|\gamma|}\left[\frac{\mu_S}{a^3}\right], \tag{7.3}$$

where $A_0 = A(T = 0)$, and $D_0 = D(T = 0)$. The term in square brackets is equal to the zero temperature saturation magnetisation, though these are purely microscopic expressions; no coarse graining has been included. The final relationship is then

$$A_0 = \frac{1}{4}\frac{D_0 M_{s,0}}{|\gamma|}, \tag{7.4}$$

where $M_{s,0} = M_s(T = 0)$ is the zero temperature saturation magnetisation. This result is very useful for calculating the exchange stiffness at zero temperature. But, this is often used incorrectly at finite temperature. There is no derived relationship between these parameters at finite temperature. Yet, in the absence of a simple expression for $A(T)$ written in easily measured finite temperature parameters, researchers improvise by making all parameters temperature dependent in that hope that it gives a reasonable guess without any further thought on the assumptions made. In practice this means that the following relationship is used

$$A(T) = \frac{1}{4}\frac{D(T)M(T)}{|\gamma|}. \tag{7.5}$$

We reiterate that equation (7.5) has no theoretical justification. Any theoretical result, computational model, or experiment using the temperature dependence of spin waves as an analogue for the exchange stiffness is missing some information about the underlying thermodynamics of the system. Readers may see this as nit-picking but the micromagnetic free energy for exchange and the linearised magnon Hamiltonian have different curvatures, so relate to the thermal averaging of different functions of spins in the ensemble. Some carefully designed experiments such as those which use perpendicular standing spin waves (PSSW) [266, 267] are more directly probing the exchange stiffness but these often neglect to include finite size and interfacial effects or rely on tweaking micromagnetic simulations to verify their analysis [268]. So, PSSW methods have similar problems to computational methods that force domain walls into the system.

7.1.2 Anisotropy

Section 5.3.1 briefly describes the Callen-Zener theory of the temperature dependence of magnetocrystalline anisotropies due to the thermal fluctuations of spins*. We will not discuss this theory further but there are a few things which suggests this is not the most general form of the theory. First, calculating the scaling of non-local interactions such as exchange, the dipole interaction and two-ion anisotropies is difficult using this theory. Both partial rotations and full/isomorphic rotations must be considered separately which increases the complexity of calculations [159]. Second, the theory is limited to the spherical harmonic representation of crystal anisotropies. Antiferromagnets can permit non-crystalline anisotropies of odd rank (a unidirectional anisotropy of the form $\cos^3\theta$, for example) but the scaling of these anisotropies aren't known, and aren't easy to calculate using Callen-Zener since time reversal no longer preserves energy. Next, deriving magnetisation power law scalings from spherical harmonics is unintuitive† because very few researchers express magnetocrystalline anisotropies as a series of spherical harmonics with anisotropy strength given by coefficients $\kappa_{l,m}$ (l and m are the usual orbital and azimuthal momenta which indexes spherical harmonics). Instead, the anisotropy is usually written using expansions of the direction cosines with coefficients K. The temperature dependence of a given K contains a convolution of the spherical hamonic coefficients $\kappa_{l,m}$ which leads to some articles misquoting the results of Callen-Zener theory. As an example, consider a cubic ferromagnet with non-negligible first and second cubic anisotropy constants

$$E = K_{\mathrm{c}1}[(m_x m_y)^2 + (m_y m_z)^2 + (m_z m_x)^2] + K_{\mathrm{c}2}[m_x m_y m_z]^2 \tag{7.6}$$

where m_x, m_y, m_z are Cartesian components of the magnetisation, and $K_{\mathrm{c}1}$, $K_{\mathrm{c}2}$ are the cubic anisotropy constants. This can be rewritten in terms of spherical harmonics as [86]

$$E = \kappa_0 + \kappa_{4,0}Y_{4,0} + \kappa_{4,4}Y_{4,4} + \kappa_{6,0}Y_{6,0} + \kappa_{6,4}Y_{6,4}, \tag{7.7}$$

with the following values of κ‡

*Changes to the crystal field splitting and spin-orbit coupling are negligible over the temperature range of magnetic ordering.

†Though it has been argued that spherical harmonics are preferable because they form an orthonormal basis, whereas direction cosines have considerable overlap leading to ambiguity in the values of K [129].

‡In general, the spherical harmonic transform (similar to a Fourier transform) calculates numeric values of the coefficients.

Table 7.1

κ	Value in terms of K
$\kappa_{0,0}$	$\frac{21K_1+K_2}{105}$
$\kappa_{4,0}$	$-\frac{11K_1+K_2}{55}$
$\kappa_{4,4}$	$-\frac{11K_1+K_2}{9240}$
$\kappa_{6,0}$	$\frac{2K_2}{231}$
$\kappa_{6,4}$	$-\frac{K_2}{41580}$

Table 7.2

$\frac{K_1(T)}{K_1(0)}$	Value in terms of $\frac{\kappa(T)}{\kappa(0)}$
$\frac{K_1(T)}{K_1(0)}$	$\frac{\kappa_4(T)}{\kappa_{4,0}(0)} - \frac{1}{11}\frac{\kappa_{6,0}(T)}{\kappa_{6,0}(0)}$
$\frac{K_2(T)}{K_2(0)}$	$\frac{\kappa_{4,0}(T)}{\kappa_{4,0}(0)}$

The values in Table 7.2 are approximations which are calculated by inspecting Table 7.1 and choosing to include only $\kappa_{4,0}$ and $\kappa_{6,0}$. The theory of Callen-Callen and Zener shows that terms with the same value of the total angular momentum l have the same anisotropy scaling (ie $\frac{\kappa_{4,0}(T)}{\kappa_{4,0}(0)} = \frac{\kappa_{4,3}(T)}{\kappa_{4,3}(0)} \equiv \frac{\kappa_4(T)}{\kappa_4(0)}$), and gives the following result

$$\frac{\kappa_4(T)}{\kappa_4(0)} \simeq \langle m_z \rangle^{10} \tag{7.8a}$$

$$\frac{\kappa_6(T)}{\kappa_6(0)} \simeq \langle m_z \rangle^{21} \tag{7.8b}$$

From the relations in the table on the left, this implies that

$$\frac{11K_1(T) + K_2(T)}{11K_1(0) + K_2(0)} \simeq \langle m_z \rangle^{10} \tag{7.9a}$$

$$K_2(T) \simeq K_2(0)\langle m_z \rangle^{21} \tag{7.9b}$$

This is usually approximated to

$$K_1(T) \simeq [K_1(0) + \frac{1}{11}K_2(0)]\langle m_z \rangle^{10} - \frac{1}{11}K_2(0)\langle m_z \rangle^{21} \tag{7.10a}$$

$$K_2(T) \simeq K_2(0)\langle m_z \rangle^{21} \tag{7.10b}$$

This creates a problem. Considering equation (7.9) in the limit that $K_1 \sim 0$, we have

$$\frac{K_2(T)}{K_2(0)} \simeq \langle m_z \rangle^{10}, \tag{7.11a}$$

$$\frac{K_2(T)}{K_2(0)} \simeq \langle m_z \rangle^{21}. \tag{7.11b}$$

This is a contradiction; K_2 cannot scale as both the 10th and 21st power of the magnetisation. This simple calculation shows the theory is not rigorous when transforming from coefficients κ to constants K–whether the contradiction is a real effect or due to an approximation wasn't investigated. Another issue is that there is often confusion between Akulov's derivation [269], and the general Callen-Zener theory [160]. This is because Akulov's derivation is reproduced in the Callen paper before the Callen-Zener theory is derived [159]. The general theory requires good knowledge of crystal symmetries, and has a high barrier to entry for those studying magnetic phenomena at micromagnetic length scales because the relationship between coefficients κ and constants K is rarely considered in this context. Akulov's derivation is much more intuitive but fails for higher order local anisotropies (the author finds it only works for $K_{\mathrm{u}1}$ and $K_{\mathrm{c}1}$) and can't be applied to any multispin interaction (exchange, magnetic dipole-dipole interaction, etc). Finally, the connection between the microscopic description and the free energy difference is not well established by this theory; a partition function is never manipulated yet the finite temperature anisotropy is called the free energy F [159, 269] even though this is not true; expectation values over using the Hamiltonian are always internal energies. Above, E has been used simply as the energy. This is acceptable for a macroscopic/continuum energy; since there is no entropy, the free energy and internal energy coincide. But, when parameterising macroscopic models from microscopic ones, the internal energy scaling is often used for exchange but the free energy scaling is used for anisotropies. In the rest of this section, we discuss a very general method of calculating the temperature dependence of continuum and mean-field parameters from a canonical ensemble based on the partition function which can be used for any energy term.

Akulov [269] made a simple conjecture; the equilibrium (easy direction) thermal fluctuations of spins can be projected onto a hard direction to measure the reduction of the potential barrier (due to crystal anisotropy) between adjacent easy directions. The equilibrium fluctuations are also applied to the easy direction to measure the finite temperature potential well. The energy difference between the finite temperature potential well and potential barrier is the energy required for the magnetisation to transition between two easy directions. The scaling of the transition barrier is precisely the tem-

perature scaling of the macrospin anisotropy constant. This is a simple, and very powerful insight which recovers the Callen-Zener power scaling for uniaxial and cubic magnetocrystalline anisotropies. This caused the author to think about the thermodynamics of magnetic systems from the viewpoint of geometry and curvature, ultimately leading to this chapter of work. In addition to the work of Akulov, Zener, and the Callens, this chapter has been heavily influenced by the following works [265, 270–278].

7.2 Classical Thermodynamics

7.2.1 Introduction

Thermodynamics–in the most abstract sense–is a quantitative description of how energy (heat, work, etc) can be added to–and extracted from–a system. Here, a 'system', is some macroscopic amount of physical material such as a tank of water, a vial of a chemical, a ferromagnet, or a package in a warehouse that needs to be moved. In this section, a brief and general description of thermodynamics will be given with the understanding that we will later discuss equilibrium statistical mechanics which focuses on the thermodynamics of states rather than thermodynamic processes. This is to prevent confusion with traditional literature which often describes the specific case of the thermodynamics of fluids and gases.

7.2.2 State Variables, Total Energy and Conjugacy

The state of any physical system is described mathematically by variables. In typical literature on the thermodynamics of gases, the named state variables are the temperature of the environment T, entropy S, the pressure of the environment p, volume V, the chemical potential of the constituent particles μ, and the number of particles N. In general, a system can be described by many other parameters besides these but we will use these as a base point to generalising the description of a system.

The internal energy of a system U is the total energy. It is the sum of all energies in the system; all kinetic and potential energies of the microscopic degrees of freedom. In the description of gases, the internal energy is

$$U = \int T\mathrm{d}S - p\mathrm{d}V + \mu\mathrm{d}N. \tag{7.12}$$

Temperature and entropy are special variables which are not specific to a given system, but the other terms are specific to the way work can be done by a container of gas molecules which can change volume and exchange particles with the environment. In general, we can write the total energy as

$$U = \int T\mathrm{d}S + \sum_i Y_i \mathrm{d}X_i, \tag{7.13}$$

where $\{Y_i\}$ are intensive variables and $\{X_i\}$ are extensive variables. The definition of intensive and extensive are not very strict but the name is often used in literature. Instead, we prefer to call these variables thermodynamic fields $\{Y_i\}$ and thermodynamic displacements $\{X_i\}$ (or macroscopic fields and macroscopic observables) which gives a physicist a better intuition of how these variables work. If a sealed piston in an engine is displaced by changing expanding, then the conjugate field (pressure) will decrease to push the system towards equilibrium. Each X_i is conjugate to the variable Y_i, this means that each Y_i is given by a partial derivative

$$Y_i = \frac{\partial U}{\partial X_i}. \tag{7.14}$$

For the classical Heisenberg model of a ferromagnet, examples of thermodynamic fields are the effective magnetic field $\mu_0\mathbf{H}^*$, skyrmion chemical potential μ_Q, and domain wall chemical potential μ_{DW}. Their conjugate thermodynamic displacements are the magnetisation $\mathbf{M}$, topological charge n_Q, and domain wall momentum $\mathbf{K}_{\mathrm{DW}}$. An equivalent thermodynamic description of a classical Heisenberg ferromagnet can be written in terms of spin waves. This description has distinct thermodynamic fields; the chemical potentials for spin waves with a specified $\mathbf{k}$-vector $\{\mu_{\mathbf{k}_i}\}$ and the corresponding thermodynamic displacements are the spin wave numbers of different $\mathbf{k}$-vectors $\{n_{k_i}\}$.

In Eq 7.13 we have written the total internal energy in integral form. Computing the integral–assuming ground state values of the thermodynamic displacement variables are zero–gives $U = TS - pV + \mu N$. We can also write the total change in internal energy

*The literature usually states this is the applied magnetic field. We make this generalisation because we are studying magnetism on crystals at the mesoscale which have complex interactions (as well as an applied magnetic field) instead of the limiting case of idealised isotropic ferromagnets. This also shows the link between classical Heisenberg model more clearly, and helps reduce confusion when considering thermodynamics.

as a differential which follows directly from Eq 7.13

$$dU = T\mathrm{d}S + \sum_i Y_i \mathrm{d}X_i \tag{7.15}$$

We now have enough information to define the four laws of thermodynamics.

7.2.3 The Zeroth Law

The zeroth law is a statement about equilibrium. It states that if two thermodynamic systems (vials of fluid, domains in a ferromagnet, etc) are both in equilibrium with a third system, then the first two systems must also be in equilibrium with each other. Equilibrium between two systems means that they are connected by some boundary which allows the flow of heat (but nothing else) and that there is no net heat flow from one system to the other. In simple terms; they have the same temperature.

In maths, this is formulated by the following. Let U_1, U_2, U_3 be the internal energies of three systems which are functions of T_s, S_s, $\{X_{s,i}\}$, $\{Y_{s,i}\}$ where $s \in \{1, 2, 3\}$ denotes the number of the system. The zeroth law can then be written mathematically as

$$(T_1 = T_3) \wedge (T_2 = T_3) \iff (T_1 = T_2), \tag{7.16}$$

where the wedge symbol $\wedge$ is the logical AND operator.

7.2.4 The First Law

The first law is a mathematical statement of conservation of energy. Before writing this, we first need to introduce work W and heat Q. Similar to the discussion of thermodynamic fields/displacements, the expression for work is dependent on the degrees of freedom of the system considered. Heat is independent of the system. Heat Q is the total change in thermal energy of a system and is written

$$Q = T\Delta S. \tag{7.17}$$

Work is how a thermodynamic system can affect other systems through its macroscopic variables. The typical description is in terms of mechanical work which interacts with other systems by changes in pressure and volume, for example a human metabolises sugars in the body to move muscles which allows them to lift a heavy box. The human applies mechanical work to the box which changes its gravitational potential energy.

But many forms of work exist dependent on the system, it could be the work done by a change in direction of the stray field of a ferromagnet on an adjacent paramagnet, how a blackbody experiences radiation pressure, or how an apple falls from a tree due to the work done by the gravitational field of the Earth. The work done by the system W is the total change in energy due to the change in thermodynamic fields, but excluding the energy unavailable due to entropy (TS). Again inspecting Eq 7.13, each conjugate pair of fields/displacements gives a unique type of work that the system can do to its environment W_i

$$W_i = \int Y_i \mathrm{d}X_i. \tag{7.18}$$

These forms of work could be mechanical (windmill), electromagnetic from mechanical (dynamos/alternators), electrochemical (batteries), thermomechanical (combustion engines, refrigerators/heat pumps), etc. The first law of thermodynamics states that any change in internal energy is the difference between the thermal energy added and the work done by the system

$$\Delta U = Q - W. \tag{7.19}$$

Instead of defining W as the work done *by* the system, one can define the work done *on* the system. The work done on the system by the environment leads to a change in sign of Eq 7.19 so it reads $\Delta U = Q + W$.

7.2.5 The Second Law

We have already partially stated the second law. The definition of the internal energy U given by Eq 7.13 is part of the statement of the second law. The second part of the second law can be formulated in many ways. Here are a few

- Heat can never pass from a colder to a warmer body without some other change (work), connected therewith occurring at the same time. - Clausius 1854 [279]
- It is impossible for a self-acting machine, unaided by any external agency to convey heat from one body to another at a higher temperature. - Kelvin/Thompson 1851 [280]
- Every process occurring in nature proceeds in the sense in which the sum of the entropies of all bodies taking part in the process is increased. In the limit, i.e. for reversible processes, the sum of the entropies remains unchanged. - Planck

1897 [280]

- In every neighbourhood of any state S of an adiabatically enclosed system there are states inaccessible from S. - Carathéodory 1966 [281]

Some of these statements are equivalent, some only partially describe what is known as the second law in modern thermodynamics. The definition we will use is that the entropy of an isolated system will always increase over time. To fully understand this, we need to define reversible and irreversible processes.

A reversible process is one which no energy is lost as friction, magnetic damping, or used to change the chemical state of a system. And, a process where the system is in equilibrium throughout the process. The statement of constant equilibrium is the same as a quasi-static process ie. so slowly that incremental changes to thermodynamic displacements X are small enough that the thermodynamic fields Y are constant. Examples are isothermal expansion of a gas, angular rotation of the magnetisation direction by an external magnetic field (hysteresis is irreversible, only processes where domain walls do not move are reversible). An irreversible process is any other process.

For reversible processes, the loop/contour integral of the thermal energy change at constant temperature is zero

$$\oint \frac{\delta Q}{T} = 0. \tag{7.20}$$

But for irreversible processes, this must be less than zero

$$\oint \frac{\delta Q}{T} < 0. \tag{7.21}$$

In Equation 7.13, the thermal energy is the first term

$$\delta Q = T\mathrm{d}S \tag{7.22}$$

So the entropy is defined by the irreversibility of a process. The entropy of a system is a measure of disorder. The contour integral of reversible processes, states that there is no change in entropy. For an irreversible process, there must be an entropy increase. This is the second law.

7.2.6 The Third Law

The third law is a weaker statement and is not often considered part of classical thermodynamics. It is, however, important in the statistical mechanical view of thermodynamics. The third law states that, in the limit that temperature goes to zero, the

entropy reaches a constant value

$$S(T \to 0) \to S_0. \tag{7.23}$$

The value of S_0 is given by the number of degenerate ground states. That is, given the number of microstates W (sets of $\{X_i, Y_i\}$) such that $U(T = 0, \{X_i\}, \{Y_i\}) = U_0$ the ground state energy, then the entropy at zero temperature is

$$S_0 = k_B \ln(W). \tag{7.24}$$

If the system has a single ground state then $S_0 = 0$. The above is valid for both discrete and continuous systems but W is not always countable. Take for example, a classical Heisenberg ferromagnet with uniaxial anisotropy. There are two ground states; $\mathbf{S}_i = \hat{\mathbf{z}} \forall i$ and $\mathbf{S}_i = -\hat{\mathbf{z}} \forall i$ so $W = 2$. But the isotropic Heisenberg ferromagnet has infinitely many ground states, so $W = \infty$. In general, for continuous systems at finite temperature, the entropy is given by the H-theorem [282, 283]

$$S = -k_B \int p(\mathbf{X}) \ln(p(\mathbf{X})) \mathrm{d}\mathbf{X}, \tag{7.25}$$

where $p(\mathbf{X}) = \frac{1}{Z} e^{-\beta \mathcal{H}(\mathbf{X})}$ is the probability of a microstate $\mathbf{X}$.

7.2.7 Thermodynamic Potentials

Thermodynamic potentials are fundamental equations. A fundamental equation is any equation from which we can obtain all knowledge about a system [284]. All thermodynamic potentials are equivalent as they can all be derived–under certain constraints, called natural variables–from the internal energy U which itself is a thermodynamic potential. The internal energy is the total energy of the system; it includes heat energy as well as all thermodynamic fields present in the system and its expression has already been given above in Eq 7.13. A new thermodynamic potential is constructed by turning one or more thermodynamic fields into an independent variable by a Legendre transformation. For example, the Helmholtz free energy is a Legendre transformation of the internal energy with respect to temperature. This constrains the temperature (a thermodynamic field) to a fixed value and the entropy now becomes an independent variable ie $U(T, \{X_i\}) \to F(S, \{X_i\})$. The number of thermodynamic potentials which can be constructed is only limited by the number of thermodynamic fields. The typical thermodynamic potentials in the literature for chemical systems are the Helmholtz free

Table 7.3: Expressions for the partition function $\mathcal{Z}$ for quantisation of energy (columns) and coordinates (rows) assuming there are only two three-dimensional variables $\mathbf{p}$ and $\mathbf{q}$ which describes the state of an object i ($i \in 1, ..., N$) in the ensemble.

Potential	Differential	Constants (Natural variables)
$U = TS + \sum_i Y_i X_i$	$\mathrm{d}U = T\mathrm{d}S + \sum_i Y_i \mathrm{d}X_i$	$\{X_i\}$
$F = \sum_i Y_i X_i$	$\mathrm{d}F = \mathrm{d}U - (T\mathrm{d}S + S\mathrm{d}T)$	T, $\{X_i\}/S$
$H = U - pV$	$\mathrm{d}H = \mathrm{d}U + p\mathrm{d}V + V\mathrm{d}p$	p, $\{X_i\}/V$
$G = U - TS - pV$	$\mathrm{d}H = \mathrm{d}F + (p\mathrm{d}V + V\mathrm{d}p)$	T, p, $\{X_i\}/\{S, V\}$

energy F, enthalpy H, and Gibbs free energy G. Each is relevant for a thermodynamic process (where work is done) for a constant thermodynamic field (ie T) and all thermodynamic displacements held constant, except the conjugate to the constant field (S). The expression for each potential is given in Table 7.3.

We are not studying processes, however. We are studying (equilibrium) states in canonical ensembles, in which case all displacements are constant [285, 286].

7.2.8 Equilibrium States in Thermodynamics

In Section 7.2.5, the second law of thermodynamics was written in terms of a thermodynamic process. It states that the entropy of any closed system will increase over time. A consequence of this is that, at equilibrium, entropy will be maximised–this is the principle of maximum entropy. By taking a Legendre transformation of the internal energy, we can write the entropy as a function of the thermodynamic displacements $S \equiv S(U, \{X_i\})$. The maximum entropy principle for an equilibrium state (the point $\mathbf{R}_0 = (U_0, \{X_{i0}\})$) imposes the following mathematical constraints

$$\left.\frac{\partial S}{\partial X_j}\right|_{\mathbf{R}_0} = 0, \qquad \left.\frac{\partial^2 S}{\partial X_j^2}\right|_{\mathbf{R}_0} < 0 \quad \forall j \tag{7.26}$$

The vanishing first derivative ensures there is no thermodynamic field acting on the system, this ensures the state is a local extremum of the entropy but doesn't determine whether this is a maximum or minimum. The second requirement for equilibrium is that the second derivative is negative. This ensures that the entropy surface is concave ie. for any infinitesimal change in a thermodynamic displacement X_1 from the value

X_{10}, given by $X_1 = X_{10} + \delta X_1$ then the entropy at the displaced point must be less than the equilibrium value, $S(X_1 + \delta X_1) < S(X_1)$.

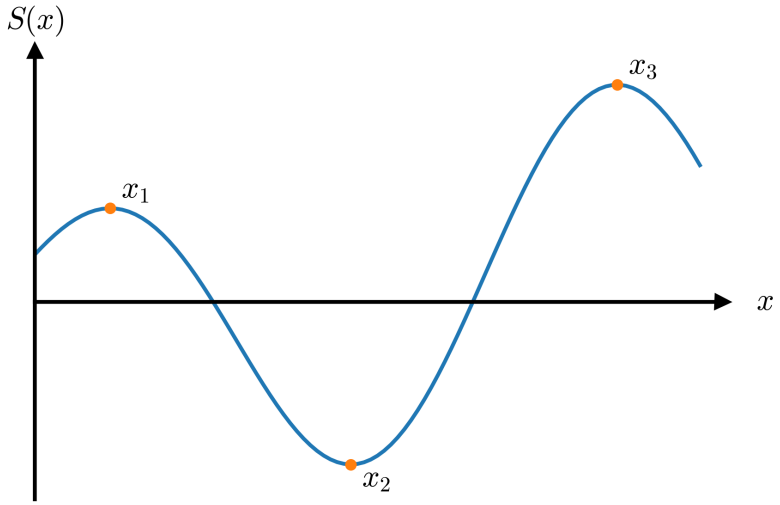

Figure 7.1: A 1-dimensional entropy surface. The points x_1, x_2, x_3 are stationary points. The point x_1 is a local maximum ($S'(x_1) = 0,\ S''(x_1) < 0$) which is sometimes called metastable. The point x_2 is the global minimum ($S'(x_2) = 0,\ S''(x_2) > 0$). The point x_3 is the global maximum ($S'(x_3) = 0,\ S''(x_3) < 0,\ S(x_3) > S(x_1)$). This is the most probable state of the system at this temperature.

We can reframe the principle of maximum entropy as a principle of minimum internal energy. Partial derivatives have the following property

$$\left(\frac{\partial z}{\partial y}\right)_x = -\left(\frac{\partial x}{\partial y}\right)_z \Big/ \left(\frac{\partial x}{\partial z}\right)_y, \tag{7.27}$$

which, along with the relation $\frac{\partial U}{\partial S} = T$ allows us to write

$$\left(\frac{\partial U}{\partial X_1}\right)_{\mathbf{R}_0} = -\left(\frac{\partial S}{\partial X_1}\right)_{\mathbf{R}_0} \Big/ \left(\frac{\partial S}{\partial X_1}\right)_{X_1} = -T\left(\frac{\partial S}{\partial X_1}\right)_{\mathbf{R}_0}. \tag{7.28}$$

A similar processes can be applied to the second derivative with the the negative sign changing the inequality. The principle of minimum energy is then

$$\left.\frac{\partial U}{\partial X_j}\right|_{\mathbf{R}_0} = 0, \qquad \left.\frac{\partial^2 U}{\partial X_j^2}\right|_{\mathbf{R}_0} > 0 \quad \forall j. \tag{7.29}$$

We can immediately write this as the principle of minimum Helmholtz free energy. Since all displacements are held constant except X_1*, any derivative of the internal energy is equal to the derivative of the Helmholtz free energy

$$\begin{aligned}
\left.\frac{\partial U}{\partial X_1}\right|_{\mathbf{R}_0} &= \left.\frac{\partial}{\partial X_1}\left(T\mathrm{d}S + \sum_i Y_i \mathrm{d}X_i \quad \text{and}\right)\right|_{\mathbf{R}_0}, \\
\left.\frac{\partial F}{\partial X_1}\right|_{\mathbf{R}_0} &= \left.\frac{\partial}{\partial X_1}\left(-S\mathrm{d}T + \sum_i Y_i \mathrm{d}X_i\right)\right|_{\mathbf{R}_0} \quad \text{with} \\
\mathrm{d}S = \mathrm{d}T = \mathrm{d}X_i = 0, &\quad \forall i \neq 1
\end{aligned} \tag{7.30}$$

which simplifies to

$$\left.\frac{\partial U}{\partial X_1}\right|_{\mathbf{R}_0} = \left.\frac{\partial F}{\partial X_1}\right|_{\mathbf{R}_0} = Y_1 \tag{7.31}$$

For the free energy, the conditions for equilibrium are

$$\left.\frac{\partial F}{\partial X_j}\right|_{\mathbf{R}_0} = 0, \qquad \left.\frac{\partial^2 F}{\partial X_j^2}\right|_{\mathbf{R}_0} > 0 \quad \forall j. \tag{7.32}$$

Note that, although the second derivatives of the internal and free energies are equal when all other quantities are fixed (denoted by $\mathbf{R}_0$), this assumes that the system is completely isolated. In practice, we are interested in a system which is coupled to a heat bath. When the temperature of the heat bath varies, entropy and other energies are exchanged, so that the second derivatives no longer equate.

7.2.9 Limits of Stability and stationary points

In the above section, the condition for equilibrium was that the second derivative of the bulk free energy with respect to a bulk thermodynamic variable was positive definite. Stable points on the internal energy (temperature not fixed) surface are a very similar concept to equilibrium points. In perfectly isolated systems at fixed temperature, all equilibrium points are stable. But, in general, not all equilibrium points are stable. The concept of stability allows small local fluctuations in macroscopic observables due to the thermodynamic contact of a system with its environment–even in equilibrium as defined by the first law. When close to a phase transition, these fluctuations can cause the spontaneous transition from one phase to another; passing sound through water

*Sometimes we are interested in non-equilibrium states where dS is considerable. Other methods must be when the entropy of the state is large. For magnetic anisotropy, any change is low entropy since exchange brings order to the system.

supercooled to below the freezing temperature 0°C locally changes molecular spacing (even if the global average spacing is constant) which causes the water to spontaneously freeze [287]. The macrostate parameters of the total system were held constant but the transition still occurred because of the local changes. Supercooled water is an example of an unstable equilibrium position.

We can formally derive the condition for stability by a thought experiment. Consider a thermodynamic system which is prepared in some state (a point on the free energy surface, $F(\{X_i\})$) and suppose it is then immediately isolated (parameters $\{X_i\}$ fixed). Now suppose the system is separated into two identical subsystems A and B which are isolated from one another–the typical thought experiment is partitioning a sealed box of gas molecules into two Fig. 7.2 but an equivalent magnetic version is given in Fig. 7.3.

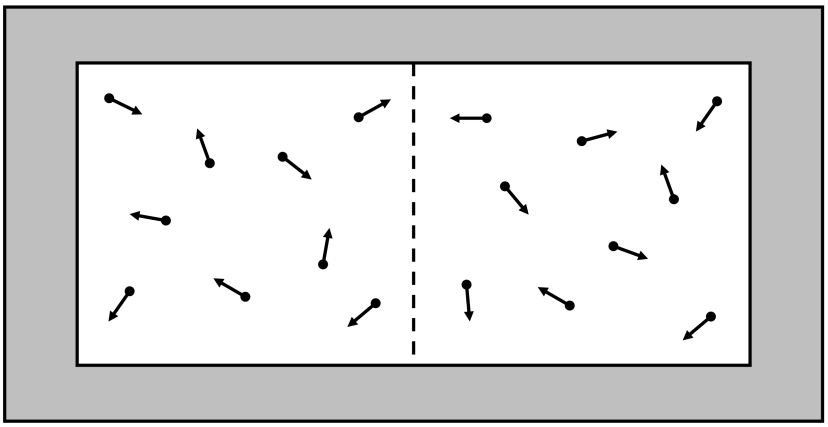

Figure 7.2: A depiction of the stability thought experiment. The grey region is a vacuum, the white region is a perfectly isolated container, points with arrows are indistinguishable gas molecules and their velocity. The black dashed line separating the two sides of the sealed container is a fictitious partition separating the system into two subsystems A (left) and B (right).

Since the subsystems are identical they have the the same macrostate which implies:

1. Both subsystems and the total system are described by the same bulk free energy functional $F_A(\{X_i\}) = F_B(\{X_i\}) = F(\{X_i\})$,

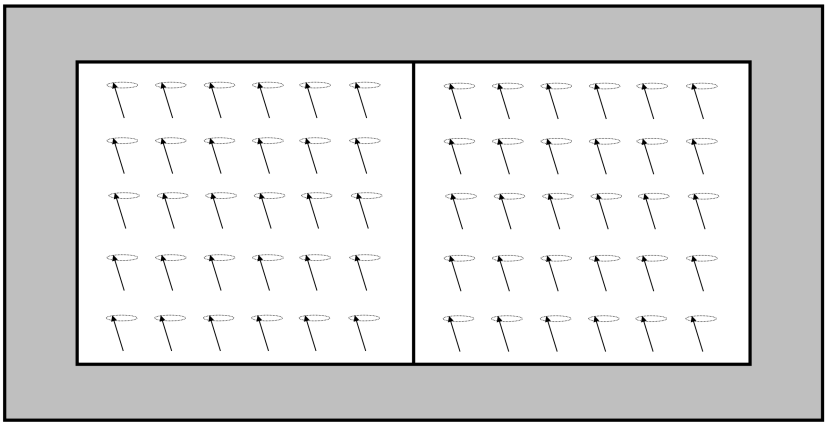

Figure 7.3: Stability thought experiment in a ferromagnet. The grey region is a vacuum, the white region is a perfectly isolated container, arrows are indistinguishable thermal classical magnetic moments (precession given be dashed line). The black dashed line separating the two sides of the sealed container is a fictitious partition separating the system into two subsystems A (left) and B (right).

2. Both subsystems have the same values of macroscopic observables $\{X_{i,A}\} = \{X_{i,B}\} = \{X_{i,0}\}$,

3. Both subsystems have the same value of the free energy $F_A = F_B = F(\{X_{i,0}\})$ and,

4. The total free energy of the system is $F(\{X_i\}) = F(\{X_{i,A}\}) + F(\{X_{i,B}\}) = 2F(\{X_{i,0}\})$.

Now suppose a process p transfers a small amount of a macroscopic parameter $X \in \{X_i\}$ from subsystem A to subsystem B (volume by moving the partition, chemical potential/temperature by Maxwell's daemon, magnetisation by spin current, etc); we can write this process mathematically by $p : (X_A, X_B) \to (X_A - \delta X, X_B + \delta X)$. Since the subsystems are initially identical then $X_A = X_B = X_0$, by applying p to the pair of subsystems (X_A, X_B) we can write $p : (X_A, X_B) \to (X_0 - \delta X,\ X_0 + \delta X)$. If the system is stable then, by the second law, the sum of the free energies of the subsystems after the process must be greater than or equal to the total free energy before the process:

$$F(X_0 - \delta X_0) + F(X_0 + \delta X_0) \geq 2F(X_0) \tag{7.33}$$

If this inequality is not met then removing the partition between the two subsystems

would cause process p (ie crystallisation of H_2O molecules) to continue until a stable equilibrium point is reached (ice). A lack of stability close to phase boundaries is the reason for coexisting phases (ie coexistence of steam and water at 100°C, coexisting hcp and fcc grains in a Co crystal, etc).

Equation (7.33) is the 1-dimensional condition for stability and, in the limit of small fluctuations $\delta X \to 0$, can be written as any point X_0 which satisfies

$$\left.\frac{\partial F}{\partial X}\right|_{X_0} = 0 \quad \text{and} \quad \left.\frac{\partial^2 F}{\partial X^2}\right|_{X_0} \geq 0. \tag{7.34}$$

These conditions are satisfied for any equilibrium macrostate ($F'(X) = 0$, $F''(X) > 0$) and any stationary inflection point ($F'(X) = 0$, $F''(X) = 0$). For any non-isolated system at the limit of stability $\partial_{xx} F = 0$, heat and work can be exchanged with the environment which allows the system to fall into the energy well depicted in Fig. 7.4. Any point $\mathbf{R}'$ such that $\partial_{xx} F(\mathbf{R}') = 0$ is a stationary point and indicates a phase transition.

7.2.10 Energy as a Regular Surface

In the previous sections, the entropy and free energy were called surfaces without justification. A surface is a two-dimensional object in three-dimensional space, higher dimensional surfaces are called manifolds–throughout we will use the term surface to describe a manifold of any dimension for brevity. Writing the bulk internal and free energies as regular parameterised surfaces (sometimes called a Monge patch, or the graph of a function with two variables) allows us to state and apply powerful tools from differential geometry to thermodynamics without proof. A regularly parameterised surface (RPS) M, is a continuous and smooth subset of $\mathbb{R}^3$ which can be written parametrically in the form $M = [u, v, G(u, v)]$. Here, continuous means that there are no holes in the surface and smooth means the surface is infinitely differentiable with respect to u and v at every point $\mathbf{r} = (u, v)$.

The constraint that surfaces must be continuous and continuously differentiable means polar coordinates are usually used so that the graph G can be written in terms

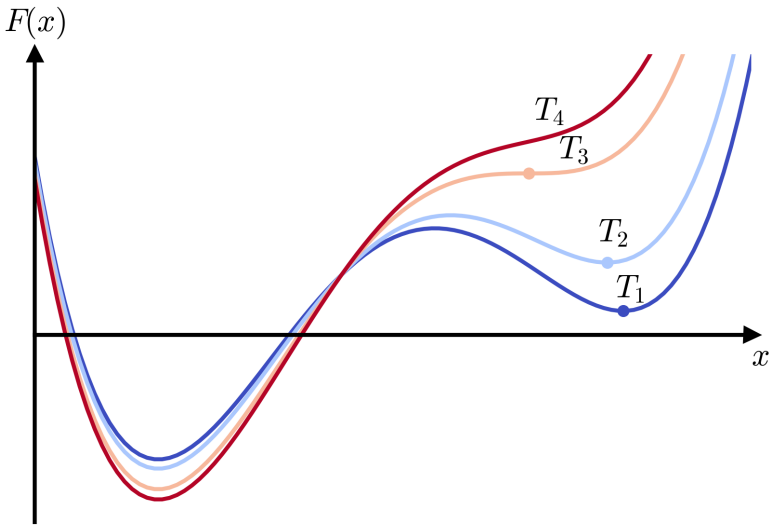

Figure 7.4: The free energy surface of a system that undergoes a first order phase transition at T_3. T_1 is the lowest temperature, the corresponding curve is coloured dark blue, T_4 is the highest temperature, the corresponding curve is dark red. Temperatures T_1, T_2, and T_3 have two equilibria (stationary points) but T_4 only has one. The second equilibrium position is added as a point on the curve. The second equilibrium position at T_3 is an inflection point so it is unstable.

of trigonometric and exponential functions (which are continuous and continuously differentiable). We can write the bulk internal energy of macrospin models of magnetic materials in this form. Let us restrict our thermodynamic system to a canonical ensemble (fixed temperature) of ferromagnetic classical magnetic moments localised on fixed lattice sites (no mechanical degrees of freedom). The order parameter is the magnetisation $\mathbf{M}$ (or sublattice magnetisations $\mathbf{M}_i$) and the thermodynamic displacements are the polar Θ_m and azimuthal Φ_m angles of the reduced magnetisation vector ($\mathbf{m} = \mathbf{M}/|\mathbf{M}|$)*. The thermodynamic field is the effective magnetic field $\mathbf{H}$ (which can include many energy terms). The internal energy surface can be constructed from a single spin Hamiltonian, $\mathcal{H}_i = \mathbf{S}_i \cdot \left(\frac{\partial \mathcal{H}}{\partial \mathbf{S}_i}\right) \equiv \mathcal{H}(\theta_i, \phi_i)$ (the case of spin-spin interactions will be considered later). We can replace the microscopic spin angles θ_i and ϕ_i with bulk order thermodynamic displacements when take the Hamiltonian expectation

*We use the reduced magnetisation as we do not want to convolute the scaling of mean field parameters and the scaling of $M_s(T)$

value. That is, we can write the bulk internal energy as

$$U(\Theta_M, \Phi_m)|_T \equiv \langle \mathcal{H} \rangle|_T (\Theta_M, \Phi_m). \tag{7.35}$$

The bulk internal energy surface at fixed temperature is then $M_U = [\Theta, \Phi, U(\Theta, \Phi)|_T]$. Some results from differential geometry will now be stated for an n-dimensional surface $M = (x_1, ..., x_n, G(x_1, ..., x_n))$. For results which are written for two-dimensional surfaces (ie $G \equiv G(x_i, x_j)$), it is assumed that all x_k, $k \neq i, j$ are fixed.

The connection with constrained Monte Carlo is now clear. Since CMC fixes the magnetisation directions Θ_M and Φ_M, it allows the direct evaluation of $\langle \mathcal{H} \rangle|_{\Theta_M, \Phi_M, T}$. In the original paper by Asselin [38], the torque is connected with the free energy. In Fig. 7.6 we clearly show that, by using CMC, the temperature dependence of the internal energy difference between an easy and hard axis for a uniaxial ferromagnet ($\Delta U(T) = \langle \mathcal{H} \rangle|_{\Theta_M = \pi/2, \Phi_M = 0, T} - \langle \mathcal{H} \rangle|_{\Theta_M = 0, T}$) is identical to the temperature dependence of the torque. The most obvious direction to investigate the discrepancy, is to carefully consider whether the partition function can be written as $Z(q) = \sum_\alpha \exp(-\beta \mathcal{H}(\xi_\alpha, q))$ (equation C1 of [38]). By definition, the partition function is the sum over all possible microstates for all possible macrostates. $Z(q)$ is a subset of the true partition function $Z = \int dq Z(q)$, $Z(q)$ is the sum over all microstates which are in the macrostate q. We make no further attempts to reconcile this contradiction, but the author is confident that the macroscopic torque measured in CMC is related to the internal energy, not the free energy (see Fig. 7.6). Next, we state some properties of surfaces from geometry.

Curvature

Consider a point $\mathbf{r}_0 = (x_0, y_0)$ on an RPS which is given by the graph of $G(x, y)$. The curvature of $G(x, y)$ at the point $\mathbf{r}_0$ along the x-direction is

$$k_x(\mathbf{r}_0) = \left[\frac{\partial^2 G}{\partial x^2} \right]_{\mathbf{r}_0} \tag{7.36}$$

The curvature of $G(x, y)$ at the point $\mathbf{r}_0$ along a generic direction $\hat{\mathbf{n}}$ is

$$k_n = \left[\frac{x_n y_{nn} - x_{nn} y_n}{(x_n^2 + y_n^2)^{3/2}} \right]_{\mathbf{r}_0} \tag{7.37}$$

First Fundamental Form

The first fundamental form $\mathbb{I}$ of an RPS which is given by the graph of $G(x, y)$ is

$$\mathbb{I} = \begin{bmatrix} (1 + G_x^2) & G_x G_y \\ G_x G_y & (1 + G_y^2) \end{bmatrix} \tag{7.38}$$

The determinant of the first fundamental form is $\det(\mathbb{I}) = 1 + G_x^2 + G_y^2$.

Second Fundamental Form

The second fundamental form $\mathbb{II}$ of an RPS which is given by the graph of $G(x, y)$ is

$$\mathbb{II} = \frac{1}{\sqrt{1 + G_x^2 + G_y^2}} \begin{bmatrix} G_{xx} & G_{xy} \\ G_{xy} & G_{yy} \end{bmatrix}. \tag{7.39}$$

The determinant of the second fundamental form is

$$\det(\mathbb{II}) = \frac{1}{\sqrt{1 + G_x^2 + G_y^2}} \left[(G_{xx} G_{yy}) - G_{xy}^2 \right] = \frac{1}{\sqrt{\det(\mathbb{I})}} |D^2 G|, \tag{7.40}$$

where $|D^2 G|$ is the Hessian determinant of G.

Principal Curvatures

The principal curvatures κ_1, κ_2 of $G(x, y)$ at a point $\mathbf{r}_0 = (x_0, y_0)$ are the maximum and minimum values of the curvature. The principal directions $\mathbf{e}_1$, $\mathbf{e}_2$ are the directions of principal curvature. The principal curvatures and principal directions at an equilibrium positions are given by the eigenvalues and eigenvectors of the second fundamental form $\mathbb{II}$.

Gaussian Curvature

Consider a point $\mathbf{r}_0 = (x_0, y_0)$ on an RPS which is given by the graph of $G(x, y)$. The Gaussian curvature $\mathbb{K}(\mathbf{r}_0)$ is the product of the two principal curvatures $\mathbb{K}(\mathbf{r}_0) = \kappa_1 \kappa_2$. Its value is the ratio of the determinants of the second and first fundamental forms which can be simplified to

$$\mathbb{K}(\mathbf{r}_0) = \frac{\det(\mathbb{II})}{\det(\mathbb{I})} = \left[\frac{(G_{xx} G_{yy}) - (G_{xy})^2}{(1 + G_x + G_y)^2} \right]_{\mathbf{r}_0} \tag{7.41}$$

If $\mathbb{K}(\mathbf{r}_0) = 0$ then one or both of the principal curvatures are zero.

Mean Curvature

The mean curvature $\mathbb{H}$ is the average of the two principal curvatures $\mathbb{H} = \frac{1}{2}(\kappa_1 + \kappa_2)$. For a Monge patch, this is given by the following expression

$$\begin{aligned} \mathbb{H} &= \frac{1}{2}\frac{\mathrm{Tr}(\mathbb{I} \circ \mathbb{II}) - \mathrm{Tr}_{\mathrm{asym}}(\mathbb{I} \circ \mathbb{II})}{\det(\mathbb{I})} \\ &= \frac{1}{2}\frac{(1+G_x^2)G_{xx} + (1+G_y^2)G_{yy} - 2G_xG_yG_{xy}}{(1+G_x^2+G_y^2)^{3/2}} \end{aligned} \tag{7.42}$$

7.2.11 Calculating Principal Curvatures

In general, if we are not at an equilibrium position–either by a constraint in an atomistic simulation, or by applying (and then removing) a small magnetic field in an experiment–then the principal curvatures are given, in terms of the mean and Gaussian curvatures $\mathbb{K}$, $\mathbb{H}$, by the following expression

$$\begin{aligned} \kappa_1 &= \mathbb{H} + \sqrt{\mathbb{H}^2 - \mathbb{K}} \\ \kappa_2 &= \mathbb{H} - \sqrt{\mathbb{H}^2 - \mathbb{K}} \end{aligned} \tag{7.43}$$

This contains both first and second derivatives of the free energy surface so any constraint of the system from equilibrium requires the free energy scaling to take into account effective thermodynamic field.

Point on a Surface

Points on a surface can be classified by the gradient and principal curvatures at that point. When studying thermodynamics, the classification of points on an energy surface determine whether that state is an equilibrium state and its stability.

A stationary point is a point $vecr_0$ on a surface $G(x, y)$ which has vanishing gradient $\nabla G_{\mathbf{r}_0} = \mathbf{0}$. In this case, the first fundamental form reduces to the identity matrix and the second fundamental form reduces to the Hessian matrix. Points on surfaces can be further classified by the values of the principal curvatures. We are only interested in a few cases

Case 1: $\kappa_1 < 0, \quad \kappa_2 < 0$

Points where both principal curvatures are negative are called concave–if you travel along the surface in any direction, the value of $\nabla G(x, y)$ will decrease.

Additionally if the point is a stationary point $\nabla G = \mathbf{0}$, then the point is a maximum. Moving along any direction will decrease the value of G. If the point is stationary and both principal curvatures are negative and of equal size $\kappa_1 = \kappa_2$, then the maxima are symmetric ie $G(x_0 \pm \epsilon, y_0) = G(x_0 \mp \epsilon, y_0) = G(x_0, y_0 \pm \epsilon)$ and the same is true of the gradient, an example is the [111] direction ($\equiv$ ($\theta = \cos^{-1}(1/\sqrt{3})$, $\phi = \pi/4$)) on the surface of a first order cubic anisotropy $f(\theta, \phi) = \sin^2\theta\cos^2\theta + \sin^4\theta\sin^2\phi\cos^2\phi$.

Case 2: $\kappa_1 = 0, \quad \kappa_2 < 0$

This point has constant gradient along the e_1 direction and the gradient decreases along the e_2 direction. If the point is a stationary point, then $G(x, y)$ is constant along e_1 and decreases along e_2. This is the case for any point on the outer surface of a tube.

Case 3: $\kappa_1 = 0, \quad \kappa_2 = 0$

This point is either any point on a surface which can be parameterised as a plane ie the surface of a sphere.

Case 4: $\kappa_1 > 0, \quad \kappa_2 = 0$

The classification of this point reads the same as *Case 2*, replacing 'decreases' with 'increases'. An example is any point on the inner surface of a tube.

Case 5: $\kappa_1 > 0, \quad \kappa_2 > 0$

These points are convex. The gradient along any direction increases. If the point is also stationary, this is a minimum point. On a free energy surface, these points are local equilibria. An example is any point $\mathbf{r} = (0\phi)$ on the surface a first order cubic anisotropy.

Case 6: $\kappa_1 < 0, \quad \kappa_2 > 0$

When the principal curvatures have opposite sign, the gradient increases in one direction and decreases in another. If this point is also a stationary point, then this is a saddle point (minimum in one direction, maximum in the other). An example is the [110] direction ($[110] \equiv (\theta = 0, \phi = \pi/2)$) on the surface of a first order cubic anisotropy.

These are summarised in Table 7.4

Table 7.4: Classification of points on a surface by their principal curvatures.

	$\kappa_1 < 0$	$\kappa_1 = 0$	$\kappa_1 > 0$
$\kappa_2 < 0$	Concave ellipsoid	Concave cylinder	Hyperboloid
$\kappa_2 = 0$	Concave cylinder	Plane	Convex cylinder
$\kappa_2 > 0$	Hyperboloid	Convex cylinder	Convex ellipsoid

7.3 Bulk Internal Energy Scaling

The literature in magnetism has never been very clear on what is meant by the 'free energy scaling' of material parameters, primarily because the thermodynamics of magnetism is difficult*. From thermodynamics we understand that entropy prevents us from extracting all of the available (internal) energy in a steam engine and that the energy which can be extracted is the free energy, but this doesn't translate well to magnetic systems. It is plausible to imagine extracting energy from domain walls or skyrmions in a ferromagnet by converting the time dependent dipole field into an electric current, so the extracted electrical power must be related to the free energy of a domain wall. However, the thought experiment doesn't translate well to spintronic devices that make use of quasiparticle excitations like magnons. The question of whether domain wall widths are related to free energies or internal energies is even more confusing. Regardless, we derive expressions for the internal energy scaling of macroscopic properties in Section 7.3.1 and by using the Gibbs-Helmholtz equation (7.73) we can easy

*The author has been dissuaded from this avenue of study at more than one conference

calculate the temperature dependence of free energies from internal energies.

Akulov's simple method of projecting equilibrium fluctuations around the z-direction of a cubic ferromagnet onto the maxima along [111] and [101] gives us a hint about something more fundamental about the free energy scaling of bulk material properties using the fluctuations (entropy) calculated from microscopic considerations. Akulov's method is attractive because simple expectation values are easy to calculate and are independent of the numerical method used. This would mean we can use advanced semi-classical dynamical methods [132] (Section 5.1) which more accurately calculates the temperature scaling of the order parameter so the validity of using a Callen-Zener magnetisation scalings and Bloch's law can be verified. These dynamical methods are very attractive from the view of computation as well; they are embarrassingly parallel algorithms that work best on GPUs. Constrained Monte Carlo, on the other hand, cannot be parallelised so calculating the bulk free energy scaling of any large system with dipole-dipole interactions is computationally very difficult. It also means we can calculate the temperature scaling of non-local interactions such as exchange, DMI and dipole-dipole interactions which cannot be written as a simple power of the magnetisation. As we will show in this section, Akulov's method doesn't work for most cases, only first order uniaxial and first order cubic anisotropies coincide with the stability coefficients and Callen-Zener theory. Outside of magnetism, the use of stability coefficients is commonplace [265, 270, 288–290] but the connection between stability coefficients and statistical mechanics (ie simulations) in any field has been missed. We develop this here so that no complicated sampling methods are required to calculate the temperature dependence of macroscopic models.

7.3.1 Stability Coefficients

There have been many attempts to calculate the scaling of micromagnetic and mean-field properties of magnetic materials from ensemble methods. But these methods don't employ the standard tools from thermodynamics which are used in other areas of physics (molecular dynamics, astrophysics and fluids) [273, 291–293]. This is because thermodynamic theory isn't usually written in terms of magnetism. The literature which does consider magnetism is in the context of macroscopic ferromagnets–bar magnets in solenoids, the effect of bulk magnetostriction on mechanical properties–or focuses on Landau

theory which does consider microscopic degrees of freedom and is only applicable near the critical temperature. None of these are very easily applicable to modern magnetism thin film ferromagnetism or multisublattice magnetism. Additionally Landau theory is of little interest to modern researchers that want to investigate properties of devices far below the critical temperature. So, much of the knowledge of the applicability of thermodynamics in magnetism has been lost, or is considered niche in the wider community.

The tools which are used extensively in molecular dynamics and astrophysics come from thermodynamics and statistical mechanics, and can be used on any system of any arbitrary constituent objects. In addition, the description of curvatures of the preceding section did not limit which points on the surface we were considering. This means we can use those expressions to calculate both equilibrium and non-equilibrium thermal stability of different bulk internal energies.

Thermodynamic stability measures more than simply the point at which a phase transition occurs, it also measures the relative stability of an equilibrium state–the internal energy scaling of a mean-field parameter in an equilibrium position. The second derivative of the internal energy with respect to an order parameter is known as a stability coefficient [265]. For equilibrium states at zero temperature, it has a singular positive value and decreases monotonically until the critical temperature. At the critical temperature, the bulk internal energy landscape becomes flat with respect to the mean-field parameter and increasing the temperature further has no effect because the order parameter vanishes. These properties are the exact requirements for a 'proper' metric with which to parameterise a macroscopic description of a microscopic system (macrospin models, micromagnetism, etc).

In general, stability coefficients can be measured with respect to an arbitrary number of variables. To calculate multi-variable stabilities, we must use the framework developed in section 7.2.11. A multivariable stability coefficient is given by the equation for the principal curvatures (7.43). Sometimes, we do not want the scaling along the direction of maximum curvature. Instead, transitions between different magnetisation states are usually along paths of minimum curvature. For a rank-4 cubic anisotropy, switching occurs via the $\langle 110 \rangle$ directions, not the $\langle 111 \rangle$ directions because the energy

barrier (and curvature) are lower. In general, the scaling along different directions are not equal–the internal energy landscape does not scale uniformly when thermal fluctuations are added to the system. In condensed matter, we parameterise the magnetisation by the the angles Θ and Φ on the unit sphere. So, for now, we will limit ourselves to the two-variable stability coefficients. The bulk internal energy scaling of a macroscopic parameter $K(T)$ is given by the ratio of the stability coefficient Υ* at temperature T and temperature $T = 0$

$$K(T) = K(0)\ \frac{\Upsilon_K(T)}{\Upsilon_K(0)}, \tag{7.44}$$

where angle brackets denote thermal averaging and the subscript K means that Υ_K is the stability coefficient of the bulk internal energy term which contains K. All stability coefficients can be written as the expectation value of magnetic moments in equilibrium. Using an atomistic method based on a canonical ensemble, the vectors of all spins can be accessed. So a stability coefficient can always be measured–the internal energy scaling with respect to temperature. Although, for studying the temperature dependence of mean-field parameters in textures like domains which are non-equilibrium states with respect to exchange (they minimise the stray field in FMs so are equilibrium states of real systems) then the internal energy difference must be calculated using different methods. This is because the entropy of a twisted state and a homoegeneous state differ. This is not included in the calculation of a stability coefficient. Instead the internal energy difference $\Delta U(T)$ due to the thermodynamic displacement X_1 between the equilibrium position $\mathbf{r}_0$ and a non-equilibrium position $\mathbf{r}'$ is given by

$$\frac{\Delta U(T, X_1)}{\Delta U(0, X_1)} = \left[\frac{\partial^2 U(T, \mathbf{r}')}{\partial^2 X_1} - \frac{\partial^2 U(T, \mathbf{r}_0)}{\partial^2 X_1}\right] \Bigg/ \left[\frac{\partial^2 U(0, \mathbf{r}')}{\partial^2 X_1} - \frac{\partial^2 U(0, \mathbf{r}_0)}{\partial^2 X_1}\right]. \tag{7.45}$$

As an example, consider the case of an easy-axis uniaxial ferromagnet which has the following Hamiltonian

$$\mathcal{H} = -\frac{1}{2}\sum_{i,j} J_{ij}\mathbf{S}_i \cdot \mathbf{S}_j - K_0 \sum_i (\mathbf{S}_i \cdot \hat{\mathbf{z}})^2, \tag{7.46}$$

where J_{ij} is the exchange interaction, $\mathbf{S}_i$ is the classical spin unit vector of spin i, and K_0 is the uniaxial anisotropy constant (the subscript 0 denotes the microscopic parameter).

*The symbol Υ is chosen to match the helicity modulus used in previous literature and originates from the symbol for surface tension (γ) used in older thermodynamics literature [288].

For a macrospin model, the bulk internal energy only has one term–a macrospin can only have a single value of the magnetisation vector (unlike micromagnetism). The bulk internal energy is then

$$U(\Theta, \Phi, T) = \langle \mathcal{H} \rangle(\Theta, \Phi) = -K(T)\cos^2(\Theta). \tag{7.47}$$

The second derivative of the internal energy with respect to Θ–assuming the magnetisation is in equilibrium so the first derivatives can be ignored–is then

$$\frac{\partial^2 U}{\partial \Theta^2} = 2K(T)\left[\cos^2(\Theta) - \sin^2(\Theta)\right], \tag{7.48}$$

which can be written in terms of the microscopic variables as

$$\begin{aligned} \frac{\partial^2 \mathcal{H}}{\partial \Theta^2} &= 2K_0 \left\langle [\cos^2(\theta) - \sin^2(\theta)] \right\rangle \\ &= 2K_0 \left\langle [(\mathbf{S}\cdot\hat{\mathbf{z}})^2 - |\mathbf{S}\times\hat{\mathbf{z}}|^2] \right\rangle \\ &= 2K_0 \left\langle (\mathbf{S}\cdot\hat{\mathbf{z}})^2 - \left[(\mathbf{S}\cdot\hat{\mathbf{x}})^2 + (\mathbf{S}\cdot\hat{\mathbf{y}})^2\right] \right\rangle. \end{aligned} \tag{7.49}$$

The final step shows that we must to choose from two orthogonal paths. This is important because, at the microscopic level, a magnetic moment given by $\mathbf{S} = [\frac{1}{\sqrt{2}}\delta, \frac{1}{\sqrt{2}}\delta, 1-\delta_z]$ contributes equally to the path which passes through $\hat{\mathbf{x}}$ and the path which passes through $\hat{\mathbf{y}}$. Ignoring the orthogonality of the directions $\hat{\mathbf{x}}$ and $\hat{\mathbf{y}}$ would reduce this 3-dimensional energy surface to a 2-dimensional one–even though fluctuations are 3-dimensional. Now, using the Cartesian basis, let's choose the path from $+\hat{\mathbf{z}}$ to $-\hat{\mathbf{z}}$ which passes through $\hat{\mathbf{x}}$ ($\Phi = 0$) so the term $(\mathbf{s}\cdot\hat{\mathbf{y}})$ does not contribute to the internal energy scaling along the orthogonal path. The stability coefficient Υ along the path $\Phi = 0$ is then

$$\Upsilon(T)|_{\Phi=0} = 2K_0 \left\langle (\mathbf{S}\cdot\hat{\mathbf{z}})^2 - (\mathbf{S}\cdot\hat{\mathbf{x}})^2 \right\rangle. \tag{7.50}$$

Since the ferromagnet is isotropic in the xy-plane, the stability coefficient along any path is given by

$$\Upsilon(T) = 2K_0 \left\langle (\mathbf{S}\cdot\hat{\mathbf{z}})^2 - \frac{1}{2}|\mathbf{S}\times\hat{\mathbf{z}}|^2 \right\rangle. \tag{7.51}$$

This is then normalised to zero temperature giving

$$\frac{K(T)}{K(0)} = \left\langle (\mathbf{S}\cdot\hat{\mathbf{z}})^2 - \frac{1}{2}|\mathbf{S}\times\hat{\mathbf{z}}|^2 \right\rangle. \tag{7.52}$$

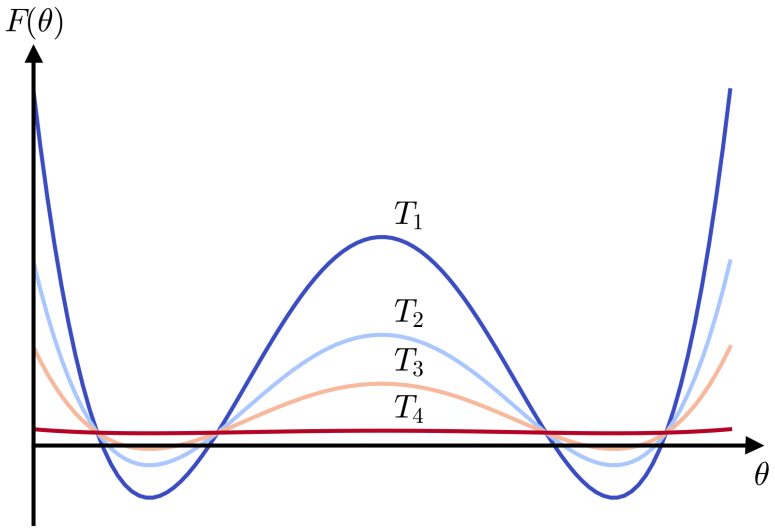

Figure 7.5: Illustration of internal energy surface of a uniaxial anisotropy at various temperatures. The anisotropy is given by the internal energy function (7.47) where Θ is the polar angle of the order parameter. The two minima are the points $\Theta = 0$ and $\Theta = \pi$ (or $\mathbf{m} = \hat{\mathbf{z}}$ and $\mathbf{m} = -\hat{\mathbf{z}}$). $T_1 = 0$, $T_4 \approx T_c$, and $T_1 < T_2 < T_3 < T_4$. The curvature of the internal energy surface is greatest for $T = 0$ and becomes flat (vanishing curvature) at $T = T_c$.

We can now calculate the bulk internal energy scaling of the uniaxial anisotropy in terms of expectation values of the microscopic parameters which accounts for the curvature of the uniaxial energy surface. This should be calculated in equilibrium using common tools like Metropolis Monte Carlo or atomistic spin dynamics and doesn't require the use of complex methods like constrained Monte Carlo or meta-dynamics [38, 294]. We can now see the connection with both Akulov's method (see Section 7.1) and the Callen-Zener theory. In the former, the equilibrium fluctuations ($\langle \cos^2 \theta \rangle$) are projected onto a hard direction ($\langle \sin^2 \theta \rangle$) and the difference between these energies is taken as the bulk internal energy scaling. Callen-Zener theory integrates the equilibrium fluctuations over the anisotropy surface. Since these both use equilibrium fluctuations, there is no change in entropy so they are calculating the internal energy scaling of the equilibrium position. We reiterate that Akulov's approach this is a crude approximation of the curvature and only works for specific edge cases like this one.

7.3.2 Exchange

Unlike magnetocrystalline anisotropy, there is some literature on the stability coefficient of exchange. In older literature, this is called the helicity modulus or spin stiffness [246–255]. Each of the previous references use different definitions of the spin stiffness and obtain different expressions for the same quantity. It was noted in 1999 that there are two definitions of the helicity modulus [295]. The original definition of the helicity modulus is described in the language of Bose superfluids in equilibrium. Bose superfluids are uniform boson gases in which have undergone condensation. This exactly describes a uniform ferromagnet in which all magnons are in the $\mathbf{k} = 0$ state. The requirement of uniformity and Bose-Einstein condensations means this cannot describe a ferromagnet with antiperiodic boundary conditions. A ferromagnet with antiperiodic boundaries would contain both $\hat{S} = 1$ and $\hat{S} = -1$ magnons on either side of the domain wall, violating the requirement of a Bose condensate. Instead it measures the collective phase of the Bosons at low temperature–it is the second derivative of the Hamiltonian with respect to the wavevector of a boson (magnon), in the limit that the spin wave vector goes to zero $\frac{\partial^2 (hf_k)}{\partial k^2}\Big|_{k\to 0}$ [246]. This is, by definition, the spin wave stiffness. The authors of the original paper weren't consistent in their definition of the helicity modulus as they didn't consider this distinction. So, the superfluid density was used to describe the difference between periodic and antiperiodic boundary conditions. This mistake created the confusion and conflicting expressions for the helicity modulus in the literature. It was also a large source of confusion for the author while developing the above thermodynamic methods for magnetism. So, while the helicity modulus is often used to describe the free energy penalty due to exchange of adding a domain to the spin system, in most cases, the expression is simply the spin wave stiffness. This is not the quantity that many set out to measure–the finite temperature scaling of the exchange stiffness is distinct from this. The temperature scaling of the spin wave stiffness describes a macrospin model of dynamics with a fundamentally different internal energy functional. In this picture, the stability coefficient for spin wave stiffness is a chemical potential for spin waves, it answers the question "How much energy will it cost to create a $\mathbf{k} = 0$ spin wave in a uniform ferromagnet which contains $\langle n_{\mathbf{k}} \rangle_T$ thermal spin waves?". This macroscpin model does not allow twists which are static textures

in magnetisation in space so cannot represent the temperature dependence of exchange stiffness.

Instead, the energy functional which is used in continuum methods like micromagnetism, and which defines the exchange stiffness, is a second order multipolar (Taylor) expansion of the exchange interaction* which introduces the required spatial degrees of freedom into the space independent Heisenberg Hamiltonian†. The relevant stability coefficient answers questions like "In a uniform ferromagnet magnetised along $\hat{\mathbf{z}}$, how much energy does it cost it to add an infinitesimal twist to the magnetisation from the z-direction towards the y-direction which propagates along the x-direction?". The energy function due to exchange in a continuum model is given by

$$E(T) = \int_V \mathrm{d}^3\mathbf{r} \;\; A^{\alpha\beta}(T) \left(\frac{\partial \mathbf{m}(\mathbf{r})}{\partial r_\alpha}\right) \cdot \left(\frac{\partial \mathbf{m}(\mathbf{r})}{\partial r_\beta}\right) \tag{7.53}$$

where $\mathbf{r}$ is the position in the continuum field, α and β are Cartesian indices, the integral is over the volume V of the magnetic system, $\mathbf{m}(\mathbf{r})$ is the unit magnetisation field, and $A^{\alpha\beta}(T)$ is the finite temperature exchange stiffness. Einstein summation of Cartesian indices is assumed. The zero temperature expression for exchange stiffness can be found by taking the second order multipolar expansion of the Heisenberg exchange Hamiltonian. The first step is to rewrite the dot product of two spins, which is defined by four angles θ_i, ϕ_i, θ_j, and ϕ_j, as a single vector which corresponds to the angular deviation of the two spins from parallel

$$\begin{aligned} \mathcal{H} &= -\frac{1}{2}\sum_{ij} J_{ij}\mathbf{S}_i \cdot \mathbf{S}_j \\ &= -\frac{1}{2}\sum_{ij} J_{ij}(\mathbf{S}_i \cdot \mathbf{S}_j) \\ &= -\frac{1}{2}\sum_{ij} J_{ij}[1 - \frac{1}{2}(\boldsymbol{\Delta}\mathbf{S}_{ij}) \cdot (\boldsymbol{\Delta}\mathbf{S}_{ij})], \end{aligned} \tag{7.54}$$

*The first order multipole expansion uniquely vanishes in equilibrium everywhere except at interfaces and surfaces.

†Interaction vectors are not necessary to completely define the Heisenberg Hamiltonian, only a set of interaction indices is required and the magnetic moments can exist anywhere in space without changing the Hamiltonian energy. Of course, real systems must be crystalline.

where $\Delta\mathbf{S}_{ij}$ can be written in a few different forms

$$\begin{aligned}\boldsymbol{\Delta}\mathbf{S}_{ij} &= (\mathbf{S}_j - \mathbf{S}_i) \\ &= [\sin(a_{ij}),\ \sin(b_{ij}),\ \sin(c_{ij})] \\ &= [\hat{\mathbf{x}}\cdot(\mathbf{S}_i\times\mathbf{S}_j),\ \hat{\mathbf{y}}\cdot(\mathbf{S}_i\times\mathbf{S}_j),\ \hat{\mathbf{z}}\cdot(\mathbf{S}_i\times\mathbf{S}_j)]\,,\end{aligned} \tag{7.55}$$

and, a_{ij}, b_{ij}, and c_{ij} are the yaw, pitch, and roll angles between spins $\mathbf{S}_i$ and $\mathbf{S}_j$*. This is an exact expansion of the dot product. The next step is to add the interaction vector for the second order multipole expansion of the discrete system

$$\mathcal{H} = -\frac{1}{2}\sum_{ij}\sum_{\alpha,\beta=x,y,z} J_{ij}\left[1 - \frac{1}{2}\left(\frac{\partial\mathbf{S}_{ij}}{\partial r_{ij}^{\alpha}}\right)\cdot\left(\frac{\partial\mathbf{S}_{ij}}{\partial r_{ij}^{\beta}}\right) r_{ij}^{\alpha} r_{ij}^{\beta}\right], \tag{7.56}$$

where $\mathbf{r}_{ij} = \mathbf{r}_j - \mathbf{r}_i$. The derivatives in the above equation are simple finite differences due to the discrete nature of the system. We retain them here because it makes the process of coarse graining when moving to micromagnetism clear. The above Hamiltonian contains a constant energy offset. We can remove this and write the interacting part of the exchange Hamiltonian as

$$\mathcal{H}_{\text{int}} = \frac{1}{4}\sum_{ij}\sum_{\alpha,\beta=x,y,z} J_{ij}\ r_{ij}^{\alpha} r_{ij}^{\beta}\left(\frac{\partial\mathbf{S}_{ij}}{\partial r_{ij}^{\alpha}}\right)\cdot\left(\frac{\partial\mathbf{S}_{ij}}{\partial r_{ij}^{\beta}}\right). \tag{7.57}$$

Information about thermal fluctuations, and magnetisation textures like domains and other nonuniformities is contained within the spin vectors $\mathbf{S}_i$. In micromagnetism, the Hamiltonian is replaced with a temperature-free energy functional (F, U, or simply E), summations over spin vectors are replaced with integrals over the volume of the magnetic material V, and derivatives of the discrete spin vectors are replaced with the derivative of a continuous magnetisation field $\frac{\partial\mathbf{S}_{ij}}{\partial\mathbf{r}_{ij}} \rightarrow \frac{\partial\mathbf{m}(\mathbf{r})}{\partial\mathbf{r}}$ which allows the coarse graining required for simulations of μm devices. Applying this transformation from microscopic Hamiltonian to macroscopic energy functional gives

$$E(\mathbf{m}(\mathbf{r})) = \int_V d\mathbf{r}^3 \sum_{\alpha,\beta=x,y,z}\left[\frac{1}{N\nu_{\text{WS}}}\sum_{ij} J_{ij} r_{ij}^{\alpha} r_{ij}^{\beta}\right]\left(\frac{\partial\mathbf{m}(\mathbf{r})}{\partial r^{\alpha}}\right)\cdot\left(\frac{\partial\mathbf{m}(\mathbf{r})}{\partial r^{\beta}}\right), \tag{7.58}$$

where N is the number of spins in the system, and ν_{WS} is the Wigner-Seitz volume. The factor in square brackets contains a summation over the discrete lattice. This allows

*These angles are loosely related to direction cosines by $\alpha_1 = \cos\left(\frac{a_{ij}}{|a_{ij}|}\right)$, $\alpha_2 = \cos\left(\frac{b_{ij}}{|b_{ij}|}\right)$, and $\alpha_3 = \cos\left(\frac{c_{ij}}{|c_{ij}|}\right)$

the macroscopic energy to be parameterised from the zero temperature microscopic model; it defines the zero temperature exchange stiffness tensor $A^{\alpha\beta}(T=0)$ which is written as

$$A^{\alpha\beta}(0) = \frac{1}{4}\frac{1}{N\,\nu_{\mathrm{WS}}}\sum_{i,j} J_{ij}\, r_{ij}^{\alpha}\, r_{ij}^{\beta}. \tag{7.59}$$

Replacing the lattice sum in the free energy function for the exchange stiffness tensor gives

$$E(\mathbf{m}(\mathbf{r})) = \int_V d\mathbf{r}^3 \sum_{\alpha,\beta=x,y,z} A^{\alpha\beta}\left(\frac{\partial \mathbf{m}(\mathbf{r})}{\partial r^{\alpha}}\right)\cdot\left(\frac{\partial \mathbf{m}(\mathbf{r})}{\partial r^{\beta}}\right), \tag{7.60}$$

We can now use the continuum energy functional and interaction Hamiltonian to calculate the stability coefficient of the exchange stiffness for Bloch-type twists*. Since the exchange stiffness measures the energy cost of putting a twist into a continuous magnetisation field, the stability coefficient calculation must include both the propagation vector and the twist angle. So, instead of applying simple derivatives, we instead wish to apply operations of the form $\frac{k^{\alpha} r_{ij}^{\alpha}}{|\mathbf{k}\cdot\mathbf{r}_{ij}|}\frac{\partial}{\partial \Delta S_{ij}^{\alpha}}$ where $\mathbf{k}$ is the unit propagation vector of the magnetisation twist of interest. The prefactor $\frac{k^{\alpha} r_{ij}^{\alpha}}{|\mathbf{k}\cdot\mathbf{r}_{ij}|}$ is unitless and normalised. It allows us to distinguish between pairs of spins which have a displacement vector parallel to the propagation vector from those which are perpendicular (so shouldn't contribute to the observable). The derivative $\frac{\partial}{\partial \Delta S_{ij}^{\alpha}}$ measures the deviation between neighbour spins in the direction parallel α. We can rewrite the prefactor using delta-like functions $\delta(\alpha) = \frac{k^{\alpha}\Delta r_{ij}^{\alpha}}{|\mathbf{k}\cdot\mathbf{r}_{ij}|}$. Using this, the stability coefficients for the exchange stiffness tensor which are sensitive to the temperature dependence of Bloch walls are given by

$$\Upsilon^{\alpha\beta}(T) = \left\langle \delta(\alpha)\delta(\beta)\frac{\partial^2 \mathcal{H}}{\partial \Delta S_{ij}^{\alpha}\,\partial \Delta S_{ij}^{\beta}}\right\rangle \tag{7.61}$$

The simplest micromagnetic models use diagonal exchange stiffness tensors so we give these terms here. We choose to write the stability coefficients in terms of the spin deviation angles a_{ij}, b_{ij}, c_{ij}

$$\Upsilon^{xx}(T) = \left\langle \frac{\partial^2 \mathcal{H}}{\partial^2 \Delta S_{ij}^{x}}\right\rangle = \left\langle \frac{\partial^2 \mathcal{H}}{\partial^2 a_{ij}}\right\rangle = \left\langle \sum_{ij} J_{ij}\delta(x)\left[\sin^2(a_{ij}) - \cos^2(a_{ij})\right]\right\rangle. \tag{7.62}$$

*Néel twists have different expressions for the exchange stability coefficients because the propagation vector and twist direction are perpendicular. In simple magnets without DMI, these will coincide but is an important detail for skyrmion research.

The temperature dependence of the diagonal components of the exchange stiffness tensor are then

$$\begin{aligned}
\frac{A^{xx}(T)}{A^{xx}(0)} &= \left\langle \sum_{ij} J_{ij}\delta(x)\left[\sin^2(a_{ij}) - \cos^2(a_{ij})\right]\right\rangle \Bigg/ \left(\sum_{ij} J_{ij}\delta(x)\right) \\
\frac{A^{yy}(T)}{A^{yy}(0)} &= \left\langle \sum_{ij} J_{ij}\delta(y)\left[\sin^2(b_{ij}) - \cos^2(b_{ij})\right]\right\rangle \Bigg/ \left(\sum_{ij} J_{ij}\delta(y)\right) \\
\frac{A^{zz}(T)}{A^{zz}(0)} &= \left\langle \sum_{ij} J_{ij}\delta(z)\left[\sin^2(c_{ij}) - \cos^2(c_{ij})\right]\right\rangle \Bigg/ \left(\sum_{ij} J_{ij}\delta(z)\right).
\end{aligned} \tag{7.63}$$

It is more intuitive to work with spin vectors rather than spin deviation angles. Transforming back to spin vectors, these are

$$\begin{aligned}
\frac{A^{xx}(T)}{A^{xx}(0)} &= \frac{1}{\sum_{ij} J_{ij}\delta(x)}\left\langle \sum_{ij} J_{ij}\delta(x)\left[(S_i^y S_j^z - S_i^z S_j^y)^2 - (S_i^z S_j^z + S_i^x S_j^x)^2\right]\right\rangle \\
\frac{A^{yy}(T)}{A^{yy}(0)} &= \frac{1}{\sum_{ij} J_{ij}\delta(y)}\left\langle \sum_{ij} J_{ij}\delta(y)\left[(S_i^z S_j^x - S_i^x S_j^z)^2 - (S_i^z S_j^z + S_i^y S_j^y)^2\right]\right\rangle \\
\frac{A^{zz}(T)}{A^{zz}(0)} &= \frac{1}{\sum_{ij} J_{ij}\delta(z)}\left\langle \sum_{ij} J_{ij}\delta(z)\left[(S_i^x S_j^y - S_i^y S_j^x)^2 - (S_i^x S_j^x + S_i^y S_j^y)^2\right]\right\rangle
\end{aligned} \tag{7.64}$$

These expressions explicitly measure the finite temperature scaling of the exchange stiffness in ferromagnetic systems which host Bloch domain walls in the equilibrium state. Similar expressions can be obtained for Néel-type twists to the magnetisation where the propagation vector and magnetisation twist direction are perpendicular. This is strictly valid for domain walls of infinite length. For very tight domain walls, the contribution to the free energy scaling due to the non-equilibrium entropy difference between the twisted and homogeneous states (dS) will be large. Using the Gibbs-Helmholtz equation to calculate the temperature dependence of the free energy allows the entropy difference in the homogeneous state at different temperatures to be inferred; it cannot calculate the entropy difference between a homogeneous state and highly non-equilibrium state (unless the internal energy difference between these states is measured). The approximate entropy contribution can be investigated by measuring the magnetisation within a domain wall, an idea which is similar to the work of Atxitia [261]. The magnetisation is a very good proxy for the entropy. The Boltzmann entropy expression, $S = k_B \ln(\Omega)$, includes the number of microstates for a given macrostate, Ω. And, although Ω is infinite in a classical three-dimensional Heisenberg model, it is proportional to the radius

of the cone that the magnetisation makes with the quantisation axis. So, the difference between the saturation magnetisation of a homogeneous ferromagnet $m_z(T)$ can be compared with the average saturation magnetisation within a domain wall which can be calculated using a rotating reference frame $m_u(T) = \sum_i \mathbf{m}(x_i) \cdot \mathbf{u}(x_i)$, where x_i are the discrete positions in the ferromagnet along the propagation vector of the domain, $\mathbf{m}(x_i)$ is the magnetisation of the layer of spins located at x_i, and $\mathbf{u}(x_i) = \frac{\mathbf{m}(x_i)}{|\mathbf{m}(x_i)|}$ is the quantisation axis for the magnetisation in the layer of spins at x_i*.

7.3.3 Comparison with constrained Monte Carlo

Constrained Monte Carlo (CMC) [38] calculates the temperature scaling of internal energy differences between different points on the internal energy surface by calculating average macroscopic torques (proportional to the first derivative of the internal energy) by fixing the order parameter direction to a non-equilibrium direction. CMC can be used for all constraints on the order parameter but in equilibrium positions the torque vanishes at all temperatures. The macroscopic torque surface is flat (zero torque for all order parameter constraints) above the critical temperature in systems which undergo a second order phase transition. When applied to magnetism, CMC is almost equivalent to the stability coefficient method of calculating bulk free energy parameters for all single-ion, local Hamiltonian terms (magnetocrystalline anisotropies), and any non-local Hamiltonian terms which do not induce magnetic order on their own (dipole-dipole interactions, two-ion anisotropies). But constrained Monte Carlo cannot calculate the temperature scaling of Heisenberg exchange, DMI or higher order exchange terms (such as biquadratic exchange).

There is another way of using constrained Monte Carlo. Instead of running a single simulation along a direction of maximum torque, you can run two simulations, one which constrains the order parameter along an easy direction, another along a hard direction. This is a direct calculation of the barrier between two adjacent easy axes (ie a numeric verification of Akulov's method). A visualisation of the different points on

*In simulations $|\mathbf{m}(T)|$ is not the correct magnetisation. Bloch's law and the quantum nature of magnetism requires a quantisation axis along which the magnetisation must be measured. So, $m_z(T)$ should be used in the bulk and $m_u(T)$ should be used in the domain walls.

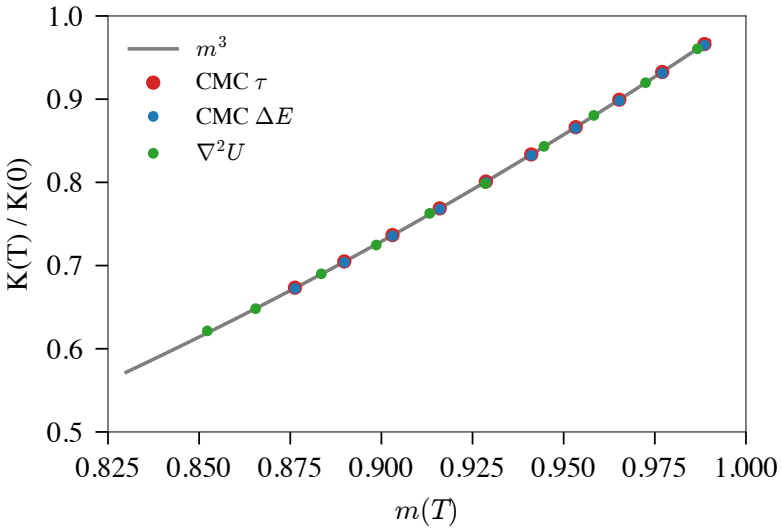

Figure 7.6: Comparison of the finite temperature scaling of the effective anisotropy in a mean field model of a uniaxial ferromagnet using two different methods of constrained Monte Carlo, and the stability coefficient method here.

the internal energy surface that each of these methods samples is given in Fig. 7.8.

Fig. 7.6 shows the extracted magnetisation scalings of the uniaxial anisotropy constant $K(m)$ for the three methods. The calculations give identical temperature dependences of the macrospin anisotropy constant. This is further verification that CMC measures internal–not free–energies. All three methods are taken from simulations using the same temperature range. Despite this, the stability coefficient method, which uses Metropolis Monte Carlo, doesn't have the same values as the two CMC methods. All three methods measure the same magnetisation scaling of the anisotropy constants ($K(m)$), but the constraint in CMC changes the magnetisation curve $m(T)$ compared to Metropolis Monte Carlo (see Fig. 7.7). In CMC, $m(T)$ is independent of the constraint direction but the difference compared with Metropolis Monte Carlo is clear. The constraint doesn't allow the system to fully relax so $m(T)$ is always higher than the value calculated using Metropolis Monte Carlo. This means the entropy is lower (and the free energy is higher) in CMC simulations. The use of the Gibbs-Helmholtz equation, which integrates the internal energy difference ($\Delta U(T) = N \times K(T)$), should only be used to calculate free energy differences when using the stability coefficient

method because Metropolis Monte Carlo allows the system to fully equilibrate.

We have now verified the validity of the stability coefficient method (for uniaxial anisotropy) by comparing with the well established CMC method. Stability coefficients allow the finite temperature scaling of any macrospin parameter (including the exchange stiffness) to be calculated in the equilibrium state of the system. Stability coefficients are trivial to extend to antiferromagnets and avoids the additional complications in CMC where users can choose to constrain a single sublattice or all sublattices. Stability coefficients can also be calculated using dynamical methods like atomistic spin dynamics which can be augmented with a quantum thermostat to obtain quantitative information about the finite temperature scaling of material parameters. This is expected to be very important for exchange stiffness which can't be written as a simple power law of the magnetisation. In materials where there are multiple exchange interactions, stability coefficients can separate their contributions to the exchange stiffness tensor as well as their temperature dependences. Comparisons of the temperature dependence of the spin wave stiffness $D(T)$ and exchange stiffness $A(T)$ are of great importance to verify, or disprove, the commonly used finite temperature relationship in equation 7.5.

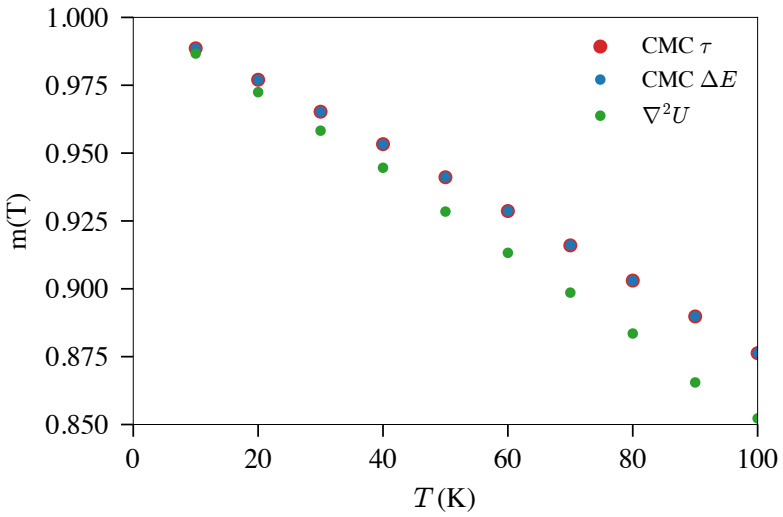

Figure 7.7: Comparison of the magnetisation curves using Metropolis Monte Carlo ($\nabla^2 U$), and constrained Monte Carlo when the constraint is 45° from the easy axis (CMC τ) and when the constraint is along the easy axis (CMC ΔE).

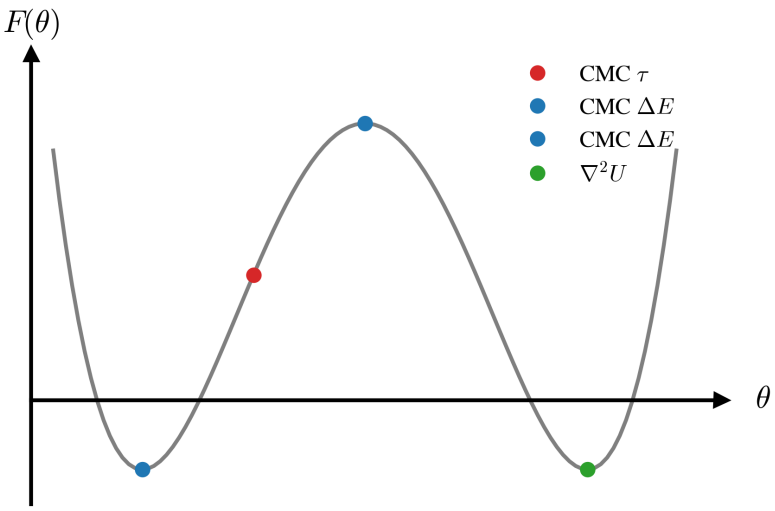

Figure 7.8: Visual representation of the points on the energy curve where the temperature scaling of anisotropy is calculated using different methods.

7.3.4 Connecting the Internal and Free Energies

We have shown that constrained Monte Carlo and stability coefficients allow the temperature scaling of material parameters used in macrospin and continuum models to be determined according to the internal energy of the ensemble. Oftentimes, we do not want the internal energy scaling. But, as discussed in many statistical physics textbooks [143], the free energy cannot be accessed easily from a canonical ensemble because it cannot be calculated by thermal averaging of microscopic degrees of freedom. Instead, the partition function must be known, which is incalculable in most systems of interest. This means various complicated Monte Carlo and ensemble methods have been developed to calculate the free energy scaling of macrosopic parameters [38, 296]. Here, we show that the free energy scaling of macrospin/continuum material parameters can be obtained from the internal energy scaling using only the definition of the free energy,

$$F \coloneqq U - TS, \tag{7.65}$$

And the definition of the internal energy in statistical mechanics,

$$U \coloneqq \langle \mathcal{H} \rangle \,. \tag{7.66}$$

First, we note that if the Hamiltonian of a system is composed of N terms–as is the case with magnetic materials–such that $\mathcal{H} = \sum_i^N \mathcal{H}_i$. Then, the internal energy can be separated into contributions from individual Hamiltonian terms

$$U = \left\langle \sum_i^N \mathcal{H}_i \right\rangle = \sum_i^N \langle \mathcal{H}_i \rangle \,. \tag{7.67}$$

Now, we return our attention to equation (7.65). The differential form of this equation is

$$dF = dU - TdS - SdT, \tag{7.68}$$

Taking the partial derivative of U with respect to T, and keeping all other parameters constant, we get

$$S = -\left.\frac{\partial F}{\partial T}\right|_U . \tag{7.69}$$

We can then substitute this expression for the entropy into the definition of the free energy (7.65), dropping the evaluation at constant U (as Eq. (7.65) satisfies this) giving

$$F = U + T\left(\frac{\partial F}{\partial T}\right). \tag{7.70}$$

We can rearrange this to

$$U = F - T\left(\frac{\partial F}{\partial T}\right), \tag{7.71}$$

which is an expansion of the chain rule. By reversing the chain rule, we can simplify this to

$$U = -T^2 \frac{\partial}{\partial T}\left(\frac{F}{T}\right). \tag{7.72}$$

This is the Helmholtz free energy equivalent of the Gibbs-Helmholtz equation. It is a linear partial differential equation which allows the free energy to be calculated self-consistently with the internal energy. The solution of the free energy from equation (7.72) is

$$F(T) - F(0) = -T\int_0^T \frac{U(\tau) - U(0)}{\tau^2} d\tau, \tag{7.73}$$

where τ is a dummy variable for temperature. This equation gives a very simple relationship between free energies and internal energies, and the integral can be calculated numerically using computer simulation measurements of $U(T)$. In the field of molecular dynamics, the term 'thermodynamic integration' can refer to one of many methods of estimating free energy differences from internal energy differences, including this one [297]. By equation (7.67), the quantity inside the integrand can be separated such

that the free energy difference is a sum of contributions from different Hamiltonian terms. First we replace the internal energies with sums of Hamiltonian terms under thermal averaging

$$\begin{aligned}\Delta F(T) &= -T\int_0^T \frac{U(\tau)-U(0)}{\tau^2}d\tau \\ &= -T\int_0^T \left[\frac{1}{\tau^2}\right]\left[\sum_i^N \left(\langle\mathcal{H}_i\rangle_\tau - \mathcal{H}_{i,0}\right)\right]d\tau,\end{aligned} \tag{7.74}$$

where $\mathcal{H}_{i,0}$ is the zero temperature (ground state) value of the i-th Hamiltonian term. We are free to move the summation outside of the integrand such that

$$\Delta F(T) = -T\sum_i^N \left[\int_0^T \left(\frac{\langle\mathcal{H}_i\rangle_\tau - \mathcal{H}_{i,0}}{\tau^2}\right)d\tau\right]. \tag{7.75}$$

Now, we write the free energy difference $\Delta F(T)$ as a sum of contributions $\Delta F(T) = \sum_i^N \Delta F_i(T)$, where each $\Delta F_i(T)$ is given by

$$\Delta F_i(T) = -T\int_0^T \left(\frac{\langle\mathcal{H}_i\rangle_\tau - \mathcal{H}_{i,0}}{\tau^2}\right)d\tau. \tag{7.76}$$

By definition (7.67), this means that the entropy of a composite Hamiltonian can also be separated into contributions from each Hamiltonian term. This does not mean that the behaviour of the system as a whole can be separated into contributions from each Hamiltonian term. In fact the opposite is true; it is well known that competing energy terms in a system can lead to complex equilibrium states that couldn't be predicted from any Hamiltonian term alone. The nuance here is that complex effect that competing Hamiltonian terms have on the surfaces F, U, and S are hidden in the thermal averages; the thermal averages are handled by numerical calculations on the composite system. This is not mutually exclusive with separating the contributions of individual Hamiltonian terms to the free energy difference. As with constrained Monte Carlo, this means that the same macrospin parameter may have a different temperature dependence in systems composed of different Hamiltonian terms (for example, see figure 1 of [298]).

The stability coefficients used earlier in this section can be used to calculate the temperature dependence of macrospin and continuum material parameters from the *free* energy, rather than the *internal* energy, as in Fig. 7.6. Previously, the stability coefficients $\Upsilon(T)$ were normalised by their zero temperature value to calculate the

temperature dependence of material parameters. Here, we first calculate the free energy scaling before normalising. To distinguish from the internal energy stability coefficients $\Upsilon(T)$, we denote the free energy stability coefficients by $\Xi(T)$. In the derivation of the Gibbs-Helmholtz relation 7.73, we assumed that, at zero temperature, the free energy and internal energy were equal ($F(0) = U(0)$). Thus, the zero temperature value of Ξ is equal to the zero temperature value of Υ ($\Xi(0) = \Upsilon(0)$). $\Xi(T)$ is calculated by

$$\Xi(T) = \Upsilon(0) - T\int_0^T \left(\frac{\Upsilon(\tau) - \Upsilon(0)}{\tau^2}\right) d\tau. \tag{7.77}$$

There are large differences between internal energy differences Υ and free energy differences Ξ. To illustrate these differences

We can replace the internal energy with the thermal average of the Hamiltonian

$$F(\Theta, \Phi)|_T = \langle \mathcal{H} \rangle |_{\Theta,\Phi,T} - TS(\Theta, \Phi)|_T \tag{7.78}$$

By taking the second derivative with respect to the Θ direction of the order parameter we arrive at

$$\left.\frac{\partial^2 F(\Theta, \Phi)}{\partial \Theta^2}\right|_{\Theta,\Phi,T} = \left\langle \left.\frac{\partial^2 \mathcal{H}}{\partial \theta^2}\right\rangle\right|_{\Theta,\Phi,T} - T \left.\frac{\partial^2 S(\Theta, \Phi)}{\partial \Theta^2}\right|_{\Theta,\Phi,T}. \tag{7.79}$$

From Eq. 7.79, it is clear that the calculations of Akulov, Callen, Zener, which calculates the temperature dependence using equilibrium thermal fluctuations, as well as constrained Monte Carlo don't include the temperature dependent curvature of the entropy, despite calling the derived energies *free energies*.

Appendix A

Direct Exchange in a Hydrogen Molecule

Consider two hydrogen nuclei (protons) separated by some fixed distance (Born-Oppenheimer approximation), with two orbiting electrons. The electron field Hamiltonian is

$$\hat{\mathcal{H}} = \hat{\mathcal{H}}_0 + \frac{1}{2}\int \mathrm{d}r_1 \int \mathrm{d}r_2 \sum_{\sigma,\sigma'} \hat{c}^\dagger_\sigma(r_1)\hat{c}^\dagger_{\sigma'}(r_2)\frac{e^2}{4\pi\epsilon_0|r_2 - r_1|}\hat{c}_{\sigma'}(r_2)\hat{c}_\sigma(r_1), \tag{A.1}$$

where $\hat{\mathcal{H}}_0 = \int dr \sum_\sigma c^\dagger_\sigma(r)\left[\frac{\hat{p}^2}{2m_e} + V(r)\right] c_\sigma(r)$ is the non-interacting electron Hamiltonian, $V(r)$ is the potential due to the hydrogen nuclei, $c^\dagger_\sigma(r)$ and $c_\sigma(r)$ are electron field operators, $\sigma = \{\uparrow, \downarrow\}$ is the spin state of an electron field, e is the magnitude of the electron charge, ϵ_0 is the permittivity of free space, r is the position. By making the tight-binding approximation, we can treat the electron-electron interaction as a perturbation such that the solutions of the interacting two-electron problem are linear combinations of the non-interacting electron orbitals of hydrogen. We can also choose the lowest energy orbitals of the hydrogen atom–an s-orbital which can contain a spin-up electron and/or a spin-down electron. The creation and annihilation operators for electrons with spin σ in s-orbitals localised on nucleus i are given by

$$\hat{c}^\dagger_{i\sigma} = \int \mathrm{d}r\, \psi_i(r)\hat{c}^\dagger_\sigma(r) \tag{A.2a}$$

$$\hat{c}_{i\sigma} = \int \mathrm{d}r\, \psi_i(r)\hat{c}_\sigma(r), \tag{A.2b}$$

where $\psi_i(r)$ is the wavefunction of an electron in an s-orbital localised at the nucleus i. Removing constant energies, the Hamiltonian is then

$$\hat{\mathcal{H}} = -\sum_{i,j}\sum_{\sigma,\sigma'} t_{ij}\, \hat{c}^\dagger_{i\sigma}\hat{c}_{j\sigma'} + \sum_{ijkl}\sum_{\sigma\sigma'} U_{ijkl}\, \hat{c}^\dagger_{i\sigma}\hat{c}^\dagger_{j\sigma'}\hat{c}_{k\sigma'}\hat{c}_{l\sigma} \tag{A.3}$$

where

$$t_{ij} = \left\langle \psi_i | \hat{\mathcal{H}}_0 | \psi_j \right\rangle \tag{A.4a}$$

$$U_{ijkl} = \frac{1}{2}\int \mathrm{d}r_1 \int \mathrm{d}r_2 \psi^\dagger_i(r_1)\psi^\dagger_j(r_2)\frac{e^2}{4\pi\epsilon_0|r_2 - r_1|}\psi_k(r_2)\psi_l(r_1), \tag{A.4b}$$

t_{ij} is the energy cost for an electron to tunnel from site i to j, and U_{ijkl} is the Coulomb repulsion of the electrons. This is the Hubbard Hamiltonian. Labelling the two hydrogen nuclei A and B, and removing small terms (assuming the overlap of electron wavefunctions is small), the interacting Hamiltonian is reduced to

$$\begin{aligned}\hat{\mathcal{H}} = &-t\sum_i \left[\hat{c}^\dagger_{i\uparrow}\hat{c}_{i+1\uparrow} + \hat{c}^\dagger_{i\downarrow}\hat{c}_{i+1\downarrow}\right] \\ &- U\sum_i \left[\hat{S}^z_i\hat{S}^z_{i+1} + \frac{1}{4}\left(\hat{n}_{i\uparrow}\hat{n}_{i\downarrow} + \hat{n}_{i\downarrow}\hat{n}_{i\uparrow}\right)\right],\end{aligned} \tag{A.5}$$

where

$$t = \left\langle \psi_A | \hat{\mathcal{H}}_0 | \psi_B \right\rangle = \left\langle \psi_B | \hat{\mathcal{H}}_0 | \psi_A \right\rangle \tag{A.6a}$$

$$U = \frac{1}{2} \int \mathrm{d}r_1 \int \mathrm{d}r_2 \psi_A^\dagger(r_1) \psi_B^\dagger(r_2) \frac{e^2}{4\pi\epsilon_0 |r_2 - r_1|} \psi_A(r_2) \psi_B(r_1), \tag{A.6b}$$

$\hat{n}_{i\sigma} = \hat{c}_{i\sigma}^\dagger \hat{c}_{i\sigma}$ is an electron number operator, and $\hat{S}_i^z = \frac{1}{2}(\hat{n}_{i\uparrow} - \hat{n}_{i\downarrow})$ is the Pauli-z spin operator. t is usually called the hopping integral, and U is the Coulomb repulsion. In the tight binding approximation, the hopping integral is negligibly small (not valid for hydrogen but the model is still useful) and we can assume that each hydrogen orbital is half filled ($\hat{n}_i = 1$) and the Hamiltonian reduces to

$$\hat{\mathcal{H}} = -2J \hat{S}_A^z \hat{S}_B^z, \tag{A.7}$$

which is the familiar Ising model where we have set the exchange coupling $J = U$. The above Hamiltonian has an additional factor of 2 compared to our definition of the Heisenberg Hamiltonian in (2.1). This is the definition typically used in the *ab-initio* electronic structure community and is a large source of confusion for researchers in magnetism*. Outside of this section we will use the definition given at the beginning of the chapter (2.1).

Since a hydrogen molecule only has a pair of spin-1/2 electrons, we did not derive Heisenberg exchange–more complex systems are required for this [300]. Direct exchange in insulators can only be ferromagnetic in sign. U is the Coulomb repulsion so can only be positive in sign, giving a ferromagnetic Ising Hamiltonian. If take the opposite limit where electron states are highly covalent, rather than ionic ($U \to \infty$), then the full Hamiltonian is not diagonalisable†. Instead we must reduce the Hilbert space to only covalent states of interest. This can be achieved by downfolding [269, 302] the matrix form of the Hamiltonian. Suppose a 4×4 operator $\mathbb{E}$ is written in the form

$$\mathbb{E} = \begin{pmatrix} \mathbb{A} & \mathbb{B} \\ \mathbb{B}^\dagger & \mathbb{C} \end{pmatrix}, \tag{A.8}$$

*For example here [299] the exchange interactions have been doubled which is why the critical temperature is close to experimental values despite using classical Monte Carlo methods which should give a T_c which is approximately half the experimental value.

†The Hamiltonian cannot be written as a Slater determinant. DFT methods such as LDA, LSD, and GGA assume linearised electron wavefunctions are given by a single Slater determinant, this is why they show poor agreement in correlated materials [301].

where $\mathbb{A}$, $\mathbb{B}$, and $\mathbb{C}$ are 2×2 operators. The operator can be partitioned from the full Hilbert space by computing

$$\mathbb{G}(E) = \begin{pmatrix} E - \mathbb{A} & \mathbb{B} \\ \mathbb{B}^\dagger & E - \mathbb{C} \end{pmatrix}^{-1} \tag{A.9}$$

We can then choose quasideterminant of $\mathbb{G}(E)$ which corresponds to the block of interest ie $\mathbb{G}(E)_{00} \sim \mathbb{A}$. Then we have $\mathbb{G}(E)_{00} = E - [\mathbb{A} + \mathbb{B}(E - \mathbb{C})^{-1}\mathbb{B}^\dagger]$, and $\hat{\mathcal{H}}' = \mathbb{A} + \mathbb{B}(E - \mathbb{C})^{-1}\mathbb{B}^\dagger$. This is an approximation but in the limit the the coupling terms $\mathbb{B}$ are small compared to the states of interest then we can replace the variable E with a constant E_0. Writing the Hubbard Hamiltonian (A.5) in matrix form ($\hat{\mathcal{H}} = \mathbb{X}[\hat{\mathcal{H}}]\mathbb{X}^\dagger$) gives

$$[\hat{\mathcal{H}}] = \begin{pmatrix} U & 0 & -t & t \\ 0 & U & -t & t \\ -t & -t & 0 & 0 \\ t & t & 0 & 0 \end{pmatrix} \tag{A.10}$$

which is written in the basis $\mathbb{X} = \left(\hat{c}^\dagger_{A\uparrow}\hat{c}^\dagger_{A\downarrow},\ \hat{c}^\dagger_{B\uparrow}\hat{c}^\dagger_{B\downarrow},\ \hat{c}^\dagger_{A\uparrow}\hat{c}^\dagger_{B\downarrow},\ \hat{c}^\dagger_{A\downarrow}\hat{c}^\dagger_{B\uparrow}\right)$ or in Dirac notation $\mathbb{X} = (|\uparrow\downarrow, 0\rangle\,,\ |0, \uparrow\downarrow\rangle\,,\ |\uparrow, \downarrow\rangle\,,\ |\downarrow, \uparrow\rangle)$. We are interested in the states in the bottom right quadrant (block). The partitioned Hamiltonian is then

$$\begin{aligned} \hat{\mathcal{H}}_{\text{eff}} &= \begin{pmatrix} -t & -t \\ t & t \end{pmatrix} \begin{pmatrix} E - U & 0 \\ 0 & E - U \end{pmatrix}^{-1} \begin{pmatrix} -t & t \\ -t & t \end{pmatrix} \\ &\approx -\frac{2t^2}{U} \begin{pmatrix} 1 & -1 \\ -1 & 1 \end{pmatrix}, \end{aligned} \tag{A.11}$$

where we have set $E = 0$ and the reduced basis is $\mathbb{X}' = (|\uparrow, \downarrow\rangle\,,\ |\downarrow, \uparrow\rangle)$. Diagonalising this Hamiltonian gives two eigenstates

$$\begin{aligned} E_1 = -\frac{4t^2}{U} \qquad & \psi_1 = \frac{1}{\sqrt{2}}\left(|\uparrow, \downarrow\rangle - |\downarrow, \uparrow\rangle\right) \\ E_2 = 0 \qquad & \psi_2 = \frac{1}{\sqrt{2}}\left(|\uparrow, \downarrow\rangle + |\downarrow, \uparrow\rangle\right). \end{aligned} \tag{A.12}$$

The first is the lowest energy state and corresponds to antiferromagnetic alignment of electron spins in covalent orbitals (singlet); the second is the high energy ferromagnetic (triplet) state. We can relate this to the exchange coupling by $J = -\frac{2t^2}{U}$.

Appendix B

Microscopic Origin of Magnetocrystalline Anisotropy

B.1 Outline

In this appendix we first derive the relativistic Hamiltonian for electrons localised on an atomic site in an electric potential V and an applied magnetic field B. The electric potential includes both the periodic crystal field potential and the potential from the atomic site. Then, in Section B.3, we consider the crystal field as a perturbation of the real spherical harmonics to show splitting of valence electron energies in crystals. Next, in Section B.4, we discuss the difference between real and complex spherical harmonics. Finally in Sections B.5.1 and B.5.2, a qualitative expression for the anisotropy in a $4f$ material is derived (B.5.1), and a quantitative expression is derived for the uniaxial anisotropy in a hexagonal $3d$ material (B.5.2).

B.2 Relativistic Origin of Spin-Orbit Coupling

Following Skomski [303], the relativistic energy of an electron in motion is given as

$$E = m_e c^2 \sqrt{1 + \frac{v^2}{c^2}}, \tag{B.1}$$

where m_e is the rest mass of an electron, v is the electron velocity measured in an inertial reference frame, and c is the speed of light. This can be expanded in a power series

$$E = m_e c^2 + \frac{1}{2} m_e v^2 - \frac{1}{8} m_e^2 v^4. \tag{B.2}$$

The first term is the rest energy of an electron, the second term is the non-relativistic kinetic energy, the third term is the first relativistic correction to the kinetic energy. If we naïvely equate the electron momentum $p = \frac{v}{c}$ we can rewrite Eq B.1 as

$$m_e^2 c^4 = (E^2 - c^2 p^2), \tag{B.3}$$

p should be a three-vector $\mathbf{p}$ so this relation isn't valid. Pauli remedied this by using a property of the Pauli matrices $(\sigma \cdot \mathbf{a})^2 = |a|^2$. The use of Pauli operators separates the electron wavefunction into two components which are the spin resolved states. This can then be used in the Dirac equation which is the relativistic analogy to the Schrödinger equation, where the wavefunction is now a Dirac two-spinor which can be thought of as a two component wavefunction in complex space. The Hamiltonian for a particle in an electromagnetic field is given by

$$\hat{\mathcal{H}} = \frac{1}{2m_e} c\hat{\alpha} \cdot \left[\hat{\sigma} \cdot (\hat{p} - \tfrac{e}{c}\mathbf{A})\right]^2 + m_e c^2 \hat{\beta} + V\mathbb{1}, \tag{B.4}$$

where $\hat{\sigma}$ is the triplet of Pauli operators $\hat{\sigma} = (\hat{\sigma}_x, \hat{\sigma}_y, \hat{\sigma}_z)$ defined by $\hat{\sigma} \cdot \mathbf{a} = a_x\hat{\sigma}_x + a_y\hat{\sigma}_y + a_z\hat{\sigma}_z$, $\hat{p}$ is the momentum operator and $\mathbf{A}$ is the vector potential of the magnetic field. The operators $\hat{\alpha}$, $\hat{\beta}$ are given below

$$\hat{\alpha} = \begin{pmatrix} 0 & \hat{\sigma} \\ \hat{\sigma} & 0 \end{pmatrix} \quad \hat{\beta} = \begin{pmatrix} \mathbb{1} & 0 \\ 0 & \mathbb{1} \end{pmatrix} \tag{B.5}$$

The Hamiltonian can be simplified further by using the vector identity

$$(\hat{\sigma} \cdot \mathbf{a})(\hat{\sigma} \cdot \mathbf{b}) = (\mathbf{a} \cdot \mathbf{b})\mathbb{1} + \mathrm{i}\sigma \cdot (\mathbf{a} \times \mathbf{b}). \tag{B.6}$$

Now the Hamiltonian can be decomposed into the form

$$\hat{\mathcal{H}} = \begin{pmatrix} m_e c^2 + V & c\hat{\sigma} \cdot (\hat{p} - \frac{e}{c}\mathbf{A}) \\ c\hat{\sigma} \cdot (\hat{p} - \frac{e}{c}\mathbf{A}) & -m_e c^2 + V \end{pmatrix}. \tag{B.7}$$

By defining the Dirac spinor as $\psi = (\psi_a, \psi_b)^\intercal$, we can decompose the Hamiltonian into two coupled equations

$$(m_e c^2 + V)\psi_a + c\hat{\sigma} \cdot (\hat{p} - \tfrac{e}{c}\mathbf{A})\psi_b = E\psi_a \tag{B.8a}$$

$$c\hat{\sigma} \cdot (\hat{p} - \tfrac{e}{c}\mathbf{A})\psi_a - (m_e c^2 - V)\psi_b = E\psi_b \tag{B.8b}$$

If we rearrange the second equation of Eq B.8 and define $W = E + mc^2$, then the solutions are given by the self-consistent equation

$$\psi_b = \frac{1}{W + 2mc^2 - V} \left[c\hat{\sigma} \cdot (\hat{p} - \tfrac{e}{c}\mathbf{A})\right] \psi_a. \tag{B.9}$$

We will now skip the derivation of the zeroth order relativistic correction which includes Zeeman interactions between electrons and the magnetic field. We can express the first coefficient of equation (B.9) as a constant K by computing the partial fractions giving

$$K = \frac{1}{W + 2m_e c^2 - V} = \frac{1}{2m_e} \left(1 - \frac{V - W}{2m_e c^2}\right)^{-1}. \tag{B.10}$$

By defining $\tilde{\mathbf{p}} = (\hat{\mathbf{p}} - \frac{e}{c}\mathbf{A})$ we can eliminate the wavefunction ψ_b. Substituting into the coupled equations (B.8), we obtain a single solution

$$\left[\frac{(\sigma \cdot \tilde{p})K(\sigma \cdot \tilde{p})}{4m^2c^2} + V\right] \psi_a = W\psi_a. \tag{B.11}$$

ψ_a is no longer correctly normalised, but this equation is exact and relativistic. To normalise, we must choose take a Taylor expansion of K and move any terms proportional

to W terms to the right hand side. The first order relativistic correction in the Taylor expansion is

$$K \approx \frac{1}{2m_e}\left(1 + \frac{V-W}{2m_e c^2}\right), \tag{B.12}$$

and the solution to the Dirac equation becomes

$$\left[\frac{(\hat{\sigma}\cdot\tilde{p})^2}{2m_e} + V - \frac{(\hat{\sigma}\cdot\tilde{p})V(\hat{\sigma}\cdot\tilde{p})}{4m_e^2c^2}\right]\psi_a = \left(1 + \frac{(\hat{\sigma}\cdot\tilde{p})^2}{4m_e^2c^2}\right)W\psi_a. \tag{B.13}$$

Now define the normalisation factor N

$$N = \left(1 + \frac{(\sigma\cdot\tilde{p})^2}{4m^2c^2}\right)^{\frac{1}{2}} \approx 1 - \frac{\hat{p}^2}{8m^2c^2}, \tag{B.14}$$

such that $\psi_a \to N^{-1}\psi$. The problem becomes

$$N^{-1}\left[\frac{(\sigma\cdot\tilde{p})^2}{2m} + V - \frac{(\sigma\cdot\tilde{p})V(\sigma\cdot\tilde{p})}{4m^2c^2}\right]N^{-1}\psi = N^{-2}W\psi. \tag{B.15}$$

The Hamiltonian, wavefunction and energy have been remornalised for consistency. The normalised Hamiltonian now takes the form

$$\hat{\mathcal{H}} = \left(1 - \frac{\hat{p}^2}{8m_e^2c^2}\right)\left[\frac{(\hat{\sigma}\cdot\tilde{p})^2}{2m_e} + V - \frac{(\hat{\sigma}\cdot\tilde{p})V(\hat{\sigma}\cdot\tilde{p})}{4m_e^2c^2}\right]\left(1 - \frac{\hat{p}^2}{8m_e^2c^2}\right). \tag{B.16}$$

Expand the first term, this becomes

$$\begin{aligned}(\hat{\sigma}\cdot\tilde{p})^2 &= \left[\hat{\sigma}\cdot(\hat{p} - \frac{e}{c}\mathbf{A})\right]^2 \\ &= \hat{p}^2 + \frac{e^2}{c^2}\mathbf{A}^2 - \frac{e}{c}(\hat{L} + 2\hat{S})\cdot\mathbf{B}),\end{aligned} \tag{B.17}$$

where $\hat{L} = \hat{\mathbf{p}} \times \mathbf{r}$ is the electron total orbital angular momentum operator and $\hat{S} = \frac{1}{2}\hat{\sigma}$ is the total spin angular momentum operator. Keeping terms up to $(v/c)^2$, the Hamiltonian simplifies to

$$\begin{aligned}\hat{\mathcal{H}} = \frac{\hat{p}^2}{2m_e} - \frac{\hat{p}^4}{8m_e^2c^2} + \frac{e^2}{2m_ec^2}\mathbf{A}^2 - \frac{e}{2m_ec}(\hat{L} + 2\hat{S})\cdot\mathbf{B} \\ + V - \frac{1}{8m_e^2c^2}\left\{\hat{p}^2, V\right\} + \frac{(\hat{\sigma}\cdot\tilde{p})V(\hat{\sigma}\cdot\tilde{p})}{4m_e^2c^2},\end{aligned} \tag{B.18}$$

where curly braces denote the anticommutator. Let's now consider the final two terms to first order

$$\begin{aligned}(\hat{\sigma}\cdot\tilde{p})V(\hat{\sigma}\cdot\tilde{p}) &= (\hat{p}V)\cdot\hat{p} + V\hat{p}^2 + \mathrm{i}\hat{\sigma}\cdot(\hat{p}V)\times\hat{p} - \tfrac{1}{2}\left\{\hat{p}^2, V\right\} \\ &= -\frac{1}{2}(\hat{p}^2V) - (\hat{p}V)\cdot\hat{p} - V\hat{p}^2.\end{aligned} \tag{B.19}$$

The final term of the first line is the spin-orbit coupling $\hat{\sigma}\cdot(\nabla V)\times\hat{p}$ which can be simplified into the usual form for $V \equiv V(r)$. All but two terms cancel giving the total Hamiltonian

$$\begin{aligned}\hat{\mathcal{H}} =& \frac{\hat{p}^2}{2m_e} - \frac{\hat{p}^4}{8m_e^2c^2} + V + \frac{\hbar^2}{8m_e^2c^2}\nabla^2V - \frac{e}{2m_ec}(\hat{L}+2\hat{S})\cdot\mathbf{B} \\ &+ \frac{\hbar^2}{2m_e^2c^2}\nabla V(\hat{L}\cdot\hat{S}) + \frac{e^2}{2m_ec^2}\mathbf{A}^2\end{aligned} \tag{B.20}$$

The first term is the non-relativistic kinetic energy of the electron, the second term is its first order relativistic correction, the third term is the Darwin term responsible for the hyper-fine structure of the atom, the fourth is the Zeeman energy for an electron in an atomic orbital, the fifth term is the spin-orbit coupling under the approximation of a spherical potential which is commonly used in most density functional theories, and the final term is a relativistic correction to the kinetic energy due to the magnetic potential.

B.3 Crystal Field Interactions and Quenching

We derived the above Hamiltonian for an atom with hydrogen-like (spherical) potentials in free space to arrive at the spin-orbit coupling (SOC) term. This is an approximation and SOC has a general more general tensor form. However, we will continue using the approximation of orbitals expressed as spherical harmonics. In materials research, we are not considering single atoms. Instead, our atoms are embedded in crystals with periodic structures. Other atoms in a crystal change the energies of valence electron. This is the crystal field splitting. Crystal field splitting can be made explicit by taking the electric potential V in equation (B.11), and separating the single-atom potential and the crystal field potential by the substitution $V = V_0(r) + V_{\mathrm{CF}}(r)$, where $V_0(r)$ is the Coulomb potential for an electron orbiting a single atom and $V_{\mathrm{CF}}(r)$ is the Coulomb potential due to other atoms in the crystal. V_{CF} allows interactions between the electron orbitals of neighbouring atoms. Fig. B.1 shows some of the real ($\mathbb{R}^3$) $3d$ electron orbitals

which are described by three quantum numbers: n the principal quantum number, l the orbital quantum number, and m the magnetic quantum number.

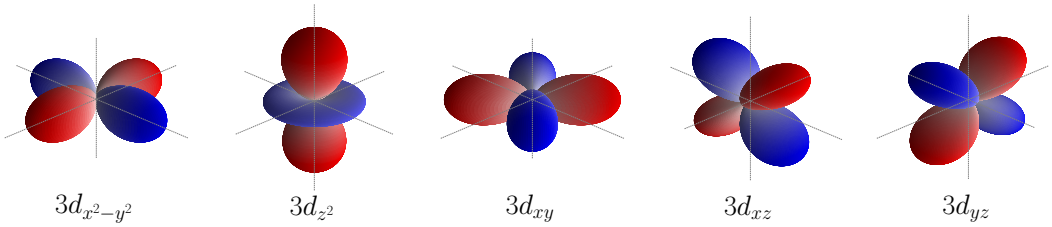

Figure B.1: The $3d$ atomic electron orbitals ($n = 3$, $l = 2$) in the basis of real spherical harmonics. Colour indicates the sign of the wavefunction. The expressions for the orbitals are given in terms of spherical harmonics in Table B.1.

Table B.1: Expressions for some of the real $3d$ orbitals given in terms of the real and complex spherical harmonics.

Orbital	Real Harmonics	Complex Harmonics
$3d_{x^2-y^2}$	$Y_{3,2}$	$\frac{1}{\sqrt{2}}(Y_3^{-2} + Y_3^2)$
$3d_{z^2}$	$Y_{3,0}$	Y_3^0
$3d_{xy}$	$Y_{3,-2}$	$\frac{\mathrm{i}}{\sqrt{2}}(Y_3^{-2} - Y_3^2)$
$3d_{xz}$	$Y_{3,1}$	$\frac{1}{\sqrt{2}}(Y_3^{-1} - Y_3^1)$
$3d_{yz}$	$Y_{3,-1}$	$\frac{\mathrm{i}}{\sqrt{2}}(Y_3^{-1} + Y_3^1)$

Intuitively, if we add in the nearest neighbour atoms from the crystal, the electron density will experience an attractive force from the nuclei of other sites because of electron charge screening. This change in potential lifts the degeneracy of the real electron orbitals. The position of these atoms will determine which of the five orbitals in Fig. B.1 has the lowest energy. Consider the orbitals $3d_{x^2-y^2}$ and $3d_{xy}$, if this is inserted into an fcc lattice with one species, there will be sites along the twelve diagonals given by $[\pm 1 \pm 10]$, $[\mp 1 \pm 10]$, $[0 \pm 1 \pm 1]$, $[0 \mp 1 \pm 1]$, $[\pm 10 \pm 1]$, and $[\mp 10 \pm 1]$. The atoms have a net positive effective charge which favours the $3d_{xy}$ orbital since the electron density is, on average, closer to the positive effective charges than the $3d_{x^2-y^2}$. This can be seen in Fig. B.2.

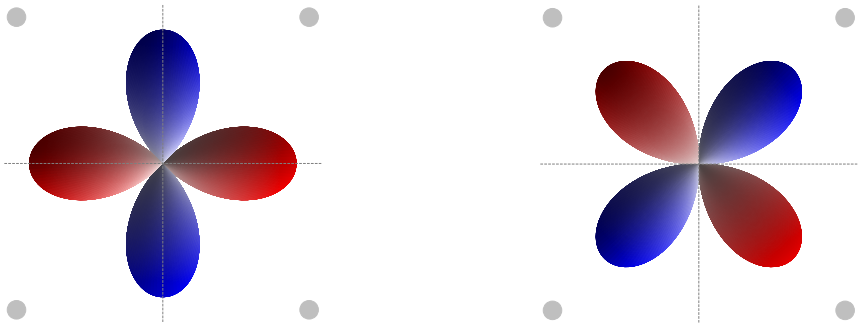

$3d_{x^2-y^2}$ $3d_{xy}$

Figure B.2: Real spherical harmonic orbitals of an electron embedded in an fcc crystal lattice. (*left*) $3d_{x^2-y^2}$ orbital and (*right*) $3d_{xy}$ orbital. Grey points represent the effective point charge of neighbouring atoms.

The lifting of electron orbital degeneracy is usually depicted as an energy-level diagram, so we will also do this here. Fig. B.3 shows the energy level diagram for an atom in an fcc crystal. The energy-level diagram would differ in a tetragonal or hexagonal crystal. In general, the localised electron wavefunctions in a crystalline material will not be described by either the real spherical harmonics, nor the complex ones. Describing the crystal field with energy level diagrams like Fig. B.3 is still useful.

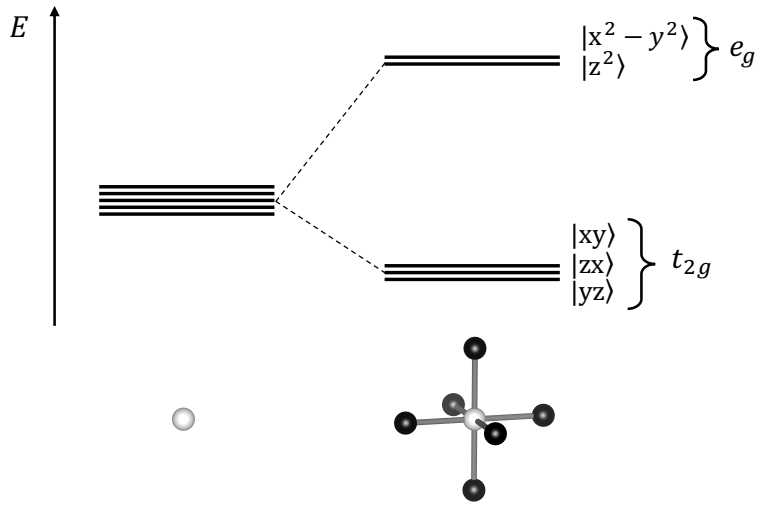

Figure B.3: Energy level diagram for the $3d$ shell of an atom in free space (left) and in an fcc crystal (right). All energy levels on the left are degenerate, crystal field interactions breaks this degeneracy on the right. In a simple cubic lattice, the $|\mathrm{xy}\rangle$ and $|\mathrm{x}^2 - \mathrm{y}^2\rangle$ states would switch places.

B.4 Quenching of Orbital Angular Momentum

The derived Hamiltonian shows that the origin of spin-orbit coupling, and as we will later see, the magnetocrystalline anisotropy arises due to the existence of a persistent orbital angular momentum. In $3d$ transition metals, it has been shown that the magnetic moment arises almost exclusively from the spin moment. So, an important question remains–if the orbital moment is quenched, why is magnetocrystalline anisotropy non-zero?

The answer lies in our choice of basis for electron orbitals. If we limit ourselves to spherical harmonic orbitals, we have the principle quantum numbers n, l and m. The spherical harmonics are independent of n as this affects the radial component of the wavefunction only. The resulting spherical harmonics Y_l^m have both real and imaginary components–an example is given below (Eq B.21)

$$Y_2^{-2} = \sqrt{\frac{3}{8\pi}} \frac{(x - iy)^2}{r}. \tag{B.21}$$

This is the valid picture when relativistic effects are ignored. If spin-orbit and crystal field interactions are included, a superposition of states $|\pm m\rangle$ is favourable. By taking the expectation value of this state, we find that the average (measurebale) orbital moment is zero. We can now construct a new orthonormal basis set which exists in real space where m is no longer a 'good' quantum number ie these quantum numbers do not describe the eigenstates. These are the states we saw above (Fig B.3), an example of the new states is given by equation (B.22). In reality the exact wavefunctions will be none of these - a mixing of appropriate orbitals takes place so a small remnant orbital moment is measured.

$$Y_l^{\pm m} = \sqrt{\frac{(-1)^{\pm 1}}{2}}(Y_l^m \pm Y_l^{-m}) \tag{B.22}$$

We can now quantify what is meant by quenching. When spin-orbit coupling is large compared to crystal field interactions, electrons have a lower energy when in orbitals with spherical symmetry (ie s-like orbitals) and the orbital moment is unquenched (non-zero). When crystal field interactions dominate, orbital momentum is quenched so the eigenstates are given by the real spherical harmonicsz

B.5 Magnetocrystalline Anisotropy

We will now look at the origins of anisotropy for two types of materials; $3d$ transition metals and the $4f$ rare-earths. The rare earths are easier to understand as it involves unquenched orbitals (large spin-orbit coupling) so the anisotropy can be considered as the energy difference between the energy levels given in Fig. B.3. The transition metals are described by almost completely quenched orbitals so the single-ion anisotropy arises as a perturbation due to spin-orbit coupling. This is the reason that rare-earths usually have a much higher anisotropy than the $3d$ transition metals. The problem may seem complicated but, in reality, when studying spin-only Hamiltonians the magnetocrystalline anisotropies have the same expressions and obey the same symmetry requirements irrespective of the basis of electron orbitals. This is only a problem for chemists and physicists which calculate electronic structures, and the relative strength of the crystal field and spin-orbit coupling determines which part of the electronic structure is diagonalised first.

B.5.1 $4f$ Rare-Earths

In these metals, the spin-orbit coupling is the dominant energy term in the single spin Hamiltonian (exchange is a many-spin effect). This means l and m are good quantum numbers and the complex basis $|\psi_{4f}\rangle \in \{|m\rangle\}$ describes the electron density. The high orbital angular momentum state $|m = \pm 3\rangle$ can be seen below

$$\langle m = \pm 3 | m = \pm 3 \rangle = |Y_3^{\pm 3}(\theta, \phi)|^2 = \frac{35}{64\pi} \sin^6(\theta) \tag{B.23}$$

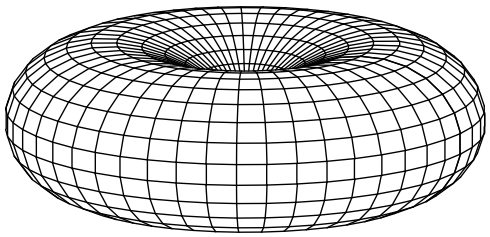

Figure B.4: Electron probability density for a 4f electron with $m = \pm 3$.

This electron density can be recast as an electric quadrupole with ellipsoidal charge density. The figure above would be represented as an oblate ellipsoid (truncated at the poles), whereas $|m = 2\rangle$ and $|m = 1\rangle$ would be prolate ellipsoids. The circular shape of the probability amplitude minimises the SOI and is unquenched. As the SOI dominates, the spin degree of freedom and the electron density are tightly bound. This means, when changing the spin orientation, we are in fact moving both the spin orientation and electron density of the $4f$ shell. The energy barrier between the easy and hard axes is then the difference in electrostatic energy due to the crystal field potential. There are many models to approximate this energy difference for various systems.

We can now qualitatively consider what form of magnetocrystalline anisotropy various materials should have. Nd^{3+} ions have a charge distribution as in Fig. B.4. Suppose this is in a lattice where its nearest neighbours are cations along the principle cartesian axes (cubic crystal). The negative crystal field interaction means these are the hard

axes and that the $\langle 111 \rangle$ directions are the easy axes as they are the points furthest away from the 6 nearest neighbour atoms (see Fig. B.5). From the phenomenological equations for MAE, we infer that this lattice must have cubic anisotropy. To ensure the $\langle 111 \rangle$ directions are easy, the constant K_1 must be less than zero, or K_2 must be greater than zero (see equation (B.24)). This simple argument can be applied to any magnetic material if the lattice symmetry and electron valence is known.

$$E = -K_2 \left[(S_x S_y)^2 + (S_y S_z)^2 + (S_z S_x)^2 \right] - K_2 \left(S_x S_y S_z \right)^2 \tag{B.24}$$

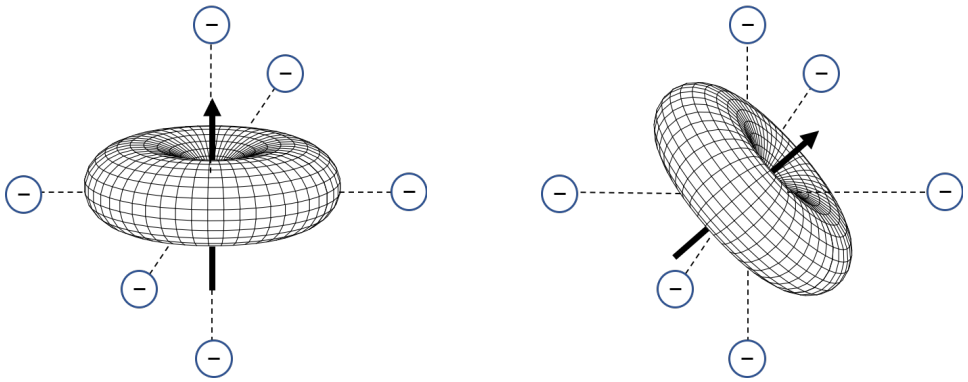

Figure B.5: Crystal field interaction of a $|n = 4, l = 3, m = 3\rangle$ electron orbital with nearest neighbour cations along the principle axes. (*left*) High energy state; (*right*) low energy state. Arrow represents the spin magnetic moment which maintains a fixed direction with respect to the spatial distribution of charge.

B.5.2 $3d$ Transition Metals

The $3d$ elements are much lighter than the $4f$ elements so the SOI is small. Now, crystal field is large and spin-orbit coupling is a perturbative effect. The orbitals in these elements are almost completely quenched so can be approximated as the real space wavevectors in the form of Eq B.22. These are static, unlike in the $4f$ elements where SOC cannot be broken by the crystal field interaction and the electron density moves with the spin orinetation. If spin-orbit coupling was zero, the energy of the magnetic system would have no angular dependence (zero anisotropy). If we now consider the magnetic Hamiltonian for a single electron in a $3d$ element with the inclusion of a uniaxial crystal field and spin-orbit coupling with respect to the two xy plane orbitals $|\psi_1\rangle = |xy\rangle$ and $|\psi_2\rangle = |x^2 - y^2\rangle$, the energy is given by

$$E_{01}|\psi\rangle = \begin{pmatrix} A & 0 \\ 0 & -A \end{pmatrix} |\psi\rangle + 2\lambda \cos\theta \begin{pmatrix} 0 & i \\ -i & 0 \end{pmatrix} |\psi\rangle \tag{B.25}$$

Where $2A$ is the crystal field alignedting - the difference in orbital energies see Fig B.3, λ is the spin-orbit coupling constant, $|\psi\rangle$ is the Dirac spinor $\begin{pmatrix} |\psi_1\rangle \\ |\psi_2\rangle \end{pmatrix}$ and θ is the angle between the spin direction and the z-axis. By diagonalising this matrix, we obtain the eigenvalues

$$\begin{aligned} E_0 &= -\sqrt{A^2 + 4\lambda^2 \cos\theta} \\ E_1 &= \sqrt{A^2 + 4\lambda^2 \cos\theta} \end{aligned} \tag{B.26}$$

Given we assumed only one valence electron, the lower energy state E_0 will be occupied. We can estimate the anisotropy constant by taking the difference between the easy and hard axes $\theta = 0°$ and $\theta = 90°$ giving

$$K_1 = \sqrt{A^2 + 4\lambda^2} - A \tag{B.27}$$

We can take an expansion for small λ which yields

$$K_1 \approx \frac{2\lambda^2}{A} \tag{B.28}$$

This approximation is specific to a uniaxial system, but this can be generalised for other anisotropies.

Appendix C

Analytic Calculation of the Dipole Anisotropy

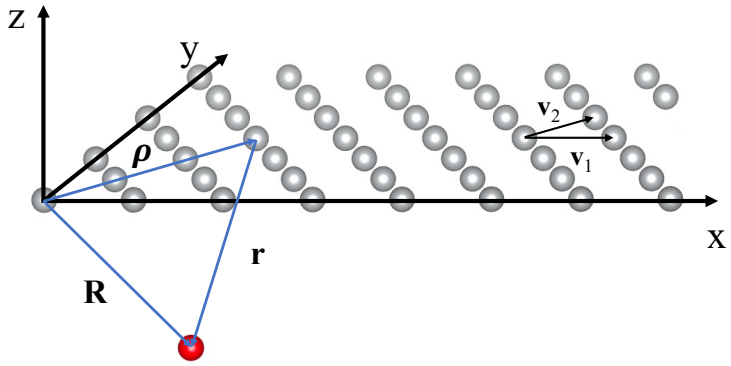

Figure C.1: A single plane of (111) textured NiO with Ni sites represented as grey spheres. Oxygen sites have been removed for clarity. Primitive intraplane vectors are denoted $\mathbf{v}_1$ and $\mathbf{v}_2$. Vectors $\boldsymbol{\rho}$, $\mathbf{R}$, and $\mathbf{r}$ are labelled. $\boldsymbol{\rho}$ is position of an atom relative to the origin and is equal to $n\mathbf{v}_1 + m\mathbf{v}_2$ where n, m are integers. $\mathbf{R}$ is the position in space we choose to calculate the effective field. $\mathbf{r} = \mathbf{R} - \boldsymbol{\rho}$ is the vector between a spin at position $\boldsymbol{\rho}$ and the point in space $\mathbf{R}$.

C.1 Preamble

Following Tsymbal *et al* [304] we will show that the dipole anisotropy can be written as $\Delta E_{\text{dip}} \sim m^2(T)$. The total dipole anisotropy of bulk NiO can be split into two contributions; intraplane dipole interactions (triangular ferromagnetic film one atom thick) and interplane dipole interactions. The intraplane contribution is well known from magnetostatics–shape anisotropy. Interplane contributions from antiparallel planes of spins cannot be calculated in this way, but its energy contribution will be a sum over atomically thin ferromagnets (which must also scale as $m^2(T)$). We can calculate both inter- and intra-plane energies on the same footing by transforming the infinite summation of spins in the magnetic scalar potential to the Fourier components (a Poisson sum) from infinite 2D triangular sheets of spins (see Figure C.1). Using this, we can calculate the magnetic field from the 2D lattice at any arbitrary point in space (including at other lattice sites) to calculate the total effective field from all neighbouring sheets. This sum in 2D k-space and another sum over neighbour planes should converge faster than the calculation in real space, and we can express the energy in terms of $m^2(T)$.

For a single (111) oriented sheet of NiO, there is only a single magnetic site in

the primitive cell, located at the origin. The intraplane vectors (see Figure C.1) are $\mathbf{v}_1 = (1/2, 0, 0)\, a'$ and $\mathbf{v}_2 = \left(-1/4, \sqrt{3}/4, 0\right) a'$ in units of $a' = \sqrt{2}a$, a is consistent with the main text. The interplane vector which connects this sheet of spins to neighbouring antiparallel sheets is $\mathbf{v}_3 = (0, \sqrt{3}/6, \sqrt{6}/6)a'$. We are applying a Fourier transform on a 2D plane, so we only need to calculate the intraplane recirprocal lattice vectors. These are $\mathbf{b}_1 = 4\pi/a' \left(1, 1/\sqrt{3}\right)$ and $\mathbf{b}_1 = 4\pi/a' \left(0, 2/\sqrt{3}\right)$. The magnetic scalar potential at some point in space $\mathbf{R} = (x, y, z)$ for a system of discrete magnetic moments $\boldsymbol{\mu}_i$ at positions $\boldsymbol{\rho}_i$ is given as

$$\Phi(\mathbf{R}) = \frac{1}{4\pi} \sum_i \frac{\boldsymbol{\mu}_i \cdot (\mathbf{R} - \boldsymbol{\rho}_i)}{|\mathbf{R} - \boldsymbol{\rho}_i|^3}, \tag{C.1}$$

This scalar potential is consistent with the definition of the dipole-dipole interaction given by equation (2) in the main text. For the next steps, we defining $\Phi' = 4\pi\Phi$ to make calculations simpler. For the 2D film of NiO, the sum over atomic sites $\boldsymbol{\rho}_i$ can be written as a sum over integers n and m, and $\boldsymbol{\rho}_{nm}$ is a linear combination of the intraplane lattice vectors

$$\boldsymbol{\rho}_{nm} = n\mathbf{v}_1 + m\mathbf{v}_2 = \left(\frac{1}{2}na' - \frac{1}{4}ma', \frac{\sqrt{3}}{4}ma', 0\right) \tag{C.2a}$$

$$\mathbf{r}_i = \mathbf{R} - \boldsymbol{\rho}_i = \left(x - \frac{1}{2}na' + \frac{1}{4}ma', y - \frac{\sqrt{3}}{4}ma', z\right) \tag{C.2b}$$

C.2 Calculating B_y

The ground state of NiO is spins lying in the (111) plane, we can choose the magnetic moments lying in the y-direction. At finite temperature, and in thermal equilibrium, we can write

$$\boldsymbol{\mu}_{nm} = \mu_S \hat{\mathbf{y}}, \quad \forall\ (n, m) \tag{C.3}$$

Substituting $\mathbf{r}_i$ and $\boldsymbol{\mu}_{nm}$ into the reduced magnetic scalar potential gives

$$\Phi'(x, y, z) = \sum_{n,m=-\infty}^{\infty} \frac{\mu_S \left(y - \frac{\sqrt{3}}{4}ma'\right)}{\left[\left(x - \frac{1}{2}na' + \frac{1}{4}ma'\right)^2 + \left(y - \frac{\sqrt{3}}{4}ma'\right)^2 + z^2\right]^{\frac{3}{2}}} \tag{C.4}$$

We make use of Poisson's summation formula to apply a Fourier transform. For a function $f(na)$ in 1D this is

$$\sum_{n=-\infty}^{\infty} f(na) = \frac{1}{a} \sum_{k=-\infty}^{\infty} \int_{-\infty}^{\infty} f(x) \mathrm{e}^{-\mathrm{i}\frac{2\pi}{a}kx} \mathrm{d}x, \tag{C.5}$$

where $\frac{2\pi}{a}$ is the reciprocal lattice vector. This can easily be generalised to two dimensions:

$$\sum_{n,m=-\infty}^{\infty} f(na, ma) = \frac{1}{a^2} \sum_{k,l=-\infty}^{\infty} \int_{-\infty}^{\infty}\int_{-\infty}^{\infty} f(x,y)\ \mathrm{e}^{-\mathrm{i}\frac{2\pi}{a}kx}\ \mathrm{e}^{-\mathrm{i}\frac{2\pi}{a}ly}\mathrm{d}x\mathrm{d}y \tag{C.6}$$

Our function is an implicit function of na, ma. We have something of the form $f \equiv f(x - \frac{1}{2}na + \frac{1}{4}ma, y - \frac{\sqrt{3}}{4}ma)$. Translations in function variables transform have the following property when applying a Fourier transform

$$\sum_{n=-\infty}^{\infty} g(na - x) = \frac{1}{a} \sum_{k=-\infty}^{\infty} \mathrm{e}^{-\mathrm{i}\frac{2\pi}{a}kx} \int_{-\infty}^{\infty} g(x')\ \mathrm{e}^{\mathrm{i}\frac{2\pi}{a}kx'}\mathrm{d}x' \tag{C.7}$$

A dummy variable x' has been introduced. There is another consideration for the magnetic potential as the lattice vectors $\mathbf{v}_1$, $\mathbf{v}_2$ are non-orthogonal. In Eq C.6 the coefficient $\frac{1}{a^2}$ must be replaced with the area subtended by the in-plane vectors $|\mathbf{v}_1 \times \mathbf{v}_2|$. The Fourier transform of Φ' is

$$\begin{aligned}\Phi'(x,y,z) = \frac{1}{|\mathbf{v}_1 \times \mathbf{v}_2|} \sum_{k,l=-\infty}^{\infty} & \mathrm{e}^{-\mathrm{i}(k\mathbf{b}_1\cdot\mathbf{R} + l\mathbf{b}_2\cdot\mathbf{R})} \\ & \times \int_{-\infty}^{\infty}\int_{-\infty}^{\infty} \mathrm{d}x'\mathrm{d}y' \frac{\mu_S y'}{[x'^2 + y'^2 + z^2]^{\frac{3}{2}}} \mathrm{e}^{\mathrm{i}(k\mathbf{b}_1\cdot\mathbf{R}' + l\mathbf{b}_2\cdot\mathbf{R}')},\end{aligned} \tag{C.8}$$

where $\mathbf{b}_1$, $\mathbf{b}_2$ are the intraplane reciprocal lattice vectors, and k, l are the Fourier coefficients. Substituting the reciprocal lattice vectors and the area of a single atom into the potential, we have

$$\begin{aligned}\Phi'(x,y,z) = \frac{8\mu_S}{\sqrt{3}a'^2} \sum_{k,l=-\infty}^{\infty} & \mathrm{e}^{-\mathrm{i}\frac{4\pi}{a'}\left(kx + \frac{1}{\sqrt{3}}ky + \frac{2}{\sqrt{3}}ly\right)} \\ & \times \int_{-\infty}^{\infty}\int_{-\infty}^{\infty} \mathrm{d}x'\mathrm{d}y' \frac{y'}{[x'^2 + y'^2 + z^2]^{\frac{3}{2}}} \mathrm{e}^{\mathrm{i}\frac{4\pi}{a'}\left(kx' + \frac{1}{\sqrt{3}}ky' + \frac{2}{\sqrt{3}}ly'\right)}\end{aligned} \tag{C.9}$$

The double integral in the above equation can be calculated analytically. Taking the result from Tsymbal [304] the integral is,

$$\int_{-\infty}^{\infty}\int_{-\infty}^{\infty} \mathrm{d}x\mathrm{d}y \frac{y}{(x^2 + y^2 + z^2)^{\frac{3}{2}}} \mathrm{e}^{\mathrm{i}\frac{2\pi}{a}Ax} \mathrm{e}^{\mathrm{i}\frac{2\pi}{a}By} = 2\pi\mathrm{i}\frac{B}{\sqrt{A^2 + B^2}} \mathrm{e}^{-\frac{2\pi}{a}\sqrt{A^2+B^2}|z|} \tag{C.10}$$

with $A = 2k$ and $B = \frac{2\sqrt{3}}{3}(k + 2l)$. After substituting A and B, the integral simplifies to

$$\int_{-\infty}^{\infty}\int_{-\infty}^{\infty} \frac{y'\mathrm{d}x'\mathrm{d}y'}{\left[x'^2 + y'^2 + z^2\right]^{\frac{3}{2}}} \mathrm{e}^{\mathrm{i}\frac{4\pi}{a'}\left(kx' + \frac{1}{\sqrt{3}}ky' + \frac{2}{\sqrt{3}}ly'\right)} = \pi\mathrm{i}\frac{(k+2l)}{\sqrt{k^2+kl+l^2}} \mathrm{e}^{-\frac{8\sqrt{3}\pi}{3a'}\sqrt{k^2+kl+l^2}|z|} \quad \text{(C.11)}$$

Substituting this into Φ' and collecting coefficients gives

$$\Phi'(x,y,z) = \frac{8}{\sqrt{3}}\frac{\mu_S\pi}{a'^2} \sum_{k,l=-\infty}^{\infty} \frac{\mathrm{i}(k+2l)}{\sqrt{k^2+kl+l^2}} \mathrm{e}^{-\frac{8\sqrt{3}\pi}{3a'}\sqrt{k^2+kl+l^2}|z|} \mathrm{e}^{-\mathrm{i}\frac{4\pi}{a'}\left(kx + \frac{1}{\sqrt{3}}ky + \frac{2}{\sqrt{3}}ly\right)} \quad \text{(C.12)}$$

The summations can be reduced from $k, l \in (-\infty, \infty)$ to $k, l \in [0, \infty)$ by splitting terms of the form $\sum_{k=-\infty}^{\infty} k\mathrm{e}^{-\mathrm{i}kx}$ into $\sum_{k=0}^{\infty}\left(k\mathrm{e}^{-\mathrm{i}kx} - k\mathrm{e}^{\mathrm{i}kx}\right)$ which can be further simplified into trigonometric functions. Splitting the first term of Φ' with k as a prefactor,

$$\begin{aligned}
&\sum_{k=-\infty}^{\infty}\sum_{l=-\infty}^{\infty} \mathrm{i}\frac{k}{\sqrt{k^2+kl+l^2}} \mathrm{e}^{-\mathrm{i}\frac{4\pi}{a'}\left(kx + \frac{1}{\sqrt{3}}ky + \frac{2}{\sqrt{3}}ly\right)} = \\
&\quad \sum_{k=1}^{\infty}\Bigg\{ \sum_{l=1}^{\infty} \mathrm{i}\Bigg[\frac{k}{\sqrt{k^2+kl+l^2}} \mathrm{e}^{-\frac{8\sqrt{3}\pi}{3a'}\sqrt{k^2+kl+l^2}|z|} \mathrm{e}^{-\mathrm{i}\frac{4\pi}{a'}\left(kx + \frac{1}{\sqrt{3}}ky + \frac{2}{\sqrt{3}}ly\right)} \\
&\qquad + \frac{k}{\sqrt{k^2-kl+l^2}} \mathrm{e}^{-\frac{8\sqrt{3}\pi}{3a'}\sqrt{k^2-kl+l^2}|z|} \mathrm{e}^{-\mathrm{i}\frac{4\pi}{a'}\left(kx + \frac{1}{\sqrt{3}}ky - \frac{2}{\sqrt{3}}ly\right)} \Bigg] \\
&\qquad\quad + \frac{k}{|k|} \mathrm{e}^{-\frac{8\sqrt{3}\pi}{3a'}|k||z|} \mathrm{e}^{-\mathrm{i}\frac{4\pi}{a'}\left(kx + \frac{1}{\sqrt{3}}ky\right)} \\
&\qquad - \sum_{l=1}^{\infty} \mathrm{i}\Bigg[\frac{k}{\sqrt{k^2-kl+l^2}} \mathrm{e}^{-\frac{8\sqrt{3}\pi}{3a}\sqrt{k^2-kl+l^2}|z|} \mathrm{e}^{-\mathrm{i}\frac{4\pi}{a'}\left(-kx - \frac{1}{\sqrt{3}}ky + \frac{2}{\sqrt{3}}ly\right)} \\
&\qquad + \frac{k}{\sqrt{k^2+kl+l^2}} \mathrm{e}^{-\frac{8\sqrt{3}\pi}{3a}\sqrt{k^2+kl+l^2}|z|} \mathrm{e}^{-\mathrm{i}\frac{4\pi}{a}\left(-kx - \frac{1}{\sqrt{3}}ky - \frac{2}{\sqrt{3}}ly\right)} \Bigg] \\
&\qquad\quad - \frac{k}{|k|} \mathrm{e}^{-\frac{8\sqrt{3}\pi}{3a'}|k||z|} \mathrm{e}^{-\mathrm{i}\frac{4\pi}{a'}\left(-kx - \frac{1}{\sqrt{3}}ky\right)} \Bigg\}
\end{aligned} \quad \text{(C.13)}$$

noting that the $k = 0$ and $l = 0$ coefficients are zero. This can be further simplified to

$$\begin{aligned}\sum_{k=-\infty}^{\infty}\sum_{l=-\infty}^{\infty} \mathrm{i}\frac{k}{\sqrt{k^2+kl+l^2}}\mathrm{e}^{-\mathrm{i}\frac{4\pi}{a'}\left(kx+\frac{1}{\sqrt{3}}ky+\frac{2}{\sqrt{3}}ly\right)} = \\ 2\sum_{k=1}^{\infty}\sum_{l=1}^{\infty}\frac{k}{\sqrt{k^2-kl+l^2}}\sin\left(\frac{4\pi}{a'}\left(kx+\frac{1}{\sqrt{3}}ky-\frac{2}{\sqrt{3}}ly\right)\right)\mathrm{e}^{-\frac{8\sqrt{3}\pi}{3a'}\sqrt{k^2-kl+l^2}|z|} \\ +2\sum_{k=1}^{\infty}\sum_{l=1}^{\infty}\frac{k}{\sqrt{k^2+kl+l^2}}\sin\left(\frac{4\pi}{a'}\left(kx+\frac{1}{\sqrt{3}}ky+\frac{2}{\sqrt{3}}ly\right)\right)\mathrm{e}^{-\frac{8\sqrt{3}\pi}{3a}\sqrt{k^2+kl+l^2}|z|} \\ +2\sum_{k=1}^{\infty}\sin\left(\frac{4\pi}{a'}\left(kx+\frac{1}{\sqrt{3}}ky\right)\right)\mathrm{e}^{-\frac{8\sqrt{3}\pi}{3a'}|k||z|} \quad \text{(C.14)}\end{aligned}$$

Next, we evaluate the second term of Φ' (with $2l$ as a prefactor)

$$\begin{aligned}\sum_{k=-\infty}^{\infty}\sum_{l=-\infty}^{\infty} \mathrm{i}\frac{2l}{\sqrt{k^2+kl+l^2}}\mathrm{e}^{-\frac{8\sqrt{3}\pi}{3a'}\sqrt{k^2+kl+l^2}|z|}\mathrm{e}^{-\mathrm{i}\frac{4\pi}{a'}\left(kx+\frac{1}{\sqrt{3}}ky+\frac{2}{\sqrt{3}}ly\right)} = \\ \sum_{k=1}^{\infty}\Bigg\{\sum_{l=1}^{\infty}\mathrm{i}\Bigg[\frac{2l}{\sqrt{k^2+kl+l^2}}\mathrm{e}^{-\frac{8\sqrt{3}\pi}{3a'}\sqrt{k^2+kl+l^2}|z|}\mathrm{e}^{-\mathrm{i}\frac{4\pi}{a'}\left(kx+\frac{1}{\sqrt{3}}ky+\frac{2}{\sqrt{3}}ly\right)} \\ -\frac{2l}{\sqrt{k^2-kl+l^2}}\mathrm{e}^{-\frac{8\sqrt{3}\pi}{3a'}\sqrt{k^2-kl+l^2}|z|}\mathrm{e}^{-\mathrm{i}\frac{4\pi}{a'}\left(kx+\frac{1}{\sqrt{3}}ky-\frac{2}{\sqrt{3}}ly\right)}\Bigg] \\ +\sum_{l=1}^{\infty}\mathrm{i}\Bigg[\frac{2l}{\sqrt{k^2-kl+l^2}}\mathrm{e}^{-\frac{8\sqrt{3}\pi}{3a'}\sqrt{k^2-kl+l^2}|z|}\mathrm{e}^{-\mathrm{i}\frac{4\pi}{a'}\left(-kx+\frac{1}{\sqrt{3}}ky+\frac{2}{\sqrt{3}}ly\right)} \\ -\frac{2l}{\sqrt{k^2+kl+l^2}}\mathrm{e}^{-\frac{8\sqrt{3}\pi}{3a'}\sqrt{k^2+kl+l^2}|z|}\mathrm{e}^{-\mathrm{i}\frac{4\pi}{a'}\left(-kx-\frac{1}{\sqrt{3}}ky-\frac{2}{\sqrt{3}}ly\right)}\Bigg]\Bigg\} \\ +\sum_{l=1}^{\infty}\mathrm{i}\left[\frac{2l}{|l|}\mathrm{e}^{-\frac{8\sqrt{3}\pi}{3a'}|l||z|}\mathrm{e}^{-\mathrm{i}\frac{4\pi}{a'}\frac{2}{\sqrt{3}}ly}-\frac{2l}{|l|}\mathrm{e}^{-\frac{8\sqrt{3}\pi}{3a'}|l||z|}\mathrm{e}^{\mathrm{i}\frac{4\pi}{a'}\frac{2}{\sqrt{3}}ly}\right] \quad \text{(C.15)}\end{aligned}$$

which can be simplified to

$$\begin{aligned}\sum_{k=-\infty}^{\infty}\sum_{l=-\infty}^{\infty} \mathrm{i}\frac{2l}{\sqrt{k^2+kl+l^2}}\mathrm{e}^{-\frac{8\sqrt{3}\pi}{3a'}\sqrt{k^2+kl+l^2}|z|}\mathrm{e}^{-\mathrm{i}\frac{4\pi}{a'}\left(kx+\frac{1}{\sqrt{3}}ky+\frac{2}{\sqrt{3}}ly\right)} = \\ -2\sum_{k=1}^{\infty}\sum_{l=1}^{\infty}\frac{2l}{\sqrt{k^2-kl+l^2}}\sin\left(\frac{4\pi}{a'}\left(kx+\frac{1}{\sqrt{3}}ky-\frac{2}{\sqrt{3}}ly\right)\right)\mathrm{e}^{-\frac{8\sqrt{3}\pi}{3a'}\sqrt{k^2-kl+l^2}|z|} \\ +2\sum_{k=1}^{\infty}\sum_{l=1}^{\infty}\frac{2l}{\sqrt{k^2+kl+l^2}}\sin\left(\frac{4\pi}{a'}\left(kx+\frac{1}{\sqrt{3}}ky+\frac{2}{\sqrt{3}}ly\right)\right)\mathrm{e}^{-\frac{8\sqrt{3}\pi}{3a'}\sqrt{k^2-kl+l^2}|z|} \\ +4\sum_{l=1}^{\infty}\sin\left(\frac{8\sqrt{3}\pi}{3a'}ly\right)\mathrm{e}^{-\frac{8\sqrt{3}\pi}{3a'}|l||z|} \quad \text{(C.16)}\end{aligned}$$

Combining equation C.14 and C.16, the reduced potential is

$$\begin{aligned}\Phi'(x,y,z) = \frac{8}{\sqrt{3}}\frac{\mu_S\pi}{a'^2}\Bigg[&2\sum_{k=1}^{\infty}\sum_{l=1}^{\infty}\frac{k}{\sqrt{k^2-kl+l^2}}\sin\left(\frac{4\pi}{a'}\left(kx+\tfrac{1}{\sqrt{3}}ky-\tfrac{2}{\sqrt{3}}ly\right)\right)\\ &\times \mathrm{e}^{-\frac{8\sqrt{3}\pi}{3a'}\sqrt{k^2-kl+l^2}|z|}+2\sum_{k=1}^{\infty}\sum_{l=1}^{\infty}\frac{k}{\sqrt{k^2+kl+l^2}}\sin\left(\frac{4\pi}{a'}\left(kx+\tfrac{1}{\sqrt{3}}ky+\tfrac{2}{\sqrt{3}}ly\right)\right)\\ &\times \mathrm{e}^{-\frac{8\sqrt{3}\pi}{3a'}\sqrt{k^2+kl+l^2}|z|}+2\sum_{k=1}^{\infty}\sin\left(\frac{4\pi}{a'}\left(kx+\tfrac{1}{\sqrt{3}}ky\right)\right)\mathrm{e}^{-\frac{8\sqrt{3}\pi}{3a'}|k||z|}\\ &-2\sum_{k=1}^{\infty}\sum_{l=1}^{\infty}\frac{2l}{\sqrt{k^2-kl+l^2}}\sin\left(\frac{4\pi}{a'}\left(kx+\tfrac{1}{\sqrt{3}}ky-\tfrac{2}{\sqrt{3}}ly\right)\right)\mathrm{e}^{-\frac{8\sqrt{3}\pi}{3a'}\sqrt{k^2-kl+l^2}|z|}\\ &+2\sum_{k=1}^{\infty}\sum_{l=1}^{\infty}\frac{2l}{\sqrt{k^2+kl+l^2}}\sin\left(\frac{4\pi}{a'}\left(kx+\tfrac{1}{\sqrt{3}}ky+\tfrac{2}{\sqrt{3}}ly\right)\right)\mathrm{e}^{-\frac{8\sqrt{3}\pi}{3a'}\sqrt{k^2-kl+l^2}|z|}\\ &+4\sum_{l=1}^{\infty}\sin\left(\frac{8\sqrt{3}\pi}{3a'}ly\right)\mathrm{e}^{-\frac{8\sqrt{3}\pi}{3a'}|l||z|}\Bigg]\end{aligned} \tag{C.17}$$

which simplifies to

$$\begin{aligned}\Phi'(x,y,z) = \frac{16}{\sqrt{3}}\frac{\mu_S\pi}{a'^2}\Bigg[&\sum_{k=1}^{\infty}\sum_{l=1}^{\infty}\frac{(k-2l)}{\sqrt{k^2-kl+l^2}}\sin\left(\frac{4\pi}{a'}\left(kx+\tfrac{1}{\sqrt{3}}ky-\tfrac{2}{\sqrt{3}}ly\right)\right)\\ &\times \mathrm{e}^{-\frac{8\sqrt{3}\pi}{3a'}\sqrt{k^2-kl+l^2}|z|}+\sum_{k=1}^{\infty}\sum_{l=1}^{\infty}\frac{(k+2l)}{\sqrt{k^2+kl+l^2}}\sin\left(\frac{4\pi}{a'}\left(kx+\tfrac{1}{\sqrt{3}}ky+\tfrac{2}{\sqrt{3}}ly\right)\right)\\ &\times \mathrm{e}^{-\frac{8\sqrt{3}\pi}{3a'}\sqrt{k^2+kl+l^2}|z|}+\sum_{k=1}^{\infty}\sin\left(\frac{4\pi}{a'}\left(kx+\tfrac{1}{\sqrt{3}}ky\right)\right)\mathrm{e}^{-\frac{8\sqrt{3}\pi}{3a'}|k||z|}\\ &+2\sum_{l=1}^{\infty}\sin\left(\frac{8\sqrt{3}\pi}{3a'}ly\right)\mathrm{e}^{-\frac{8\sqrt{3}\pi}{3a'}|l||z|}\Bigg]\end{aligned} \tag{C.18}$$

Now we must transform the reduced potential back into a magnetic field. The field is written

$$\mathbf{B}(x,y,z) = -\mu_0\nabla\Phi(x,y,z) = -\frac{\mu_0}{4\pi}\nabla\Phi'(x,y,z) \tag{C.19}$$

First calculating $\frac{\partial \Phi'}{\partial x}$

$$\frac{\partial \Phi'}{\partial x} = \frac{16}{\sqrt{3}} \frac{\mu_S \pi}{a'^2} \Bigg[\sum_{k=1}^{\infty} \sum_{l=1}^{\infty} \frac{(k-2l)}{\sqrt{k^2-kl+l^2}} \left(\frac{4\pi}{a'} k \right) \cos\left(\frac{4\pi}{a'} \left(kx + \tfrac{1}{\sqrt{3}} ky - \tfrac{2}{\sqrt{3}} ly \right) \right) \times \mathrm{e}^{-\frac{8\sqrt{3}\pi}{3a'} \sqrt{k^2-kl+l^2}|z|} + \sum_{k=1}^{\infty} \sum_{l=1}^{\infty} \frac{(k+2l)}{\sqrt{k^2+kl+l^2}} \left(\frac{4\pi}{a'} k \right) \times \cos\left(\frac{4\pi}{a'} \left(kx + \tfrac{1}{\sqrt{3}} ky + \tfrac{2}{\sqrt{3}} ly \right) \right) \mathrm{e}^{-\frac{8\sqrt{3}\pi}{3a'} \sqrt{k^2+kl+l^2}|z|} + \sum_{k=1}^{\infty} \left(\frac{4\pi}{a'} k \right) \cos\left(\frac{4\pi}{a'} \left(kx + \tfrac{1}{\sqrt{3}} ky \right) \right) \mathrm{e}^{-\frac{8\sqrt{3}\pi}{3a'} |k||z|} \Bigg] \quad \text{(C.20)}$$

which can be simplified to

$$\frac{\partial \Phi'}{\partial x} = \frac{64}{\sqrt{3}} \frac{\mu_S \pi^2}{a'^3} \Bigg[\sum_{k=1}^{\infty} \sum_{l=1}^{\infty} \frac{(k-2l)k}{\sqrt{k^2-kl+l^2}} \cos\left(\frac{4\pi}{a'} \left(kx + \tfrac{1}{\sqrt{3}} ky - \tfrac{2}{\sqrt{3}} ly \right) \right) \times \mathrm{e}^{-\frac{8\sqrt{3}\pi}{3a'} \sqrt{k^2-kl+l^2}|z|} + \sum_{k=1}^{\infty} \sum_{l=1}^{\infty} \frac{(k+2l)k}{\sqrt{k^2+kl+l^2}} \cos\left(\frac{4\pi}{a'} \left(kx + \tfrac{1}{\sqrt{3}} ky + \tfrac{2}{\sqrt{3}} ly \right) \right) \times \mathrm{e}^{-\frac{8\sqrt{3}\pi}{3a'} \sqrt{k^2+kl+l^2}|z|} + \sum_{k=1}^{\infty} k \cos\left(\frac{4\pi}{a'} \left(kx + \tfrac{1}{\sqrt{3}} ky \right) \right) \mathrm{e}^{-\frac{8\sqrt{3}\pi}{3a'} |k||z|} \Bigg] \quad \text{(C.21)}$$

Then calculating $\frac{\partial \Phi'}{\partial y}$

$$\frac{\partial \Phi'}{\partial y} = \frac{16}{\sqrt{3}} \frac{\mu_S \pi}{a'^2} \Bigg[\sum_{k=1}^{\infty} \sum_{l=1}^{\infty} \frac{(k-2l)}{\sqrt{k^2-kl+l^2}} \left(\frac{4\pi}{a'} (\tfrac{1}{\sqrt{3}} k - \tfrac{2}{\sqrt{3}} l) \right) \cos\left(\frac{4\pi}{a'} \left(kx + \tfrac{1}{\sqrt{3}} ky - \tfrac{2}{\sqrt{3}} ly \right) \right) \mathrm{e}^{-\frac{8\sqrt{3}\pi}{3a'} \sqrt{k^2-kl+l^2}|z|} + \sum_{k=1}^{\infty} \sum_{l=1}^{\infty} \frac{(k+2l)}{\sqrt{k^2+kl+l^2}} \times \left(\frac{4\pi}{a'} (\tfrac{1}{\sqrt{3}} k + \tfrac{2}{\sqrt{3}} l) \right) \cos\left(\frac{4\pi}{a'} \left(kx + \tfrac{1}{\sqrt{3}} ky + \tfrac{2}{\sqrt{3}} ly \right) \right) \mathrm{e}^{-\frac{8\sqrt{3}\pi}{3a'} \sqrt{k^2+kl+l^2}|z|} + \sum_{k=1}^{\infty} \left(\frac{4\sqrt{3}\pi}{3a'} k \right) \cos\left(\frac{4\pi}{a'} \left(kx + \tfrac{1}{\sqrt{3}} ky \right) \right) \mathrm{e}^{-\frac{8\sqrt{3}\pi}{3a'} |k||z|} + 2 \sum_{l=1}^{\infty} \left(\frac{8\sqrt{3}}{3a'} l \right) \cos\left(\frac{8\sqrt{3}\pi}{3a'} ly \right) \mathrm{e}^{-\frac{8\sqrt{3}\pi}{3a'} |l||z|} \Bigg] \quad \text{(C.22)}$$

which can be simplified to

$$\frac{\partial\Phi}{\partial y} = \frac{64}{3}\frac{\mu_S\pi^2}{a'^3}\Bigg[\sum_{k=1}^{\infty}\sum_{l=1}^{\infty}\frac{(k-2l)^2}{\sqrt{k^2-kl+l^2}}\cos\left(\frac{4\pi}{a'}\left(kx+\tfrac{1}{\sqrt{3}}ky-\tfrac{2}{\sqrt{3}}ly\right)\right) \times \mathrm{e}^{-\frac{8\sqrt{3}\pi}{3a'}\sqrt{k^2-kl+l^2}|z|} + \sum_{k=1}^{\infty}\sum_{l=1}^{\infty}\frac{(k+2l)^2}{\sqrt{k^2+kl+l^2}}\cos\left(\frac{4\pi}{a'}\left(kx+\tfrac{1}{\sqrt{3}}ky+\tfrac{2}{\sqrt{3}}ly\right)\right) \mathrm{e}^{-\frac{8\sqrt{3}\pi}{3a'}\sqrt{k^2+kl+l^2}|z|} + \sum_{k=1}^{\infty}k\cos\left(\frac{4\pi}{a'}\left(kx+\tfrac{1}{\sqrt{3}}ky\right)\right)\mathrm{e}^{-\frac{8\sqrt{3}\pi}{3a'}|k||z|} + 2\sum_{l=1}^{\infty}2l\cos\left(\frac{8\sqrt{3}\pi}{3a'}ly\right)\mathrm{e}^{-\frac{8\sqrt{3}\pi}{3a'}|l||z|}\Bigg] \quad \text{(C.23)}$$

We want to calculate B_y. Using equation C.19, this is

$$B_y = -\frac{16}{3}\frac{\mu_S\mu_0\pi}{a'^3}\Bigg[\sum_{k=1}^{\infty}\sum_{l=1}^{\infty}\frac{(k-2l)^2}{\sqrt{k^2-kl+l^2}}\cos\left(\frac{4\pi}{a'}\left(kx+\tfrac{1}{\sqrt{3}}ky-\tfrac{2}{\sqrt{3}}ly\right)\right) \times \mathrm{e}^{-\frac{8\sqrt{3}\pi}{3a'}\sqrt{k^2-kl+l^2}|z|} + \sum_{k=1}^{\infty}\sum_{l=1}^{\infty}\frac{(k+2l)^2}{\sqrt{k^2+kl+l^2}}\cos\left(\frac{4\pi}{a'}\left(kx+\tfrac{1}{\sqrt{3}}ky+\tfrac{2}{\sqrt{3}}ly\right)\right) \times \mathrm{e}^{-\frac{8\sqrt{3}\pi}{3a'}\sqrt{k^2+kl+l^2}|z|} + \sum_{k=1}^{\infty}k\cos\left(\frac{4\pi}{a'}\left(kx+\tfrac{1}{\sqrt{3}}ky\right)\right)\mathrm{e}^{-\frac{8\sqrt{3}\pi}{3a'}|k||z|} + 2\sum_{l=1}^{\infty}2l\cos\left(\frac{8\sqrt{3}\pi}{3a'}ly\right)\mathrm{e}^{-\frac{8\sqrt{3}\pi}{3a'}|l||z|}\Bigg] \quad \text{(C.24)}$$

For this to be useful, the harmonics must be summed over, and the coordinates of an atom in another film by inputted as $\mathbf{R} = (x, y, z)$. This gives the dipole field due to a (111) sheet of NiO at arbitrary distance. The same procedure needs to be undertaken for a film magnetised out-of-plane to calculate the energy difference.

C.3 Calculating $B_{\mathbf{x}}$

For consistency, we can check the anisotropy is easy plane by calculating $\mathbf{B}_x$ and checking its value is equal to $\mathbf{B}_y$. For completeness, we include the derivation of the dipolar field for spins lying in the x-direction here. The reduced magnetic potential is

$$\Phi'(x,y,z) = \frac{8\mu_S}{\sqrt{3}a'^2}\sum_{k,l=-\infty}^{\infty}\mathrm{e}^{-\mathrm{i}\frac{4\pi}{a'}\left(kx+\frac{ky}{\sqrt{3}}+\frac{2ly}{\sqrt{3}}\right)}\int_{-\infty}^{\infty}\int_{-\infty}^{\infty}\frac{x'}{\left[x'^2+y'^2+z^2\right]^{\frac{3}{2}}} \times \mathrm{e}^{-\frac{4\pi}{\sqrt{3}a'}\left(kx+\frac{ky}{\sqrt{3}}+\frac{2ly}{\sqrt{3}}\right)}\mathrm{d}x'\mathrm{d}y' \quad \text{(C.25)}$$

The integral is identical to the one in C.9 upon relabelling x and y giving

$$\Phi' = \frac{16\pi\mu_S}{a'^2}\sum_{k,l=-\infty}^{\infty}\frac{k}{\sqrt{(k+2l)^2+3k^2}}\mathrm{i}\mathrm{e}^{-\mathrm{i}\frac{4\pi}{a'}\left(kx+\frac{ky}{\sqrt{3}}+\frac{2ly}{\sqrt{3}}\right)}\mathrm{e}^{-\frac{4\pi}{\sqrt{3}a'}\sqrt{(k+2l)^2+3k^2}|z|} \tag{C.26}$$

Unlike C.9, when separated, $k=0$ gives are no terms

$$\begin{aligned}\Phi' = \frac{16\pi\mu_S}{a'^2}\Bigg[&\sum_{k=1}^{\infty}\frac{1}{2\mathrm{i}}\left(\mathrm{e}^{\mathrm{i}\frac{4\pi}{a'}\left(kx+\frac{ky}{\sqrt{3}}\right)}-\mathrm{e}^{-\mathrm{i}\frac{4\pi}{a'}\left(kx+\frac{ky}{\sqrt{3}}\right)}\right)+\sum_{k,l,=1}^{\infty}\Bigg\{\frac{k}{2\mathrm{i}\sqrt{k^2+kl+l^2}}\\&\left(\mathrm{e}^{\mathrm{i}\frac{4\pi}{a'}\left(kx+\frac{ky}{\sqrt{3}}+\frac{2ly}{\sqrt{3}}\right)}-\mathrm{e}^{-\mathrm{i}\frac{4\pi}{a'}\left(kx+\frac{ky}{\sqrt{3}}+\frac{2ly}{\sqrt{3}}\right)}\right)\mathrm{e}^{-\frac{8\pi}{\sqrt{3}a'}\sqrt{k^2+kl+l^2}|z|}\\+\frac{k}{2\mathrm{i}\sqrt{k^2-kl+l^2}}&\left(\mathrm{e}^{\mathrm{i}\frac{4\pi}{a'}\left(kx+\frac{ky}{\sqrt{3}}-\frac{2ly}{\sqrt{3}}\right)}-\mathrm{e}^{-\mathrm{i}\frac{4\pi}{a'}\left(kx+\frac{ky}{\sqrt{3}}-\frac{2ly}{\sqrt{3}}\right)}\right)\mathrm{e}^{-\frac{8\pi}{\sqrt{3}a}\sqrt{k^2-kl+l^2}|z|}\end{aligned} \tag{C.27}$$

This can be reduced to

$$\begin{aligned}\Phi' = \frac{16\pi\mu_S}{a'^2}\Bigg[&\sum_{k=1}^{\infty}\sin\left(\frac{4\pi}{a'}k\left(x+\frac{y}{\sqrt{3}}\right)\right)\mathrm{e}^{-\frac{8\pi}{\sqrt{3}}k|z|}+\sum_{k,l,=1}^{\infty}\Bigg\{\frac{k}{\sqrt{k^2+kl+l^2}}\\&\times\sin\left(\frac{4\pi}{a'}\left(kx+\frac{ky}{\sqrt{3}}+\frac{2ly}{\sqrt{3}}\right)\right)\mathrm{e}^{-\frac{8\pi}{\sqrt{3}a'}\sqrt{k^2+kl+l^2}|z|}\\&+\frac{k}{\sqrt{k^2-kl+l^2}}\sin\left(\frac{4\pi}{a'}\left(kx+\frac{ky}{\sqrt{3}}-\frac{2ly}{\sqrt{3}}\right)\right)\mathrm{e}^{-\frac{8\pi}{\sqrt{3}a'}\sqrt{k^2-kl+l^2}|z|}\Bigg\}\Bigg]\end{aligned} \tag{C.28}$$

As before, reintroduce a factor $\frac{1}{4\pi}$ and differentiate to get the dipolar field

$$\begin{aligned}\mathrm{B}_x = -\frac{4\mu_0\mu_S}{a'^2}\Bigg[&\sum_{k=1}^{\infty}\left(\frac{4\pi}{a'}k\right)\cos\left(\frac{4\pi}{a'}k\left(x+\frac{y}{\sqrt{3}}\right)\right)\mathrm{e}^{-\frac{8\pi}{\sqrt{3}}k|z|}+\sum_{k,l,=1}^{\infty}\Bigg\{\left(\frac{4\pi}{a'}k\right)\\&\times\frac{k}{\sqrt{k^2+kl+l^2}}\cos\left(\frac{4\pi}{a'}\left(kx+\frac{ky}{\sqrt{3}}+\frac{2ly}{\sqrt{3}}\right)\right)\mathrm{e}^{-\frac{8\pi}{\sqrt{3}a'}\sqrt{k^2+kl+l^2}|z|}\\&+\left(\frac{4\pi}{a'}k\right)\frac{k}{\sqrt{k^2-kl+l^2}}\cos\left(\frac{4\pi}{a'}\left(kx+\frac{ky}{\sqrt{3}}-\frac{2ly}{\sqrt{3}}\right)\right)\mathrm{e}^{-\frac{8\pi}{\sqrt{3}a'}\sqrt{k^2-kl+l^2}|z|}\Bigg\}\Bigg]\end{aligned} \tag{C.29}$$

Collecting $\frac{4\pi}{a'}$ terms we have

$$\begin{aligned}\mathrm{B}_x = -\frac{16\mu_0\mu_S}{a'^3}\Bigg[&\sum_{k=1}^{\infty}k\cos\left(\frac{4\pi}{a'}k\left(x+\frac{y}{\sqrt{3}}\right)\right)\mathrm{e}^{-\frac{8\pi}{\sqrt{3}}k|z|}+\sum_{k,l,=1}^{\infty}\Bigg\{\frac{k^2}{\sqrt{k^2+kl+l^2}}\\&\cos\left(\frac{4\pi}{a'}\left(kx+\frac{ky}{\sqrt{3}}+\frac{2ly}{\sqrt{3}}\right)\right)\mathrm{e}^{-\frac{8\pi}{\sqrt{3}a'}\sqrt{k^2+kl+l^2}|z|}\\&+\frac{k^2}{\sqrt{k^2-kl+l^2}}\cos\left(\frac{4\pi}{a'}\left(kx+\frac{ky}{\sqrt{3}}-\frac{2ly}{\sqrt{3}}\right)\right)\mathrm{e}^{-\frac{8\pi}{\sqrt{3}a'}\sqrt{k^2-kl+l^2}|z|}\Bigg\}\Bigg]\end{aligned} \tag{C.30}$$

C.4 Calculating B_z

The reduced magnetic scalar potential for an out-of-plane spin configuration is given by

$$\Phi'(x,y,z) = \sum_{n,m=-\infty}^{\infty} \frac{\mu_S z}{\left[\left(x - \frac{1}{2}na' + \frac{1}{4}ma'\right)\right)^2 + \left(y - \frac{\sqrt{3}}{4}ma'\right)^2 + z^2\right]^{\frac{3}{2}}} \tag{C.31}$$

Upon applying a Fourier transform this becomes

$$\Phi'(x,y,z) = \frac{8\mu_S}{\sqrt{3}a'^2} \sum_{k,l=-\infty}^{\infty} \mathrm{e}^{-\mathrm{i}\frac{4\pi}{a'}\left(kx + \frac{ky}{\sqrt{3}} + \frac{2ly}{\sqrt{3}}\right)} \int_{-\infty}^{\infty}\int_{-\infty}^{\infty} \frac{z\mathrm{d}x'\mathrm{d}y'}{\left[x'^2 + y'^2 + z^2\right]^{\frac{3}{2}}} \times \mathrm{e}^{\mathrm{i}\frac{4\pi}{a'}\left(kx + \frac{ky}{\sqrt{3}} + \frac{2ly}{\sqrt{3}}\right)} \tag{C.32}$$

The double integral can be simplified by letting the exponential function take the form $\mathrm{e}^{i(ax+by)}$ where a and b are now dummy coefficients. The following integral can be calculated analytically

$$\int_{-\infty}^{\infty}\int_{-\infty}^{\infty} \mathrm{d}x\mathrm{d}y \; \frac{z \; \mathrm{e}^{iax} \; \mathrm{e}^{iby}}{\left[x^2 + y^2 + z^2\right]^{\frac{3}{2}}} \tag{C.33}$$

Rewriting in cylindrical polar coordinates this becomes

$$\int_0^{\infty}\int_0^{2\pi} \mathrm{d}\theta\mathrm{d}r \; \frac{z \; r \, \mathrm{e}^{ir(a\sin\theta + b\cos\theta)}}{\left[r^2 + z^2\right]^{\frac{3}{2}}} \tag{C.34}$$

The integral over θ be factorised to give

$$\int_0^{\infty} \mathrm{d}r \frac{z}{\left[r^2 + z^2\right]^{\frac{3}{2}}} \int_0^{2\pi} \mathrm{e}^{ir(a\sin\theta + b\cos\theta)} \, \mathrm{d}\theta \tag{C.35}$$

To compute the inner integral, we need the following result from the definition of the zeroth order Bessel function of the first kind

$$2\pi J_0(x) = \int_0^{2\pi} e^{ix\sin\theta} \, \mathrm{d}\theta = \int_0^{2\pi} e^{ix\cos\theta} \, \mathrm{d}\theta \tag{C.36}$$

Extending this result to the case when the exponent is a sum of trigonometric functions gives

$$\int_0^{2\pi} e^{ix(a\sin\theta + b\cos\theta)} \, \mathrm{d}\theta = 2\pi J_0(x\sqrt{a^2 + b^2}) \tag{C.37}$$

Our simplified integral is therefore

$$\int_0^{\infty} \mathrm{d}r \frac{z}{\left[r^2 + z^2\right]^{\frac{3}{2}}} \int_0^{2\pi} \mathrm{e}^{ir(a\sin\theta + b\cos\theta)} \, \mathrm{d}\theta = \int_0^{\infty} \frac{z \, r \, \mathrm{d}r}{\left[r^2 + z^2\right]^{\frac{3}{2}}} \left[2\pi J_0(r \; \sqrt{a^2 + b^2})\right] \tag{C.38}$$

The integral over r is a standard result, its derivation is more detailed than required for this calculation. The result is

$$2\pi \int_0^\infty \frac{z\, r\, J_0\left(r\sqrt{a^2+b^2}\right)}{\left[r^2+z^2\right]^{\frac{3}{2}}} dr = 2\pi \frac{z\ \mathrm{e}^{-\sqrt{a^2+b^2}|z|}}{|z|} \tag{C.39}$$

Now we can return to the reduced potential, upon substitution this yields

$$\Phi'(x,y,z) = \frac{16\pi\mu_S}{\sqrt{3}a'^2}\ \mathrm{sign}(z) \sum_{k,l=-\infty}^{\infty} \mathrm{e}^{-\mathrm{i}\frac{4\pi}{a'}\left(kx+\frac{1}{\sqrt{3}}ky+\frac{2}{\sqrt{3}}ly\right)} \mathrm{e}^{-\frac{8\pi}{\sqrt{3}a'}\sqrt{k^2+kl+l^2}|z|} \tag{C.40}$$

As with the in-plane calculation, the sum can be split into trigonometric functions. Explicitly for the case when $l=0$, we have a term

$$\sum_{k=-\infty}^{\infty} \Bigg|_{l=0} \mathrm{e}^{-\frac{4\pi}{a'}(kx+\frac{1}{\sqrt{3}}ky)}\ \mathrm{e}^{-\frac{8\pi}{\sqrt{3}a'}|k||z|} = 2\sum_{k=1}^{\infty} \cos\left(\frac{4\pi}{a'}\left(kx+\frac{1}{\sqrt{3}}ky\right)\right) \mathrm{e}^{-\frac{8\pi}{\sqrt{3}a'}k|z|} \tag{C.41}$$

Expanding the summations we obtain

$$\begin{aligned}\Phi' = \frac{16\pi\mu_S}{\sqrt{3}a'^2}\mathrm{sign}(z)\Bigg[&\sum_{k=1}^{\infty}\left(\mathrm{e}^{\mathrm{i}\frac{4\pi}{a'}k\left(x+\frac{y}{\sqrt{3}}\right)}+\mathrm{e}^{-\mathrm{i}\frac{4\pi}{a'}k\left(x+\frac{y}{\sqrt{3}}\right)}\right)\mathrm{e}^{-\frac{8\pi}{\sqrt{3}}k|z|}\\ &+\sum_{l=1}^{\infty}\left(\mathrm{e}^{\mathrm{i}\frac{8\pi}{\sqrt{3}a'}ly}+\mathrm{e}^{-\mathrm{i}\frac{8\pi}{\sqrt{3}a'}ly}\right)\mathrm{e}^{-\frac{8\pi}{\sqrt{3}a'}l|z|}+\left[\sum_{k=1}^{\infty}+\sum_{k=-1}^{-\infty}\right]\\ &\times\left[\sum_{l=1}^{\infty}+\sum_{l=-1}^{-\infty}\right]\mathrm{e}^{-\mathrm{i}\frac{4\pi}{a'}\left(kx+\frac{ky}{\sqrt{3}}+\frac{2ly}{\sqrt{3}}\right)}\mathrm{e}^{-\frac{8\pi}{\sqrt{3}a'}\sqrt{k^2+kl+l^2}|z|}\Bigg]\end{aligned} \tag{C.42}$$

The final term inside the double summation can be rewritten as

$$\begin{aligned}\sum_{k,l,=1}^{\infty}\Bigg\{&\left(\mathrm{e}^{\mathrm{i}\frac{4\pi}{a'}\left(kx+\frac{ky}{\sqrt{3}}+\frac{2ly}{\sqrt{3}}\right)}+\mathrm{e}^{-\mathrm{i}\frac{4\pi}{a'}\left(kx+\frac{ky}{\sqrt{3}}+\frac{2ly}{\sqrt{3}}\right)}\right)\mathrm{e}^{-\frac{8\pi}{\sqrt{3}}\sqrt{k^2+kl+l^2}|z|}\\ &+\left(\mathrm{e}^{\mathrm{i}\frac{4\pi}{a'}\left(kx+\frac{ky}{\sqrt{3}}+\frac{2ly}{\sqrt{3}}\right)}+\mathrm{e}^{-\mathrm{i}\frac{4\pi}{a'}\left(kx+\frac{ky}{\sqrt{3}}+\frac{2ly}{\sqrt{3}}\right)}\right)\mathrm{e}^{-\frac{8\pi}{\sqrt{3}}\sqrt{k^2+kl+l^2}|z|}\Bigg\}\end{aligned} \tag{C.43}$$

We can rewrite this as

$$\begin{aligned}\Phi' = \frac{32\pi\mu_S}{\sqrt{3}a'^2}\mathrm{sign}(z)\Bigg[&\sum_{k=1}^{\infty}\cos\left(\frac{4\pi}{a'}(kx+\tfrac{ky}{\sqrt{3}})\right)\mathrm{e}^{-\frac{8\pi}{\sqrt{3}a'}k|z|}+\sum_{l=1}^{\infty}\cos\left(\frac{8\pi}{\sqrt{3}a'}ly\right)\mathrm{e}^{-\frac{8\pi}{\sqrt{3}a'}l|z|}\\ &+\sum_{k,l=1}^{\infty}\Bigg\{\cos\left(\frac{4\pi}{a'}(kx+\tfrac{ky}{\sqrt{3}}+\tfrac{2ly}{\sqrt{3}})\right)\mathrm{e}^{-\frac{8\pi}{\sqrt{3}a'}\sqrt{k^2+kl+l^2}|z|}\\ &+\cos\left(\frac{4\pi}{a'}(kx+\tfrac{ky}{\sqrt{3}}-\tfrac{2ly}{\sqrt{3}})\right)\mathrm{e}^{-\frac{8\pi}{\sqrt{3}a'}\sqrt{k^2-kl+l^2}|z|}\Bigg\}\Bigg]\end{aligned} \tag{C.44}$$

By reintroducing the factor $\frac{1}{4\pi}$ and differentiating, we yield the effective field

$$\begin{aligned}
\mathrm{B}_z = -\frac{8\mu_0\mu_S}{\sqrt{3}a'^2}\mathrm{sign}(z)\Bigg[\sum_{k=1}^{\infty}\left(-\frac{8\pi}{\sqrt{3}a'}k\ \mathrm{sign}(z)\right)\cos\left(\frac{4\pi}{a'}(kx+\tfrac{ky}{\sqrt{3}})\right)\mathrm{e}^{-\frac{8\pi}{\sqrt{3}a'}k|z|} \\
+\sum_{l=1}^{\infty}\left(-\frac{8\pi}{\sqrt{3}a'}l\ \mathrm{sign}(z)\right)\cos\left(\frac{8\pi}{\sqrt{3}a'}ly\right)\mathrm{e}^{-\frac{8\pi}{\sqrt{3}a'}l|z|}+\sum_{k,l=1}^{\infty}\Bigg\{\Big(\frac{-8\pi}{\sqrt{3}a'} \\
\times\sqrt{k^2+kl+l^2}\mathrm{sign}(z)\Big)\cos\left(\frac{4\pi}{a'}(kx+\tfrac{ky}{\sqrt{3}}+\tfrac{2ly}{\sqrt{3}})\right)\mathrm{e}^{\frac{-8\pi}{\sqrt{3}a'}\sqrt{k^2+kl+l^2}|z|}+\Big(\frac{-8\pi}{\sqrt{3}a'} \\
\times\sqrt{k^2-kl+l^2}\mathrm{sign}(z)\Big)\cos\left(\frac{4\pi}{a'}(kx+\tfrac{ky}{\sqrt{3}}-\tfrac{2ly}{\sqrt{3}})\right)\mathrm{e}^{-\frac{8\pi}{\sqrt{3}a'}\sqrt{k^2-kl+l^2}|z|}\Bigg\}\Bigg] \qquad \text{(C.45)}
\end{aligned}$$

Factoring out $-\frac{8\pi}{\sqrt{3}a'}\mathrm{sign}(z)$ gives

$$\begin{aligned}
\mathrm{B}_z = \frac{64\pi\mu_0\mu_S}{3a'^3}\Bigg[\sum_{k=1}^{\infty}k\cos\left(\frac{4\pi}{a'}(kx+\tfrac{ky}{\sqrt{3}})\right)\mathrm{e}^{-\frac{8\pi}{\sqrt{3}a'}k|z|}+\sum_{l=1}^{\infty}l\cos\left(\frac{8\pi}{\sqrt{3}a'}ly\right) \\
\times\mathrm{e}^{-\frac{8\pi}{\sqrt{3}a'}l|z|}+\sum_{k,l=1}^{\infty}\Bigg\{\sqrt{k^2+kl+l^2}\cos\left(\frac{4\pi}{a'}(kx+\tfrac{ky}{\sqrt{3}}+\tfrac{2ly}{\sqrt{3}})\right)\mathrm{e}^{-\frac{8\pi}{\sqrt{3}a'}\sqrt{k^2+kl+l^2}|z|} \\
+\sqrt{k^2-kl+l^2}\cos\left(\frac{4\pi}{a'}(kx+\tfrac{ky}{\sqrt{3}}-\tfrac{2ly}{\sqrt{3}})\right)\mathrm{e}^{-\frac{8\pi}{\sqrt{3}a'}\sqrt{k^2-kl+l^2}|z|}\Bigg\}\Bigg] \qquad \text{(C.46)}
\end{aligned}$$

C.5 Calculating the Dipole Anisotropy

Now both the in-plane and out-of-plane magnetic field from an atomic film of (111) textured NiO have been derived, the above equations are analytic and only the first few (~ 10) harmonics will have to be summed for the field to converge to sufficient precision. The energy can then be calculated by taking the dot product of the field with a spin direction which is parallel, or antiparallel to the spin direction considered.

The position vector $\mathbf{R} = (x, y, z)$ does not have to be close to the origin as all terms are periodic with the reciprocal lattice vectors. Recalling the intraplane translation vectors $\mathbf{v}_1 = (1/2, 0, 0)\, a'$ and $\mathbf{v}_2 = \left(-1/4, \sqrt{3}/4, 0\right) a'$, and the interplane lattice vector $\mathbf{v}_3$ and is $\mathbf{v}_3 = (0, \sqrt{3}/6, \sqrt{6}/6)a'$ where $a' = \sqrt{2}a$ as defined at the beginning. The displacement vector between the origin and an atom in the nth layer is given by substituting $\mathbf{R}_n = n\mathbf{v}_3$, where n is an integer, into the analytic form of the dipolar field (this is not the closest atom, but this is irrelevant for infinite systems). The out-of-plane dipole-dipole energy for a single spin at the origin due to an ensemble of spins in

thermal equilibrium assuming the zeroth layer of spins is pointing in the $+z$-direction can be calculated by summing over layers. The energy is given by

$$E_z = -\mu_S \sum_n (-1)^n B_z(\mathbf{R}_n) \tag{C.47}$$

where the factor $(-1)^n$ accounts for the antiparallel alignment of neighbouring sheets. We are free to choose the thermal sublattice magnetisation because we assume the anisotropy–and the external applied field strength in an experiment to force this state–is small enough not to affect the thermodynamics of the sublattice magnetisation. The same approximation is made in the calculation of Bloch's law, and Kubo's extension to antiferromagnets [148]. The dipole energy with the spins lying in the x-direction is

$$\begin{aligned} E_x = -\frac{8\mu_0\mu_S^2}{a'^3} \sum_{n=-\infty}^{\infty} (-1)^n \Bigg[\sum_{k=1}^{\infty} k \cos\left(k\mathbf{b}_1 \cdot \mathbf{R}_n\right) \mathrm{e}^{-\frac{8\pi}{\sqrt{3}}k|z|} + \sum_{k,l,=1}^{\infty} \Bigg\{ \frac{k^2}{\sqrt{k^2+kl+l^2}} \\ \times \cos\left((k\mathbf{b}_1 + l\mathbf{b}_2) \cdot \mathbf{R}_n\right) \mathrm{e}^{-\frac{8\pi}{\sqrt{3}a'}\sqrt{k^2+kl+l^2}|z|} + \frac{k^2}{\sqrt{k^2-kl+l^2}} \\ \times \cos\left((k\mathbf{b}_1 - l\mathbf{b}_2) \cdot \mathbf{R}_n\right) \mathrm{e}^{-\frac{8\pi}{\sqrt{3}a'}\sqrt{k^2-kl+l^2}|z|} \Bigg\} \Bigg] \end{aligned} \tag{C.48}$$

The dipole energy with spins lying in the z-direction is

$$\begin{aligned} E_z = \frac{64\pi\mu_0\mu_S^2}{3a'^3} \sum_{n=-\infty}^{\infty} (-1)^n \Bigg[\sum_{k=1}^{\infty} k \cos\left(k\mathbf{b}_1 \cdot \mathbf{R}_n\right) \mathrm{e}^{-\frac{8\pi}{\sqrt{3}a'}k|z|} + \sum_{l=1}^{\infty} l \cos\left(l\mathbf{b}_2 \cdot \mathbf{R}_n\right) \\ \times \mathrm{e}^{-\frac{8\pi}{\sqrt{3}a'}l|z|} + \sum_{k,l=1}^{\infty} \Bigg\{ \sqrt{k^2+kl+l^2} \cos\left((k\mathbf{b}_1 + l\mathbf{b}_2) \cdot \mathbf{R}_n\right) \mathrm{e}^{-\frac{8\pi}{\sqrt{3}a'}\sqrt{k^2+kl+l^2}|z|} \\ + \sqrt{k^2-kl+l^2} \cos\left((k\mathbf{b}_1 - l\mathbf{b}_2) \cdot \mathbf{R}_n\right)\right) \mathrm{e}^{-\frac{8\pi}{\sqrt{3}a'}\sqrt{k^2-kl+l^2}|z|} \Bigg\} \Bigg] \end{aligned} \tag{C.49}$$

Let's define $\varphi_{kl}^{\pm} = \sqrt{k^2 \pm kl + l^2}$ to write this more succinctly, this gives

$$\begin{aligned} E_x = -\frac{8\mu_0\mu_S^2}{a'^3} \sum_{n=-\infty}^{\infty} (-1)^n \Bigg[\sum_{k=1}^{\infty} k \cos\left(k\mathbf{b}_1 \cdot \mathbf{R}_n\right) \mathrm{e}^{-\frac{8\pi}{\sqrt{3}}k|z|} + \sum_{k,l,=1}^{\infty} \Bigg\{ \frac{k^2}{\varphi_{kl}^{+}} \times \\ \cos\left((k\mathbf{b}_1 + l\mathbf{b}_2) \cdot \mathbf{R}_n\right) \mathrm{e}^{-\frac{8\pi}{\sqrt{3}a'}\varphi_{kl}^{+}|z|} + \frac{k^2}{\varphi_{kl}^{-}} \cos\left((k\mathbf{b}_1 - l\mathbf{b}_2) \cdot \mathbf{R}_n\right) \mathrm{e}^{-\frac{8\pi}{\sqrt{3}a'}\varphi_{kl}^{-}|z|} \Bigg\} \Bigg], \end{aligned} \tag{C.50}$$

and

$$E_z = \frac{64\pi\mu_0\mu_S^2}{3a'^3}\sum_{n=-\infty}^{\infty}(-1)^n\Bigg[\sum_{k=1}^{\infty}k\cos\left(k\mathbf{b}_1\cdot\mathbf{R}_n\right)\mathrm{e}^{-\frac{8\pi}{\sqrt{3}a'}k|z|}+\sum_{l=1}^{\infty}l\cos\left(l\mathbf{b}_2\cdot\mathbf{R}_n\right)\times\mathrm{e}^{-\frac{8\pi}{\sqrt{3}a'}l|z|}+\sum_{k,l=1}^{\infty}\Bigg\{\varphi_{kl}^{+}\cos\left((k\mathbf{b}_1+l\mathbf{b}_2)\cdot\mathbf{R}_n\right)\mathrm{e}^{-\frac{8\pi}{\sqrt{3}a'}\varphi_{kl}^{+}|z|}+\varphi_{kl}^{-}\cos\left((k\mathbf{b}_1-l\mathbf{b}_2)\cdot\mathbf{R}_n\right)\mathrm{e}^{-\frac{8\pi}{\sqrt{3}a'}\varphi_{kl}^{-}|z|}\Bigg\}\Bigg] \tag{C.51}$$

We can calculate the effective uniaxial anisotropy energy difference by $K(T)=\langle\Delta E\rangle = E_x - E_z$, remembering that all calculated energies thus far are for a single atom. The thermal energy difference is

$$\Delta E = -\frac{88\pi\mu_0\mu_S^2}{3a'^3}\sum_{n=-\infty}^{\infty}(-1)^n\Bigg[\sum_{k=1}^{\infty}k\cos\left(k\mathbf{b}_1\cdot\mathbf{R}_n\right)\mathrm{e}^{-\frac{8\pi}{\sqrt{3}a'}k|z|}+\frac{64}{88}\sum_{l=1}^{\infty}l\cos\left(l\mathbf{b}_2\cdot\mathbf{R}_n\right)\mathrm{e}^{-\frac{8\pi}{\sqrt{3}a'}l|z|}+\sum_{k,l=1}^{\infty}\Bigg\{\left(\varphi_{kl}^{+}+\frac{k^2}{\varphi_{kl}^{+}}\right)\cos\left((k\mathbf{b}_1+l\mathbf{b}_2)\cdot\mathbf{R}_n\right)\mathrm{e}^{-\frac{8\pi}{\sqrt{3}a'}\varphi_{kl}^{+}|z|}+\left(\varphi_{kl}^{-}+\frac{k^2}{\varphi_{kl}^{-}}\right)\times\cos\left((k\mathbf{b}_1-l\mathbf{b}_2)\cdot\mathbf{R}_n\right)\mathrm{e}^{-\frac{8\pi}{\sqrt{3}a'}\varphi_{kl}^{-}|z|}\Bigg\}\Bigg] \tag{C.52}$$

Using

$$\varphi_{kl}^{+}+\frac{k^2}{\varphi_{kl}^{+}}=\frac{k^2+(\varphi_{kl}^{+})^2}{\varphi_{kl}^{+}}=\frac{k^2+k^2+kl+l^2}{\sqrt{k^2+kl+l^2}}=\frac{2k^2+kl+l^2}{\sqrt{k^2+kl+l^2}}, \tag{C.53}$$

and

$$\varphi_{kl}^{-}+\frac{k^2}{\varphi_{kl}^{-}}=\frac{k^2+(\varphi_{kl}^{-})^2}{\varphi_{kl}^{-}}=\frac{k^2+k^2-kl+l^2}{\sqrt{k^2-kl+l^2}}=\frac{2k^2-kl+l^2}{\sqrt{k^2-kl+l^2}} \tag{C.54}$$

We can simplify this to

$$\Delta E = -\frac{88\pi\mu_0\mu_S^2}{3a'^3}\sum_{n=-\infty}^{\infty}(-1)^n\Bigg[\sum_{k=1}^{\infty}k\cos\left(k\mathbf{b}_1\cdot\mathbf{R}_n\right)\mathrm{e}^{-\frac{8\pi}{\sqrt{3}a'}k|z|}+\frac{64}{88}\sum_{l=1}^{\infty}l\cos\left(l\mathbf{b}_2\cdot\mathbf{R}_n\right)\mathrm{e}^{-\frac{8\pi}{\sqrt{3}a'}l|z|}+\sum_{k,l=1}^{\infty}\Bigg\{\frac{2k^2+kl+l^2}{\sqrt{k^2+kl+l^2}}\times\cos\left((k\mathbf{b}_1+l\mathbf{b}_2)\cdot\mathbf{R}_n\right)\mathrm{e}^{-\frac{8\pi}{\sqrt{3}a'}\sqrt{k^2+kl+l^2}|z|}+\frac{2k^2-kl+l^2}{\sqrt{k^2-kl+l^2}}\times\cos\left((k\mathbf{b}_1-l\mathbf{b}_2)\cdot\mathbf{R}_n\right)\mathrm{e}^{-\frac{8\pi}{\sqrt{3}a'}\sqrt{k^2-kl+l^2}|z|}\Bigg\}\Bigg] \tag{C.55}$$

Remembering that a' is not the cubic lattice parameter, substituting $a = a'/\sqrt{2}$ gives

$$\Delta E = -\frac{176\sqrt{2}\pi\mu_0\mu_S^2}{3a^3}\sum_{n=-\infty}^{\infty}(-1)^n\Bigg[\sum_{k=1}^{\infty}k\cos\left(k\mathbf{b}_1\cdot\mathbf{R}_n\right)\mathrm{e}^{-\frac{8\sqrt{6}\pi}{3a}k|z|} + \frac{64}{88}\sum_{l=1}^{\infty}l\cos\left(l\mathbf{b}_2\cdot\mathbf{R}_n\right)\mathrm{e}^{-\frac{8\sqrt{6}\pi}{3a}l|z|} + \sum_{k,l=1}^{\infty}\Bigg\{\frac{2k^2+kl+l^2}{\sqrt{k^2+kl+l^2}}\cos\left((k\mathbf{b}_1+l\mathbf{b}_2)\cdot\mathbf{R}_n\right) \times \mathrm{e}^{-\frac{8\sqrt{6}\pi}{3a}\sqrt{k^2+kl+l^2}|z|} + \frac{2k^2-kl+l^2}{\sqrt{k^2-kl+l^2}}\cos\left((k\mathbf{b}_1-l\mathbf{b}_2)\cdot\mathbf{R}_n\right)) \times \mathrm{e}^{-\frac{8\sqrt{6}\pi}{3a}\sqrt{k^2-kl+l^2}|z|}\Bigg\}\Bigg] \quad \text{(C.56)}$$

Rewriting z in terms of $\mathbf{R}_n$ gives

$$\Delta E(T) = -\frac{176\sqrt{2}\pi\mu_0\mu_S^2}{3a^3}\sum_{n=-\infty}^{\infty}(-1)^n\Bigg[\sum_{k=1}^{\infty}k\cos\left(k\mathbf{b}_1\cdot\mathbf{R}_n\right)\mathrm{e}^{-\frac{8\sqrt{6}\pi}{3a}k|\mathbf{R}_n\cdot\hat{\mathbf{z}}|} + \frac{64}{88}\sum_{l=1}^{\infty}l\cos\left(l\mathbf{b}_2\cdot\mathbf{R}_n\right)\mathrm{e}^{-\frac{8\sqrt{6}\pi}{3a}l|\mathbf{R}_n\cdot\hat{\mathbf{z}}|} + \sum_{k,l=1}^{\infty}\Bigg\{\frac{2k^2+kl+l^2}{\sqrt{k^2+kl+l^2}}\cos\left((k\mathbf{b}_1+l\mathbf{b}_2)\cdot\mathbf{R}_n\right) \mathrm{e}^{-\frac{8\sqrt{6}\pi}{3a}\sqrt{k^2+kl+l^2}|\mathbf{R}_n\cdot\hat{\mathbf{z}}|} + \frac{2k^2-kl+l^2}{\sqrt{k^2-kl+l^2}}\cos\left((k\mathbf{b}_1-l\mathbf{b}_2)\cdot\mathbf{R}_n\right)) \times \mathrm{e}^{-\frac{8\sqrt{6}\pi}{3a}\sqrt{k^2-kl+l^2}|\mathbf{R}_n\cdot\hat{\mathbf{z}}|}\Bigg\}\Bigg], \quad \text{(C.57)}$$

This concludes the derivation. We have derived an analytic expression which shows the dipole anisotropy can be written as proportional to μ_S^2.In the thermodynamic limit we can write this as $\langle\mu_S^2\rangle \approx \mu_S^2[m(T)]^2$. The expression was calculated numerically for finite ranges in the summation and we obtain a zero temperature value for the effective uniaxial anisotropy constant of $K_u = -0.4695\text{meV/moment}$.

Appendix D

Exchange Magnons in NiO

Following the standard methods given in [148], we will calculate the linear magnon Hamiltonian for NiO assuming a two sublattice model–an eight sublattice model is possible but is unnecessarily complicated for our use of the magnon Hamiltonian. First, we want to write the classical Hamiltonian (4.17) of the main text in terms of quantum mechanical Pauli operators. We distinguish operators from functions by using a hat so the Hamiltonian function $\mathcal{H}$ becomes the Hamiltonian operator $\hat{\mathcal{H}}$, for example. The Hamiltonian operator for NiO is an XYZ model

$$\hat{\mathcal{H}} = -\frac{1}{2}\sum_{i,j}\mathcal{J}_{ij}\left[\hat{S}_i^x\hat{S}_j^x + \hat{S}_i^y\hat{S}_j^y + \hat{S}_i^z\hat{S}_j^z\right], \tag{D.1}$$

where $\mathcal{J}_{ij} = J_{ij}/S^2$, S is the spin quantum number, and $\hat{S}^x$, $\hat{S}^y$, $\hat{S}^z$ are the Pauli operators. Next, we rewrite this in terms of the spin ladder operators $\hat{S}^+ = \hat{S}^x + \mathrm{i}\hat{S}^y$ and $\hat{S}^- = \hat{S}^x - \mathrm{i}\hat{S}^y$ which can be inverted to give $\hat{S}^x = \frac{1}{2}\left[\hat{S}^+ + \hat{S}^-\right]$ and $\hat{S}^y = \frac{1}{2\mathrm{i}}\left[\hat{S}^+ - \hat{S}^-\right]$. The Hamiltonian is now

$$\hat{\mathcal{H}} = -\frac{1}{2}\sum_{i,j}\mathcal{J}_{ij}\left[\hat{S}_i^z\hat{S}_j^z + \frac{1}{2}\left(\hat{S}_i^+\hat{S}_j^- + \hat{S}_i^-\hat{S}_j^+\right)\right]. \tag{D.2}$$

We now introduce Holstein-Primakoff boson creation and annihilation operators for both the 'up' and 'down' sublattices. These are $\hat{a}^\dagger$, $\hat{a}$, $\hat{b}^\dagger$, $\hat{b}$. If we index spins on the 'up' sublattice by $\uparrow$ and 'down' spins by $\downarrow$, then the Holstein-Primakoff operators are related to the spin operators by

$$\hat{S}_\uparrow^z = S - \hat{a}_\uparrow^\dagger\hat{a}_\uparrow \tag{D.3a}$$

$$\hat{S}_\uparrow^+ = \sqrt{2S}\left(1 - \frac{\hat{a}_\uparrow^\dagger\hat{a}_\uparrow}{2S}\right)^{1/2}\hat{a}_\uparrow \tag{D.3b}$$

$$\hat{S}_\uparrow^- = \sqrt{2S}\hat{a}_\uparrow^\dagger\left(1 - \frac{\hat{a}_\uparrow^\dagger\hat{a}_\uparrow}{2S}\right)^{1/2} \tag{D.3c}$$

$$\hat{S}_\downarrow^z = -S + \hat{b}_\downarrow^\dagger\hat{b}_\downarrow \tag{D.3d}$$

$$\hat{S}_\downarrow^+ = \sqrt{2S}\left(1 - \frac{\hat{b}_\downarrow^\dagger\hat{b}_\downarrow}{2S}\right)^{1/2}\hat{b}_\downarrow \tag{D.3e}$$

$$\hat{S}_\downarrow^- = \sqrt{2S}\hat{b}_\downarrow^\dagger\left(1 - \frac{\hat{b}_\downarrow^\dagger\hat{b}_\downarrow}{2S}\right)^{1/2}. \tag{D.3f}$$

We want a magnon Hamiltonian which is bilinear in boson operators (linear in magnon number operators), $\hat{\mathcal{H}}^{(2)}$. The above can then be simplified by a Taylor expansion about $\hat{a}_\uparrow^\dagger \hat{a}_\uparrow = 0$ or $\hat{b}_\uparrow^\dagger \hat{b}_\uparrow = 0$ giving

$$\hat{S}_\uparrow^z = S - \hat{a}_\uparrow^\dagger \hat{a}_\uparrow \tag{D.4a}$$

$$\hat{S}_\uparrow^+ = \sqrt{2S}\hat{a}_\uparrow \tag{D.4b}$$

$$\hat{S}_\uparrow^- = \sqrt{2S}\hat{a}_\uparrow^\dagger \tag{D.4c}$$

$$\hat{S}_\downarrow^z = -S + \hat{b}_\downarrow^\dagger \hat{b}_\downarrow \tag{D.4d}$$

$$\hat{S}_\downarrow^+ = \sqrt{2S}\hat{b}_\downarrow \tag{D.4e}$$

$$\hat{S}_\downarrow^- = \sqrt{2S}\hat{b}_\downarrow^\dagger. \tag{D.4f}$$

Now we separate the Hamiltonian operator into sublattices giving

$$\begin{aligned}
\hat{\mathcal{H}} = &-\frac{1}{2}\sum_{i,j\in\uparrow} \mathcal{J}_{1+}\delta(|\mathbf{r}_{ij}|,|\mathbf{v}_1|)\left[\hat{S}_i^z\hat{S}_j^z + \frac{1}{2}\left(\hat{S}_i^+\hat{S}_j^- + \hat{S}_i^-\hat{S}_j^+\right)\right] \\
&-\frac{1}{2}\sum_{i,j\in\downarrow} \mathcal{J}_{1+}\delta(|\mathbf{r}_{ij}|,|\mathbf{v}_1|)\left[\hat{S}_i^z\hat{S}_j^z + \frac{1}{2}\left(\hat{S}_i^+\hat{S}_j^- + \hat{S}_i^-\hat{S}_j^+\right)\right] \\
&-\sum_{i\in\uparrow.\, j\in\downarrow} \mathcal{J}_{1-}\delta(|\mathbf{r}_{ij}|,|\mathbf{v}_1|)\left[\hat{S}_i^z\hat{S}_j^z + \frac{1}{2}\left(\hat{S}_i^+\hat{S}_j^- + \hat{S}_i^-\hat{S}_j^+\right)\right] \\
&-\sum_{i\in\uparrow.\, j\in\downarrow} \mathcal{J}_{2}\delta(|\mathbf{r}_{ij}|,|\mathbf{v}_2|)\left[\hat{S}_i^z\hat{S}_j^z + \frac{1}{2}\left(\hat{S}_i^+\hat{S}_j^- + \hat{S}_i^-\hat{S}_j^+\right)\right]
\end{aligned} \tag{D.5}$$

where δ are Kronecker deltas, $\mathbf{r}_{ij} = \mathbf{r}_j - \mathbf{r}_i$ is the displacement vector between spins i and j, $|\mathbf{v}_1| = \frac{1}{\sqrt{2}}a$ is the nearest neighbour distance, and $|\mathbf{v}_2| = a$ is the next nearest neighbour distance. The final two terms don't double count interactions so there is no factor of $\frac{1}{2}$. Further splitting into Hamiltonians for each exchange term $\hat{\mathcal{H}} = \hat{\mathcal{H}}_{1+} + \hat{\mathcal{H}}_{1-} + \hat{\mathcal{H}}_2$ and substituting the Holstein-Primakoff operators, we get

$$\begin{aligned}
\hat{\mathcal{H}}_{1+} = &-\frac{1}{2}\sum_{i,j\in\uparrow} \mathcal{J}_{1+}\delta(|\mathbf{r}_{ij}|,|\mathbf{v}_1|)\left[\left(S-\hat{a}_i^\dagger\hat{a}_i\right)\left(S-\hat{a}_j^\dagger\hat{a}_j\right) + S\left(\hat{a}_i\hat{a}_j^\dagger + \hat{a}_i^\dagger\hat{a}_j\right)\right] \\
&-\frac{1}{2}\sum_{i,j\in\downarrow} \mathcal{J}_{1+}\delta(|\mathbf{r}_{ij}|,|\mathbf{v}_1|)\left[\left(\hat{b}_i^\dagger\hat{b}_i - S\right)\left(\hat{b}_j^\dagger\hat{b}_j - S\right) + S\left(\hat{b}_i\hat{b}_j^\dagger + \hat{b}_i^\dagger\hat{b}_j\right)\right],
\end{aligned} \tag{D.6}$$

$$\hat{\mathcal{H}}_{1-} = -\sum_{i\in\uparrow.\, j\in\downarrow} \mathcal{J}_{1-}\delta(|\mathbf{r}_{ij}|,|\mathbf{v}_1|)\left[\left(S-\hat{a}_i^\dagger\hat{a}_i\right)\left(\hat{b}_j^\dagger\hat{b}_j - S\right) + S\left(\hat{a}_i\hat{b}_j + \hat{a}_i^\dagger\hat{b}_j^\dagger\right)\right], \tag{D.7}$$

and,

$$\hat{\mathcal{H}}_2 = -\sum_{i\in\uparrow.\, j\in\downarrow} \mathcal{J}_2\delta(|\mathbf{r}_{ij}|,|\mathbf{v}_2|)\left[\left(S-\hat{a}_i^\dagger\hat{a}_i\right)\left(\hat{b}_j^\dagger\hat{b}_j - S\right) + S\left(\hat{a}_i\hat{b}_j + \hat{a}_i^\dagger\hat{b}_j^\dagger\right)\right]. \tag{D.8}$$

Again, we only wish a linear theory. Ignoring constant energy terms and those with more than two boson operators we have

$$\begin{aligned}\hat{\mathcal{H}}_{1+} = &-\frac{1}{2}\sum_{i,j\in\uparrow} \mathcal{J}_{1+}S\delta(|\mathbf{r}_{ij}|,|\mathbf{v}_1|)\left[\hat{a}_i\hat{a}_j^\dagger + \hat{a}_i^\dagger\hat{a}_j - \hat{a}_i^\dagger\hat{a}_i - \hat{a}_j^\dagger\hat{a}_j\right]\\ &-\frac{1}{2}\sum_{i,j\in\downarrow} \mathcal{J}_{1+}S\delta(|\mathbf{r}_{ij}|,|\mathbf{v}_1|)\left[\hat{b}_i\hat{b}_j^\dagger + \hat{b}_i^\dagger\hat{b}_j - \hat{b}_i^\dagger\hat{b}_i - \hat{b}_j^\dagger\hat{b}_j\right],\end{aligned} \tag{D.9}$$

$$\hat{\mathcal{H}}_{1-} = \sum_{i\in\uparrow.\, j\in\downarrow} \mathcal{J}_{1-}S\delta(|\mathbf{r}_{ij}|,|\mathbf{v}_1|)\left[\hat{a}_i\hat{b}_j + \hat{a}_i^\dagger\hat{b}_j^\dagger - \hat{a}_i^\dagger\hat{a}_i - \hat{b}_j^\dagger\hat{b}_j\right], \tag{D.10}$$

and,

$$\hat{\mathcal{H}}_2 = \sum_{i\in\uparrow.\, j\in\downarrow} \mathcal{J}_2S\delta(|\mathbf{r}_{ij}|,|\mathbf{v}_2|)\left[\hat{a}_i\hat{b}_j + \hat{a}_i^\dagger\hat{b}_j^\dagger - \hat{a}_i^\dagger\hat{a}_i - \hat{b}_j^\dagger\hat{b}_j\right]. \tag{D.11}$$

Since $\hat{\mathcal{H}}_{1-}$ and $\hat{\mathcal{H}}_2$ have the same expressions of magnon operators we can combine them. The total magnon Hamiltonian is then $\hat{\mathcal{H}} = \hat{\mathcal{H}}_{\uparrow\downarrow} + \hat{\mathcal{H}}_{\parallel}$. So,

$$\begin{aligned}\hat{\mathcal{H}}_{\parallel} = &-\frac{1}{2}\sum_{i,j\in\uparrow} \mathcal{J}_{1+}S\delta(|\mathbf{v}_1|)\left[\hat{a}_i\hat{a}_j^\dagger + \hat{a}_i^\dagger\hat{a}_j - \hat{a}_i^\dagger\hat{a}_i - \hat{a}_j^\dagger\hat{a}_j\right]\\ &-\frac{1}{2}\sum_{i,j\in\downarrow} \mathcal{J}_{1+}S\delta(|\mathbf{v}_1|)\left[\hat{b}_i\hat{b}_j^\dagger + \hat{b}_i^\dagger\hat{b}_j - \hat{b}_i^\dagger\hat{b}_i - \hat{b}_j^\dagger\hat{b}_j\right],\end{aligned} \tag{D.12}$$

$$\hat{\mathcal{H}}_{\uparrow\downarrow} = S\sum_{i\in\uparrow.\, j\in\downarrow} \left(\mathcal{J}_2\delta(|\mathbf{v}_2|) + \mathcal{J}_{1-}\delta(|\mathbf{v}_1|)\right)\left[\hat{a}_i\hat{b}_j + \hat{a}_i^\dagger\hat{b}_j^\dagger - \hat{a}_i^\dagger\hat{a}_i - \hat{b}_j^\dagger\hat{b}_j\right]. \tag{D.13}$$

Now we can take a Fourier transform so we can work with delocalised excitations. The fourier transformation is given by

$$\hat{a}_i \to \frac{1}{\sqrt{2N_\uparrow}}\sum_{\mathbf{k}} \hat{a}_{\mathbf{k}}\mathrm{e}^{\mathrm{i}\mathbf{k}\cdot\mathbf{r}_i} \tag{D.14a}$$

$$\hat{a}_i^\dagger \to \frac{1}{\sqrt{2N_\uparrow}}\sum_{\mathbf{k}} \hat{a}_{\mathbf{k}}^\dagger\mathrm{e}^{-\mathrm{i}\mathbf{k}\cdot\mathbf{r}_i} \tag{D.14b}$$

$$\hat{b}_i \to \frac{1}{\sqrt{2N_\downarrow}}\sum_{\mathbf{k}} \hat{b}_{\mathbf{k}}\mathrm{e}^{-\mathrm{i}\mathbf{k}\cdot\mathbf{r}_i} \tag{D.14c}$$

$$\hat{b}_i^\dagger \to \frac{1}{\sqrt{2N_\downarrow}}\sum_{\mathbf{k}} \hat{b}_{\mathbf{k}}^\dagger\mathrm{e}^{\mathrm{i}\mathbf{k}\cdot\mathbf{r}_i} \tag{D.14d}$$

The Fourier transforms of $\hat{a}_i$ and $\hat{b}_i$ differ in sign of the exponential. This is because they carry angular momenta of opposite sign. By imposing orthonormality, we replace terms like $\hat{a}_i\hat{a}_j^\dagger$ by $N_\uparrow^{-1}\sum_{\mathbf{k}}\hat{a}_{\mathbf{k}}\hat{a}_{\mathbf{k}}^\dagger \mathrm{e}^{-\mathrm{i}\mathbf{k}\cdot\mathbf{r}_{ij}}$. Or, by applying the canonical commutation relation $\left[\hat{a}_{\mathbf{k}},\hat{a}_{k'}^\dagger\right]=\delta_{kk'}$*, this becomes $\hat{a}_i\hat{a}_j^\dagger \to N_\uparrow^{-1}\sum_{\mathbf{k}}\hat{a}_{\mathbf{k}}^\dagger\hat{a}_{\mathbf{k}}\mathrm{e}^{-\mathrm{i}\mathbf{k}\cdot\mathbf{r}_{ij}}$. By the conservation of moment, terms like $\hat{a}_i\hat{b}_j^\dagger$ transform as $\hat{a}_i\hat{b}_j^\dagger \to (N_\uparrow N_\downarrow)^{-1/2}\sum_{\mathbf{k}}\hat{a}_{\mathbf{k}}\mathrm{e}^{\mathrm{i}\mathbf{k}\cdot\mathbf{r}_i}\,\hat{b}_{-k}^\dagger\mathrm{e}^{\mathrm{i}(-\mathbf{k})\cdot\mathbf{r}_j}$. Applying these conditions, we have

$$\begin{aligned}\hat{\mathcal{H}}_\parallel =& -\frac{S}{4N_\uparrow}\sum_{i,j\in\uparrow}\sum_{\mathbf{k}}\mathcal{J}_{1+}\delta(|\mathbf{v}_1|)\left[\hat{a}_{\mathbf{k}}\hat{a}_{\mathbf{k}}^\dagger\mathrm{e}^{\mathrm{i}\mathbf{k}\cdot\mathbf{r}_{ij}}+\hat{a}_{\mathbf{k}}^\dagger\hat{a}_{\mathbf{k}}\mathrm{e}^{-\mathrm{i}\mathbf{k}\cdot\mathbf{r}_{ij}}-2\hat{a}_{\mathbf{k}}^\dagger\hat{a}_{\mathbf{k}}\right]\\ &-\frac{S}{4N_\downarrow}\sum_{i,j\in\downarrow}\mathcal{J}_{1+}\delta(|\mathbf{v}_1|)\left[\hat{b}_{\mathbf{k}}\hat{b}_{\mathbf{k}}^\dagger\mathrm{e}^{-\mathrm{i}\mathbf{k}\cdot\mathbf{r}_{ij}}+\hat{b}_{\mathbf{k}}^\dagger\hat{b}_{\mathbf{k}}\mathrm{e}^{\mathrm{i}\mathbf{k}\cdot\mathbf{r}_{ij}}-2\hat{b}_{\mathbf{k}}^\dagger\hat{b}_{\mathbf{k}}\right],\end{aligned} \tag{D.15}$$

$$\begin{aligned}\hat{\mathcal{H}}_{\uparrow\downarrow} =& \frac{S}{2\sqrt{N_\uparrow N_\downarrow}}\sum_{i\in\uparrow.\,j\in\downarrow}\sum_{\mathbf{k}}\left(\mathcal{J}_2\delta(|\mathbf{v}_2|)+\mathcal{J}_{1-}\delta(|\mathbf{v}_1|)\right)\left[\hat{a}_{\mathbf{k}}\hat{b}_{\mathbf{k}}\mathrm{e}^{-\mathrm{i}\mathbf{k}\cdot\mathbf{r}_{ij}}\right.\\ &\left.+\hat{a}_{\mathbf{k}}^\dagger\hat{b}_{\mathbf{k}}^\dagger\mathrm{e}^{\mathrm{i}\mathbf{k}\cdot\mathbf{r}_{ij}}-\hat{a}_{\mathbf{k}}^\dagger\hat{a}_{\mathbf{k}}-\hat{b}_{\mathbf{k}}^\dagger\hat{b}_{\mathbf{k}}\right].\end{aligned} \tag{D.16}$$

Since the sum over $\mathbf{k}$ is symmetric, this can be written as

$$\begin{aligned}\hat{\mathcal{H}}_\parallel =& -\frac{1}{4N_\uparrow}\sum_{i,j\in\uparrow}\sum_{\mathbf{k}}\mathcal{J}_{1+}S\delta(|\mathbf{v}_1|)\left[\hat{a}_{\mathbf{k}}^\dagger\hat{a}_{\mathbf{k}}\left(\mathrm{e}^{\mathrm{i}\mathbf{k}\cdot\mathbf{r}_{ij}}+\mathrm{e}^{-\mathrm{i}\mathbf{k}\cdot\mathbf{r}_{ij}}\right)-2\hat{a}_{\mathbf{k}}^\dagger\hat{a}_{\mathbf{k}}\right]\\ &-\frac{1}{4N_\downarrow}\sum_{i,j\in\downarrow}\mathcal{J}_{1+}S\delta(|\mathbf{v}_1|)\left[\hat{b}_{\mathbf{k}}^\dagger\hat{b}_{\mathbf{k}}\left(\mathrm{e}^{\mathrm{i}\mathbf{k}\cdot\mathbf{r}_{ij}}+\mathrm{e}^{-\mathrm{i}\mathbf{k}\cdot\mathbf{r}_{ij}}\right)-2\hat{b}_{\mathbf{k}}^\dagger\hat{b}_{\mathbf{k}}\right],\end{aligned} \tag{D.17}$$

$$\begin{aligned}\hat{\mathcal{H}}_{\uparrow\downarrow} =& \frac{S}{2\sqrt{N_\uparrow N_\downarrow}}\sum_{i\in\uparrow.\,j\in\downarrow}\sum_{\mathbf{k}}\left(\mathcal{J}_2\delta(|\mathbf{v}_2|)+\mathcal{J}_{1-}\delta(|\mathbf{v}_1|)\right)\left[\frac{1}{2}\hat{a}_{\mathbf{k}}\hat{b}_{\mathbf{k}}\left(\mathrm{e}^{\mathrm{i}\mathbf{k}\cdot\mathbf{r}_{ij}}+\mathrm{e}^{-\mathrm{i}\mathbf{k}\cdot\mathbf{r}_{ij}}\right)\right.\\ &\left.+\frac{1}{2}\hat{a}_{\mathbf{k}}^\dagger\hat{b}_{\mathbf{k}}^\dagger\left(\mathrm{e}^{\mathrm{i}\mathbf{k}\cdot\mathbf{r}_{ij}}+\mathrm{e}^{-\mathrm{i}\mathbf{k}\cdot\mathbf{r}_{ij}}\right)-\hat{a}_{\mathbf{k}}^\dagger\hat{a}_{\mathbf{k}}-\hat{b}_{\mathbf{k}}^\dagger\hat{b}_{\mathbf{k}}\right].\end{aligned} \tag{D.18}$$

We can then identify trigonometric functions giving

$$\begin{aligned}\hat{\mathcal{H}}_\parallel =& -\frac{1}{4N_\uparrow}\sum_{i,j\in\uparrow}\sum_{\mathbf{k}}\mathcal{J}_{1+}S\delta(|\mathbf{v}_1|)\left[2\hat{a}_{\mathbf{k}}^\dagger\hat{a}_{\mathbf{k}}\cos\left(\mathbf{k}\cdot\mathbf{r}_{ij}\right)-2\hat{a}_{\mathbf{k}}^\dagger\hat{a}_{\mathbf{k}}\right]\\ &-\frac{1}{4N_\downarrow}\sum_{i,j\in\downarrow}\mathcal{J}_{1+}S\delta(|\mathbf{v}_1|)\left[2\hat{b}_{\mathbf{k}}^\dagger\hat{b}_{\mathbf{k}}\cos\left(\mathbf{k}\cdot\mathbf{r}_{ij}\right)-2\hat{b}_{\mathbf{k}}^\dagger\hat{b}_{\mathbf{k}}\right],\end{aligned} \tag{D.19}$$

$$\begin{aligned}\hat{\mathcal{H}}_{\uparrow\downarrow} =& \frac{S}{2\sqrt{N_\uparrow N_\downarrow}}\sum_{i\in\uparrow.\,j\in\downarrow}\sum_{\mathbf{k}}\left(\mathcal{J}_2\delta(|\mathbf{v}_2|)+\mathcal{J}_{1-}\delta(|\mathbf{v}_1|)\right)\left[\hat{a}_{\mathbf{k}}\hat{b}_{\mathbf{k}}\cos\left(\mathbf{k}\cdot\mathbf{r}_{ij}\right)\right.\\ &\left.+\hat{a}_{\mathbf{k}}^\dagger\hat{b}_{\mathbf{k}}^\dagger\cos\left(\mathbf{k}\cdot\mathbf{r}_{ij}\right)-\hat{a}_{\mathbf{k}}^\dagger\hat{a}_{\mathbf{k}}-\hat{b}_{\mathbf{k}}^\dagger\hat{b}_{\mathbf{k}}\right].\end{aligned} \tag{D.20}$$

*We do not care about offsets so this becomes $\hat{a}_{\mathbf{k}}\hat{a}_{\mathbf{k}}^\dagger=\hat{a}_{\mathbf{k}}^\dagger\hat{a}_{\mathbf{k}}$

We can now evaluate the sum over spins but must also ensure we sum over the exponentials correctly. First we must introduce the structure factors $\gamma_{\mathbf{k}}$ which are given by

$$\gamma_{\mathbf{k}}^{+} = (z_{1+})^{-1} \sum_{\boldsymbol{\delta}_{1+}} \cos\left(\mathbf{k} \cdot \boldsymbol{\delta}_{1+}\right) \tag{D.21a}$$

$$\gamma_{\mathbf{k}}^{-} = (z_{1-})^{-1} \sum_{\boldsymbol{\delta}_{1-}} \cos\left(\mathbf{k} \cdot \boldsymbol{\delta}_{1-}\right) \tag{D.21b}$$

$$\gamma_{\mathbf{k}}^{(2)} = (z_{2})^{-1} \sum_{\boldsymbol{\delta}_{2}} \cos\left(\mathbf{k} \cdot \boldsymbol{\delta}_{2}\right), \tag{D.21c}$$

where z is the number of neighbours for a given exchange interaction. In our case $z_{1-} = z_{1+} = z_2 = 6$. The summations over spins are given by

$$\sum_{i,j\in\uparrow} \mathcal{J}_{1+}\delta(|\mathbf{v}_1|)\cos\left(\mathbf{k}\cdot\mathbf{r}_{ij}\right) \to 2N_{\uparrow}\mathcal{J}_{1+}z_{1+}\gamma_{\mathbf{k}}^{+} \tag{D.22a}$$

$$\sum_{i\in\uparrow,\, j\in\downarrow} \mathcal{J}_{1-}\delta(|\mathbf{v}_1|)\cos\left(\mathbf{k}\cdot\mathbf{r}_{ij}\right) \to 2(N_{\uparrow}+N_{\downarrow})\mathcal{J}_{1-}z_{1-}\gamma_{\mathbf{k}}^{-} \tag{D.22b}$$

$$\sum_{i\in\uparrow,\, j\in\downarrow} \mathcal{J}_{2}\delta(|\mathbf{v}_2|)\cos\left(\mathbf{k}\cdot\mathbf{r}_{ij}\right) \to 2(N_{\uparrow}+N_{\downarrow})\mathcal{J}_{2}z_{2}\gamma_{\mathbf{k}}^{(2)} \tag{D.22c}$$

Now assuming $N_{\uparrow} = N_{\downarrow} = N/2$, we can write the Hamiltonian terms as

$$\hat{\mathcal{H}}_{\parallel} = \mathcal{J}_{1+}zS\sum_{\mathbf{k}}(\hat{a}_{\mathbf{k}}^{\dagger}\hat{a}_{\mathbf{k}} + \hat{b}_{\mathbf{k}}^{\dagger}\hat{b}_{\mathbf{k}})(1-\gamma_{\mathbf{k}}^{-}) \tag{D.23}$$

$$\hat{\mathcal{H}}_{\uparrow\downarrow} = -Sz\sum_{\mathbf{k}}\left[(\mathcal{J}_2+\mathcal{J}_{1-})(\hat{a}_{\mathbf{k}}^{\dagger}\hat{a}_{\mathbf{k}} + \hat{b}_{\mathbf{k}}^{\dagger}\hat{b}_{\mathbf{k}}) + (\mathcal{J}_2\gamma_{\mathbf{k}}^{(2)} + \mathcal{J}_{1-}\gamma_{\mathbf{k}}^{-})(\hat{a}_{\mathbf{k}}\hat{b}_{\mathbf{k}} + \hat{a}_{\mathbf{k}}^{\dagger}\hat{b}_{\mathbf{k}}^{\dagger})\right]. \tag{D.24}$$

The bosonic excitations $\hat{a}^{\dagger}$, $\hat{b}^{\dagger}$ are not linearised; the excitations are coupled. It's more convenient to work in an orthonormal basis of the excitations so that we can calculate the energies of these independent excitations. This means that the linearised magnons are not localised to a single sublattice. The process of linearising magnons is called a Bogoliubov transformation but this is exactly the same procedure as diagonalising a matrix by calculating eigenvalues and eigenvectors (though with a non-trivial metric for compatibility with commutation relations [85, 305]). Choosing the basis $X = (\hat{a}_{\mathbf{k}}, \hat{b}_{-k}^{\dagger})$ then we can the Hamiltonian as $\hat{\mathcal{H}} = X^{\dagger}\mathbb{H}X$ where $\mathbb{H}$ is the following matrix

$$\mathbb{H} = \begin{bmatrix} \mathcal{A}_{\mathbf{k}} & \mathcal{B}_{\mathbf{k}} \\ \mathcal{B}_{\mathbf{k}} & \mathcal{A}_{\mathbf{k}} \end{bmatrix} \tag{D.25}$$

where $\mathcal{A}_{\mathbf{k}} = Sz\left(\mathcal{J}_{1+}(1-\gamma_{\mathbf{k}}^{-}) - \mathcal{J}_{1-} - \mathcal{J}_2\right)$ and $\mathcal{B}_{\mathbf{k}} = -Sz\left(\mathcal{J}_{1-}\gamma_k^{+} + \mathcal{J}_2\gamma_k^{(2)}\right)$. Introducing linearised/diagonalised boson operators $\hat{\alpha}_{\mathbf{k}}^{\dagger}$, $\hat{\alpha}_{\mathbf{k}}$, $\hat{\beta}_{\mathbf{k}}^{\dagger}$, and $\hat{\beta}_{\mathbf{k}}$, which are related by the transformation

$$\begin{bmatrix} \hat{a}_{\mathbf{k}} \\ \hat{b}_{-k}^{\dagger} \end{bmatrix} = \begin{bmatrix} u_{\mathbf{k}} & -v_{\mathbf{k}} \\ -v_{\mathbf{k}} & u_{\mathbf{k}} \end{bmatrix} \begin{bmatrix} \hat{\alpha}_{\mathbf{k}} \\ \hat{\beta}_{-k}^{\dagger}. \end{bmatrix} \tag{D.26}$$

The eigenvector components are $u_{\mathbf{k}} = \sqrt{(\mathcal{A}_{\mathbf{k}} + hf_{\mathbf{k}})/2hf_{\mathbf{k}}}$, $v_{\mathbf{k}} = \sqrt{(\mathcal{A}_{\mathbf{k}} - hf_{\mathbf{k}})/2hf_{\mathbf{k}}}$. The Hamiltonian can now be written as $\hat{\mathcal{H}} = Y^{\dagger}(hf_{\mathbf{k}}\mathbb{1})Y$ with $Y = (\hat{\alpha}_{\mathbf{k}}, \hat{\beta}_{-k}^{\dagger})^{\top}$. The eigenfrequency is then $hf_{\mathbf{k}} = \sqrt{\mathcal{A}_{\mathbf{k}}^2 - \mathcal{B}_{\mathbf{k}}^2}$ which can be expanded to

$$hf_{\mathbf{k}} = \frac{z}{S}\sqrt{\left(J_{1+}(1-\gamma_{\mathbf{k}}^{+}) - J_{1-} - J_2\right)^2 - \left(J_{1-}\gamma_{\mathbf{k}}^{-} + J_2\gamma_{\mathbf{k}}^{(2)}\right)^2}. \tag{D.27}$$

Bibliography

[1] S. Sharma, R. Chandel, P. Kr. Pal, and R. S. R. Rathor, "Performance Analysis of CNTs as an Application for Future VLSI Interconnects," Microelectronics and Solid State Electronics **1**, 69–73 (2012).

[2] Atsufumi Hirohata, Keisuke Yamada, Yoshinobu Nakatani, Ioan-Lucian Prejbeanu, Bernard Diény, Philipp Pirro, and Burkard Hillebrands, "Review on spintronics: Principles and device applications," J. Magn. Magn. Mater. **509**, 166711 (2020).

[3] E Y Vedmedenko, R K Kawakami, D D Sheka, P Gambardella, A Kirilyuk, A Hirohata, C Binek, O Chubykalo-Fesenko, S Sanvito, B J Kirby, J Grollier, K Everschor-Sitte, T Kampfrath, C-Y You, and A Berger, "The 2020 magnetism roadmap," J. Phys. D: Appl. Phys. **53**, 453001 (2020).

[4] StorageNewsletter.com, "Beautiful Life for SSDs in 1Q21," .

[5] Peter Clarke, "MRAM set to replace SRAM, says TSMC roadmap," .

[6] Giovanni Finocchio, Supriyo Bandyopadhyay, Peng Lin, Gang Pan, J Joshua Yang, Riccardo Tomasello, Christos Panagopoulos, Mario Carpentieri, Vito Puliafito, Johan Åkerman, *et al.*, "Roadmap for unconventional computing with nanotechnology," arXiv preprint arXiv:2301.06727 (2023).

[7] Francesco Bova, Avi Goldfarb, and Roger G. Melko, "Commercial applications of quantum computing," EPJ Quantum Technol. **8**, 2 (2021).

[8] Yohannes W. Getahun, Felicia S. Manciu, Mark R. Pederson, and Ahmed A. El-Gendy, "Room temperature colossal superparamagnetic order in aminofer-

roceneâ€“graphene molecular magnets," Applied Physics Letters **122**, 241903 (2023).

[9] J Tejada, E M Chudnovsky, E del Barco, J M Hernandez, and T P Spiller, "Magnetic qubits as hardware for quantum computers," Nanotechnology **12**, 181–186 (2001).

[10] Otto Stern, "Ein Weg zur experimentellen Prüfung der Richtungsquantelung im Magnetfeld," Z. Phys. **7**, 249–253 (1921).

[11] NobelPrize.org, "The nobel prize in physics 1943," .

[12] Baptiste Savoie, "A rigorous proof of the Bohr–van Leeuwen theorem in the semi-classical limit," Rev. Math. Phys. **27**, 1550019 (2015).

[13] Bernard Rodmacq, Karine Dumesnil, Philippe Mangin, and Martine Hennion, "Biquadratic magnetic coupling in NiFe/Ag multilayers," Phys. Rev. B **48**, 3556–3559 (1993).

[14] W. Heisenberg, "Mehrkörperproblem und Resonanz in der Quantenmechanik," Z. Phys. **38**, 411–426 (1926).

[15] Paul Adrien Maurice Dirac, "On the theory of quantum mechanics," Proceedings of the Royal Society of London. Series A, Containing Papers of a Mathematical and Physical Character **112**, 661–677 (1926).

[16] P. W. Anderson, "Antiferromagnetism. Theory of Superexchange Interaction," Phys. Rev. **79**, 350–356 (1950).

[17] Clarence Zener, "Interaction between the *d*-shells in the transition metals. ii. ferromagnetic compounds of manganese with perovskite structure," Phys. Rev. **82**, 403–405 (1951).

[18] M. A. Ruderman and C. Kittel, "Indirect Exchange Coupling of Nuclear Magnetic Moments by Conduction Electrons," Phys. Rev. **96**, 99–102 (1954).

[19] Tadao Kasuya, "A Theory of Metallic Ferro- and Antiferromagnetism on Zener's Model," Prog. Theor. Phys. **16**, 45–57 (1956).

[20] Kei Yosida, "Magnetic Properties of Cu-Mn Alloys," Phys. Rev. **106**, 893–898 (1957).

[21] I. Dzyaloshinsky, "A thermodynamic theory of "weak" ferromagnetism of antiferromagnetics," J. Phys. Chem. Solids **4**, 241–255 (1958).

[22] Tôru Moriya, "Anisotropic superexchange interaction and weak ferromagnetism," Phys. Rev. **120**, 91–98 (1960).

[23] P. W. Anderson, "New Approach to the Theory of Superexchange Interactions," Phys. Rev. **115**, 2–13 (1959).

[24] John B. Goodenough, "Theory of the role of covalence in the perovskite-type manganites [La, M(II)]MnO_3," Phys. Rev. **100**, 564–573 (1955).

[25] Junjiro Kanamori, "Theory of the Magnetic Properties of Ferrous and Cobaltous Oxides, I," Progress of Theoretical Physics **17**, 177–196 (1957).

[26] John B. Goodenough, "An interpretation of the magnetic properties of the perovskite-type mixed crystals $La_{1-x}Sr_xCoO_{3-\lambda}$," J. Phys. Chem. Solids **6**, 287–297 (1958).

[27] Junjiro Kanamori, "Superexchange interaction and symmetry properties of electron orbitals," J. Phys. Chem. Solids **10**, 87–98 (1959).

[28] A. Aharoni, *Chapter 6 Introduction to the Theory of Ferromagnetism*, International Series of Monographs on Physics (Clarendon Press, 2000).

[29] Alexander G Gurevich and Gennadii A Melkov, "Chapter 6 - magnetostatic waves and oscillations," in *Magnetization oscillations and waves* (CRC press, 1996).

[30] Sophie F. Weber, Andrea Urru, Sayantika Bhowal, Claude Ederer, and Nicola A. Spaldin, "Surface magnetization in antiferromagnets: Classification, example materials, and relation to magnetoelectric responses," (2023), arXiv:2306.06631 [cond-mat.mtrl-sci] .

[31] Andrea Urru and Nicola A. Spaldin, "Magnetic octupole tensor decomposition and second-order magnetoelectric effect," Ann. Phys. **447**, 168964 (2022).

[32] Xi He, Yi Wang, Ning Wu, Anthony N. Caruso, Elio Vescovo, Kirill D. Belashchenko, Peter A. Dowben, and Christian Binek, "Robust isothermal electric control of exchange bias at room temperature," Nat. Mater. **9**, 579–585 (2010).

[33] Natascha Hedrich, Kai Wagner, Oleksandr V. Pylypovskyi, Brendan J. Shields, Tobias Kosub, Denis D. Sheka, Denys Makarov, and Patrick Maletinsky, "Nanoscale mechanics of antiferromagnetic domain walls," Nat. Phys. **17**, 574–577 (2021).

[34] Sophie F. Weber and Nicola A. Spaldin, "Characterizing and Overcoming Surface Paramagnetism in Magnetoelectric Antiferromagnets," Phys. Rev. Lett. **130**, 146701 (2023).

[35] Ka Shen, "Magnon Spin Relaxation and Spin Hall Effect Due to the Dipolar Interaction in Antiferromagnetic Insulators," Phys. Rev. Lett. **124**, 077201 (2020).

[36] D. A. Garanin, "Fokker-Planck and Landau-Lifshitz-Bloch equations for classical ferromagnets," Phys. Rev. B **55**, 3050–3057 (1997).

[37] U Atxitia, D Hinzke, and U Nowak, "Fundamentals and applications of the Landau–Lifshitz–Bloch equation," J. Phys. D: Appl. Phys. **50**, 033003 (2016).

[38] P. Asselin, R. F. L. Evans, J. Barker, R. W. Chantrell, R. Yanes, O. Chubykalo-Fesenko, D. Hinzke, and U. Nowak, "Constrained Monte Carlo method and calculation of the temperature dependence of magnetic anisotropy," Phys. Rev. B **82**, 054415 (2010).

[39] T.L. Gilbert, "Classics in Magnetics A Phenomenological Theory of Damping in Ferromagnetic Materials," IEEE Trans. Magn. **40**, 3443–3449 (2004).

[40] Takao Kotani and Mark van Schilfgaarde, "Spin wave dispersion based on the quasiparticle self-consistent *GW* method: NiO, MnO and α-MnAs," Journal of Physics: Condensed Matter **20**, 295214 (2008).

[41] L. Landau and E. Lifshits, "On the theory of the dispersion of magnetic permeability in ferromagnetic bodies," Phys. Zeitsch. der Sow. **8**, 153–169 (1935).

[42] Candra Kurniawan, Dede Djuhana, Bambang Soegijono, and Dong-Hyun Kim, "Micromagnetic investigation of the sub-nanosecond magnetic pulse driven domain wall motion in CoFeB nanowire," Curr. Appl. Phys. **27**, 98–102 (2021).

[43] V. Raposo, F. García-Sánchez, U. Atxitia, and E. Martínez, "Realistic micromagnetic description of all-optical ultrafast switching processes in ferrimagnetic alloys," Phys. Rev. B **105**, 104432 (2022).

[44] Claas Abert, Florian Bruckner, Christoph Vogler, and Dieter Suess, "Efficient micromagnetic modelling of spin-transfer torque and spin-orbit torque," AIP Advances **8**, 056008 (2017).

[45] B L Gyorffy, A J Pindor, J Staunton, G M Stocks, and H Winter, "A first-principles theory of ferromagnetic phase transitions in metals," J. Phys. F: Met. Phys. **15**, 1337–1386 (1985).

[46] Olle Eriksson, Anders Bergman, Lars Bergqvist, and Johan Hellsvik, *Atomistic spin dynamics: foundations and applications* (Oxford university press, 2017).

[47] Y. Nambu, J. Barker, Y. Okino, T. Kikkawa, Y. Shiomi, M. Enderle, T. Weber, B. Winn, M. Graves-Brook, J. M. Tranquada, T. Ziman, M. Fujita, G. E. W. Bauer, E. Saitoh, and K. Kakurai, "Observation of Magnon Polarization," Phys. Rev. Lett. **125**, 027201 (2020).

[48] Alexander G Gurevich and Gennadii A Melkov, "Chapter 11 - Spin-spin relaxation," in *Magnetization oscillations and waves* (CRC press, 1996).

[49] Alexander G Gurevich and Gennadii A Melkov, *Magnetization oscillations and waves* (CRC press, 1996).

[50] Libor Šmejkal, Jairo Sinova, and Tomas Jungwirth, "Emerging Research Landscape of Altermagnetism," Phys. Rev. X **12**, 040501 (2022).

[51] Zexin Feng, Xiaorong Zhou, Libor Šmejkal, Lei Wu, Zengwei Zhu, Huixin Guo, Rafael González-Hernández, Xiaoning Wang, Han Yan, Peixin Qin, Xin Zhang, Haojiang Wu, Hongyu Chen, Ziang Meng, Li Liu, Zhengcai Xia, Jairo Sinova, Tomáš Jungwirth, and Zhiqi Liu, "An anomalous Hall effect in altermagnetic ruthenium dioxide," Nat. Electron. **5**, 735–743 (2022).

[52] Libor Šmejkal, Anna Birk Hellenes, Rafael González-Hernández, Jairo Sinova, and Tomas Jungwirth, "Giant and Tunneling Magnetoresistance in Unconventional Collinear Antiferromagnets with Nonrelativistic Spin-Momentum Coupling," Phys. Rev. X **12**, 011028 (2022).

[53] Libor Šmejkal, Allan H. MacDonald, Jairo Sinova, Satoru Nakatsuji, and Tomas Jungwirth, "Anomalous Hall antiferromagnets," Nat. Rev. Mater. **7**, 482–496 (2022).

[54] O Fedchenko, L Šmejkal, M Kallmayer, Ya Lytvynenko, K Medjanik, S Babenkov, D Vasilyev, M Kläui, J Demsar, G Schönhense, M Jourdan, J Sinova, and H J Elmers, "Direct observation of antiferromagnetic parity violation in the electronic structure of Mn_2Au," J. Phys.: Condens. Matter **34**, 425501 (2022).

[55] Libor Šmejkal, Jairo Sinova, and Tomas Jungwirth, "Beyond Conventional Ferromagnetism and Antiferromagnetism: A Phase with Nonrelativistic Spin and Crystal Rotation Symmetry," Phys. Rev. X **12**, 031042 (2022).

[56] A. P. Cracknell and S. J. Joshua, "The space group corepresentations of antiferromagnetic NiO," Math. Proc. Camb. Philos. Soc. **66**, 493–504 (1969).

[57] J.M. Perez-Mato, S.V. Gallego, E.S. Tasci, L. Elcoro, G. de la Flor, and M.I. Aroyo, "Symmetry-Based Computational Tools for Magnetic Crystallography," Annu. Rev. Mater. Res. **45**, 217–248 (2015).

[58] A. M. Balagurov, I. A. Bobrikov, S. V. Sumnikov, V. Yu. Yushankhai, and N. Mironova-Ulmane, "Magnetostructural phase transitions in NiO and MnO: Neutron diffraction data," JETP Lett. **104**, 88–93 (2016).

[59] M. T. Hutchings and E. J. Samuelsen, "Measurement of Spin-Wave Dispersion in NiO by Inelastic Neutron Scattering and Its Relation to Magnetic Properties," Phys. Rev. B **6**, 3447–3461 (1972).

[60] Eric Ressouche, Nolwenn Kernavanois, Louis-Pierre Regnault, and Jean-Yves Henry, "Magnetic structures of the metal monoxides NiO and CoO re-investigated by spherical neutron polarimetry," Phys. B: Condens. Matter **385-386**, 394–397 (2006).

[61] J. Baruchel, M. Schlenker, K. Kurosawa, and S. Saito, "Antiferromagnetic S-domains in NiO," Philos. Mag. B **43**, 853–860 (1981).

[62] Walter L. Roth and Glen A. Slack, "Antiferromagnetic Structure and Domains in Single Crystal NiO," J. Appl. Phys. **31**, S352–S353 (1960).

[63] A. Schrön, C. Rödl, and F. Bechstedt, "Crystalline and magnetic anisotropy of the 3d-transition metal monoxides MnO, FeO, CoO, and NiO," Phys. Rev. B **86**, 115134 (2012).

[64] Junjiro Kanamori, "Theory of the magnetic properties of ferrous and cobaltous oxides, i," Prog. Theor. Phys. **17**, 177–196 (1957).

[65] Roman Khymyn, Ivan Lisenkov, Vasil S. Tiberkevich, Andrei N. Slavin, and Boris A. Ivanov, "Transformation of spin current by antiferromagnetic insulators," Phys. Rev. B **93**, 224421 (2016).

[66] Théophile Chirac, Jean-Yves Chauleau, Pascal Thibaudeau, Olena Gomonay, and Michel Viret, "Ultrafast antiferromagnetic switching in NiO induced by spin transfer torques," Phys. Rev. B **102**, 134415 (2020).

[67] Mojtaba Alaei and Homa Karimi, "A deep investigation of NiO and MnO through the first principle calculations and Monte Carlo simulations," Electron. Struct. **5**, 025001 (2023).

[68] J. Milano, L. Steren, and M. Grimsditch, "Effect of Dipolar Interaction on the Antiferromagnetic Resonance Spectra of NiO," Phys. Rev. Lett. **93**, 077601 (2004).

[69] Guangmeng He, Huimin Zhang, Jinyang Ni, Boyu Liu, Changsong Xu, and Hongjun Xiang, "Microscopic Magnetic Origin of Rhombohedral Distortion in NiO," Chin. Phys. Lett. **39**, 067501 (2022).

[70] J. Zaanen, G. A. Sawatzky, and J. W. Allen, "Band gaps and electronic structure of transition-metal compounds," Phys. Rev. Lett. **55**, 418–421 (1985).

[71] J. Kuneš, V. I. Anisimov, S. L. Skornyakov, A. V. Lukoyanov, and D. Vollhardt, "NiO: Correlated Band Structure of a Charge-Transfer Insulator," Phys. Rev. Lett. **99**, 156404 (2007).

[72] M. E. Lines and E. D. Jones, "Antiferromagnetism in the face-centered cubic lattice. ii. magnetic properties of MnO," Phys. Rev. **139**, A1313–A1327 (1965).

[73] C. G. Shull, W. A. Strauser, and E. O. Wollan, "Neutron Diffraction by Paramagnetic and Antiferromagnetic Substances," Phys. Rev. **83**, 333–345 (1951).

[74] W. L. Roth, "Magnetic Structures of MnO, FeO, CoO, and NiO," Phys. Rev. **110**, 1333–1341 (1958).

[75] W. L. Roth, "Multispin Axis Structures for Antiferromagnets," Phys. Rev. **111**, 772–781 (1958).

[76] Hisamoto Kondoh, Enji Uchida, Yoshihide Nakazumi, and Takeo Nagamiya, "Magnetic Anisotropy Measurements of NiO Single Crystal," J. Phys. Soc. Jpn. **13**, 579–586 (1958).

[77] W. L. Roth, "Neutron and Optical Studies of Domains in NiO," J. Appl. Phys. **31**, 2000–2011 (1960).

[78] Hisamoto Kondoh and Tadao Takeda, "Observation of Antiferromagnetic Domains in Nickel Oxide," J. Phys. Soc. Jpn. **19**, 2041–2051 (1964).

[79] Enji Uchida, Nobuo Fukuoka, Hisamoto Kondoh, Tadao Takeda, Yoshihide Nakazumi, and Takeo Nagamiya, "Magnetic Anisotropy of Single Crystals of NiO and MnO," J. Phys. Soc. Jpn. **23**, 1197–1203 (1967).

[80] Takemi Yamada, "Spin Configuration in Antiferromagnetic Domain Walls of the NiO-Type Crystals," J. Phys. Soc. Jpn. **21**, 650–664 (1966).

[81] Takemi Yamada, Shozo Saito, and Yasumitsu Shimomura, "Magnetic Anisotropy, Magnetostriction, and Magnetic Domain Walls in NiO. II. Experiment," J. Phys. Soc. Jpn. **21**, 672–680 (1966).

[82] Jerome I. Kaplan, "Magnetic Dipolar Interactions in MnO and in Ferrites," J. Chem. Phys. **22**, 1709–1712 (1954).

[83] F. Keffer and W. O'Sullivan, "Problem of Spin Arrangements in MnO and Similar Antiferromagnets," Phys. Rev. **108**, 637–644 (1957).

[84] Takemi Yamada, "Magnetic Anisotropy, Magnetostriction, and Magnetic Domain Walls in NiO. I. Theory," J. Phys. Soc. Jpn. **21**, 664–671 (1966).

[85] Sergio M. Rezende, Antonio Azevedo, and Roberto L. Rodríguez-Suárez, "Introduction to antiferromagnetic magnons," J. Appl. Phys. **126**, 151101 (2019).

[86] Robert R. Birss, *Symmetry and magnetism*, Series of monographs on selected papers in solid state physics, Vol. 3 (North-Holland Pub. Co., 1964).

[87] E. Hartmann, *An Introduction to Crystal Physics* (Univ. Coll. Cardiff Press, 1984).

[88] E Ascher, "Magnetic anisotropy: A reformulation and its consequences," Helv. Phys. Acta **39**, 466–476 (1966).

[89] Christian Tzschaschel, Kensuke Otani, Ryugo Iida, Tsutomu Shimura, Hiroaki Ueda, Stefan Günther, Manfred Fiebig, and Takuya Satoh, "Ultrafast optical excitation of coherent magnons in antiferromagnetic NiO," Phys. Rev. B **95**, 174407 (2017).

[90] Mois Ilia Aroyo, Juan Manuel Perez-Mato, Cesar Capillas, Eli Kroumova, Svetoslav Ivantchev, Gotzon Madariaga, Asen Kirov, and Hans Wondratschek, "Bilbao Crystallographic Server: I. Databases and crystallographic computing programs," Z. Krist. - Cryst. Mater. **221**, 15–27 (2006).

[91] D. B. Litvin, "Spin point groups," Acta Crystallogr. Sect. A **33**, 279–287 (1977).

[92] K. C. Erb and J. Hlinka, "Vector and bidirector representations of magnetic point groups," Phase Transitions **93**, 1–42 (2019).

[93] Samuel V. Gallego, Jesus Etxebarria, Luis Elcoro, Emre S. Tasci, and J. Manuel Perez-Mato, "Automatic calculation of symmetry-adapted tensors in magnetic and non-magnetic materials: a new tool of the Bilbao Crystallographic Server," Acta Crystallogr. Sect. A Found. Adv. **75**, 438–447 (2019).

[94] Simon Foner, "High-field antiferromagnetic resonance in Cr_2O_3," Phys. Rev. **130**, 183–197 (1963).

[95] Erik Brok, Kim Lefmann, Pascale P. Deen, Bente Lebech, Henrik Jacobsen, Gøran Jan Nilsen, Lukas Keller, and Cathrine Frandsen, "Polarized neutron powder diffraction studies of antiferromagnetic order in bulk and nanoparticle NiO," Phys. Rev. B **91**, 014431 (2015).

[96] F. L. A. Machado, P. R. T. Ribeiro, J. Holanda, R. L. Rodríguez-Suárez, A. Azevedo, and S. M. Rezende, "Spin-flop transition in the easy-plane antiferromagnet nickel oxide," Phys. Rev. B **95**, 104418 (2017).

[97] Eric Ressouche, Nolwenn Kernavanois, Louis-Pierre Regnault, and Jean-Yves Henry, "Magnetic structures of the metal monoxides NiO and CoO re-investigated by spherical neutron polarimetry," Phys. B: Condens. Matter **385-386**, 394–397 (2006).

[98] Hongsong Qiu, Lifan Zhou, Caihong Zhang, Jingbo Wu, Yuanzhe Tian, Shaodong Cheng, Shaobo Mi, Haibin Zhao, Qi Zhang, Di Wu, Biaobing Jin, Jian Chen, and Peiheng Wu, "Ultrafast spin current generated from an antiferromagnet," Nat. Phys. **17**, 388–394 (2020).

[99] Takuya Higuchi, Natsuki Kanda, Hiroharu Tamaru, and Makoto Kuwata-Gonokami, "Selection Rules for Light-Induced Magnetization of a Crystal with Threefold Symmetry: The Case of Antiferromagnetic NiO," Phys. Rev. Lett. **106**, 047401 (2011).

[100] S. Baierl, J. H. Mentink, M. Hohenleutner, L. Braun, T.-M. Do, C. Lange, A. Sell, M. Fiebig, G. Woltersdorf, T. Kampfrath, and R. Huber, "Terahertz-Driven Nonlinear Spin Response of Antiferromagnetic Nickel Oxide," Phys. Rev. Lett. **117**, 197201 (2016).

[101] M. Fiebig, D. Fröhlich, Th. Lottermoser, V. V. Pavlov, R. V. Pisarev, and H.-J Weber, "Second Harmonic Generation in the Centrosymmetric Antiferromagnet NiO," Phys. Rev. Lett. **87**, 137202 (2001).

[102] Takuya Satoh, Sung-Jin Cho, Ryugo Iida, Tsutomu Shimura, Kazuo Kuroda, Hiroaki Ueda, Yutaka Ueda, B. A. Ivanov, Franco Nori, and Manfred Fiebig, "Spin Oscillations in Antiferromagnetic NiO Triggered by Circularly Polarized Light," Phys. Rev. Lett. **105**, 077402 (2010).

[103] T. Kohmoto, T. Moriyasu, S. Wakabayashi, H. Jinn, M. Takahara, and K. Kakita, "Observation of Ultrafast Magnon Dynamics in Antiferromagnetic Nickel Oxide by Optical Pump-Probe and Terahertz Time-Domain Spectroscopies," J. Infrared, Millim., Terahertz Waves **39**, 77–92 (2017).

[104] Tobias Kampfrath, Alexander Sell, Gregor Klatt, Alexej Pashkin, Sebastian Mährlein, Thomas Dekorsy, Martin Wolf, Manfred Fiebig, Alfred Leitenstorfer, and Rupert Huber, "Coherent terahertz control of antiferromagnetic spin waves," Nat. Photonics **5**, 31–34 (2010).

[105] M. dos Santos Dias, N. Biniskos, F. J. dos Santos, K. Schmalzl, J. Persson, F. Bourdarot, N. Marzari, S. Blügel, T. Brückel, and S. Lounis, "Topological magnons driven by the Dzyaloshinskii-Moriya interaction in the centrosymmetric ferromagnet Mn_5Ge_3," (2022), arXiv:2211.16925 [cond-mat.str-el] .

[106] Tapan Chatterji, G. J. McIntyre, and P.-A. Lindgard, "Antiferromagnetic phase transition and spin correlations in NiO," Phys. Rev. B **79**, 172403 (2009).

[107] C.F. Van Doorn and P. de V. Du Plessis, "A neutron scattering investigation of the order of the magnetic transition in NiO," Phys. Lett. A **66**, 141–144 (1978).

[108] D. Betto, Y. Y. Peng, S. B. Porter, G. Berti, A. Calloni, G. Ghiringhelli, and N. B. Brookes, "Three-dimensional dispersion of spin waves measured in NiO by resonant inelastic x-ray scattering," Phys. Rev. B **96**, 020409 (2017).

[109] A. K. Cheetham and D. A. O. Hope, "Magnetic ordering and exchange effects in the antiferromagnetic solid solutions $Mn_xNi_{1-x}O$," Phys. Rev. B **27**, 6964–6967 (1983).

[110] Glen A. Slack, "Crystallography and Domain Walls in Antiferromagnetic NiO Crystals," J. Appl. Phys. **31**, 1571–1582 (1960).

[111] H. A. Alperin, "Neutron Diffraction Investigation of the Magnetic Structure of Nickel Oxide," J. Appl. Phys. **31**, S354–S355 (1960).

[112] N. C. Tombs and H. P. Rooksby, "Structure of Monoxides of some Transition Elements at Low Temperatures," Nature **165**, 442–443 (1950).

[113] H. P. Rooksby, "A note on the structure of nickel oxide at subnormal and elevated temperatures," Acta Crystallogr. **1**, 226–226 (1948).

[114] Y. Noguchi, M. Uchino, H. Hikosaka, T. Atou, K. Kusaba, K. Fukuoka, T. Mashimo, and Y. Syono, "Equation of state of NiO studied by shock compression," J. Phys. Chem. Solids **60**, 509–514 (1999).

[115] T. Eto, S. Endo, M. Imai, Y. Katayama, and T. Kikegawa, "Crystal structure of NiO under high pressure," Phys. Rev. B **61**, 14984–14988 (2000).

[116] V. Fernandez, C. Vettier, F. de Bergevin, C. Giles, and W. Neubeck, "Observation of orbital moment in NiO," Phys. Rev. B **57**, 7870–7876 (1998).

[117] S. K. Kwon and B. I. Min, "Unquenched large orbital magnetic moment in NiO," Phys. Rev. B **62**, 73–75 (2000).

[118] R.J. Radwanski and Z. Ropka, "Orbital moment in CoO and in NiO," Phys. B: Condens. Matter **345**, 107–110 (2004).

[119] Ioannis Petousis, David Mrdjenovich, Eric Ballouz, Miao Liu, Donald Winston, Wei Chen, Tanja Graf, Thomas D. Schladt, Kristin A. Persson, and Fritz B. Prinz, "High-throughput screening of inorganic compounds for the discovery of novel dielectric and optical materials," Sci. Data **4**, 160134 (2017).

[120] P. Kuiper, G. Kruizinga, J. Ghijsen, G. A. Sawatzky, and H. Verweij, "Character of holes in $Li_xNi_{1-x}O$ and their magnetic behavior," Phys. Rev. Lett. **62**, 221–224 (1989).

[121] G. A. Sawatzky and J. W. Allen, "Magnitude and Origin of the Band Gap in NiO," Phys. Rev. Lett. **53**, 2339–2342 (1984).

[122] Ibério de P. R. Moreira, Francesc Illas, and Richard L. Martin, "Effect of Fock exchange on the electronic structure and magnetic coupling in NiO," Phys. Rev. B **65**, 155102 (2002).

[123] Wei-Bing Zhang, Yu-Lin Hu, Ke-Li Han, and Bi-Yu Tang, "Pressure dependence of exchange interactions in NiO," Phys. Rev. B **74**, 054421 (2006).

[124] D. S. Rodbell and J. Owen, "Sublattice Magnetization and Lattice Distortions in MnO and NiO," J. Appl. Phys. **35**, 1002–1003 (1964).

[125] Sergey V. Faleev, Mark van Schilfgaarde, and Takao Kotani, "All-electron self-consistent *GW* approximation: Application to Si, MnO, and NiO," Phys. Rev. Lett. **93**, 126406 (2004).

[126] P. D. Battle, A. K. Cheetham, and G. A. Gehring, "A neutron diffraction study of the structure of the antiferromagnet $Co_pNi_{1-p}O$," J. Appl. Phys. **50**, 7578–7580 (1979).

[127] W. Low, "Paramagnetic and Optical Spectra of Divalent Nickel in Cubic Crystalline Fields," Phys. Rev. **109**, 247–255 (1958).

[128] R. Skomski and D.J. Sellmyer, "Anisotropy of rare-earth magnets," J. Rare Earths **27**, 675–679 (2009).

[129] R. R. Birss and G. J. Keeler, "The advantages of using spherical harmonics to analyse data on magnetocrystalline anisotropy and other non-linear anisotropic properties," physica status solidi (b) **64**, 357–366 (1974).

[130] Freeman J. Dyson, "General Theory of Spin-Wave Interactions," Phys. Rev. **102**, 1217–1230 (1956).

[131] C. H. Woo, Haohua Wen, A. A. Semenov, S. L. Dudarev, and Pui-Wai Ma, "Quantum heat bath for spin-lattice dynamics," Phys. Rev. B **91**, 104306 (2015).

[132] Joseph Barker and Gerrit E. W. Bauer, "Semiquantum thermodynamics of complex ferrimagnets," Phys. Rev. B **100**, 140401 (2019).

[133] Hichem Dammak, Yann Chalopin, Marine Laroche, Marc Hayoun, and Jean-Jacques Greffet, "Quantum Thermal Bath for Molecular Dynamics Simulation," Phys. Rev. Lett. **103**, 190601 (2009).

[134] F. Bloch, "Zur Theorie des Ferromagnetismus," Z. Phys. **61**, 206–219 (1930).

[135] Freeman J. Dyson, "Thermodynamic Behavior of an Ideal Ferromagnet," Phys. Rev. **102**, 1230–1244 (1956).

[136] R. F. L. Evans, U. Atxitia, and R. W. Chantrell, "Quantitative simulation of temperature-dependent magnetization dynamics and equilibrium properties of elemental ferromagnets," Phys. Rev. B **91**, 144425 (2015).

[137] J Anders, C R J Sait, and S A R Horsley, "Quantum Brownian motion for magnets," New J. Phys. **24**, 033020 (2022).

[138] Hazime Mori, "Transport, Collective Motion, and Brownian Motion," Prog. Theor. Phys. **33**, 423–455 (1965).

[139] Hazime Mori, "A Continued-Fraction Representation of the Time-Correlation Functions," Prog. Theor. Phys. **34**, 399–416 (1965).

[140] Ryogo Kubo and Kazuhisa Tomita, "A General Theory of Magnetic Resonance Absorption," J. Phys. Soc. Jpn. **9**, 888–919 (1954).

[141] Yiyan Sun, Young-Yeal Song, Houchen Chang, Michael Kabatek, Michael Jantz, William Schneider, Mingzhong Wu, Helmut Schultheiss, and Axel Hoffmann, "Growth and ferromagnetic resonance properties of nanometer-thick yttrium iron garnet films," Applied Physics Letters **101**, 152405 (2012).

[142] Takahiro Moriyama, Kensuke Hayashi, Keisuke Yamada, Mutsuhiro Shima, Yutaka Ohya, and Teruo Ono, "Intrinsic and extrinsic antiferromagnetic damping in NiO," Phys. Rev. Mater. **3**, 051402 (2019).

[143] David P Landau and Kurt Binder, *A guide to Monte Carlo simulations in statistical physics*, 4th ed. (Cambridge University Press, Cambridge, England, 2014).

[144] B. Rosenstein, Hoi-Lai Yu, and A. Kovner, "Critical exponents of new universality classes," Phys. Lett. B **314**, 381–386 (1993).

[145] C A F Vaz, J A C Bland, and G Lauhoff, "Magnetism in ultrathin film structures," Rep. Prog. Phys. **71**, 056501 (2008).

[146] Matthias Troyer and Uwe-Jens Wiese, "Computational Complexity and Fundamental Limitations to Fermionic Quantum Monte Carlo Simulations," Phys. Rev. Lett. **94**, 170201 (2005).

[147] Matthias Troyer, Masatoshi Imada, and Kazuo Ueda, "Critical Exponents of the Quantum Phase Transition in a Planar Antiferromagnet," J. Phys. Soc. Jpn. **66**, 2957–2960 (1997).

[148] Ryogo Kubo, "The Spin-Wave Theory of Antiferromagnetics," Phys. Rev. **87**, 568–580 (1952).

[149] P. D. Loly, "Calculation of Watson-Like Sums (Integrals)," Phys. Rev. B **4**, 4103–4105 (1971).

[150] Takehiko Oguchi, "Theory of Spin-Wave Interactions in Ferro- and Antiferromagnetism," Phys. Rev. **117**, 117–123 (1960).

[151] Ulrich Köbler, A. Hoser, J. Englich, A. Snezhko, M. Kawakami, M. Beyss, and K. Fischer, "On the Failure of the Bloch–Kubo–Dyson Spin Wave Theory," J. Phys. Soc. Jpn. **70**, 3089–3097 (2001).

[152] Carsten Timm and P. J. Jensen, "Schwinger boson theory of anisotropic ferromagnetic ultrathin films," Phys. Rev. B **62**, 5634–5646 (2000).

[153] Shivam Ghosh, Hitesh J. Changlani, and Christopher L. Henley, "Schwinger boson mean field perspective on emergent spins in diluted Heisenberg antiferromagnets," Phys. Rev. B **92**, 064401 (2015).

[154] J. A. Eisele and F. Keffer, "Effects of Anisotropy on Thermodynamic Properties of Antiferromagnets," Phys. Rev. **96**, 929–933 (1954).

[155] Suman Mandal, Krishnakumar S. R. Menon, Francesco Maccherozzi, and Rachid Belkhou, "Strain-induced nonequilibrium magnetoelastic domain structure and spin reorientation of NiO(100)," Phys. Rev. B **80**, 184408 (2009).

[156] Alireza Kashir, Veronica Goian, Daseob Yoon, Byeong-Gwan Cho, Yoon Hee Jeong, Gil-Ho Lee, and Stanislav Kamba, "Strain effect on magnetic-exchange-induced phonon splitting in NiO films," J. Phys.: Condens. Matter **32**, 405607 (2020).

[157] Natalia Rinaldi-Montes, Pedro Gorria, David Martínez-Blanco, Antonio B. Fuertes, Inés Puente-Orench, Luca Olivi, and Jesús A. Blanco, "Size effects on the Neel temperature of antiferromagnetic NiO nanoparticles," AIP Adv. **6**, 056104 (2016).

[158] I. Negovetic and J. Konstantinović, "The critical behaviour of spontaneous magnetization in the antiferromagnetic NiO," Solid State Commun. **13**, 249–252 (1973).

[159] H.B. Callen and E. Callen, "The present status of the temperature dependence of magnetocrystalline anisotropy, and the power law," J. Phys. Chem. Solids **27**, 1271–1285 (1966).

[160] C. Zener, "Classical Theory of the Temperature Dependence of Magnetic Anisotropy Energy," Phys. Rev. **96**, 1335–1337 (1954).

[161] N. Inaba, Y. Uesaka, and M. Futamoto, "Compositional and temperature dependence of basic magnetic properties of CoCr-alloy thin films," IEEE Trans. Magn. **36**, 54–60 (2000).

[162] Biplab K. Chatterjee, C. K. Ghosh, and K. K. Chattopadhyay, "Temperature dependence of magnetization and anisotropy in uniaxial $NiFe_2O_4$ nanomagnets: Deviation from the callen-callen power law," Journal of Applied Physics **116**, 153904 (2014).

[163] J. J. Rhyne and A. E. Clark, "Magnetic Anisotropy of Terbium and Dysprosium," J. Appl. Phys. **38**, 1379–1380 (1967).

[164] Naofumi Kobayashi, Kazushige Hyodo, and Akimasa Sakuma, "Effects of spin fluctuation on the magnetic anisotropy constant of itinerant electron magnets," Jpn. J. Appl. Phys. **55**, 100306 (2016).

[165] O. N Mryasov, U Nowak, K. Y Guslienko, and R. W Chantrell, "Temperature-dependent magnetic properties of FePt: Effective spin Hamiltonian model," Eur. Lett. (EPL) **69**, 805–811 (2005).

[166] M. D. Kuz'min, "Linear theory of magnetocrystalline anisotropy and magnetostriction in exchange-dominated 3d-4f intermetallics," Phys. Rev. B **46**, 8219–8226 (1992).

[167] R. Skomski, A. Kashyap, and D.J. Sellmyer, "Finite-temperature anisotropy of PtCo magnets," IEEE Trans. Magn. **39**, 2917–2919 (2003).

[168] J.M.D. Coey, "Intrinsic magnetic properties of compounds with the $Nd_2Fe_{14}B$ structure," J. Less Common Met. **126**, 21–34 (1986).

[169] T. Holstein and H. Primakoff, "Field Dependence of the Intrinsic Domain Magnetization of a Ferromagnet," Phys. Rev. **58**, 1098–1113 (1940).

[170] Olivier Delaire, Karol Marty, Matthew B Stone, Paul RC Kent, Matthew S Lucas, Douglas L Abernathy, David Mandrus, and Brian C Sales, "Phonon softening and metallization of a narrow-gap semiconductor by thermal disorder," Proceedings of the National Academy of Sciences **108**, 4725–4730 (2011).

[171] F. Keffer and R. Loudon, "Simple Physical Theory of Spin Wave Interactions," J. Appl. Phys. **32**, S2–S7 (1961).

[172] Charles Kittel and Herbert Kroemer, *Thermal physics*, Vol. 9690 (Wiley New York, 1969).

[173] Tapan Chatterji, "Chapter 6 - Magnetic Excitations," in *Neutron Scattering from Magnetic Materials*, edited by Tapan Chatterji (Elsevier Science, Amsterdam, 2006) pp. 245–331.

[174] Stephen W Lovesey, *Theory of neutron scattering from condensed matter* (Clarendon Press, 1984).

[175] G Wenzel and M Wagner, "Magnon renormalisation in Heisenberg antiferromagnets," J. Phys. C: Solid State Phys. **10**, 5043–5056 (1977).

[176] Tuto Nakamura and Micheline Bloch, "Temperature Dependence of the Exchange Stiffness in Ferrimagnets," Phys. Rev. **132**, 2528–2539 (1963).

[177] G. Pepy, "Spin waves in MnO; from 4°K to temperatures close to T_N," J. Phys. Chem. Solids **35**, 433–444 (1974).

[178] Micheline Bloch, "Magnon Renormalization in Ferromagnets Near the Curie Point," Phys. Rev. Lett. **9**, 286–287 (1962).

[179] K. Grobsky and B. N. Harmon, "Spin-wave temperature dependence of gadolinium," J. Appl. Phys. **49**, 2147–2149 (1978).

[180] M W Stringfellow, "Observation of spin-wave renormalization effects in iron and nickel," J. Phys. C: Solid State Phys. **1**, 950–965 (1968).

[181] Takeo Izuyama and Ryogo Kubo, "Some Considerations on the Magnetic Carriers in Ferromagnetic Transition Metals," J. Appl. Phys. **35**, 1074–1081 (1964).

[182] S. R. Chinn, R. W. Davies, and H. J. Zeiger, "Spin-Wave Theory of Two-Magnon Raman Scattering in a Two-Dimensional Antiferromagnet," Phys. Rev. B **4**, 4017–4023 (1971).

[183] Ryogo Kubo, "The Spin-Wave Theory as a Variational Method and Its Application to Antiferromagnetism," Rev. Mod. Phys. **25**, 344–351 (1953).

[184] Kun Chen and D. P. Landau, "Spin-dynamics study of the dynamic critical behavior of the three-dimensional classical Heisenberg ferromagnet," Phys. Rev. B **49**, 3266–3274 (1994).

[185] Joseph Barker and Gerrit E. W. Bauer, "Thermal Spin Dynamics of Yttrium Iron Garnet," Phys. Rev. Lett. **117**, 217201 (2016).

[186] Erik G. Brandt and Olle Edholm, "Dynamic Structure Factors from Lipid Membrane Molecular Dynamics Simulations," Biophys. J. **96**, 1828–1838 (2009).

[187] J. W. Lynn and H. A. Mook, "Temperature dependence of the dynamic susceptibility of nickel," Phys. Rev. B **23**, 198–206 (1981).

[188] M. Grimsditch, Sudha Kumar, and R.S. Goldman, "A Brillouin scattering investigation of NiO," J. Magn. Magn. Mater. **129**, 327–333 (1994).

[189] M. Grimsditch, L. E. McNeil, and D. J. Lockwood, "Unexpected behavior of the antiferromagnetic mode of NiO," Phys. Rev. B **58**, 14462–14466 (1998).

[190] Hisamoto Kondoh, "Antiferromagnetic Resonance in NiO in Far-infrared Region," J. Phys. Soc. Jpn. **15**, 1970–1975 (1960).

[191] A Roggenbuck, H Schmitz, A Deninger, I Cámara Mayorga, J Hemberger, R Güsten, and M Grüninger, "Coherent broadband continuous-wave terahertz spectroscopy on solid-state samples," New J. Phys. **12**, 043017 (2010).

[192] Arman Amirzhan, Paul Chevalier, Jeremy Rowlette, H. Ted Stinson, Michael Pushkarsky, Timothy Day, Henry O. Everitt, and Federico Capasso, "A quantum cascade laser-pumped molecular laser tunable over 1 thz," APL Photonics **7**, 016107 (2022).

[193] A. Fisher, Y. Park, M. Lenz, A. Ody, R. Agustsson, T. Hodgetts, A. Murokh, and P. Musumeci, "Single-pass high-efficiency terahertz free-electron laser," Nat. Photonics **16**, 441–447 (2022).

[194] A. J. Sievers and M. Tinkham, "Far Infrared Antiferromagnetic Resonance in MnO and NiO," Phys. Rev. **129**, 1566–1571 (1963).

[195] D. A. Tennant, B. Lake, A. J. A. James, F. H. L. Essler, S. Notbohm, H.-J. Mikeska, J. Fielden, P. Kögerler, P. C. Canfield, and M. T. F. Telling, "Anomalous dynamical line shapes in a quantum magnet at finite temperature," Phys. Rev. B **85**, 014402 (2012).

[196] D. L. Quintero-Castro, B. Lake, A. T. M. N. Islam, E. M. Wheeler, C. Balz, M. Månsson, K. C. Rule, S. Gvasaliya, and A. Zheludev, "Asymmetric Thermal Line Shape Broadening in a Gapped 3D Antiferromagnet: Evidence for Strong Correlations at Finite Temperature," Phys. Rev. Lett. **109**, 127206 (2012).

[197] E. Aytan, B. Debnath, F. Kargar, Y. Barlas, M. M. Lacerda, J. X. Li, R. K. Lake, J. Shi, and A. A. Balandin, "Spin-phonon coupling in antiferromagnetic nickel oxide," Appl. Phys. Lett. **111**, 252402 (2017).

[198] Pavel Stremoukhov, Davies Carl S, Ansar Safin, Sergey Nikitov, and Andrei Kirilyuk, "Phononic manipulation of antiferromagnetic domains in NiO," New J. Phys. **24**, 023009 (2022).

[199] T. Thomson, "Chapter 10 - magnetic properties of metallic thin films," in *Metallic Films for Electronic, Optical and Magnetic Applications*, edited by Katayun Barmak and Kevin Coffey (Woodhead Publishing, 2014) pp. 454–546.

[200] Sangita S. Kalarickal, Pavol Krivosik, Mingzhong Wu, Carl E. Patton, Michael L. Schneider, Pavel Kabos, T. J. Silva, and John P. Nibarger, "Ferromagnetic resonance linewidth in metallic thin films: Comparison of measurement methods," Journal of Applied Physics **99**, 093909 (2006).

[201] A. Fainstein, E. Winkler, A. Butera, and J. Tallon, "Magnetic interactions and magnon gap in the ferromagnetic superconductor $RuSr_2GdCu_2O_8$," Phys. Rev. B **60**, R12597–R12600 (1999).

[202] M. Belmeguenai, T. Martin, G. Woltersdorf, M. Maier, and G. Bayreuther, "Frequency- and time-domain investigation of the dynamic properties of interlayer-exchange-coupled $Ni_{81}Fe_{19}$/Ru/$Ni_{81}Fe_{19}$ thin films," Phys. Rev. B **76**, 104414 (2007).

[203] Chi-Kuen Lo, "Instrumentation for ferromagnetic resonance spectrometer," in *Ferromagnetic Resonance*, edited by Orhan Yalcin (IntechOpen, Rijeka, 2013) Chap. 2.

[204] I. Neudecker, G. Woltersdorf, B. Heinrich, T. Okuno, G. Gubbiotti, and C.H. Back, "Comparison of frequency, field, and time domain ferromagnetic resonance methods," J. Magn. Magn. Mater. **307**, 148–156 (2006).

[205] G. M. Smith, J. C. G. Lesurf, R. H. Mitchell, and P. C. Riedi, "Quasi-optical cw mm-wave electron spin resonance spectrometer," Review of Scientific Instruments **69**, 3924–3937 (1998).

[206] C. D. Batista, K. Hallberg, and A. A. Aligia, "Electron spin resonance of defects in the haldane system Y_2BaNiO_5," Phys. Rev. B **60**, R12553–R12556 (1999).

[207] H. Kikuchi, H. Ohta, S. Okubo, I. Kagomiya, M. Toki, K. Kohn, and K. Shiratori, "ESR study on magnetic ordering of spin-frustrated antiferromagnet $ZnCr_2O_4$ single crystal," in *EPR in the 21st Century*, edited by Asako Kawamori, Jun Yamauchi, and Hitoshi Ohta (Elsevier Science B.V., Amsterdam, 2002) pp. 755–758.

[208] Gail E. Fanucci, J. Krzystek, Mark W. Meisel, Louis-Claude Brunel, and Daniel R. Talham, "Antiferromagnetic Resonance as a Tool for Investigating Magnetostructural Correlations: The Canted Antiferromagnetic State of $KMnPO_4{\cdot}H_2O$ and a Series of Manganese Phosphonates," J. Am. Chem. Soc. **120**, 5469–5479 (1998).

[209] J. Ubbink, J.A. Poulis, H.J. Gerritsen, and C.J. Gorter, "Anti-ferromagnetic resonance in copper chloride," Physica **18**, 361–368 (1952).

[210] J Ubbink, J.A Poulis, and C.J Gorter, "Paramagnetic resonance in iron alums," Physica **17**, 213–220 (1951).

[211] Yuan Zhang, Junfeng Dai, Xiangli Zhong, Dongwen Zhang, Gaokuo Zhong, and Jiangyu Li, "Probing ultrafast dynamics of ferroelectrics by time-resolved pump-probe spectroscopy," Advanced Science **8**, 2102488 (2021).

[212] Simon Foner, "High-field antiferromagnetic resonance in mnf_2 using pulsed fields and millimeter wavelengths," Phys. Rev. **107**, 683–685 (1957).

[213] David MacNeill, Justin T. Hou, Dahlia R. Klein, Pengxiang Zhang, Pablo Jarillo-Herrero, and Luqiao Liu, "Gigahertz frequency antiferromagnetic resonance and strong magnon-magnon coupling in the layered crystal $crcl_3$," .

[214] A. A. Mukhin, V. Yu. Ivanov, V. D. Travkin, A. Pimenov, A. Loidl, and A. M. Balbashov, "Antiferromagnetic resonance in the canted phase of $La_{1-x}Sr_xMnO_3$: Experimental evidence against electronic phase separation," Europhysics Letters **49**, 514 (2000).

[215] A.A. Mukhin, A.N. Lobanov, M. Goiran, J. Leotin, and A.A. Volkov, "Quasioptical study of antiferromagnetic resonance in $YFeO_3$ at submillimeter wavelength under high pulsed magnetic fields," Journal of Magnetic Resonance **195**, 60–66 (2008).

[216] Takahiro Moriyama, Kensuke Hayashi, Keisuke Yamada, Mutsuhiro Shima, Yutaka Ohya, Yaroslav Tserkovnyak, and Teruo Ono, "Enhanced antiferromagnetic resonance linewidth in NiO/Pt and NiO/Pd," Phys. Rev. B **101**, 060402 (2020).

[217] Zhe Wang, S. Kovalev, N. Awari, Min Chen, S. Germanskiy, B. Green, J.-C. Deinert, T. Kampfrath, J. Milano, and M. Gensch, "Magnetic field dependence of antiferromagnetic resonance in NiO," Appl. Phys. Lett. **112**, 252404 (2018).

[218] P Bowlan, S A Trugman, D A Yarotski, A J Taylor, and R P Prasankumar, "Using ultrashort terahertz pulses to directly probe spin dynamics in insulating antiferromagnets," Journal of Physics D: Applied Physics **51**, 194003 (2018).

[219] Natsuki Kanda, Takuya Higuchi, Hirokatsu Shimizu, Kuniaki Konishi, Kosuke Yoshioka, and Makoto Kuwata-Gonokami, "The vectorial control of magnetization by light," Nat. Commun. **2**, 362 (2011).

[220] A. M. Kalashnikova, A. V. Kimel, R. V. Pisarev, V. N. Gridnev, P. A. Usachev, A. Kirilyuk, and Th. Rasing, "Impulsive excitation of coherent magnons and

phonons by subpicosecond laser pulses in the weak ferromagnet $febo_3$," Phys. Rev. B **78**, 104301 (2008).

[221] Alexander G Gurevich and Gennadii A Melkov, "Chapter 3 - Antiferromagnets and Ferrites," in *Magnetization oscillations and waves* (CRC press, 1996).

[222] Alexander G Gurevich and Gennadii A Melkov, "Chapter 9 - Nonlinear oscillations of magnetization," in *Magnetization oscillations and waves* (CRC press, 1996).

[223] R D Averitt and A J Taylor, "Ultrafast optical and far-infrared quasiparticle dynamics in correlated electron materials," J. Phys.: Condens. Matter **14**, R1357–R1390 (2002).

[224] A.I. Akhiezer, V.G. Bar'yakhtar, and S.V. Peletminskii, *Spin Waves*, North-Holland series in low temperature physics (North-Holland Publishing Company, 1968).

[225] VS L'vov and MI Shirokov, "Nonlinear theory of parametric excitation of spin waves in antiferromagnets," Zh. Eksp. Teor. Fiz **67**, 1932–1948 (1974).

[226] Alexander G Gurevich and Gennadii A Melkov, "Chapter 10 - Parametric excitation of magnetic oscillations and waves," in *Magnetization oscillations and waves* (CRC press, 1996).

[227] D.J. Lockwood, M.G. Cottam, and J.H. Baskey, "One- and two-magnon excitations in NiO," J. Magn. Magn. Mater. **104-107**, 1053–1054 (1992).

[228] J Milton Pereira and M.G Cottam, "Spin waves in Heisenberg antiferromagnetic films with (001), (011), and (111) surfaces," J. Magn. Magn. Mater. **226-230**, 1648–1649 (2001).

[229] J Milton Pereira and M.G Cottam, "Spin waves in heisenberg antiferromagnetic films with (001), (011), and (111) surfaces," Journal of Magnetism and Magnetic Materials **226-230**, 1648–1649 (2001), proceedings of the International Conference on Magnetism (ICM 2000).

[230] I. Sänger, V. V. Pavlov, M. Bayer, and M. Fiebig, "Distribution of antiferromagnetic spin and twin domains in NiO," Phys. Rev. B **74**, 144401 (2006).

[231] D. Bossini, M. Pancaldi, L. Soumah, M. Basini, F. Mertens, M. Cinchetti, T. Satoh, O. Gomonay, and S. Bonetti, "Ultrafast Amplification and Nonlinear Magnetoelastic Coupling of Coherent Magnon Modes in an Antiferromagnet," Phys. Rev. Lett. **127**, 077202 (2021).

[232] M. Takahara, H. Jinn, S. Wakabayashi, T. Moriyasu, and T. Kohmoto, "Observation of coherent acoustic phonons and magnons in an antiferromagnet NiO," Phys. Rev. B **86**, 094301 (2012).

[233] Junichi Nishitani, Takeshi Nagashima, and Masanori Hangyo, "Coherent control of terahertz radiation from antiferromagnetic magnons in nio excited by optical laser pulses," Phys. Rev. B **85**, 174439 (2012).

[234] Junichi Nishitani, Kohei Kozuki, Takeshi Nagashima, and Masanori Hangyo, "Terahertz radiation from coherent antiferromagnetic magnons excited by femtosecond laser pulses," Applied Physics Letters **96**, 221906 (2010).

[235] P Bowlan, S A Trugman, D A Yarotski, A J Taylor, and R P Prasankumar, "Using ultrashort terahertz pulses to directly probe spin dynamics in insulating antiferromagnets," J. Phys. D: Appl. Phys. **51**, 194003 (2018).

[236] Pavel Stremoukhov, Ansar Safin, Casper F. Schippers, Reinoud Lavrijsen, Maurice Bal, Uli Zeitler, Alexandr Sadovnikov, Kamyar Saeedi Ilkhchy, Sergey Nikitov, and Andrei Kirilyuk, "Strongly nonlinear antiferromagnetic dynamics in high magnetic fields," (2022), arXiv:2211.00353 [cond-mat.mtrl-sci] .

[237] Y Mukai, H Hirori, T Yamamoto, H Kageyama, and K Tanaka, "Nonlinear magnetization dynamics of antiferromagnetic spin resonance induced by intense terahertz magnetic field," New J. Phys. **18**, 013045 (2016).

[238] O Gomonay and D Bossini, "Linear and nonlinear spin dynamics in multi-domain magnetoelastic antiferromagnets," J. Phys. D: Appl. Phys. **54**, 374004 (2021).

[239] Sarah Jenkins, Roy. W. Chantrell, and Richard F. L. Evans, "Atomistic simulations of the magnetic properties of Ir_xMn_{1-x} alloys," Phys. Rev. Mater. **5**, 034406 (2021).

[240] Hans T. Nembach, Justin M. Shaw, Mathias Weiler, Emilie Jué, and Thomas J. Silva, "Linear relation between Heisenberg exchange and interfacial Dzyaloshinskii–Moriya interaction in metal films," Nat. Phys. **11**, 825–829 (2015).

[241] Jamileh Beik Mohammadi, Bartek Kardasz, Georg Wolf, Yizhang Chen, Mustafa Pinarbasi, and Andrew D. Kent, "Reduced Exchange Interactions in Magnetic Tunnel Junction Free Layers with Insertion Layers," ACS Appl. Electron. Mater. **1**, 2025–2029 (2019).

[242] Yifan Zhou, Rhodri Mansell, Sergio Valencia, Florian Kronast, and Sebastiaan van Dijken, "Temperature dependence of the Dzyaloshinskii-Moriya interaction in ultrathin films," Phys. Rev. B **101**, 054433 (2020).

[243] Sarah Schlotter, Parnika Agrawal, and Geoffrey S. D. Beach, "Temperature dependence of the Dzyaloshinskii-Moriya interaction in Pt/Co/Cu thin film heterostructures," Applied Physics Letters **113**, 092402 (2018).

[244] Khulaif Alshammari, Eloi Haltz, Mohammed Alyami, Mannan Ali, Paul S. Keatley, Christopher H. Marrows, Joseph Barker, and Thomas A. Moore, "Scaling of Dzyaloshinskii-Moriya interaction with magnetization in Pt/Co(Fe)B/Ir multilayers," Phys. Rev. B **104**, 224402 (2021).

[245] Kodai Niitsu, "Temperature dependence of magnetic exchange stiffness in iron and nickel," J. Phys. D: Appl. Phys. **53**, 39LT01 (2020).

[246] Michael E. Fisher, Michael N. Barber, and David Jasnow, "Helicity Modulus, Superfluidity, and Scaling in Isotropic Systems," Phys. Rev. A **8**, 1111–1124 (1973).

[247] Rajiv R. P. Singh and David A. Huse, "Microscopic calculation of the spin-stiffness constant for the spin-(1/2 square-lattice Heisenberg antiferromagnet," Phys. Rev. B **40**, 7247–7251 (1989).

[248] K. K. Mon, "Monte Carlo studies of spin-stiffness fluctuations in the two-dimensional classical Heisenberg model," Phys. Rev. B **44**, 6809–6811 (1991).

[249] P. Azaria, B. Delamotte, T. Jolicoeur, and D. Mouhanna, "Spin stiffness of canted antiferromagnets," Phys. Rev. B **45**, 12612–12615 (1992).

[250] C. J. Hamer, Zheng Weihong, and J. Oitmaa, "Spin-wave stiffness of the Heisenberg antiferromagnet at zero temperature," Phys. Rev. B **50**, 6877–6888 (1994).

[251] M Caffarel, P Azaria, B Delamotte, and D Mouhanna, "Monte Carlo Calculation of the Spin Stiffness of the Two-Dimensional Heisenberg Model," Eur. Lett. (EPL) **26**, 493–498 (1994).

[252] A. Billoire, "Monte Carlo simulation at very low temperature: The spin stiffness of the two-dimensional Heisenberg model," Phys. Rev. B **54**, 990–993 (1996).

[253] A.S.T. Pires, "Calculation of the spin stiffness for the anisotropic classical Heisenberg model using a self-consistent harmonic approximation," Solid State Commun. **100**, 791–794 (1996).

[254] T. Pardini, R. R. P. Singh, A. Katanin, and O. P. Sushkov, "Spin stiffness of the anisotropic heisenberg model on the square lattice and a possible mechanism for pinning of the electronic liquid crystal direction in underdoped $YBa_2Cu_3O_{6.45}$," Phys. Rev. B **78**, 024439 (2008).

[255] M. G. Gonzalez, E. A. Ghioldi, C. J. Gazza, L. O. Manuel, and A. E. Trumper, "One dimensionalization in the spin-1 Heisenberg model on the anisotropic triangular lattice," Phys. Rev. B **96**, 174423 (2017).

[256] R. Moreno, R. F. L. Evans, S. Khmelevskyi, M. C. Muñoz, R. W. Chantrell, and O. Chubykalo-Fesenko, "Temperature-dependent exchange stiffness and domain wall width in Co," Phys. Rev. B **94**, 104433 (2016).

[257] P. Dürrenfeld, F. Gerhard, J. Chico, R. K. Dumas, M. Ranjbar, A. Bergman, L. Bergqvist, A. Delin, C. Gould, L. W. Molenkamp, and J. Åkerman, "Tunable damping, saturation magnetization, and exchange stiffness of half-Heusler NiMnSb thin films," Phys. Rev. B **92**, 214424 (2015).

[258] A. N. Bogdanov and I. E. Dragunov, "Metastable states, spin–reorientation transitions, and domain structures in planar hexagonal antiferromagnets," Low Temp. Phys. **24**, 852–857 (1998).

[259] R. Lebrun, A. Ross, O. Gomonay, V. Baltz, U. Ebels, A.-L. Barra, A. Qaiumzadeh, A. Brataas, J. Sinova, and M. Kläui, "Long-distance spin-transport across

the Morin phase transition up to room temperature in ultra-low damping single crystals of the antiferromagnet α-Fe_2O_3," Nat. Commun. **11**, 6332 (2020).

[260] A. M. Belemuk and S. M. Stishov, "Phase Transitions in Chiral Magnets: Classical Monte Carlo Calculations," J. Exp. Theor. Phys. **131**, 752–760 (2020).

[261] U. Atxitia, D. Hinzke, O. Chubykalo-Fesenko, U. Nowak, H. Kachkachi, O. N. Mryasov, R. F. Evans, and R. W. Chantrell, "Multiscale modeling of magnetic materials: Temperature dependence of the exchange stiffness," Phys. Rev. B **82**, 134440 (2010).

[262] Levente Rózsa, Unai Atxitia, and Ulrich Nowak, "Temperature scaling of the Dzyaloshinsky-Moriya interaction in the spin wave spectrum," Phys. Rev. B **96**, 094436 (2017).

[263] Yuta Toga, Masamichi Nishino, Seiji Miyashita, Takashi Miyake, and Akimasa Sakuma, "Anisotropy of exchange stiffness based on atomic-scale magnetic properties in the rare-earth permanent magnet $Nd_2Fe_{14}B$," Phys. Rev. B **98**, 054418 (2018).

[264] Qihua Gong, Min Yi, Richard F. L. Evans, Bai-Xiang Xu, and Oliver Gutfleisch, "Calculating temperature-dependent properties of $nd_2fe_{14}B$ permanent magnets by atomistic spin model simulations," Phys. Rev. B **99**, 214409 (2019).

[265] Pablo G. Debenedetti, "On the relationship between principal fluctuations and stability coefficients in multicomponent systems," J. Chem. Phys. **84**, 1778–1787 (1986).

[266] Gyung-Min Choi, "Exchange stiffness and damping constants of spin waves in CoFeB films," J. Magn. Magn. Mater. **516**, 167335 (2020).

[267] Karampuri Yadagiri, Yuxi Wang, and Tao Wu, "Temperature-Dependent Exchange Stiffness of Spin-Wave in Ta/CoFeB by Ferromagnetic Resonance Spectroscopy," IEEE Trans. Magn. **57**, 1–7 (2021).

[268] H. J. Waring, Y. Li, N. A. B. Johansson, C. Moutafis, I. J. Vera-Marun, and T. Thomson, "Exchange stiffness constant determination using multiple-mode FMR perpendicular standing spin waves," Journal of

Applied Physics **133**, 063901 (2023), https://pubs.aip.org/aip/jap/article-pdf/doi/10.1063/5.0135024/16707585/063901_1_online.pdf .

[269] N Akulov, "Zur quantentheorie der temperaturabhängigkeit der magnetisierungskurve," Zeitschrift für Physik **100**, 197–202 (1936).

[270] R. Gilmore, "Length and curvature in the geometry of thermodynamics," Phys. Rev. A **30**, 1994–1997 (1984).

[271] Robert Gilmore, *Catastrophe Theory* (Wiley, 2007).

[272] Robert F. Sekerka, "13 - thermodynamics of fluid-fluid interfaces," in *Thermal Physics*, edited by Robert F. Sekerka (Elsevier, Amsterdam, 2015) pp. 185–213.

[273] Eldred H Chimowitz, *Introduction to critical phenomena in fluids* (Oxford University Press, 2005).

[274] Francisco Nogueira Lima, "Thermodynamic stability conditions as an eigenvalues fundamental problem," in *Recent Developments in the Solution of Nonlinear Differential Equations*, edited by Bruno Carpentieri (IntechOpen, Rijeka, 2021) Chap. 21.

[275] A. N. Galdina, "Supercritical behavior of thermodynamic systems," J. Phys. Electron. **27**, 19–26 (2019).

[276] Yuki Sughiyama, Dimitri Loutchko, Atsushi Kamimura, and Tetsuya J. Kobayashi, "Hessian geometric structure of chemical thermodynamic systems with stoichiometric constraints," Phys. Rev. Res. **4**, 033065 (2022).

[277] F. Weinhold, "Metric geometry of equilibrium thermodynamics," J. Chem. Phys. **63**, 2479–2483 (1975).

[278] George Ruppeiner, "Thermodynamic curvature measures interactions," Am. J. Phys. **78**, 1170–1180 (2010).

[279] Ti-Wei Xue and Zeng-Yuan Guo, "What Is the Real Clausius Statement of the Second Law of Thermodynamics?" Entropy **21**, 926 (2019).

[280] M. J. Moran, H. N. Shapiro, D. D. Boettner, and M. B. Bailey, *Fundamentals of engineering thermodynamics* (John Wiley & Sons, 2010).

[281] Francis W. Sears, "Modified Form of Carathéodory's Second Axiom," Am. J. Phys. **34**, 665–666 (1966).

[282] Carlo Cercignani, *Ludwig Boltzmann: the man who trusted atoms* (OUP Oxford, 2006).

[283] Richard Chace Tolman, *The principles of statistical mechanics* (Courier Corporation, 1979).

[284] Donald H Andrews, *The Collected Works of J. Willard Gibbs. Two volumes* (ACS Publications, 1929).

[285] Herbert B Callen, "Thermodynamics and an introduction to thermostatistics," John Wiley & Sons, New York (1960).

[286] L Tisza, "Generalized thermodynamics," (1966).

[287] Takaaki Inada, Xu Zhang, Akira Yabe, Makoto Tanaka, and Yoshiyuki Kozawa, "Effect of ultrasonic vibration on freezing of supercooled water," (1999).

[288] Vladimir Semenchenko, Norman G. Anderson, and R Kennedy, "Surface phenomena in metals and alloys," (1962).

[289] V. N. Kartsev and I. V. Bogomolova, "Thermodynamic stability and structure of liquid-phase systems," J. Struct. Chem. **47**, S159–S166 (2006).

[290] D Yamada, "Thermodynamics of black holes in the Schrödinger space," Class. Quantum Gravity **26**, 075006 (2009).

[291] Pamela Mills, Charles F. Anderson, and M. Thomas Record, "Grand canonical Monte Carlo calculations of thermodynamic coefficients for a primitive model of DNA-salt solutions," J. Phys. Chem. **90**, 6541–6548 (1986).

[292] Nathan A. Mahynski, Jeffrey R. Errington, and Vincent K. Shen, "Multivariable extrapolation of grand canonical free energy landscapes," The Journal of Chemical Physics **147**, 234111 (2017).

[293] M. Dehghani, "Thermodynamic properties of novel black hole solutions in the Einstein–Born–Infeld-dilaton gravity theory," Eur. Phys. J. C **80**, 996 (2020).

[294] Balázs Nagyfalusi, László Udvardi, and László Szunyogh, "Metadynamics study of the temperature dependence of magnetic anisotropy and spin-reorientation transitions in ultrathin films," Phys. Rev. B **100**, 174429 (2019).

[295] Nikolai V. Prokof'ev and Boris V. Svistunov, "Two definitions of superfluid density," Phys. Rev. B **61**, 11282–11284 (2000).

[296] Fugao Wang and D. P. Landau, "Efficient, Multiple-Range Random Walk Algorithm to Calculate the Density of States," Phys. Rev. Lett. **86**, 2050–2053 (2001).

[297] Wenwu Xu, Andrew P. Horsfield, David Wearing, and Peter D. Lee, "Classical and quantum calculations of the temperature dependence of the free energy of argon," Comput. Mater. Sci. **144**, 36–41 (2018).

[298] Richard F. L. Evans, Levente Rózsa, Sarah Jenkins, and Unai Atxitia, "Temperature scaling of two-ion anisotropy in pure and mixed anisotropy systems," Phys. Rev. B **102**, 020412 (2020).

[299] Adam Jacobsson, Biplab Sanyal, Marjana Ležaić, and Stefan Blügel, "Exchange parameters and adiabatic magnon energies from spin-spiral calculations," Phys. Rev. B **88**, 134427 (2013).

[300] Yurii A Izyumov, "Strongly correlated electrons: the t-J model," Physics-Uspekhi **40**, 445–476 (1997).

[301] Paul Ziesche, Stefan Kurth, and John P. Perdew, "Density functionals from LDA to GGA," Comput. Mater. Sci. **11**, 122–127 (1998).

[302] Per-Olov Löwdin, "A Note on the Quantum-Mechanical Perturbation Theory," J. Chem. Phys. **19**, 1396–1401 (1951).

[303] Ralph Skomski, *Simple Models of Magnetism* (Oxford University Press, 2008).

[304] E. Tsymbal, "Evaluation of the magnetic dipolar fields from layered systems on atomic scale," J. Magn. Magn. Mater. **130**, L6–L12 (1994).

[305] R. M. White, M. Sparks, and I. Ortenburger, "Diagonalization of the Antiferromagnetic Magnon-Phonon Interaction," Phys. Rev. **139**, A450–A454 (1965).